TU Delft

Delft University of Technology

CMOS Integrated Circuits to Interface with a 2D Array of Ultrasound Transducers for Ultrasound Brain Stimulation

Rivandi, H.

DOI
10.4233/uuid:6437f79e-9448-4577-b135-28712825d47e

Publication date
2024

Document Version
Final published version

Citation (APA)
Rivandi, H. (2024). *CMOS Integrated Circuits to Interface with a 2D Array of Ultrasound Transducers for Ultrasound Brain Stimulation*. [Dissertation (TU Delft), Delft University of Technology]. https://doi.org/10.4233/uuid:6437f79e-9448-4577-b135-28712825d47e

Important note
To cite this publication, please use the final published version (if applicable).
Please check the document version above.

Copyright
Other than for strictly personal use, it is not permitted to download, forward or distribute the text or part of it, without the consent of the author(s) and/or copyright holder(s), unless the work is under an open content license such as Creative Commons.

Takedown policy
Please contact us and provide details if you believe this document breaches copyrights.
We will remove access to the work immediately and investigate your claim.

This work is downloaded from Delft University of Technology.
For technical reasons the number of authors shown on this cover page is limited to a maximum of 10.

CMOS INTEGRATED CIRCUITS TO INTERFACE WITH A 2D ARRAY OF ULTRASOUND TRANSDUCERS FOR ULTRASOUND BRAIN STIMULATION

CMOS INTEGRATED CIRCUITS TO INTERFACE WITH A 2D ARRAY OF ULTRASOUND TRANSDUCERS FOR ULTRASOUND BRAIN STIMULATION

Dissertation

for the purpose of obtaining the degree of doctor
at Delft University of Technology,
by the authority of the Rector Magnificus, prof. dr. ir. T.H.J.J. van der Hagen,
chair of the Board for Doctorates,
to be defended publicly on
Monday 9 December 2024 at 17:30 o'clock

by

Hassan Rivandi

Master of Science in Electrical Engineering,
Ferdowsi University of Mashhad, Mashhad, Iran,
born in Sabzevar, Iran.

This dissertation has been approved by the:

Promotor: Prof. dr. ir. W.A. Serdijn
Copromotor: Dr. T.M. Lopes Marta da Costa

Composition of the doctoral committee:

Rector Magnificus	chairperson
Prof.dr.ir. W.A. Serdijn	Delft University of Technology, promotor
Dr. T.M. Lopes Marta da Costa	Delft University of Technology, copromotor
Independent members:	
Prof.dr. P.J. French	Delft University of Technology
Prof.dr.ir. N. de Jong	Delft University of Technology
Prof.dr. K.L. Shepard	Columbia University, United States
Prof.dr. M. Bicho dos Santos	Technical University of Lisbon, Portugal
Dr. M. Kiani	Pennsylvania State University, United States

Keywords: Ultrasound neuromodulation, phased array transmitter ASIC, ultrasound transducer, ultrasound-guided, beamforming circuit
Printed by: Gildeprint
Cover: Maede Shakeri

Copyright © 2024 by Hassan Rivandi

ISBN 978-94-6384-683-7

An electronic version of this dissertation is available at
http://repository.tudelft.nl/.

To Faride,
for your unwavering support, love, and endless encouragement throughout this journey.

Contents

Summary

Neurological disorders profoundly affect quality of life, impairing essential functions like memory, cognition, and movement. Traditional treatments are often limited due to the complexity of the brain, the invasiveness of procedures, or the poor precision of the treatment. Ultrasound (US) neuromodulation offers a promising and minimally invasive alternative, using ultrasound waves to modulate neural activity in deep brain regions with high spatial resolution. Despite its potential, a technological gap limits preclinical ultrasound neuromodulation studies, as current ultrasound devices are too bulky and imprecise for flexible and continuous neuromodulation in freely moving rodents. Moreover, precise targeting is essential for effective neuromodulation, necessitating fine control over the focal spot location. This thesis aims to discover new system-level and circuit-level approaches to designing a miniaturized, power-efficient, and high-spatial-resolution 2D phased array transmitter application-specific integrated circuit (ASIC). These approaches are guided by the vision of implementing a miniaturized ultrasound transducer device for precise ultrasound neuromodulation in freely moving rodents, ultimately laying the foundation for future clinical applications in neurological disorder treatment.

The thesis begins with a literature review to determine the acoustic parameters required for effective ultrasound neuromodulation. Then, a comprehensive system-level study using the k-Wave Matlab toolbox is conducted, examining factors critical to the design of a 2D phased array transducer. This study highlights how parameters such as driving voltage, phase quantization resolution, frequency, and array length significantly impact the performance of the 2D phased array ultrasound transducer by influencing key acoustic and electrical attributes. Optimizing these parameters is essential to achieving high focal gain and spatial resolution while minimizing power consumption. The study finds that a three-bit phase resolution is optimal for accurate ultrasound beam steering. Additionally, while increasing array length improves spatial resolution and phased array gain, it also increases the overall size of the ultrasound transducer, constrained by the small brain sizes of rodents in preclinical studies. This study demonstrates that higher frequencies enhance spatial resolution and phased array gain. However, due to kerf limitations in the dicing manufacturing process of piezoelectric transducers, increasing frequency reduces the effective area of the transducers. Moreover, the pitch size should be reduced with increasing frequency in order to avoid the appearance of the grating lobes in the beam profile, forming a tradeoff between the frequency and the available area for the beamforming channels. Since higher frequencies are desired, particularly for applications in which higher spatial resolution is needed, high-voltage beamforming channels have been developed to investigate the highest frequency that allows for implementing a high-voltage beamforming channel. In this regard, two beamforming channels have been implemented and validated in TSMC 180-nm BCD technology, allowing for driving the ultrasound transducers with 12-MHz 36-V pulses. On the other hand, the power consumption of the beamforming channels has a crucial impact on the overall power efficiency of

the ASIC. Therefore, a power-efficient HV pulser is developed, leading to 40.9% power consumption reduction with respect to the conventional HV pulser.

Utilizing the proposed beamforming channels, a prototype 2D phased array transmitter ASIC is developed to validate the findings of the initial system-level study. The transmitter ASIC includes a 12×12 array of beamforming channels that generate 12-MHz pulses with 20-V amplitude. The phasing circuitry in the ASIC generates the required delay for each beamforming channel, hence allowing the ASIC to steer the ultrasound beam. The measurement results proved the functionality of the phased-array transmitter ASIC in terms of phase quantization, showing a maximum DNL of 0.35 LSB. Furthermore, the ASIC allows for controlling the driving voltage and the burst duration, as needed for US neuromodulation applications. Based on the prototype 2D phased array transmitter ASIC, a US-guided US transmitter ASIC is developed for preclinical US neuromodulation experiments in freely moving rats. Considering the size of the rat's brain, the size of the ASIC is limited to 5×5 mm^2. Given the prior discussion, the frequency was set to 12 MHz to achieve higher spatial resolution and phased array gain. Taking into account the proposed 20-V beamforming channel, the size of the 2D array was set to 66×66. According to the author's knowledge, this is the first transmitter ASIC that allows for preclinical US neuromodulation experiments on freely moving animals. Moreover, a temperature sensor was added to the ASIC to monitor the temperature rise in the ASIC. In order to monitor the location of the focal spot during the US neuromodulation, synthetic aperture US imaging capabilities are added to the ASIC to track the tissue displacement caused by the US neuromodulation push. In this regard, the ASIC includes eight groups of receiver channels that will be connected to 96 piezoelectric transducers using an analog multiplexer. To prevent side lobes in the beam profile, a system-level study was conducted to determine the optimal placement of receiver channels within the 2D array. The study revealed that a random distribution of receiver elements among the 2D transmitter elements is the most effective arrangement for minimizing side lobe appearance. To the best of the author's knowledge, this is the first ultrasound neuromodulation ASIC with integrated imaging capabilities. The measurement results proved the functionality of the ASIC in generating 20-V 12-MHz pulses with a programmable burst duration. The simulation results have shown that the receiver channels are capable of recording the echoes required for US imaging to monitor the location of the focal spot.

In summary, this thesis describes innovations in system-level and circuit-level integrated circuit design for developing an ultrasound ASIC that can be integrated with a 2D array of piezoelectric transducers, forming a miniaturized phased array US transducer that allows 3D US beam steering and focusing with the highest combination of spatial resolution and penetration depth in the context of pre-clinical studies. The ASIC includes the receiver channels that can be used for US imaging, allowing for monitoring real-time monitoring of the location of the focal spot during the US neuromodulation. This US ASIC leads to the emergence of miniaturized US transducers compatible with preclinical behavioral experiments in rodents, paving the way for the development of therapies to treat neurological disorders in humans.

Samenvatting

Neurologische aandoeningen hebben een diepgaande invloed op de kwaliteit van leven en verstoren essentiële functies zoals geheugen, cognitie en beweging. Traditionele behandelingen zijn vaak beperkt door de complexiteit van het brein, de invasiviteit van de procedures, of de lage precisie van de behandeling. Neuromodulatie met behulp van ultrageluid (Engels: ultrasound (US)) biedt een veelbelovende en minimaal invasieve alternatieve behandelingsoptie, waarbij ultrasone golven worden gebruikt om neurale activiteit in diepere hersengebieden met hoge spatiële resolutie te moduleren. Hoewel het veel potentie heeft, wordt preklinisch onderzoek naar ultrasone neuromodulatie gehinderd door een technologische achterstand: huidige ultrasone-apparatuur is vaak te groot en onnauwkeurig voor flexibele en continue neuromodulatie in vrij bewegende proefdieren. Nauwkeurige sturing is daarnaast cruciaal voor effectieve neuromodulatie, wat een fijne controle over het focuspunt vereist. Dit proefschrift richt zich op het onderzoeken van nieuwe methoden op systeem- en circuitniveau voor het ontwerpen van een applicatie-specifieke geïntegreerde schakeling (ASIC) voor een miniatuur, energie-efficiënt, twee-dimensionaal fasegestuurd array met een hoge resolutie. Deze methoden zijn gericht op de implementatie van een miniatuur ultrasone transducent voor nauwkeurige neuromodulatie bij loslopende proefdieren, wat uiteindelijk een basis legt voor toekomstige klinische toepassingen bij de behandeling van neurologische aandoeningen.

Het proefschrift begint met een literatuurstudie om de benodigde akoestische parameters voor effectieve ultrasone neuromodulatie vast te stellen. Vervolgens wordt een uitgebreide systeemstudie uitgevoerd met behulp van de k-Wave Matlab-toolbox om factoren te onderzoeken die essentieel zijn voor het ontwerp van een twee-dimensionaal fasegestuurd array van transducenten. Deze studie toont aan hoe parameters zoals aanstuurspanning, fasekwantisatieresolutie, frequentie en array-lengte van de aanzienlijke invloed hebben op de prestaties van de twee-dimensionaal fasegestuurd array van ultrasone transducent door de akoestische en elektrische eigenschappen te beïnvloeden. Optimalisatie van deze parameters is essentieel om een hoge versterking en spatiële resolutie in het focuspunt te bereiken terwijl het energieverbruik wordt geminimaliseerd. Uit de resultaten blijkt dat een fasekwantisatieresolutie van drie bits optimaal is voor nauwkeurige ultrasone bundelsturing. Verder verbetert een langer array de spatiële resolutie en versterking van het fasegestuurde array, maar vergroot dit ook de totale grootte van de transducent, welke wordt beperkt door de kleine hersenomvang van de proefdieren in preklinisch onderzoek. De studie laat zien dat hogere frequenties de spatiële resolutie en versterking van het gefaseerde array verbeteren, maar door beperkingen in het fabricageproces van piëzo-elektrische transducenten leidt een frequentieverhoging tot een verkleining van het effectieve oppervlak van de transducenten. Bovendien moet de elementafstand worden verkleind bij toenemende frequentie om te voorkomen dat er roosterlobben in het bundelprofiel verschijnen, wat resulteert in een afweging tussen de frequentie en de beschikbare ruimte voor de bundelvormingskanalen. Omdat hogere frequenties gewenst zijn,

vooral bij toepassingen waar een hogere spatiële resolutie vereist is, zijn er hoogspannings bundelvormingskanalen ontwikkeld om te onderzoeken wat de hoogste frequentie is die het mogelijk maakt om een hoogspannings-bundelvormings-kanaal te implementeren. In dit verband zijn twee bundelvormingskanalen geïmplementeerd en gevalideerd in TSMC 180-nm BCD-technologie, waarmee 12-MHz 36-V pulsen naar de ultrasone transducenten kunnen worden gestuurd. Aan de andere kant heeft het energieverbruik van de bundelvormingskanalen een cruciale invloed op de energie-efficiëntie van de ASIC. Daarvoor is een energie-efficiënte hoogspannings-pulser ontwikkeld, wat resulteert in een reductie van 40.9% in energieverbruik ten opzichte van de conventionele HV-pulser.

Met behulp van de bundelvormingskanalen is een prototype zender-ASIC van een 2D fasegestuurd array ontwikkeld om de resultaten van de initiële systeemstudie te valideren. De zender-ASIC omvat een 12×12 array van bundelvormingskanalen die 12-MHz pulsen met een amplitude van 20 V genereren. De fasecircuits in de ASIC genereren de benodigde vertraging voor elk bundelvormings-kanaal, waardoor de ASIC de ultrasone bundel kan sturen. Uit de meetresultaten blijkt dat de phased-array zender-ASIC functioneert in termen van fasekwantisatie, met een maximale differentiële niet-lineariteit (DNL) van 0.35 LSB. Bovendien kan de ASIC de stuursignaalspanning en de burst-duur regelen, zoals nodig is voor toepassingen van US-neuromodulatie. Op basis van het prototype 2D fasegestuurde array is een door US-gestuurde US zender-ASIC ontwikkeld voor preklinische US-neuromodulatie-experimenten bij vrij bewegende ratten. Gezien de hersenomvang van de rat is de grootte van de ASIC beperkt tot 5×5 mm^2. Zoals versterking van het eerder besproken is het frequentie ingesteld op 12 MHz om een hogere spatiële resolutie en 2D fasegestuurde array te bereiken. Met het voorgestelde 20-V bundelvormings-kanaal is de grootte van de 2D-array ontworpen op 66×66. Voor zover bij de auteur bekend, is dit de eerste zender-ASIC die preklinische US-neuromodulatie-experimenten bij vrij bewegende dieren mogelijk maakt. Daarnaast is een temperatuursensor toegevoegd aan de ASIC om de temperatuurstijging in de ASIC te monitoren. Om de locatie van het brandpunt tijdens de US-neuromodulatie te monitoren, zijn er beeldvormingsmogelijkheden aan de ASIC toegevoegd om de verplaatsing van weefsel die wordt veroorzaakt door de US-neuromodulatie te volgen. De ASIC bevat acht groepen ontvangstkanalen die worden aangesloten op 96 piëzo-elektrische transducenten via een analoge multiplexer. Om zijlobben in het straalprofiel te voorkomen, is er een systeemstudie uitgevoerd om de optimale plaatsing van ontvangstkanalen binnen de 2D-array te bepalen. De studie toont aan dat een willekeurige verdeling van ontvangstelementen binnen de 2D-zenderelementen de meest effectieve opstelling is om het optreden van zijlobben te minimaliseren. Voor zover bij de auteur bekend, is dit de eerste ultrasone neuromodulatie-ASIC met geïntegreerde beeldvormingsmogelijkheden. De meetresultaten bevestigen de functionaliteit van de ASIC in het genereren van 20-V 12-MHz pulsen met een programmeerbare burstduur. De simulatie-resultaten toonden aan dat de ontvangstkanalen in staat zijn om de echo's te registreren die nodig zijn voor US-beeldvorming om de locatie van het brandpunt te monitoren.

Samenvattend beschrijft dit proefschrift innovaties in geïntegreerde schakelingen op systeem- en circuitniveau voor de ontwikkeling van een ultrageluid-ASIC die kan worden geïntegreerd met een 2D-array van piëzo-elektrische transducenten, waarmee een miniatuur fasegestuurde array van US transducenten wordt gerealiseerd die 3D ultrasone bun-

delsturing en -focussering mogelijk maakt met de hoogste combinatie van spatiële resolutie en penetratiediepte in de context van preklinische studies. De ASIC bevat ontvangstkanalen die kunnen worden gebruikt voor US-beeldvorming, wat realtime monitoring van de focuslocatie tijdens de US-neuromodulatie mogelijk maakt. Deze US-ASIC draagt bij aan de ontwikkeling van miniatuur US-transducenten die geschikt zijn voor preklinische gedragsexperimenten bij proefdieren en legt een basis voor toekomstige therapieën voor de behandeling van neurologische aandoeningen bij mensen.

Acknowledgements

In the first week of lockdown due to the global COVID-19 pandemic, I began my PhD studies at TU Delft. Now, as this journey comes to an end, I am filled with gratitude for the support I have received from countless individuals. Their expertise, encouragement, and friendship have been invaluable, and I am deeply grateful for their presence throughout this challenging yet rewarding period.

Firstly, I would like to express my heartfelt gratitude to my supervisory team, Tiago Costa and Wouter Serdijn. They have provided invaluable support, guiding me with expertise and patience through the challenges I encountered. I am sincerely thankful for their mentorship and encouragement, which have been the cornerstone of my research. I also want to thank my dissertation committee members, Paddy French, Nico de Jong, Kenneth Shepard, Marcelino Santos, and Mehdi Kiani, for their support.

My appreciation also extends to my colleagues and collaborators for sharing their invaluable experience: Achilleas, Arn, Clementine, Dante, Eckardt, Frans, Leon, Massimo, Mate, Michiel, Qinwen, Ronald, Vasiliki, Alessandro, Amin, Avic, Christos, Gustavo, Javad, Mohammad, Peng, Ronaldo, Samaneh, Sampi, Suman, Virgilio, Xiao, Alireza, Andra, Arash, Bakr, Beatriz, Can, Cesc, Chenyan, Diogo, Eshani, Evelyne, Gandhi, Hoda, Ignasi, Johan, Joshua, Kambiz, Kimia, Konstantina, Limitha, Liwen, Lisa, Lukas, Marios, Masumeh, Mojtaba, Mustafeez, Nasim, Nikola, Niloufar, Nandor, Nuriel, Petra, Raphael, Rui, Samuel, Stefania, Stijn, Tao, Tianqi, Xiaoxi, Xinling, Yihan, Aitor, Anand, Berend, Cecelia, Christiaan, Chunyan, Dario, Django, Eduardo, Flavia, Hidde, Ignas, Ines, Ishaan, Joost, Nerea, all three Niels, Patricia, Rajvi, Reka, Shuang, Tom, Xinyu, Zeyao. I also thank Yidi and Yihao for having me as their supervisor on their master's degree. I express my gratitude to Antoon, Ali, Atef, Brian, Chris, Esther, Filip, Ger, Kellen, Lukasz, Marion, Ron, Tarique, and Zu-yao for their technical and administrative support. I would like to thank all my friends at TU Delft, as well as anyone I may have unintentionally forgotten to name.

I am also grateful to my advisors and mentors during my master's and bachelor's degrees, who inspired my initial passion for research and provided me with the foundations I needed to pursue this path: Javad Haddadnia, Majid Baghaei, Mehdi Saberi, Mohammad Hadi Shahrokh, Mohammad Maymandi, Mohammad Taherzadeh, Rahim Ildarabadi, Reza Lotfi, and many others. I also thank all my friends, peers, and colleagues at Ferdowsi University of Mashhad and Hakim Sabzevari.

I would also like to acknowledge my friends in Delft, who have been my companions and support network: Ali, Amin, Amir Hossein, Arash, Armina, Behnam, Behnoush, Ehsan, Elaheh, Elmira, Farideh, Farzad, Forough, Freshteh, Hamraz, Hamed, Helda, Iman, Javad, Kosar, Maede, Mahdi, Mahsa, Masumeh, Mohammad, Niloufar, Peyman, Ramin, Samaneh, Shiva, Sobhan, Zahra, Zeynab. Their camaraderie and encouragement have added immeasurable joy to my life here and made this journey far more memorable.

Finally, I am deeply grateful to my family and my family-in-law. My parents' unwavering support, love, and encouragement have been a constant source of strength, as has

the kindness and backing of my extended family. Their belief in me has provided a steady foundation throughout this journey, and I am profoundly thankful for all they have done.

To my beloved wife, Farideh, thank you for your patience, understanding, and steadfast support, which have been my anchor through the highs and lows of this PhD journey. Your presence and encouragement have been invaluable, and I am forever grateful for the sacrifices you have made and the love you have given.

This thesis is as much a product of my efforts as it is of the support and encouragement I have received from all of you. Thank you.

Hassan Rivandi
Delft, November 2024

1

Introduction

1.1. Motivation

Neurological disorders influence the human's quality of life by impacting essential aspects such as memory, cognition, personality, and movements. Given the profound impact of these human capabilities, neurological disorders are the leading cause of illness and disability worldwide, affecting over one in three individuals [1]. These disorders not only cause great suffering to individuals but also place a significant burden on families, caregivers, and healthcare systems worldwide [2]. Despite neurological disorders being among the most prevalent conditions, historical data from recent years indicate a rapid growth in their incidence. The global prevalence of diabetic neuropathy, as an example, has witnessed a more than threefold increase since 1990, notwithstanding advancements in the healthcare system [3]. Similar upward trends have been observed in the number of incidents of dominant neurological disorders, such as Alzheimer's disease, amyotrophic lateral sclerosis (ALS), epilepsy and seizures, Parkinson's disease, and stroke [4]–[7]. Furthermore, the emergence of neurological disorders associated with COVID-19, including cognitive impairments and Guillain-Barré syndrome, which were previously unreported, now contribute to more than 23 million cases globally [8]–[11]. This rapid trend in the prevalence of neurological disorders emphasizes the crucial need for precise diagnostic techniques and the development of more effective therapeutic interventions.

Pharmaceutical medications represent the traditional approach to treating diseases. However, their effectiveness in treating neurological disorders is notably limited. The complexity of the nervous system, the challenge of drug delivery to the brain due to the impermeable blood-brain barrier [12], and the variability in disease progression across individuals make developing effective pharmaceutical interventions for neurological disorders particularly challenging [13]. Moreover, developing new pharmaceutical medicines demands significant financial investment and a prolonged timeline, while the overall yield is low [14]. Furthermore, conventional drugs affect the entire body and, hence, often induce side effects [15]. Therefore, conventional pharmaceuticals have limited effectiveness in treating neurological conditions, leading to an urgent need for personalized, precise, more efficient, and cost-effective therapies.

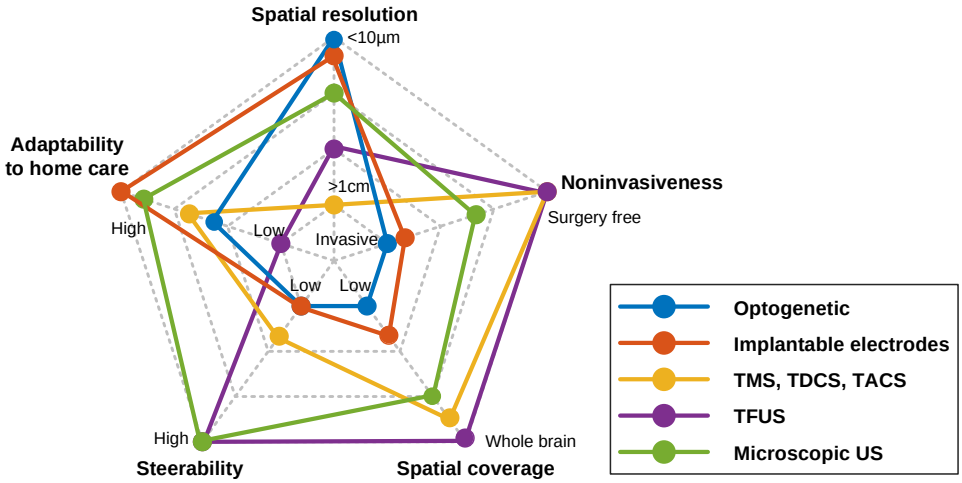

Fig. 1.1: Comparison of different neuromodulation approaches in terms of their spatial coverage, spatial resolution, steerability, adaptability to home care, and invasiveness. TMS, TDCS, TACS, and TFUS represent transcranial magnetic stimulation, transcranial direct current stimulation, transcranial alternative current stimulation, and transcranial focused ultrasound stimulation.

Non-pharmaceutical treatments based on neuromodulation are emerging as a promising avenue for managing neurological disorders. They work based on modulating, either stimulation (activation) or inhibition (suppression), of the neuronal activity. These approaches have shown the potential to address a spectrum of neurological disorders by stimulation or suppression of nerve activity [16]. Since the early 2000s, neuromodulation has been utilized in clinical treatments. It first gained approval for the treatment of Parkinson's disease [17]. Following this, it received approval to treat conditions such as epilepsy [18] and essential tremor [19]. Furthermore, extensive research is currently being conducted to explore the potential of neuromodulation in treating a variety of other conditions, including major depression [20], retinitis pigmentosa [21], and tinnitus [22]. As research and clinical trials continue to advance, neuromodulation could revolutionize the treatment of neurological diseases, offering more personalized and effective therapies.

Currently, neuromodulation can be executed through a variety of modalities, including electrical [23], electromagnetic [24], optical [25], and acoustic [26] approaches. Fig. 1.1 compares key specifications of different non-pharmacological neuromodulation approaches regarding their spatial coverage, spatial resolution, adaptability to home care, steerability, and invasiveness. Spatial coverage refers to the ability of the neuromodulation method to modulate different brain regions with a single device, whereas steerability describes the ability to modulate various brain regions without needing to reposition the neurostimulator. Treating certain neurological disorders demands regular neuromodulation, making it essential for the neuromodulation method to be manageable at home with minimal impact on the patient's daily life. This is shown with adaptability to the home care index. Furthermore, neuromodulation techniques should minimize potential risks for patients, a concern directly addressed by the noninvasiveness factor. Last but not least, the precision of the modulation is defined by spatial resolution. Poor precision or accuracy

may also influence other brain regions, leading to unwanted side effects. Thus, effective neuromodulation requires high spatial resolution coupled with high accuracy [27].

Electrical neuromodulation using implantable electrodes involves the surgical insertion of electrodes into specific regions of neural tissues. These electrodes produce electrical pulses that can modulate the neural activity. Deep brain stimulation (DBS), which is a type of electrical stimulation where electrodes are inserted deep into the brain, is employed to treat a variety of disabling neurological conditions such as Parkinson's disease [28] and chronic pain [29]. While DBS involves surgically implanting electrodes in specialized medical facilities, the DBS system allows patients to follow their treatment at home without the need to visit the hospitals frequently. Moreover, this modality allows precise neural stimulation at the cost of low spatial coverage and steerability [27]. DBS is considered an invasive technique since it needs implanting electrodes in the brain, potentially causing tissue damage and infection and, hence, restricting its use to a limited group of patients [30]. As an example, DBS has been used in clinical practices to treat Parkinson's disease for more than twenty years; however, only less than 5% of subjects are eligible to undergo DBS [31], [32].

Optogenetics can excite or inhibit neuronal activity through specific wavelengths of light [33]. Although optogenetics offers precise spatial resolution down to neuron size, it necessitates genetic modifications of the neural tissue, presenting risks or feasibility concerns in human applications. Furthermore, optogenetics entails implanting fiber-optic or light-emitting diodes (LEDs) into specific regions of neural tissues, which may result in tissue inflammation and damage [34], [35].

Transcranial magnetic stimulation (TMS) is one of the conventional methods to modulate neuronal activity. In this technique, a coil positioned near the skull employs high-current pulses to create a variable magnetic field, leading to the induction of current within the brain's conductive tissues [36]. In this modality, the depth of penetration is limited, mainly due to the field divergence and the size of the required coils [37]. Improving the penetration depth requires larger coils, which increases the overall size of the device. Furthermore, TMS exhibits poor spatial resolution and requires frequent visits to health care providers to undergo the treatment [27].

Transcranial direct and alternating current stimulation (TDCS, TACS) can modulate neural activity by applying direct and alternating mA-level currents to the tissue beneath the electrodes [38], [39]. Similar to TMS, TDCS and TACS suffer from poor spatial resolution and limited depth of penetration.

In recent years, ultrasound (US) neuromodulation has gained attention as a noninvasive modality to stimulate neural activity in both the central and peripheral nervous systems. In contrast to other neuromodulation modalities, noninvasive ultrasound waves can penetrate into deep regions in the brain and perform precise neuromodulation [40]. Tyler and his group have pioneered the use of ultrasound waves to modulate the brain activity of mice [41]. Currently, various research groups have successfully demonstrated noninvasive ultrasound neuromodulation across a range of species, including rodents [42], sheep [43], monkeys [44], and humans [45], through employing diverse acoustic parameters. Consequently, accumulating evidence proves that ultrasound can effectively alter neural activity, although the precise mechanisms underlying ultrasound neuromodulation are still not fully understood [44].

Although ultrasound offers a noninvasive and precise neuromodulation modality, technological challenges hinder its full potential in treating neurological disorders. Due to the bulky form factor of conventional ultrasound transducers used in clinical research, only acute clinical research during hospital visits is currently possible [40]. Moreover, the bulky size of these transducers confines the clinical experiments to transcranial focused ultrasound stimulation (TFUS). Given the necessity to mitigate ultrasound attenuation in the skull, the sonication frequency is restricted to below 1 MHz; hence, TFUS suffers from low spatial resolution [46]. Therefore, precise home treatments using ultrasound neuromodulation demand an implantable transducer, also known as microscopic ultrasound [27]. This implantable ultrasound neurostimulator can be placed directly on the brain surface with a partially removed skull. Microscopic ultrasound allows for the utilization of higher sonication frequency, offering a better spatial resolution [46]. While this approach does not provide the same level of noninvasiveness as TFUS, it is comparatively less invasive than DBS since the transducer is placed on top of the brain rather than surgically implanted deep within the brain. In addition, unlike TFUS, microscopic ultrasound does not need frequent hospital visits for treatment, making it more adaptable to home care. However, unlike TFUS which is extensively used in clinical trials, microscopic US neuromodulation is still a concept. In summary, as shown in Fig. 1.1, microscopic US shows promises as a minimally invasive, adaptable to home care, and precise neuromodulation modality, which shows higher potential in treating neurological disorders compared with other neuromodulation techniques.

Despite the tremendous potential of both TFUS and microscopic ultrasound, there are still challenges to their use in both preclinical and clinical research and therapies. Within the conventional pathway of drug development, as shown in Fig. 1.2, a technological gap in the preclinical studies impedes the adoption of ultrasound therapy in clinical applications. Preclinical studies play an essential role before clinical trials to ensure the safety and efficacy of a new treatment or medication. These preclinical studies mainly involve animal experiments in rodents, the commonly used animal models in these studies. Since rodent's genetic, biological, and behavioral characteristics closely resemble those of humans, they are effective animal models for studying the biological effects of new treatments. However, preclinical research for ultrasound neuromodulation lacks a proper ultrasound transducer to fit the rodent heads. As shown in Fig. 1.3, most of the ultrasound transducers reported in the literature for preclinical research are bulky, limiting the experiments to head-fixed anesthetized animals [47], [48]. Therefore, these transducers not only compromise the experiment's precision but also do not allow for the conduct of behavioral studies on freely moving animals. To overcome this limitation, small form factor US transducers have been developed that suit preclinical experiments on rodents [49]–[52]. Although these transducers enable experiments on freely moving rodents, they are based on single-element transducers with a fixed focal spot. These transducers utilize low frequencies, which results in poor spatial resolution. Moreover, since reliable ultrasound neuromodulation demands accurate targeting, it is crucial to maintain fine control over the focal spot location of the ultrasound transducer. Currently, researchers employ a 3D mechanical stage to modify the focal spot's position, which significantly increases the system's overall bulkiness [47]. Some advanced works have explored ultrasound phased array technology for neuromodulation, which allows for electronically focusing of ultrasound

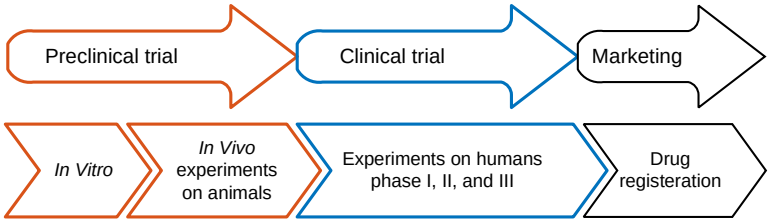

Fig. 1.2: Conventional drug development path.

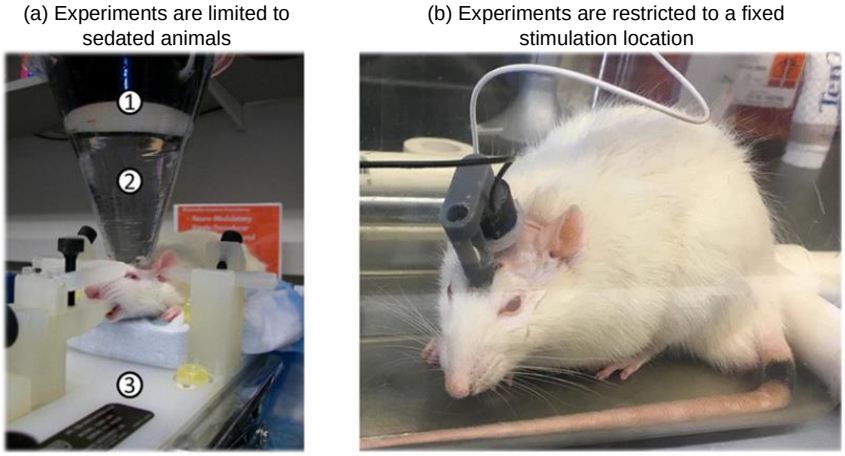

Fig. 1.3: Conventional ultrasound transducers for preclinical research on rats. (a) Reprinted from [47] ©2012, with permission from Elsevier. (b) Reprinted from [49] under CC BY 4.0.

waves in the three-dimensional space, with high coverage of the brain of rodents [40], [53]. However, they either suffer from low spatial resolution because of employing a low operation frequency [53] or insufficient focal pressure to achieve US neuromodulation [40]. In addition, current US neuromodulation devices suffer from a reliable monitoring system to track the location of the focal spot and the US intensity delivered to the tissue [54]. Consequently, the currently available ultrasound transducers for preclinical experiments restrict the potential of ultrasound neuromodulation. Therefore, this research thesis aims to develop a minimally invasive miniaturized ultrasound transducer to enable researchers to successfully perform US neuromodulation in freely moving rodents, with high spatial resolution and three-dimensional control of the focal spot anywhere in the brain.

1.2. Objective

Preclinical studies on ultrasound neuromodulation demand a miniaturized US transducer that allows electronic beam steering. As discussed in the previous section, 2D US phased arrays allow for electronic beam steering, which is indispensable for preclinical studies on US neuromodulation. Electronic beam steering enables researchers to study the influence of ultrasound on different brain regions without the mechanical movement of the transducer. Consequently, studying different brain regions helps to understand brain functions

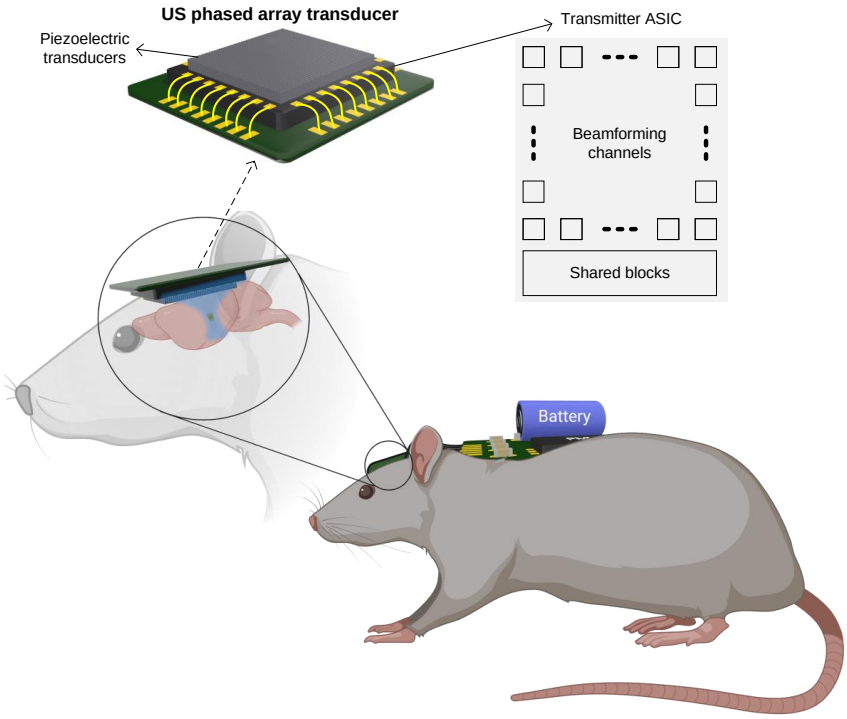

Fig. 1.4: Conceptual 2D phased array US transmitter for preclinical research on rodents.

towards discovering new treatments for neurological disorders. In addition to the small size and electronic beam steering, reliable US neuromodulation on rodents requires precise spatial resolution and enough acoustic pressure at the focal spot, allowing neuroscientists to perform successful experiments.

This thesis aims to develop a wearable ultrasound transducer system designed for ultrasound neuromodulation studies in rodents, as illustrated in Fig. 1.4. This miniaturized transducer paves the way for groundbreaking studies on the effects of ultrasound on neural activity, offering a minimally invasive method to stimulate or suppress neuronal functions *in vivo*. This system is lightweight and fits comfortably on rodents, in this case rats, ensuring minimal stress and impact on the animal's natural behaviors. This conceptual system consists of a parent and a child board; the parent board includes the battery, the power management unit (PMU), the Bluetooth module, and the microcontroller unit (MCU), and the child board consists of the ultrasound transducer. A flexible connector connects these two boards, transferring required power supplies and commands from the parent board to the child board. A battery supplies power to the PMU, which provides the required voltage levels for the ultrasound transducer and MCU. Bluetooth module conveys the data from the user to the MCU. Then, the MCU translates this data to the commands for the ultrasound transducer. The child board is securely fixed to the skull using screws and dental cement, ensuring the transducer remains stable and undisturbed by the animal's movements. The child board involves the 2D US phased array transducer, which includes

a phased array transmitter application specific integrated circuit (ASIC) and a 2D array of US transducer elements directly integrated on the ASIC.

Under the scope of this research thesis, the objective is to develop a 2D phased array transmitter ASIC required by the proposed commercial system of Fig. 1.4. The development process involves three essential steps. First, a comprehensive system analysis is needed to optimize all relevant design variables, ensuring optimal performance. Second, high-frequency and power-efficient beamforming channels are required to achieve high spatial resolution and power efficiency. Finally, developing a power-efficient architecture is needed for developing a 2D phased array transmitter ASIC to interface with a 2D array of US transducer elements.

First of all, a comprehensive system analysis is needed to optimize the implementation of the 2D phased array transmitter ASIC. This crucial step in the design process aims to study the propagation of ultrasound waves generated by a phased array US transducer within the brain. This analysis will consider several critical factors, including the transducer's dimension, the piezoelectric material, the sonication frequency, the amplitude of the driving signals, and the electrical impedance of the piezoelectric transducer. These factors play an essential role in achieving the required spatial resolution and intensity at the focal spot. Therefore, the system-level analysis facilitates the design of a power-efficient 2D phased array transmitter ASIC, ensuring extended battery life and preventing thermal damage to the brain. This system-level analysis includes circuit-level simulations coupled with acoustic wave propagation simulations.

The system-level study is followed by the development of beamforming circuits to drive the ultrasound transducers. The electronic circuits are implemented utilizing high-voltage complementary metal-oxide-semiconductor (CMOS) chips to minimize the overall size of the ultrasound transducer. Beamforming channels play a critical role in the overall power efficiency of the transmitter ASIC. Moreover, as will be discussed in Chapter 3, the area of the beamforming channel defines the operation frequency of the array and, hence, the spatial resolution of the 2D phased array transducer. Therefore, before implementing the 2D transmitter ASIC, it is important to optimize the beamforming channels in terms of power efficiency and area.

Subsequently, the work continues toward implementing 2D phased array transmitter ASICs to drive the 2D array of piezoelectric transducers. First, a 2D ASIC is developed for proof of concept of the system-level analysis. The second ASIC targets the application of preclinical research on US neuromodulation in rats, as shown in Fig 1.4. The ASICs perform internal beamforming to implement a phased array configuration, which is required for electronic beam steering. Furthermore, the ASICs deliver adjustable high-voltage pulses with the desired sonication frequency to control the spatial resolution and the delivered intensity to the tissue. Moreover, the ASIC allows for US imaging to monitor the location of the focal spot as well as the US intensity delivered to the tissue. Additionally, the ASICs are compatible with direct integration of the piezoelectric transducers on top of the CMOS chip, resulting in a compact ultrasound transducer. Furthermore, a selected number of channels and reduced parasitic capacitance leads to lower power consumption.

In summary, this project aims to develop area and power-efficient CMOS electronics for driving a 2D array of US transducers, which trigger the emergence of US neuromodu-

lation devices compatible with preclinical behavioral experiments in rodents.

1.3. Thesis Organization

This thesis is composed of seven chapters. Chapter 2 presents a comprehensive literature study on the transducers for ultrasound neuromodulation. First, this chapter describes the recent findings in the field of ultrasound neuromodulation to gain insight into the required sonication parameters for successful US neuromodulation. Then, it explores the development of ultrasound transducers, discussing the optimum focusing techniques and the piezoelectric materials for ultrasound neuromodulation. Next, recent transmitter ASICs are discussed to comprehend the latest implemented architectures. In the end, a discussion is provided to define the research questions of this research thesis.

Chapter 3 provides a system-level analysis to study the propagation of ultrasound waves in the brain using the k-Wave toolbox in Matlab. Consequently, a phased array ultrasound transducer is conceptualized and simulated to meet the needed sonication parameters for reliable ultrasound neuromodulation in rats. This system-level study not only defines the size and sonication frequency of the piezoelectric transducer but also optimizes the transmitter ASIC in terms of complexity and power consumption.

Chapters 4 and 5 present the transistor-level implementation of the electronic circuits to drive the phased array of piezoelectric transducers. Chapter 4 introduces the proposed beamforming channels. First, it tries to achieve the maximum sonication frequency while delivering high-voltage pulses to the piezoelectric transducers. Then, it proposes a beamforming channel to improve the power efficiency. Chapter 5 presents a 2D phased array transmitter ASIC to verify the system-level analysis of Chapter 3. The ASIC comprises an array of 12×12 beamforming channels that can deliver 12-MHz pulses with an amplitude of 20 V to the piezoelectric transducers. Electrical measurements have been conducted to verify the capability of the designed circuits to drive piezoelectric transducers and to perform the electronic beam steering.

Chapter 6 presents a US-guided US neuromodulation ASIC for preclinical US neuromodulation studies on rats. This device includes 66×66 elements, in which 4228 elements are transmitters and 96 elements are receivers. The ASIC includes two phases of US neuromodulation and US imaging. In the US neuromodulation phase, the transmitter elements transmit 12-MHz phased pulses to drive piezoelectric transducer elements with an amplitude of 20 V. In the imaging phase, the transmitters drive the transducer elements in such a way as to transmit compound planar waves with multiple angles while the receiver channels can record the resulting echoes.

Chapter 7 concludes the thesis by summarizing the main contributions and providing recommendations for future research.

2

Emerging Transducers for US Neuromodulation

2.1. Basic Principles of Ultrasound

Ultrasound waves are acoustic waves that have a frequency beyond the range of human hearing (>20kHz). The concept of ultrasound, while it is a relatively modern medical tool, has deep roots in nature. Various animal species, such as bats, dolphins, and some species of whales, utilize ultrasound waves to navigate, hunt, and communicate within their environments. These creatures emit high-frequency sound waves and interpret the received echoes, a phenomenon called echolocation.

2.1.1. Pressure Wave

Since ultrasound waves are mechanical waves, they need a medium to travel through. Ultrasound waves are typically longitudinal waves, particularly in fluid mediums such as air, water, and biological tissues. However, they may propagate as transverse waves in solids such as bones. In a longitudinal ultrasound wave, the particles of the medium move back and forth in the same direction the wave travels, creating a pattern of compression and rarefaction [55], as shown in Fig. 2.1. Consequently, this displacement causes pressure variation from the baseline pressure, generating a pressure wave [56]. Pressure is typically a positive value; however, depending on the ambient pressure within the medium and the amplitude of the pressure wave, the pressure can be negative, as shown in Fig. 2.2. In fact, large pressure amplitudes in the rarefaction phase pull the particles apart and cause negative pressure. If the negative pressure is sufficiently strong, it can cause cavitation, which is the formation of small gas bubbles in the tissue [56].

The key physical properties of US waves are frequency, velocity, wavelength, pressure amplitude, power, and intensity, as illustrated in Fig. 2.2. Frequency (f) refers to the number of oscillations or cycles a sound wave completes in one second. Pressure amplitude (p) is the maximum change in pressure from the ambient pressure level caused by the ultrasound wave.

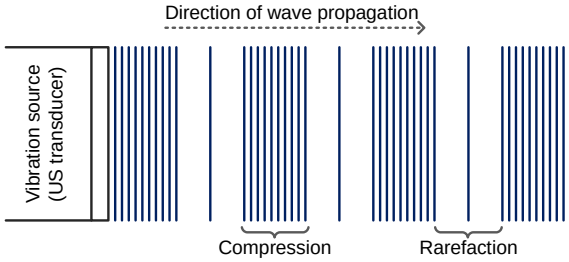

Fig. 2.1: Longitudinal propagation of US waves causing pressure variation [56].

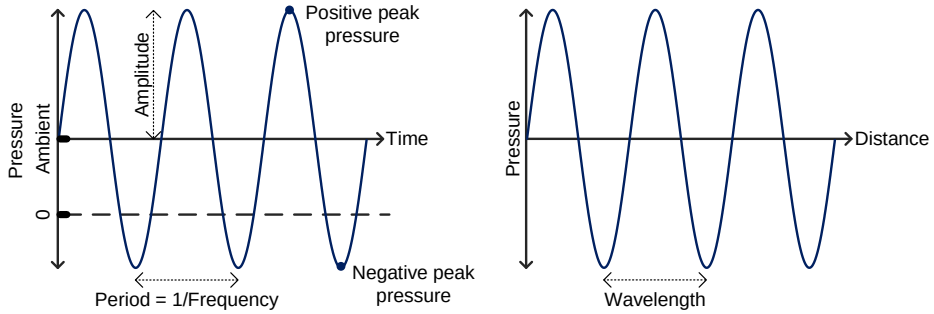

Fig. 2.2: A ultrasound wave with sinusoidal waveform in a linear medium. The figure describes the frequency, wavelength, and amplitude definitions.

The velocity (v), often called the speed of sound, is the rate at which sound waves travel through a medium, depending on the medium's properties. The wavelength (λ) is defined as the distance over which a wave's shape repeats in space at a fixed moment. The sound wavelength depends on the velocity and the frequency [55], which can be represented as

$$\lambda = \frac{v}{f} \tag{2.1}$$

Power in ultrasound waves is quantified as the amount of energy transferred per unit of time, measured in watts (W), and it represents the total energy of transmitted ultrasound waves to the tissue or medium per second. Intensity (I) is defined as the amount of energy flowing through a unit area per unit of time in the direction of the wave propagation. It is calculated from power divided by the area and measured in watts per square meter (W/m^2) [57].

2.1.2. Interaction of US Waves with Medium

The interaction of ultrasound waves with a medium is influenced by the physical properties of the medium. One of the most important physical characteristics of a medium is density, which is a measure of its mass per unit volume. The density can be determined by

$$\rho = \frac{m}{V} \tag{2.2}$$

where ρ, m, and V are the density, mass, and volume of the medium, respectively. Denser materials, which have more massive particles, have more inertia against movement. Since ultrasound wave propagation involves the periodic movement of medium particles, the wave velocity is lower in dense mediums, as expressed below

$$v = \sqrt{\frac{K}{\rho}} \tag{2.3}$$

where K is the bulk modulus of the medium, which is inversely related to the compressibility of a medium. Compressibility is a measure of the relative volume change of a substance in response to a change in pressure. Materials with lower density, like gases, are more compressible. In contrast, materials with higher density exhibit less compressibility due to lower particle spacing. In materials with low compressibility, minimal particle movement is needed for energy transfer, leading to a higher ultrasound wave velocity [56].

The acoustic impedance of a medium also influences the behavior of the sound waves in the medium. The acoustic impedance is directly proportional to the density and the speed of the sound in the medium. The unit of acoustic impedance is kg/(m²·s) or Rayls, and is defined by

$$Z = \rho \cdot v \tag{2.4}$$

As US waves travel along heterogeneous media, they suffer from attenuation in the form of reflection, scattering, refraction, and absorption [58]. Attenuation refers to the overall propagation losses that cause a decrease in US beam intensity or a change in the direction of the US beam. These forms of attenuation are described below.

When US waves encounter an acoustic impedance mismatch at the boundary between two mediums, a fraction of the US beam passes through the interface to the second medium while the remaining fraction is redirected backward. The nature of the interface, its size or shape, determines whether this impedance mismatch causes reflection or scattering. When the interface is smooth and larger than one wavelength of the US beam, reflection occurs, as shown in Fig 2.3(a). In this case, the US beam is reflected at the same angle as its angle of incidence. The reflected beam is referred to as the echo, which is used to form images in US imaging applications. The intensity of the echo is influenced by the acoustic mismatch between the two mediums and the angle of incidence. At a zero incidence angle, the relationship between the intensity of the echo and the intensity of the incident beam can be described by

$$\frac{I_r}{I_i} = \frac{(Z_1 - Z_2)^2}{(Z_1 + Z_2)^2} \tag{2.5}$$

where I_r, I_i, Z_1, and Z_2 are the intensity of the reflected echo, the intensity of the incident beam at the interface, the acoustic impedance of the first medium, and the acoustic impedance of the second medium, respectively. On the other hand, when the reflecting medium is irregular in shape or smaller than one wavelength of the ultrasound waves, the US beam is redirected in multiple directions, as illustrated in Fig. 2.3(b). This phenomenon, known as scattering, does not follow the straightforward equations for regular reflection. Instead, the direction of the scattered beam depends on the size of the second medium and the length of the US beam.

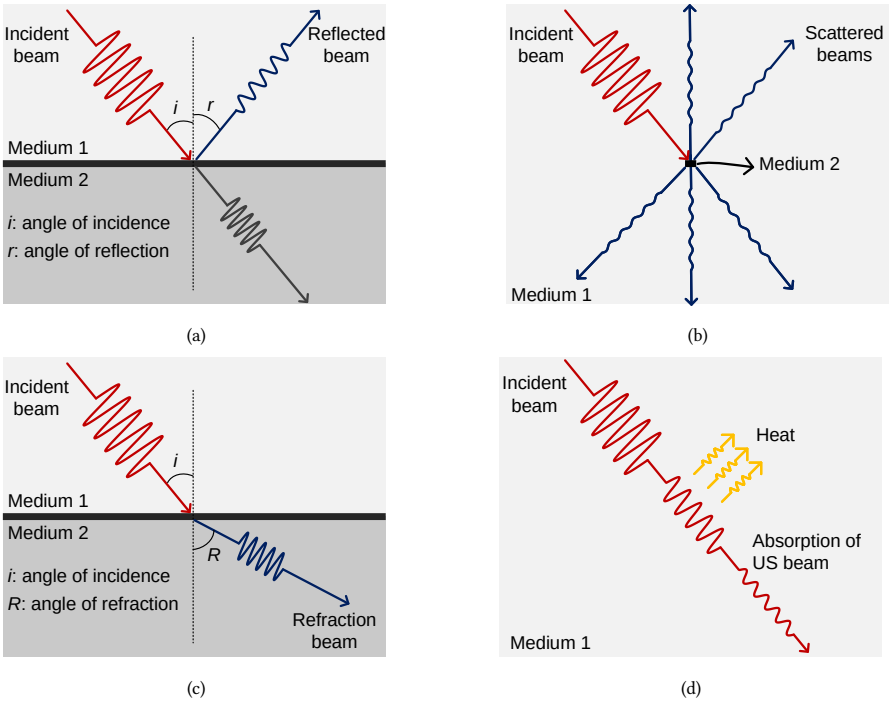

Fig. 2.3: (a) reflection, (b) scattering, (c) refraction, and (d) absorption of ultrasound waves when interaction with mediums.

As US waves travel between two mediums that have different velocities, the change in the wavelength alters the direction of the US beam; this phenomenon is known as refraction, as shown in Fig 2.3(c). According to Snell's law, the relationship between the angle of the incident beam and the angle of the refracted beam is calculated from

$$\frac{\text{Sin } i}{\text{Sin } R} = \frac{v_1}{v_2} \tag{2.6}$$

where i, R, v_1, and v_2 are the angle of the incident beam, the angle of the refraction beam, and the velocity of US waves in the first and second medium, respectively [56].

As the US waves travel in the medium, they transform into a different form of energy, mainly heat, by means of absorption, as depicted in Fig. 2.3(d). The absorption of ultrasound waves in a medium depends on the frequency of the US waves. High-frequency US waves are absorbed more rapidly than lower frequencies. This is because high-frequency US waves have shorter wavelengths and interact more frequently with the medium, resulting in higher energy losses [56]. Absorption is one of the main causes of acoustic attenuation in the skull, which limits the frequency of TFUS to the sub-MHz range to minimize the US attenuation and deliver sufficiently high acoustic intensities to the target brain region. The type of the medium has a critical effect on the acoustic attenuation. The ultrasound attenuation coefficient (α) is a measure of how quickly the intensity of ultrasound waves decreases as they propagate through a medium.

Table 2.1: Properties of different tissues. v, α, y, ρ, and Z are sound velocity, attenuation coefficient, power law exponent, density, and acoustic impedance of the medium [58].

Tissue	v (m/s)	α (dB/MHz^y-cm)	y	ρ (kg/m^3)	Z (MRayls)
Water @ 20°C	1482	0.002	2.0	997	1.482
Blood	1584	0.14	1.2	1060	1.679
Brain	1562	0.58	1.3	1035	1.617
Fat	1430	0.6	1.0	928	1.327
Muscle	1580	0.57	1.0	1041	1.645
Bone	3198	3.54	0.9	1990	6.364

Table 2.1 compares critical physical parameters of different mediums, which are velocity, attenuation factor, density, and acoustic impedance of the medium. It is evident that bone shows higher attenuation of US waves compared with soft tissues. Water has similar properties as soft tissues, making it a good medium to model the behavior of US waves in soft tissues. However, the US attenuation in water is much smaller than in soft tissues.

2.2. Ultrasound Neuromodulation

This section describes the recent findings in the field of ultrasound neuromodulation. Recent advancements have expanded our understanding of US neuromodulation, paving the way for the development of noninvasive and precise therapies to treat neurological disorders. After reviewing the latest research on ultrasound neuromodulation, this section summarizes the optimum sonication parameters for reliable US neuromodulation. Then, we will delve into the state-of-the-art findings to gain insight into the mechanisms of ultrasound neuromodulation, discussing how ultrasonic waves interact with neural tissues to activate or suppress neuronal activity. In the end, this section explores the potential safety concerns associated with US neuromodulation.

2.2.1. Sonication Parameters

Sonication parameters play an essential role in ensuring both the efficacy and safety of ultrasound neuromodulation. This discussion aims to provide an overview of the parameters used in US neuromodulation, including the acoustic and safety indexes.

Fig. 2.4 illustrates a typical waveform utilized in ultrasound neuromodulation. This waveform is characterized by its specific frequency (f), inter-stimulation intervals (ISI), sonication duration (SD), pulse repetition frequency (PRF), DC (DC), and pressure amplitude (p). The frequency of the US waveform is determined by the frequency of the US transducer. The stimulation frequency impacts the penetration depth and spatial resolution of the ultrasound beam as well as the acoustic attenuation in the tissue. High-frequency sound waves have lower wavelengths and hence provide better spatial resolution. However, as the frequency increases, the acoustic attenuation, mainly due to absorption, increases as well. Consequently, these losses limit the applied frequency, particularly in transcranial US stimulation, since the US waves must pass through the skull. A comprehensive analysis of the influence of US stimulation frequency on other acoustic parameters is provided in Chapter 3.

In ultrasound neuromodulation, the inter-stimulation interval refers to the periods

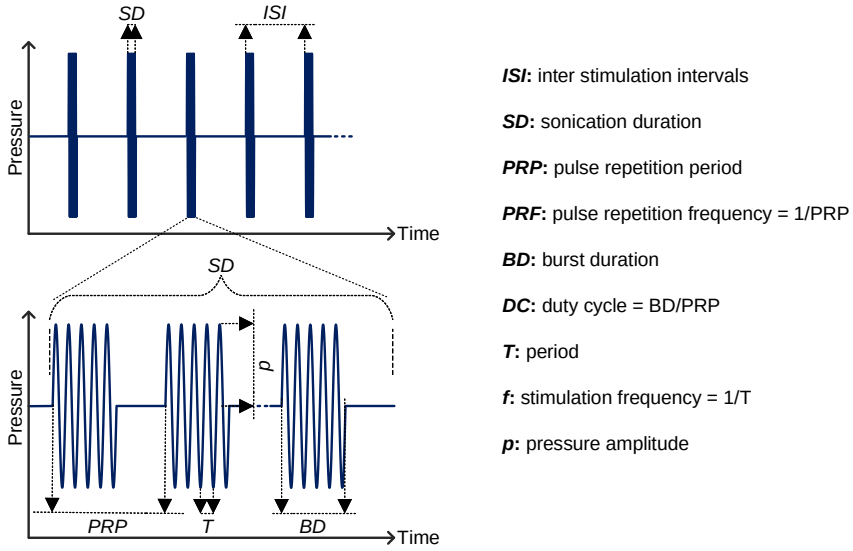

Fig. 2.4: A typical ultrasound pressure waveform used in ultrasound neuromodulation [59].

between two consecutive ultrasound stimulation sessions. The sonication duration is the total time interval of an ultrasound stimulation session. In ultrasound neuromodulation, a burst of pulses is used rather than continuous pulsing. The frequency and *DC* of this burst define the burst repetition frequency and the *DC* of the stimulation. These time intervals help ensure that neural tissues can recover from any permanent physiological changes induced by ultrasound stimulation. Moreover, proper time intervals can help avoid cumulative thermal or mechanical effects that could result in tissue damage or undesirable neuromodulation outcomes [60]. The value of these parameters varies significantly depending on the specific goals of the neuromodulation, the target tissue, and the safety considerations. Evidence from the previous studies on US neuromodulation has shown that longer stimulation duration results in inhibition of neuronal activity, while shorter duration leads to excitation [61], [62].

Apart from the timing parameters of the ultrasound neuromodulation waveforms, other important parameters relate to the amplitude. Firstly, p denotes the amplitude of the pressure wave applied to the tissue, whereas p_i indicates the instantaneous pressure. For assessing the ultrasound power density, instantaneous intensity (I_i) is utilized. I_i [W/cm^2] can be determined by

$$I_\mathrm{i} = \frac{p_\mathrm{i}^2}{\rho \cdot \nu} \tag{2.7}$$

where ρ and ν are the medium's density and the sound velocity in the medium. This equation shows that I_i is directly proportional to the square of the p_i and inversely proportional to ρ and ν [59].

US neuromodulation demands sufficient acoustic intensity to modulate neuronal activity. However, excessive intensity may cause thermal or mechanical damage to the tissue. Therefore, to ensure safety in ultrasound neuromodulation, monitoring the temporal and

average power delivered to the tissue is crucial. Spatial-peak pulse average (I_{SPPA}) measures the average intensity during the burst duration and can be calculated from

$$I_{SPPA} = \frac{1}{BD} \cdot \int_0^{BD} I_i(t)\, dt \tag{2.8}$$

where BD is the pulse duration [63]. Assuming a sinusoidal pressure waveform, (2.8) can be rewritten as

$$I_{SPPA} = \frac{p^2}{2 \cdot \rho \cdot v} \tag{2.9}$$

Another important way to quantify the power delivered to the tissue is by means of spatial-peak temporal average (I_{SPTA}), which determines the average intensity over the entire sonication duration, providing an estimation of the tissue heating [64], [65]. I_{SPTA} [W/cm^2] is given by

$$I_{SPTA} = \frac{1}{SD} \cdot \int_0^{SD} I_i(t)\, dt \tag{2.10}$$

Other parameters used to evaluate the safety of ultrasound include mechanical index (MI) and thermal index (TI). MI [MPa/MHz$^{1/2}$] provides an estimate of the likelihood of potential inertial cavitation in the tissue [66]. MI is expressed as

$$MI = \frac{PNP}{\sqrt{f}} \tag{2.11}$$

where PNP, as shown in Fig. 2.2, is the peak negative pressure applied to the tissue, and f is the sonication frequency. The ideal value of the MI should be below 1.9 MPa/MHz$^{1/2}$ to avoid the bioeffects [67]. On the other hand, TI gives insight into assessing the likelihood of temperature rise in the tissue, which may cause heat-induced adverse biological effects. TI is defined as the steady-state temperature increase in the tissues as a result of exposure to an ultrasound beam [59]. The maximum allowed thermal index varies from 0.6-1.3 depending on the type of tissue [67].

2.2.2. A Review of US Neuromodulation Studies

After years of studies on ultrasound neuromodulation, extensive research has demonstrated that ultrasound can effectively stimulate and suppress neural activity across various models, including humans [68], animals [69], and cells [62]. Examples of US neuromodulation setups are shown in Fig. 2.5. This technique has been applied to both peripheral [70] and central [61] nerve systems, showing that US can modulate nerves in superficial [43] and deep [71] regions. Due to the diverse sonication parameters employed in these studies [26], there has been a need for a thorough review to determine the most effective sonication parameters to modulate neuronal activity with ultrasound.

Research on using ultrasound to modulate the activity of electrically excitable tissues has a long and evolving history, dating back a century. In 1929, Harvey's experiments demonstrated that ultrasound could induce cardiac muscle contractions in frogs and turtles, a response akin to that observed with electrical stimulation [72]. In the 1950s, ultrasound has also been applied to the brain, predominantly for deep brain ablation aimed

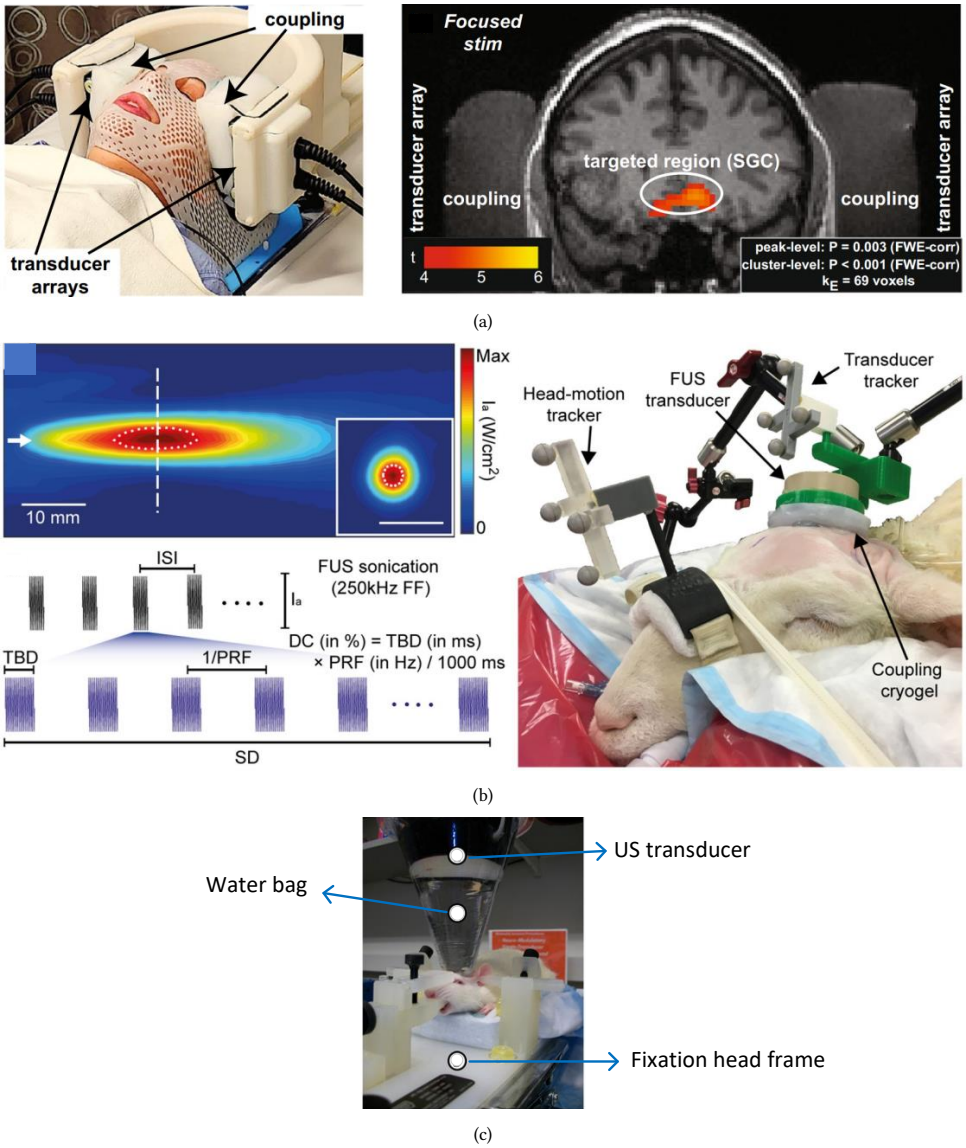

Fig. 2.5: Examples of setups for performing US neuromodulation on (a) human, reprinted from [68] under CC BY 4.0, (b) sheep, reprinted from [69] under CC BY 4.0, (c) rat, reprinted from [47] ©2012, with permission from Elsevier.

at treating movement disorders [73], [74]. In 2010, Tufail's research showed that ultrasound neuromodulation could elicit local field potentials in the somatomotor cortex of anesthetized rats, leading to an advance in understanding the potential of US neuromodulation [75]. Since Tufail's findings, interest in ultrasound neuromodulation has surged, as evidenced by the sharp increase in related publications over recent years [57], [76].

Previous experiments on ultrasound neuromodulation utilized a wide range of son-

ication parameters, highlighting the dependency of reported sonication parameters on various factors such as the target tissue and the setup of the ultrasound stimulation [63]. These sonication parameters vary depending on whether the stimulation subject is animal or human or whether the target is within the peripheral or central nervous system. Therefore, it is essential to consider these assumptions when exploring US neuromodulation studies. Thus, in the description below, the US neuromodulation studies are sorted based on subject and anesthesia level. Then, a discussion on the sonication parameters used in these studies is provided.

There is a wide range of studies exploring the effect of ultrasound on various animals, particularly rodents. [61], [77]–[80] have demonstrated that ultrasound can activate neural activity in the hippocampus and motor cortex of rats. They have used values of sonication frequency, I_{SPTA}, *PRF*, and *DC* in the range of 0.35-2.5 MHz, 0.25-4.47 W/cm^2, 0.5-2 kHz, and 1-50%, covering broad ranges, especially for the applied intensity. Ultrasound neuromodulation has also been applied to mice to evoke activity in various sites in the animal spinal cord, cortex, sub-cortical structures, and peripheral nerves [81]–[86]. Although these works have used similar frequency and *PRF*, the reported intensity to achieve stimulation changes considerably. The small size of the mouse's brain, the large size of the ultrasound focal spot, and the attenuation in the skull may explain this discrepancy [63], [78]. Besides the activation, ultrasound inhibition of visually evoked potentials is reported in rats [87], rabbits [88], and cats [89]. Moreover, ultrasound has been used to suppress seizure-like activities in various animal models [90], [91]. However, these experiments are limited to sedated animals, limiting the seizure frequency and the ultrasound efficacy [61], [63]. Therefore, studying US suppression for epilepsy demands a wearable ultrasound transducer, allowing experiments on freely moving animals.

In the studies described in rodents, the ultrasound frequency is such that the focal spot has a size in the same order of magnitude as the rodent brain, which results in low spatial resolution. For that reason, larger animals are normally utilized for that purpose and for an intermediate step towards translation to humans. [69] demonstrated that stimulating the primary sensorimotor of sheep generates electrophysiological responses without any adverse effect. [92] also reported that ultrasound stimulation of primary sensorimotor (SM1) and visual (V1) brain areas in sheep generates electromyographic and electroencephalographic responses. [44] shown that US stimulation of the central sulcus in monkeys causes downstream activations in the off-target somatosensory brain region. [93] reported that ultrasound elicits extensive activation across cortical and sub-cortical brain regions of guinea pigs, proving that ultrasound can activate the ascending auditory system through a cochlear pathway. [94] utilized ultrasound to target the thalamic nucleus of pigs; the experimental results prove selective inhibition of somatosensory evoked potentials (SSEP) without any tissue damage. [95] demonstrated that ultrasound can suppress the auditory evoked potentials (AEPs) in pigs using different intensities, proving that higher ultrasound intensities result in stronger suppression. These experiments used a broad range of sonication parameters; the sonication frequency was kept below 1 MHz, mostly 500 kHz. The *PRF* and *DC* were in the range of 0.01-4 kHz and 10-50 %, respectively, while I_{SPTA} varied from 0.5-10 W/cm^2. The reported intensities were higher than the intensities used in small animals, which can be due to the thicker skulls of these animals.

In addition to animals, previous studies demonstrated that ultrasound can activate and

suppress neural activity in humans. [96]–[99] have reported that the primary somatosensory cortex stimulation evoked electroencephalographic responses in healthy humans, while no tissue damage was detected. [100] showed that ultrasound stimulation of the primary visual cortex in humans leads to elicited activation of the stimulated area and the network of regions involved in visual cognitive processes. [71] demonstrated that ultrasound modulation of the sensory thalamus in humans can suppress the sensory evoked potentials (SEPs). The reported intensities for activation or suppression of neural activity in humans are higher than those in animal experiments, varying from 0.5-17.5 W/cm^2. The other sonication parameters, such as *DC*, *PRF*, and sonication frequency, are similar to the parameters used in experiments with large animals.

In many experiments involving small animals, researchers have commonly used anesthesia to restrict the animals' movements. This contrasts with studies on humans, in vitro environments, and larger animals, where anesthesia is typically not employed. Research has shown that anesthesia can raise the threshold intensity needed for effective neuromodulation. For example, [49] demonstrated that stimulating the motor cortex in anesthetized rats with 80 mg/kg Ketamine needs approximately 2.5 times higher intensity to elicit the same response as in experiments involving freely moving animals. This underscores the impact of anesthesia on the efficacy of US neuromodulation, highlighting the need for wearable US transducers for experiments on awake and freely moving animals.

By analyzing the studies on US neuromodulation, a conclusion can be drawn regarding the sonication parameters. The majority of studies have utilized frequencies below 1 MHz, primarily driven by the need to minimize acoustic attenuation in the skull, which increases with frequency. However, the use of these lower frequencies often results in larger ultrasound focal spots, which reduces the precision of the neuromodulation. Conversely, higher frequencies are favored for their ability to achieve higher spatial resolution, enhancing the accuracy and effectiveness of the stimulation. Despite the common use of lower frequencies, there have been experiments that utilized higher frequencies. [101] reported the stimulation of ion channels using a 1.47 GHz sonication frequency. Additionally, [102] demonstrated that applying an 8 MHz ultrasound beam to the scalp over the frontotemporal cortex effectively reduced chronic pain. On the other hand, [66] has shown that higher frequencies require higher intensities to elicit the same effect as lower frequencies. However, [26] has demonstrated that the threshold intensity to perform a successful US neuromodulation does not rise significantly with increasing frequency. In summary, high-frequency ultrasound waves offer higher spatial resolution at the cost of higher US threshold intensity and skull attenuation.

Regarding the *PRF* and *DC*, previous works have commonly employed a *PRF* ranging from 0.5 to 1.5 kHz, paired with a *DC* between 36% and 50%. Previous studies indicate that a higher *PRF* tends to correlate with a higher stimulation success rate [86], [103], [104]; however, exceeding a *PRF* of 2-3 kHz does not improve the success rate further [105]. Similarly, while a *DC* of 50% is most frequently utilized, it has been observed that increasing the *DC* up to 60% can reduce the threshold intensity necessary for successful stimulation [61], [105]. Despite this, increasing the *DC* beyond 60% does not significantly enhance success rates, indicating an optimal upper limit for the *DC* [62]. Interestingly, some studies have achieved successful ultrasound neuromodulation with *DC*s of less than 5% [79], [106]–[108]. These findings suggest that while a *DC* of 50% is widely used by

neuroscientists, lower *DC*s can also lead to the same result.

Finally, the threshold intensity to evoke neuronal activity also varies substantially across different study subjects. Since the thickness of human skulls differs from that of animals, human studies employed higher intensities to elicit neural responses successfully [81]–[86], [96]–[99]. Additionally, even within the same study subject, different studies have reported a wide range of threshold intensities, generally with a trend that higher intensities lead to higher success rates [61]. This variability in required intensities can be attributed to several factors. Different target regions within the brain may respond differently to ultrasound stimulation. For example, stimulating the thalamus demands higher intensity than the motor cortex [63]. Moreover, the type of neuromodulation, whether it aims to stimulate or suppress neuronal activity, also significantly impacts the required intensity levels. For instance, studies have shown that suppression of neuronal activity typically requires lower intensities than stimulation [59].

In summary, reported sonication parameters vary among different studies. This highlights the need for a wearable US transducer that not only generates the required sonication parameters for a successful US neuromodulation but also allows adjusting these parameters according to the needs of researchers.

2.2.3. Mechanism of US Neuromodualtion

Despite over fifty years of research into the neuromodulatory effects of ultrasound, the exact mechanism behind ultrasound neuromodulation remains elusive. To grasp how ultrasound influences neuronal activity, it is essential to understand the complex nature and causes of nerve impulses. Various stimuli, including electrical, chemical, mechanical, and thermal changes, can cause excitatory and inhibitory responses [26]. Therefore, the nature of nerve impulses suggests a possible mechanical or thermal mechanism for modulating neuronal activity with ultrasound [63].

Absorption of the US waves in the tissue can result in a temperature rise, leading to modulating neuronal activity. Even slight temperature changes, on the order of a few degrees, can impact neural activity by altering the amplitude and duration of action potentials (APs), excitation thresholds, spiking rates, and afterhyperpolarization kinetics [26], [109]. The thermal effects of ultrasound on neuronal activity depend on the sonication parameters of the incident ultrasound beam. At higher US intensities, the thermal effects can cause severe biological alterations such as tissue homogenization, protein denaturation, and DNA fragmentation, resulting in cellular death [110]. Conversely, thermal effects at lower ultrasound intensities cause ultrastructural synaptic changes and decrease in synaptic vesicle count, which eventually leads to evoking neuronal responses [110]. Furthermore, the sonication duration impacts thermal modulation, where slow and prolonged heating of neuronal tissue may inhibit action potential generation by affecting ion channel activities [90]. On the other hand, rapid temperature increases can temporarily alter the plasma membrane capacitance, leading to action potential generation [63], [111].

High-intensity ultrasound waves traveling in a fluid cause negative pressure, which can resonate, expand, and collapse gas bubbles and, hence, lead to cavitation [57]. There are two types of cavitation: non-inertial and inertial cavitation. In non-inertial cavitation, also known as stable cavitation, the bubbles do not collapse but oscillate over several cycles of the ultrasound wave. Non-inertial cavitation is considered less destructive than iner-

tial cavitation but can still influence biological processes. Inertial cavitation involves the rapid collapse of bubbles that form in the medium. The collapse happens so quickly that it generates significant energy, potentially causing high temperatures and shock waves [57]. While cavitation is rare in the nervous system due to the absence of gas bubbles, microcavitation may still occur within neurons. Consequently, this can lead to sonoporation by increasing membrane permeability by forming pores in the lipid bilayer. These microcavitations may cause capacitive changes in the membrane, allowing the neuron to reach its threshold and generate an action potential, known as the 'intramembrane cavitation hypothesis' [112], [113].

Another possible mechanism behind ultrasound neuromodulation involves the activation of mechanosensitive ion channels [114]–[116]. These channels are specialized proteins embedded in the cell membrane that respond to mechanical stimuli, such as stretching or compression, to allow the flow of ions across the neuron's membrane, which can alter the electrical potential of the neuron and lead to changes in neuronal activity. Since ultrasound waves may lead to acoustic radiation forces on the membrane of neurons, it has been hypothesized that this may be the mechanism for ultrasound neuromodulation [114]–[116]. This process can result in either the excitation or inhibition of the neuronal activity, depending on the types of ions that flow through the channels. Transient receptor potential (TRP) channel is an example of such mechanosensitive ion channels, which are particularly sensitive to mechanical forces induced by ultrasound waves [117].

Another hypothesis for the mechanism of US neuromodulation based on the vibration of microtubules is presented in [102]. According to this hypothesis, megahertz ultrasound waves are within the resonance frequency of microtubules. Therefore, US waves allow for the vibration of microtubules when their propagation direction is aligned with the long-axis microtubules. Since microtubules are connected to actin filaments in dendritic spines, these vibrations could be translated as electrical responses [112], [118]. In summary, although previous studies have shown that radiation force and mechanosensitive ion channels play a vital role in US neuromodulation, understanding the complete mechanism behind US neuromodulation demands more research studies.

2.2.4. Safety of US Neuromodualtion

Ultrasound wave propagation in the tissue impacts the cells in the medium, which may lead to structural or functional changes depending on the sonication parameters of the incident beam. Consequently, it may cause harmful bioeffects, leading to reversible or irreversible effects on the tissue [119]. In reality, both reversible and irreversible effects are utilized to develop ultrasound therapeutics, such as US blood-brain barrier (BBB) opening and ablation [120], [121]. However, unwanted bioeffects raise concerns over the severe side effects and safety of ultrasound beams. Here, a brief study on the safety of ultrasound neuromodulation is provided.

The primary mechanisms through which ultrasound exerts biological effects as it travels through the tissue are thermal and mechanical. Mechanical effects largely stem from the presence of gas, either due to acoustic cavitation or the use of microbubble contrast agents [119]. Conversely, thermal effects are mainly caused by the absorption of ultrasound waves within the tissue, resulting in excessive heat generation [26]. The severity of these biological effects depends on the ultrasound beam's intensity and frequency, which

may result in tissue damage, such as bleeding, cellular damage, and cell death [59].

Bleeding is a potential mechanical effect of ultrasound waves due to cavitation. Although it is relatively uncommon and mostly reported under conditions of deliberately applying high US intensities in experimental studies [59]. For instance, one study exposed 37 rats to ultrasound beams with an I_{SPTA} of 11.2 W/cm^2, significantly higher than the FDA's safety limit of 0.72 W/cm^2. This experiment resulted in findings of hemosiderin in some areas of one rat, suggesting the possibility of localized bleeding, although no other animals in the study exhibited signs of bleeding [61]. In another study involving eight sheep, prolonged sonication with an I_{SPTA} of 3.3 W/cm^2 is utilized to assess the safety of US neuromodulation. This led to the observation of micro-hemorrhages in the primary visual cortex of four sheep, indicating that high-intensity ultrasound may cause microscopic bleeding under certain conditions [92]. Therefore, exceeding the safety limits for the mechanical index may cause adverse effects during ultrasound neuromodulation.

Regarding the thermal effects, the extent of the temperature rise is influenced by various sonication parameters. On one hand, sonications at higher frequencies result in higher absorption, thereby generating excessive heat [57]. On the other hand, the sonication duration also affects temperature increase, with longer durations causing higher temperature rises in the tissue [83]. Previous studies investigating the effects of temperature increases due to ultrasound have reported that these rises remain within the FDA's safe limits where typical sonication parameters are utilized [122], [123]. There have been no documented cases of cellular damage, cell death, or behavioral changes attributed to temperature increases in the tissue [59].

In summary, the safety of ultrasound neuromodulation has been well-documented in numerous studies, indicating that harmful effects are typically absent when sonication parameters adhere to safety guidelines [26], [59], [121], [124]. Consequently, ultrasound neuromodulation is considered a safe technique, provided the FDA's guidelines are followed. This adherence minimizes the risk associated with US neuromodulation in clinical and research applications.

2.3. Ultrasound Transducers

2.3.1. The Piezoelectric Effect

Different approaches exist to convert electrical pulses to ultrasound waves and vice versa. However, the most prevalent method, particularly in clinical ultrasound devices, is based on a phenomenon called the piezoelectric effect. This effect is observed in certain crystalline materials and involves the reversible conversion of mechanical and electrical energies from one to another [56]. Piezoelectricity was discovered in 1880 by Pierre and Jacques Curie in several materials, including quartz crystals. The term "piezoelectric" derives from the Greek word 'piezein,' meaning to press, which aptly describes how the piezoelectric effect works. When the piezoelectric material is deformed, the ions in each unit cell are displaced, causing an electric polarization and, hence, an electrical potential across the material. In other words, the piezoelectric material generates an electric charge in response to applied mechanical stress on its surface; thus, it converts mechanical energy into electrical energy [125]. As shown in Fig. 2.6, the polarity of the generated charge also changes between the compression and stretching phases. Conversely, when a potential

Fig. 2.6: Piezoelectric phenomenon during compression and stretching [56].

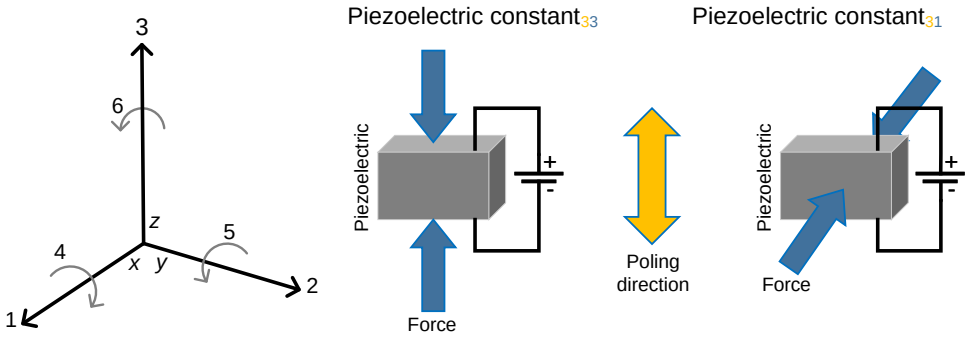

Fig. 2.7: Orientations of the piezoelectric crystal, showing two different configurations as an example [127].

difference is applied between the two surfaces of the piezoelectric material, the crystal will respond by expanding or contracting, converting electrical energy into mechanical energy [56].

2.3.2. Critical Piezoelectric Material Parameters

In the field of materials science, describing the properties of piezoelectric materials involves a variety of specific parameters. Due to the anisotropic nature and permanent polarization of these materials, these factors are typically represented using matrix notation to capture directional dependencies. The directions within the matrix are designated by the numbers 1, 2, and 3, corresponding to the x, y, and z axes, respectively. Each parameter is generally expressed with two subscripts that show the direction of the two related quantities, for instance, the direction of the electric field and the mechanical response [126]. Fig. 2.7 depicts two different crystallographic orientations of the piezoelectric crystal relative to the electrical poling direction.

The piezoelectric material's shape or geometry also plays a crucial role in determining the transducer parameters. Thickness-expander geometry is the most common shape of piezoelectric materials. Fig. 2.8(a) illustrates this geometry for rectangular and disk-shape transducers. In this geometry, the lateral dimensions are much larger than the thickness, and the poling is parallel to the applied electric field. Therefore, the displacements of the piezoelectric material are dominated by the thickness direction. In this case, the resonances in the lateral directions happen at very low frequencies. The best piezoelectric parameters describing the behavior of a piezoelectric transducer with thickness-expander geometry are the thickness mode parameters, such as k_t, which is the thickness mode electromechanical coupling efficiency. The geometries where the thickness is comparable to or smaller than the width, in one-dimensional (1D) arrays, or both the width and

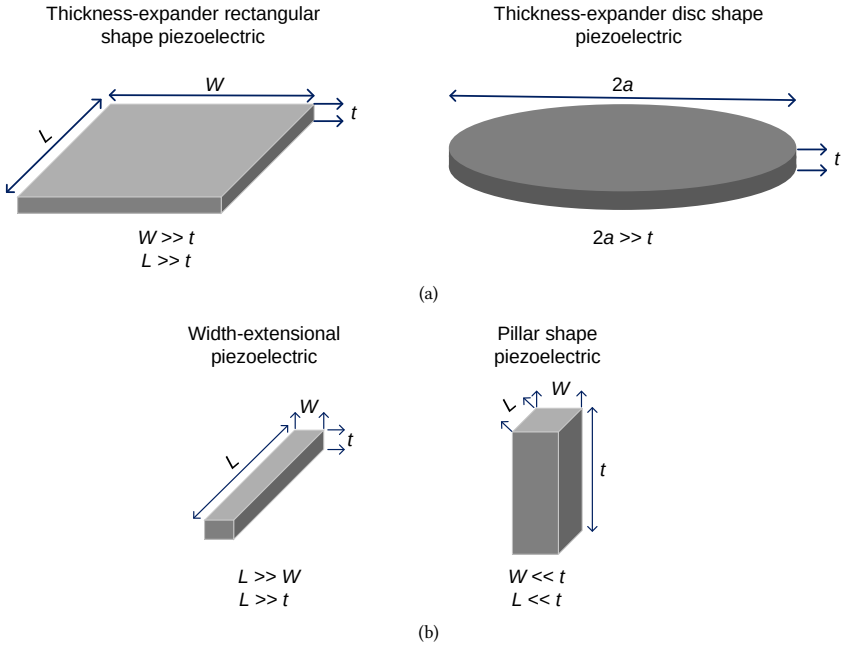

Fig. 2.8: Different geometries of piezoelectric materials; poling direction is along the z-axis. (a) thickness-expander resonance mode, (b) width-extensional and pillar resonance mode [58].

length, in two-dimensional (2D) arrays, are called the width-extensional and the pillar shape piezoelectric, respectively, as shown in Fig. 2.8(b). In these geometries, the appropriate piezoelectric parameters are in the direction of 33 [58].

The piezoelectric charge coefficient, often denoted as d, is the most important parameter in piezoelectric materials, expressing the material's sensitivity in the transformation from mechanical energy into electrical energy and vice versa. It is defined as the electric charge generated per unit area in response to a mechanical stress or the mechanical strain produced per unit electric field. It is typically expressed in units of coulombs per newton (C/N) or meters per volt (m/V), depending on the direct or reverse piezoelectric effect. A higher d indicates a more sensitive material, which is desirable in precise ultrasound sensors and actuators. As explained above, d_{33} describes the charge produced when mechanical force is applied parallel to the polarization direction, while d_{31} measures the charge when stress is applied perpendicular to the polarization direction in one axis. d_{15} expresses the charge generated perpendicular to both the polar axis and the direction of mechanical shear. This coefficient is particularly relevant when the stress is shear stress and the electric polarization occurs in an orthogonal direction. d_{33} is the most important piezoelectric charge coefficient parameter in high-power and imaging applications because it deals with direct compression or expansion along the polling axis, offering the highest piezoelectric effect per unit of stress [128], [129].

Another important parameter in piezoelectric materials is the electromechanical coupling coefficient, denoted as k, which quantifies the efficiency of a piezoelectric material in converting electrical energy into mechanical energy and vice versa. Unlike the piezo-

electric charge coefficient, k is a dimensionless coefficient that measures the effectiveness of the energy conversion process. The value of k can range from 0 to 1 (or from 0% to 100%), where a value of 1 (or 100%) indicates a perfect conversion with no energy loss, though such an ideal situation is not achievable in practical scenarios. Higher values of k indicate more efficient energy conversion, making such piezoelectric material desirable for various ultrasound applications. There are different types of electromechanical coupling factors depending on the mode of operation, such as k_t for thickness mode, k_{33}, k_{31}, and k_{15} depending on the direction of the induced polarization and the direction of the mechanical stress [130], [131]. The electromechanical coupling coefficient is defined as the square root of the ratio of stored mechanical energy in the piezoelectric material to the supplied electrical energy or vice versa. The thickness mode electromechanical coupling coefficient is expressed as:

$$k_t = \sqrt{\frac{\text{Stored mechanical energy}}{\text{Input electrical energy}}} = \sqrt{\frac{e_{33}^2}{C_{33}^D \cdot \epsilon_{33}^S}} \tag{2.12}$$

where e_{33} is the piezoelectric stress constant; C_{33}^D is the elastic constant, and ϵ_{33}^S is the clamped dielectric permittivity [126]. The appropriate coupling coefficient for the thickness expander mode is k_t, while the proper electromechanical coupling coefficient for pillar-mode and width-extensional modes is k_{33} [58], as depicted in Fig. 2.8. The piezoelectric stress constant, denoted as e, expresses the charge generated per unit of applied force or the mechanical strain per unit of electrical voltage applied. This constant describes how effectively a piezoelectric material can convert mechanical energy into electrical energy under stress. It is expressed in units such as coulombs per square meter (C/m^2) or volts per meter (V/m). This parameter plays an essential role in applications where mechanical force needs to be directly converted into an electrical signal, such as in ultrasound imaging or piezoelectric energy harvesting applications [58]. The elastic constant of piezoelectric materials, denoted typically as C^D, is a crucial mechanical parameter that quantifies the stiffness or rigidity of the material under mechanical stress. It is defined as the ratio of stress to strain in a piezoelectric crystal, indicating how much force is needed to deform the material. The elastic constant is expressed in units of Pascals (Pa) or Newtons per square meter (N/m^2) [58]. Finally, the dielectric permittivity, expressed by ϵ, is the ability of a material to hold an electrical charge. This parameter is expressed under conditions where the piezoelectric material is restricted from deforming, providing a measure of the material's intrinsic dielectric response independent of its piezoelectric deformation capabilities. The clamped dielectric permittivity is important for calculating the clamp capacitance, which is part of the electrical model of the piezoelectric transducers. The clamp capacitance is written as:

$$C_{33}^S = \frac{\epsilon_{33}^S \cdot A}{t} \tag{2.13}$$

where A and t are the area and the thickness of the piezoelectric material [126].

Similar to the acoustic medium, the piezoelectric transducers also present acoustic impedance to the propagation of ultrasound waves. The acoustic impedance of the piezoelectric material should ideally match the acoustic impedance of the medium to minimize

the reflection and maximize the transmission of the ultrasound energy. Piezoelectric materials mostly have high acoustic impedance, while the human body has significantly lower acoustic impedance. Therefore, maximizing the energy transfer from the transducer to the human tissues requires effective acoustic matching. In practice, matching layers are applied over the piezoelectric materials to bring their acoustic impedance closer to that of the tissue and, hence, enhance the efficiency of the acoustic energy transfer [132].

The resonance frequency is another critical operational parameter that affects the performance of the US transducers. Since the piezoelectric materials are electromechanical devices, their resonance can be translated to an electrical and mechanical resonance. In the mechanical resonance frequency, the piezoelectric materials exhibit the maximum displacement, while in the electrical resonance, they show the minimum electrical impedance. The mechanical resonance frequency, f_{m}, is determined from

$$f_{\mathrm{m}} = \frac{v}{\lambda} = \frac{v}{2t} \tag{2.14}$$

where v and λ are the velocity and wavelength of US waves in the piezoelectric material, and t is the thickness of the piezoelectric material. Electrical impedance spectroscopy is an indirect but useful way to examine the resonant behavior of the piezoelectric material. As depicted in Fig. 2.9, the electrical impedance spectroscopy reveals the electrical resonance and anti-resonance frequency and its harmonics, the electrical resonance frequencies in the other directions of the piezoelectric transducer, and their harmonics. The electrical resonance and anti-resonance frequencies happen when the electrical impedance is the minimum and maximum value, respectively. At the electrical resonance frequency, the phase of the impedance of the piezoelectric transducer is close to zero, behaving as a resistive load. Generally, the mechanical resonance frequency is inversely proportional to the thickness of the piezoelectric material. However, it also depends on the size of the piezoelectric transducer. Piezoelectric transducers in the width-extensional or pillar modes have lower electrical resonance frequency than the thickness-expander mode with the same thickness [133].

Bandwidth is a key parameter in piezoelectric transducers that determines how well the transducer can handle frequency variations in the signals it transmits or receives. For piezoelectric transducers, bandwidth is defined as the frequency range where the transducer generates an adequate level of pressure, usually measured between points where the pressure falls off, typically by 3 dB from the peak pressure. The quality factor (Q) is an indication that quantifies the ratio between resonance frequency and bandwidth. Quality factor measures the damping characteristics of the transducer and its ability to maintain oscillation at its resonance frequency. In applications like ultrasound imaging, the bandwidth influences the resolution of the images. A wider bandwidth, in other words, lower Q, allows for transmitting a shorter pulse duration and receiving signals with a broader frequency range, leading to better resolution and finer details. However, lower Q results in higher damping and, hence, higher power consumption to drive the US transducer. On the other hand, in US neuromodulation applications, higher Q allows for higher oscillation of the piezoelectric transducer, improving the transmit efficiency [40].

In addition to the mechanical and electrical properties of the piezoelectric materials, reliable US transducers demand the characterization of piezoelectric materials based on

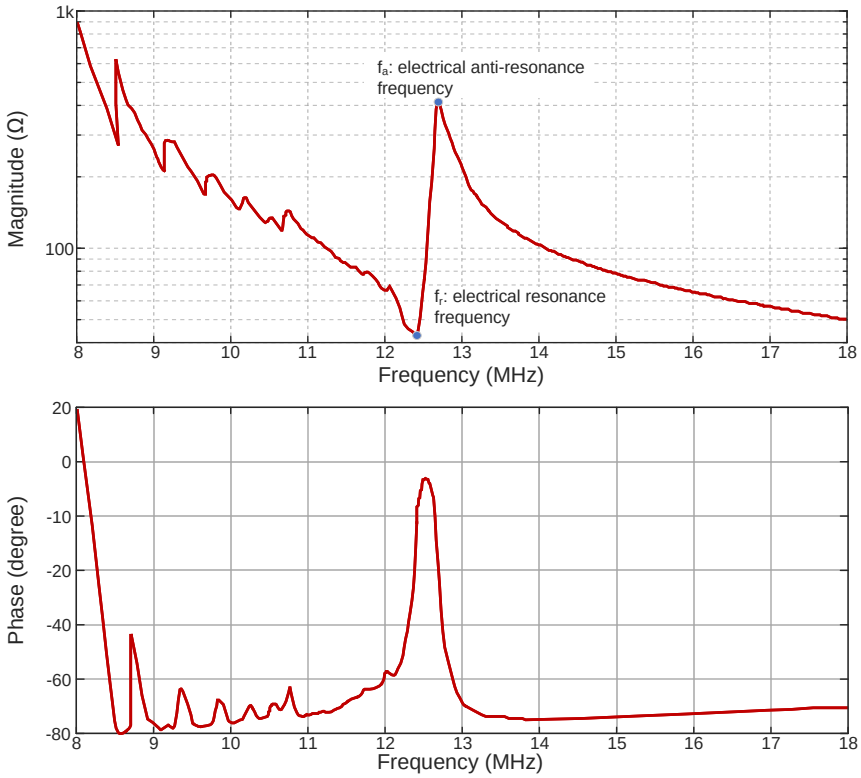

Fig. 2.9: The measured electrical impedance of a PZT-5H piezoelectric transducer. This figure shows the electrical resonance and anti-resonance frequency.

the temperature change. The Curie temperature, denoted as T_C, is the most critical thermal property of a piezoelectric material, which represents the thermal threshold in which piezoelectric materials undergo a phase transition, losing their polar alignment and, consequently, their inherent piezoelectric properties. Commercial piezoelectric materials have a Curie temperature of around 350°C but have a maximum recommended operation temperature of around 150-250°C [134].

2.3.3. US Beam Shape

As the generated US waves by the transducer propagate in the medium, they form an ultrasound beam, which characterizes the spatial distribution of US pressure with the distance from the transducer. In most applications, the US transducers are designed to have a narrow beam, generating a focal spot where the pressure is the maximum. As the US waves propagate away from the focal zone, they undergo divergence and, hence, lose their energy density. According to the inverse square law for US waves, the intensity of the US wave after the focal spot, i.e., in the far field, is calculated from

$$I = \frac{p}{4\pi r^2} \tag{2.15}$$

where p is the pressure at the source, and r is the distance from the source. It is evident that after the focal spot, as the distance from the transducer increases, the intensity drops significantly.

Fig. 2.10 illustrates the generated US beam profile by a disc shape unfocused transducer. The region between the transducer and the focal zone is called the near field or the Fresnel zone. The US beam in the near field exhibits multiple pressure peaks due to the way US waves interfere with each other when emitted from a transducer [56]. After the near field, the US waves converge to a small space, leading to a focal region. The US intensity in the focal spot is the maximum, making the focal spot the most useful region in the beam profile in many applications such as US neuromodulation. The spatial resolution of the focal spot is a key characteristic in evaluating the performance of the US transducers. The spatial resolutions in the axial and lateral directions are called depth of field (*DOF*) and full width at half maximum (*FWHM*). The spatial resolution depends on the aperture size of the US transducer; the higher the aperture size, the finer the spatial resolution. However, since the spatial resolution is limited by the wavelength of the US waves, increasing the aperture size of the transducer does not improve the spatial resolution beyond the wavelength of the US waves. Therefore, another way to improve the spatial resolution is increasing the resonance frequency to have a smaller US wavelength; more details are provided in Chapter 3. Another critical property of the US focal spot is the US intensity at the focal spot, which depends on the aperture size of the transducer and US wavelength. Therefore, larger transducers driven by higher frequencies result in higher intensity at the focal spot [40]. The natural depth of the focal spot (Z) also depends on the resonance frequency and the aperture size of the transducer's diameter. It can be written as:

$$Z = \frac{f \cdot a^2}{v} \tag{2.16}$$

where f, a, and v are the resonance frequency, the radius of the transducer, and the sound velocity in the medium.

Beyond the focal spot, the US beam starts to diverge, which increases the beam width. This region is called the far field, the Fraunhofer zone. As illustrated in Fig. 2.10, the US intensity drastically decreases with its distance from the focal spot, which is in agreement with Equation 2.15. The behavior of the transducer in the far field is predictable with high precision, making this region a reliable zone for operation [27].

2.3.4. Focusing of The US Beam

The characteristics of the focal spot, including its intensity and spatial resolution, play an important role in the efficacy of ultrasound applications. For instance, in ultrasound imaging, a narrower focal spot enhances the resolution of the US images, allowing for more detailed visualizations of internal structures, which is crucial for accurate diagnoses. Similarly, in therapeutic ultrasound applications, a high-resolution focal spot ensures precise targeting. This precision not only improves the effectiveness of treatments but also substantially reduces the potential adverse side effects by affecting the surrounding tissues. In this regard, the ability to focus ultrasound waves effectively plays a key role in achieving a high-intensity and high-spatial-resolution focal spot. Advanced focusing techniques have been employed to form a focused focal spot. These techniques involve mechanical

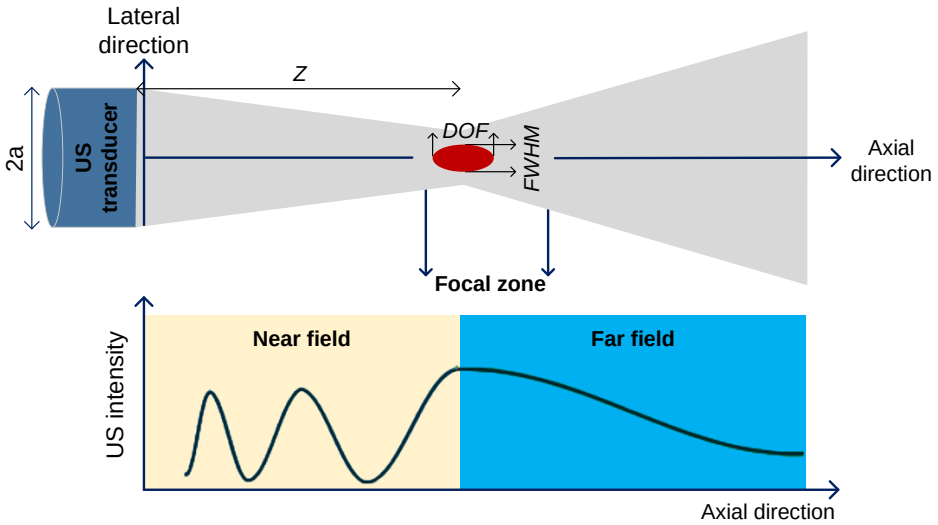

Fig. 2.10: The beam profile and acoustic intensity of a disc-shaped ultrasound transducer along the axial and lateral directions [27].

means, such as the use of curved transducers and acoustic lenses or sophisticated electronic methods like phased array beamforming.

In terms of mechanical focusing methods, curved ultrasound transducers utilize a straightforward mechanical approach to focus ultrasound beams by leveraging the inherent shape of their surfaces. These transducers feature a curved emitting surface, as illustrated in Fig. 2.11(a), where the degree of curvature is tailored to the required focal depth. As ultrasound waves are emitted, they naturally diverge from the surface but are directed by the concave shape to converge at a common focal point [135]. The location of this focal point is determined by the radius of the curvature; a smaller radius results in a shorter focal length, bringing the focal spot closer, while a larger radius increases the focal length, positioning the focal spot farther from the transducer. This method offers the advantages of simplicity and cost-effectiveness since it does not rely on complex electronic controls or additional components. However, its main limitation is forming a fixed focal length, necessitating manual adjustment of the transducer's position relative to the target to control the location of the focal spot, which relies on a complex mechanical setup [56], [136].

In a different way, similar to optical lenses, focusing US waves can effectively be achieved using acoustic lenses, which manipulate the path of the US waves to form a focused focal spot. Among the different types of acoustic lenses, curved and Fresnel lenses are the most widely used lenses. A curved acoustic lens, as shown in Fig. 2.11(b), utilizes its curved shape to redirect the US waves through refraction, concentrating them at a focal point [56]. Alternatively, the Fresnel lens, like its optical counterpart, employs a series of concentric rings, each designed in a way to adjust the phase of the US waves passing through, as shown in Fig. 2.11(c). This design ensures that the waves converge in phase at the focal point, resulting in constructive interference and, hence, forming a focused focal

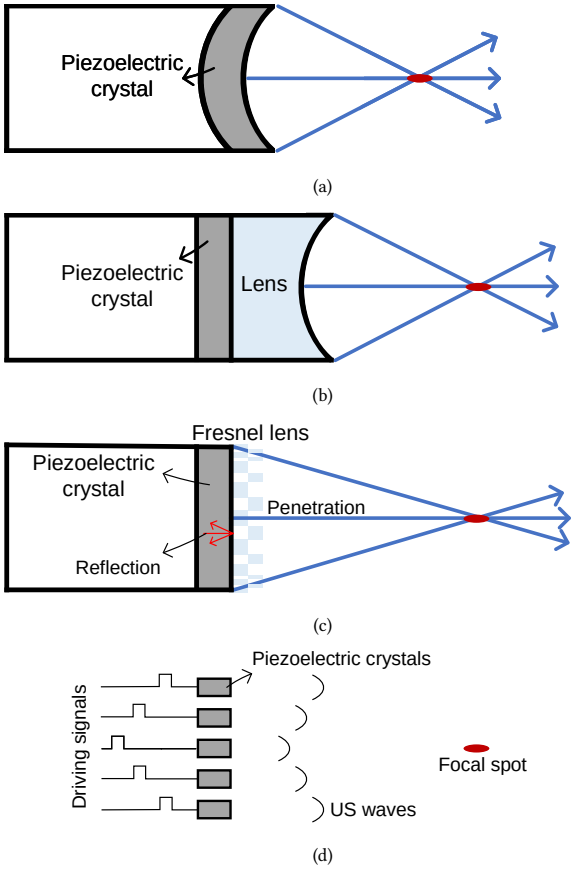

Fig. 2.11: Mechanical methods of focusing US waves using (a) curved ultrasound transducer, (b) curved acoustic lens, and (c) Fresnel lens (a) phased array configuration

spot. While the Fresnel lens offers the advantages of being thinner and less bulky than the curved lens, adjusting the focal spot in both types typically requires physical movement of the transducer, mirroring the limitations seen with curved transducers [137], [138].

Modern US biomedical applications, such as ultrasound drug delivery [139], ablation [140], and neuromodulation [40], demand US beam steering to adjust the location of the focal spot. While mechanical focusing techniques can create high-intensity and high-resolution focal spots, they lack the capability for beam steering, necessitating the development of a steerable and focused US transducer. Phased array transducers meet these advanced demands by employing an array of small piezoelectric elements, each controlled independently by a specific driver, as shown in Fig. 2.11(d). This configuration allows for the arbitrary adjustment of the ultrasound phases emitted by each element. The phases are carefully chosen to be proportional to each element's distance from the intended focal spot, ensuring that when the waves converge at the focal spot, they are in phase, creating a sharply focused area of ultrasound energy [141]. Moreover, by adjusting the phase of each element, the location of the focal spot can be electronically shifted without physically mov-

ing the transducer. This ability is crucial for applications requiring precise targeting and manipulation of the ultrasound focal spot. Different array configurations can perform this technique. An annular ring array [142] can alter the focal distance, while 1D arrays control the beam along the depth and a single lateral axis [143]–[145]. More complex 2D phased arrays allow for comprehensive steering in all directions, providing the ability to adjust the focal spot both axially and laterally [40], [53]. This level of control makes phased array transducers invaluable in cutting-edge medical ultrasound applications, where steerability and precision are paramount. A comprehensive study of 2D ultrasound phased arrays is provided in Chapter 3.

2.3.5. US Transducers' Losses

New US biomedical applications, such as battery-powered US imaging probes, US neuromodulation, and power delivery to implanted devices, demand power-efficient transducers. A power-efficient transducer is not only beneficial for prolonged battery life but also minimizes the risk of tissue damage caused by the generated heat. First of all, designing a power-efficient transducer demands a study of the US transducer's losses. Generally, there are two types of losses: electrical and mechanical losses.

The driving circuits are utilized to deliver proper electrical pulses to the US transducer. However, not all the power consumed by the electronic circuits is delivered to the US transducer. The electrical power losses involve power consumption of the core circuits, which perform beamforming, the switching losses in the electronic circuits that deliver HV pulses to the US transducers, and the losses due to the parasitic capacitance of the wiring and the transducer. Another source of electrical losses is the inherent resistance of the piezoelectric materials to the electric field, which is called dielectric losses [146]. These losses don't contribute to the electromechanical conversion process and ultimately end up being converted into heat. The generated excessive heat may cause damage to the electronic circuits, the piezoelectric transducer, and the surrounding tissue.

The mechanical losses in the piezoelectric transducers are another source of losses. The mechanical losses include the piezoelectric coefficient losses, which happen due to the electromechanical behavior of the piezoelectric transducer [147]. Furthermore, as the piezoelectric materials and other mechanical layers, such as backing layers, vibrate, internal friction occurs, causing mechanical losses [146]. These mechanical losses result in mechanical energy being converted to heat, decreasing the efficiency of the energy conversion process. Furthermore, the acoustic impedance mismatch between the US transducer and the medium is another source of the mechanical losses. When the acoustic impedance of the transducer material significantly differs from that of the medium, such as human tissue, part of the ultrasound energy is reflected back to the transducer rather than being transmitted into the medium. To address this challenge, transducers are often designed with one or more acoustic matching layers that minimize the acoustic impedance mismatch between the piezoelectric transducer and the medium. Furthermore, as the US waves travel through the tissue, they face attenuation due to the reflection, scattering, and absorption, affecting the overall efficiency. Hence, to design a power-efficient ultrasound neuromodulation device, all of the abovementioned loss mechanisms should be considered in a co-designed manner.

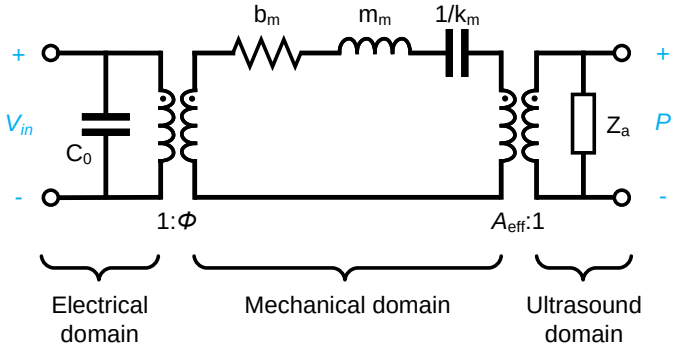

Fig. 2.12: Mason's equivalent model for ultrasound transducers [149].

2.3.6. Electrical Model of US Transducer

US transducers are electromechanical devices, in other words, they include both mechanical and electrical components. In this regard, the proper design of the electronic driver demands an electrical model for the ultrasound transducer, which mimics both the mechanical and electrical behaviors of the US transducer. The electrical model enables predictive analysis and simulation, allowing the engineers to optimize their US system before the physical implementation. This electrical model should mimic crucial parameters of an ultrasound transducer, which include the resonance frequency, the clamp capacitance, the electromechanical coupling coefficient, and the transducer's electrical impedance. The electromechanical coupling coefficient models the overall efficiency of the US transducer. The resonance frequency, electrical impedance, and clamp capacitance enable the design of a proper pulser to drive the US transducer.

In terms of piezoelectric transducer modeling, the Mason model is one of the common electrical equivalent circuits for piezoelectric transducers [148]. As shown in Fig. 2.12, the Mason model involves three parts: the electrical, mechanical, and ultrasound domains. In the electrical domain, V_{in} and C_0 represent the applied pulse and the clamp capacitance of the piezoelectric transducer. The electromechanical coupling is modeled with a transformer with a ratio of 1 to ϕ, describing the conversion of the electrical energy to the mechanical energy. In the mechanical domain, the inductor mimics the system's mass, which is a measure of the inertia of the system. The capacitor models the inverse of the piezoelectric stiffness. Higher stiffness results in lower capacitance. The value of the inductor and the capacitor model the resonance frequency of the piezoelectric transducer. The resistor also represents the damping of the piezoelectric transducer, which mainly depends on the quality factor of the piezoelectric transducer. Finally, in the acoustic domain, the acoustic impedance Z_{a} models the generation of US waves. The main drawback of the Mason model is its limitation on modeling the behavior of the transducer in a broad frequency range since it is most accurate at frequencies near the fundamental resonance of the transducer [149]. At higher frequencies, or when multiple modes of vibration are present, the model's accuracy can diminish because it may not account for the interactions between different harmonic modes [150].

Another equivalent circuit to represent the electromechanical behavior of the piezoelectric transducer is the Kirmholtz, Leedom, and Mathaei (KLM) model [151]. As shown

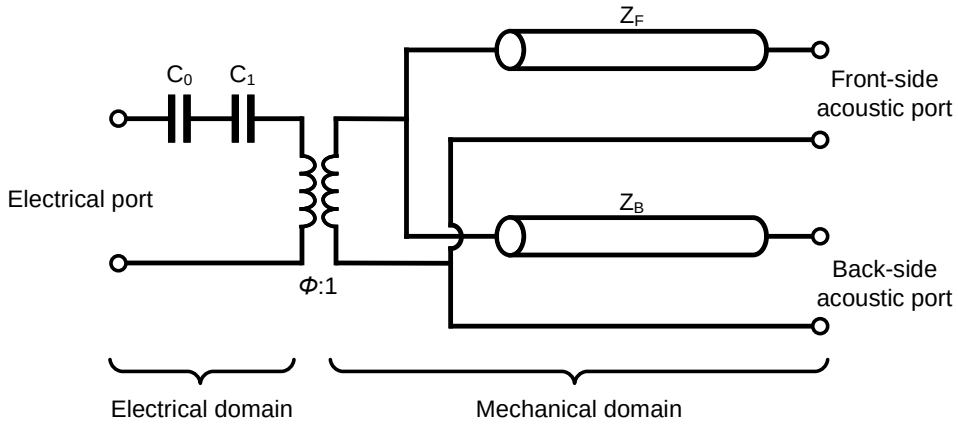

Fig. 2.13: KLM model for ultrasound transducers [151].

in Fig. 2.13, in this equivalent circuit, the transducer is modeled using transmission lines, and a transformer. This model involves three ports: one for the electrical pulses and two ports for the acoustic waves in the front and back sides of the transducer. The electrical domain includes two capacitors, C_0 and C_1. C_0 models the clamp capacitance of the US transducer and can be calculated from Equation 2.13. C_1 represents a capacitor related to the transducer dimension and k_t. This capacitor is negligible in comparison with C_0. The electromechanical coupling between the electrical and mechanical domains is represented using a transformer with a turn ratio of 1:ϕ, where ϕ can be found from

$$\phi = k_t \cdot \sqrt{\frac{\pi}{\omega_0 \cdot C_0 Z_c}} \cdot \mathrm{sinc}\left(\frac{\omega}{2 \cdot \omega_0}\right) \tag{2.17}$$

where k_t, Z_c, and ω_0 are the thickness-mode electromechanical coupling coefficient, the acoustic impedance of the US transducer, and the half-wavelength resonance frequency, that can be calculated from

$$\omega_0 = \frac{\pi \cdot v}{t} \tag{2.18}$$

where the v and t are the sound velocity in the US transducer and the thickness of the US transducer. The generated acoustic waves by the transformer pass through two transmission lines to reach the back and front sides of the piezoelectric transducer. The length of each transmission line is $t/2$, corresponding to half of the transducer thickness. The generated acoustic waves interface with two characteristic impedances of Z_F and Z_B, representing the acoustic impedances in the back and front sides of the US transducer [27].

The Mason and KLM models offer relatively accurate models for the US transducers. However, these models are too complicated for most of the electrical simulations. Therefore, a simple model is required to mimic the impedance and the resonance frequency of the US transducer. The simple Butterworth-Van Dyke (BVD) model, illustrated in Fig. 2.14(a), encompasses both of these aspects [152]. Although this mode does not provide any insight into the electromechanical conversion, the simplicity of this model enables effective electrical simulations of various US transducers. The BVD model involves an RLC circuit, corresponding to the mechanical domain of the US transducer. L_s and C_s model

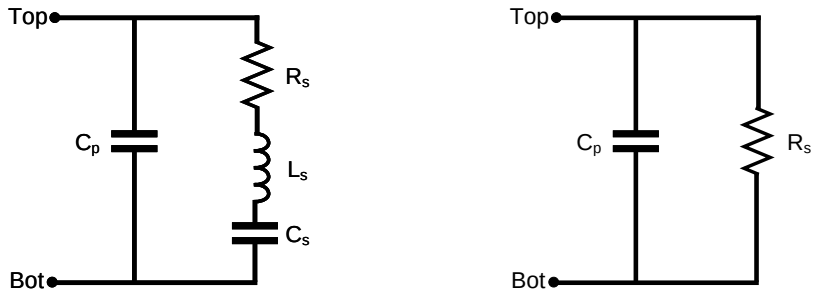

Fig. 2.14: (a) The BVD equivalent circuit (b) the simplified BVD model for a transducer operating at the resonance frequency [152].

the mass and the stiffness of the US transducer, defining the resonance frequency of the US transducer. C_s and L_s can be described as

$$C_s = C_P \cdot \left(\left(\frac{f_p}{f_s} \right)^2 - 1 \right) \tag{2.19}$$

$$L_s = \frac{1}{(2\pi \cdot f_s)^2 \cdot C_s} \tag{2.20}$$

where f_p is the parallel resonance frequency in which the real part of the resonator's impedance reaches its maximum value. Similarly, f_s represents the series resonance frequency in which the real part of the resonator's admittance reaches its maximum value [153]. C_p models the clamp capacitance of the US transducer and can be calculated as

$$C_p = \frac{-\mathrm{Im}(Z_s)}{2\pi \cdot f_s \cdot |Z_s|^2} \tag{2.21}$$

where where Z_s is the resonator's impedance at its series resonance frequency [153]. R_s represents the electro-mechanical conversion and the electrical impedance of the US transducer at the resonance frequency and can be written as [153]

$$R_s = \frac{|Z_s|^2}{\mathrm{Re}(Z_s)} \tag{2.22}$$

At the resonance frequency, the impedance of the inductor and the capacitor cancel each other [154]–[156]. Thus, the simplified model of the US transducer at the resonance frequency consists of a resistor and a capacitor, as depicted in Fig. 2.14(b). This equivalent circuit is valued for its simplicity, but it is applicable only at the resonance frequency. Furthermore, while US transducers only consume power during electrical transitions, this model accounts for continuous DC current dissipation. Consequently, this model is not valid after the transitions and does not provide an accurate representation of the total power consumption of the US transducer.

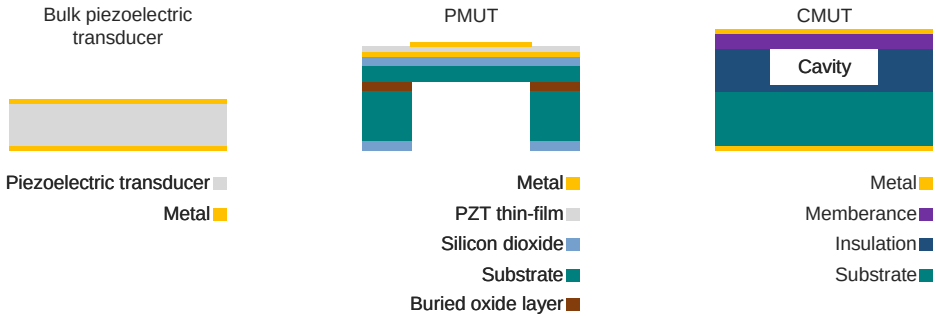

Fig. 2.15: Cross-section schematic of the bulk piezoelectric transducer, PMUT, and CMUT [157].

2.3.7. US Transducer Material

The choice of materials used in ultrasound transducers impacts the performance, efficiency, frequency range, biocompatibility, and high-volume production costs of the transducers. Therefore, choosing the right material for the US transducer primarily depends on the application of the transducer. Currently, as shown in Fig. 2.15, US transducers are mostly implemented using either piezoelectric materials, in the form of bulk transducers or piezoelectric micromachined ultrasound transducers (PMUTs), or capacitive micromachined ultrasound transducers (CMUTs). This section discusses the materials used in ultrasound transducers for medical applications, highlighting the primary benefits and limitations of each material type.

Bulk piezoelectric transducers utilize a broad range of materials that exhibit piezoelectric effects and are widely used in various applications due to their strong piezoelectric properties (Fig. 2.15). Lead zirconate titanate (PZT), a ceramic-based piezoelectric, is among the most prevalent materials with a high piezoelectric constant. PZTs offer high electromechanical coupling coefficients, typically ranging from 0.5 to 0.7, and large quality factors, making them an effective choice for high-intensity therapeutic US applications [129], [158]. However, in US imaging applications, a damping backing layer is needed to reduce Q. Moreover, PZT has high acoustic impedance, resulting in an acoustic impedance mismatch between the transducer and the human tissue and, hence, large acoustic losses. In this regard, the PZT-based transducers generally require matching layers to minimize the acoustic impedance mismatch with the human body, thereby improving the overall efficiency of the US system [159], [160].

In recent years, relaxor ferroelectrics such as lead magnesium niobate-lead titanate (PMN-PT) have gained significant attention due to their exceptional electromechanical coefficient, which can be as high as 0.95 [161]. This leads to greater sensitivity and higher energy conversion efficiency, paving the way for implementing portable and wearable US medical solutions. Similar to PZT, PMN-PT also experiences significant acoustic impedance mismatch when interfaced with human tissue. PMN-PT is more fragile and has a lower Curie temperature compared to PZT; consequently, developing PMN-PT transducers requires careful assembly and fabrication techniques [126], [162]. Modern piezoelectric composites not only achieve electromechanical coupling coefficients comparable to those of PMN-PT but also offer the advantage of reduced acoustic impedance mismatch with human tissue. Additionally, they offer greater mechanical flexibility than PZT, although these

advantages come at the expense of a more complex fabrication process [163], [164].

Despite the great performance of PZT and PMN-PT transducers, both contain lead. Although lead has a great impact on the piezoelectric properties of the transducers, it is a highly toxic metal that can cause harmful environmental effects. When devices containing lead are disposed of improperly, the lead can leach into soil and groundwater, posing serious risks to the ecosystems. Furthermore, piezoelectric transducers have been recently studied in the context of wearable and implantable biomedical devices; thus, coming into direct contact with the human body, which raises concerns about the biocompatibility of lead-based ultrasound transducers [165]. Therefore, researchers are pursuing lead-free ultrasound transducers that can still achieve comparable performance with PZT and PMN-PT. The polymeric-based transducers, such as polyvinylidene fluoride (PVDF), are among the biocompatible piezoelectric materials. PVDF has a low acoustic impedance mismatch with water and human tissue, allowing high energy transfer between the transducer and the human body. Moreover, unlike rigid piezoelectric ceramics, PVDF is highly flexible, which can be used in developing flexible ultrasound transducers [131], [166], [167]. However, the advantages of PVDF come at the cost of a very low electromechanical coupling and piezoelectric charge coefficients [130], [168]. Other lead-free piezoelectric materials, such as barium titanate (BaTiO3), also offer biocompatibility. However, their low Curie temperatures, approximately 130°C, and modest electromechanical coupling coefficients, typically around 0.5, limit the performance of BaTiO3 [169], [170].

In PMUTs, as depicted in Fig. 2.15, transduction occurs when an AC signal is applied across a suspended piezoelectric flexural membrane, typically made of PZT or aluminum nitride (AlN) [171]. The membranes in PMUTs are softer than bulk PZT, which naturally improves acoustic matching with soft tissues, eliminating the need for additional acoustic matching layers. This feature makes PMUTs particularly suitable for sensing applications [172]. However, the electromechanical coupling coefficient of PMUTs is significantly lower than that of bulk PZT transducers, making them less suitable for power-efficient ultrasound therapeutic applications [157], [173].

Finally, utilizing advanced microfabrication techniques, researchers have developed CMUT transducers, which operate based on the principles of capacitance changes rather than piezoelectric effects. As shown in Fig. 2.15, CMUTs consist of a thin flexible membrane suspended over a cavity. Below this membrane, there is a fixed substrate which, together with the membrane, forms a CMUT US transducer [157], [174]. The main advantage of CMUTs is using fabrication methods compatible with the CMOS manufacturing process. Compared with PZT, CMUTs are characterized by a lower electromechanical coupling coefficient and lower quality factor, leading to a higher bandwidth. Moreover, they benefit from higher acoustic matching with the soft tissue [175]. Although the lower Q of CMUTs leads to better axial resolution in US imaging applications, their lower electromechanical coefficient restricts their applications in US therapies, where high-intensity US focal spots are required [176], [177].

2.4. Driving Electronics

Ultrasound systems require electronic circuits to drive their transducers. Traditional single-element transducers utilize external electronic circuits that supply the necessary high-voltage pulses to the US transducers, as shown in Fig. 2.16(a). In contrast, more complex

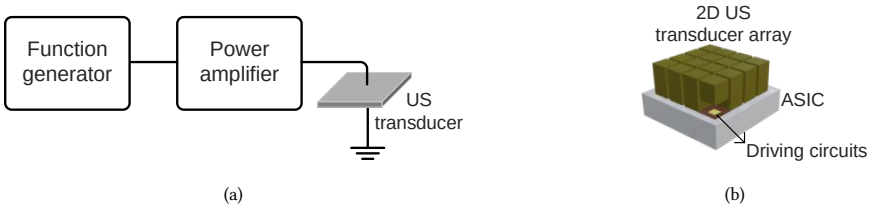

(a) (b)

Fig. 2.16: (a) The conventional bench-top setup to drive single-element and low-density 2D US transducer array. (b) Transmitter ASIC capable of driving even high-density 2D US transducer array.

systems such as phased arrays demand sophisticated driving circuits, where each transducer element is paired with a dedicated driver. One such example of an advanced electronic system is the Verasonics Vantage [178], which offers significant flexibility but also consumes considerable space, thereby limiting its utility in both clinical and research applications. A major drawback of these systems is their reliance on wired connections to drive the ultrasound transducer arrays, which restricts the size of the arrays they can support. An alternative approach to overcome these limitations involves employing CMOS technology to create specific driving circuits for larger ultrasound arrays, as depicted in Fig. 2.16(b). While ASICs do not offer the same level of flexibility as traditional bench-top circuits, they can support much larger transducer arrays with smaller pitch sizes. Furthermore, pixel-level pitch-matched ASICs facilitate the direct integration of ultrasound transducers on the CMOS chips, which will be discussed in Section 2.5. This integration not only allows for larger transducer arrays in a chip form factor but also improves its power efficiency, offering a significant advancement over conventional approaches.

As CMOS technology allows for the implementation of application-specific circuits, a variety of ASICs for US neuromodulation have been developed. [143], [179] have implemented a 1D array of driving circuits, which deliver 60-V and 50-V pulses to the US transducers. [40] have developed 26×26 phased array transmitter ASIC for US neuromodulation, which is shown in Fig. 2.17(a). The 2D array is capable of driving the piezoelectric transducers with 8.4-MHz bursts of pulses while performing 6-bit phase quantization. Although this ASIC allows precise beam steering, the amplitude of the driving pulses is limited to 5 V, which restricts the acoustic pressure to 100 KPa. [53] has published a 2D phased array ASIC delivering 60-V adjustable pulses to an array of CMUT transducers, as illustrated in Fig. 2.17(b). Moreover, the ASIC offers a 4-bit phase quantization, enabling arbitrary US beam steering. However, the low operation frequency of 3.4 MHz limits the spatial resolution of the US focal spot.

In addition to US neuromodulation, there are ASICs developed for other US therapeutic applications, such as US ablation and US power delivery to the implants. [180] presents a 32×32 array of drivers, which deliver 60-V pulses to a CMUT array. This 2D array generates an 8.5-Mpa focal point, proving its capability to perform tissue ablation using high-intensity focused ultrasound (HIFU). [181] also has developed a 32×32 array catheter for US ablation. The US transducer is capable of generating 13 MPa acoustic pressure with 60-V pulses. [182] has implemented a 32×32 ASIC for US ablation applications. The ASIC supplies 60-V pulses with 10-bit phase quantitation to the US transducers. [183] has developed a US transmitter ASIC for power delivery to implanted devices. The transmitter ASIC has shown a 69% power reduction compared with conventional pulsers.

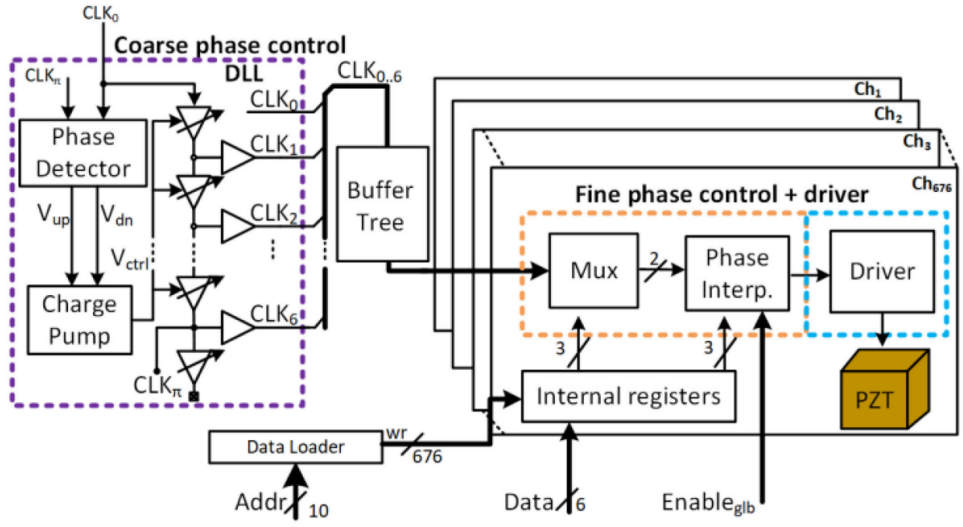

(a)

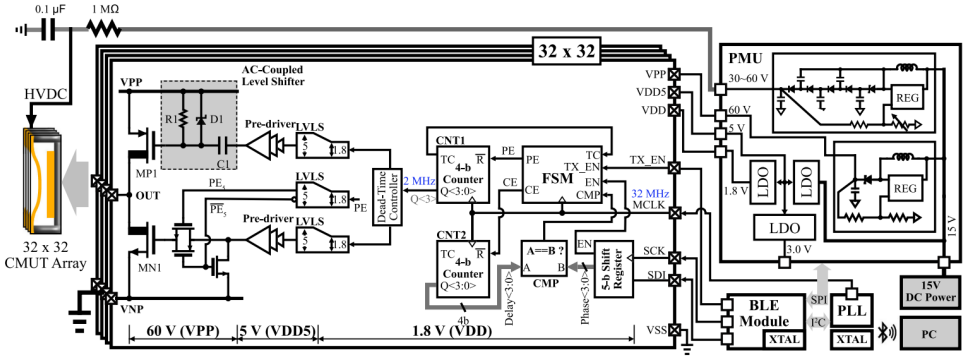

(b)

Fig. 2.17: Architecture of the transmitter ASIC for US neuromodulation; (a) reprinted from [40], ©2021, with permission from IEEE, (b) reprinted from [53], ©2021, with permission from IEEE.

[184] has designed a transceiver ASIC capable of transmitting and receiving US power. The transmitter has used a stack of low-voltage transistors to deliver 15-V pulses to the US transducers.

In the realm of US imaging, there has been a great effort to minimize the overall size of the US transducers using CMOS technology. Furthermore, the mm-sized US transducers combined with flexible catheters allow for real-time imaging from inside the body [185]. To decrease the overall size of the transducer, US imaging ASICs utilize a single ASIC to implement both transmitting and receiving channels. Moreover, utilizing 2D architectures improves the overall resolution of the US images [186]. However, conventional 2D US transducers require an external imaging system to interpret the analog data generated by the ASIC. Therefore, each imaging channel in the ASIC requires one external cable to

transmit the analog data to the imaging system; hence, the number of interconnects limits the array size [187]. To implement larger arrays, sub-array beamforming techniques have been utilized to reduce the number of required cables. This technique shifts part of the beamforming operations from the imaging system to the ASIC [188], [189]. To further reduce the cable count, the analog receiving signals can be converted to digital data using analog-to-digital converters (ADCs) and, consequently, a time division multiplexer can be utilized to connect several receivers to one cable [190], [191].

In summary, CMOS technology has paved the way for advancing US technology for biomedical applications. In the scope of this thesis, CMOS integrated circuits have been developed for US neuromodulation applications. Building on top of the knowledge reported in the literature, 2D phased array ASICs are proposed in Chapter 5 and Chapter 6 to enable researchers to perform US neuromodulation experiments on animal models.

2.5. Integration of ASIC with US Transducer

A miniaturized ultrasound phased array system on ASIC is fundamentally composed of two key components: driving electronics and ultrasound transducers. Achieving a compact ultrasound system depends crucially on the effective interconnection between the US transducer array and the ASIC. In simpler systems, such as low-density 1D arrays, wire connections typically suffice for linking the ASIC to the transducer array [192], as depicted in Fig. 2.18(a). Yet, the situation becomes more complex with high-density 2D arrays, particularly interfacing with a pixel-level pitch-matched ASIC. In these 2D ASICs, each beamforming channel is aligned with a transducer element, and each pulser drives its respective transducer element. There are two primary methods to address the interconnection challenge between ASICs and 2D transducer arrays. The first method, flip-chip bonding, provides a direct connection between the transducer elements and their corresponding electronic drivers on the ASIC, as shown in Fig. 2.18(b). The second method is monolithic integration, where the transducers are directly fabricated onto the ASICs, as illustrated in Fig. 2.18(c). Each of these approaches offers unique advantages and potential challenges, depending on the pitch size and the type of the transducer material.

In ultrasound systems using 2D transducer arrays with relatively large pitch sizes, exceeding 250 µm, as shown in Fig. 2.19(a), an interposer PCB board can be employed to facilitate the connection between the transducer array and the ASIC via flip-chip bonding to the interface board [182], [194]. The ASIC pulsers are linked to the 2D array using through-hole vias embedded in the interface board. While using an interface board is straightforward and cost-effective, it introduces parasitic capacitance to the transducers, which reduces the overall power efficiency. Additionally, this technique is limited to arrays with large pitch sizes because of constraints related to implementing small-size vias on PCBs. As depicted in Fig. 2.19(b), to overcome these limitations and enable the development of dense transducer arrays, the compatibility of CMUT transducers with CMOS microfabrication processes is utilized to perform a direct integration using through-silicon vias [193]. This compatibility allows for the development of through-wafer vias that directly connect the transducer elements on the top side to the flip-chip bond pads on the backside. This approach facilitates the direct integration of dense CMUT arrays to the ASICs using standard industry flip-chip bonding techniques. However, it's important to note that while this method is technologically advanced, it is typically more expensive

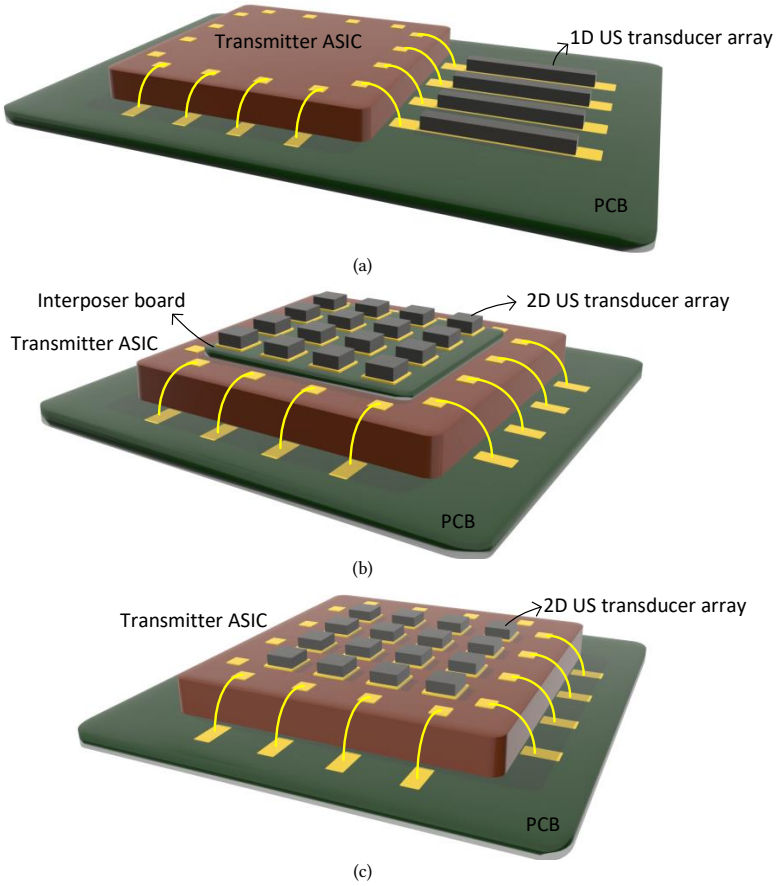

Fig. 2.18: Different techniques of integration of the transmitter ASIC and the US transducer array. (a) Wire bonding the ASIC and the US transducer array to a PCB. (b) Integration of the ASIC and the US transducer array using an interposer board. (c) Direct integration of the ASIC and the US transducer array.

due to the need to develop through-wafer vias. Moreover, this integration technique is specifically suited for CMUT arrays, which generally exhibit lower transmission efficiency compared to piezoelectric transducers. This technique, therefore, while promising, carries its own set of trade-offs in terms of cost and transducer efficiency.

The monolithic integration method involves directly fabricating a 2D array of piezoelectric transducers onto the ASIC. This technique requires aligning the size of the ASIC pads with the transducer elements. This process typically uses commercially available piezoelectric sheets, which are covered with conductive metals on both sides. First of all, as shown in Fig. 2.20, to establish an electrical connection between the piezoelectric elements and the ASIC pads, either a conductive epoxy or an anisotropic conductive film (ACF) is applied to the CMOS chip. Since this integration method relies on dicing the piezoelectric on the CMOS substrate, the dicing saw may go through the CMOS chip and cause damage to the electrical circuits. To mitigate this risk, as depicted in Fig. 2.20(a), a sacri-

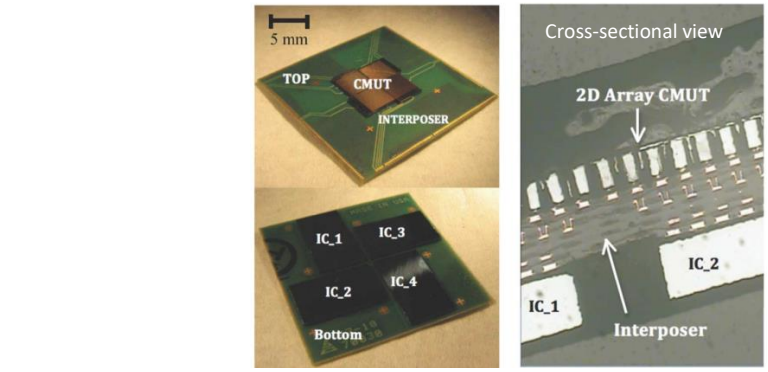

(a)

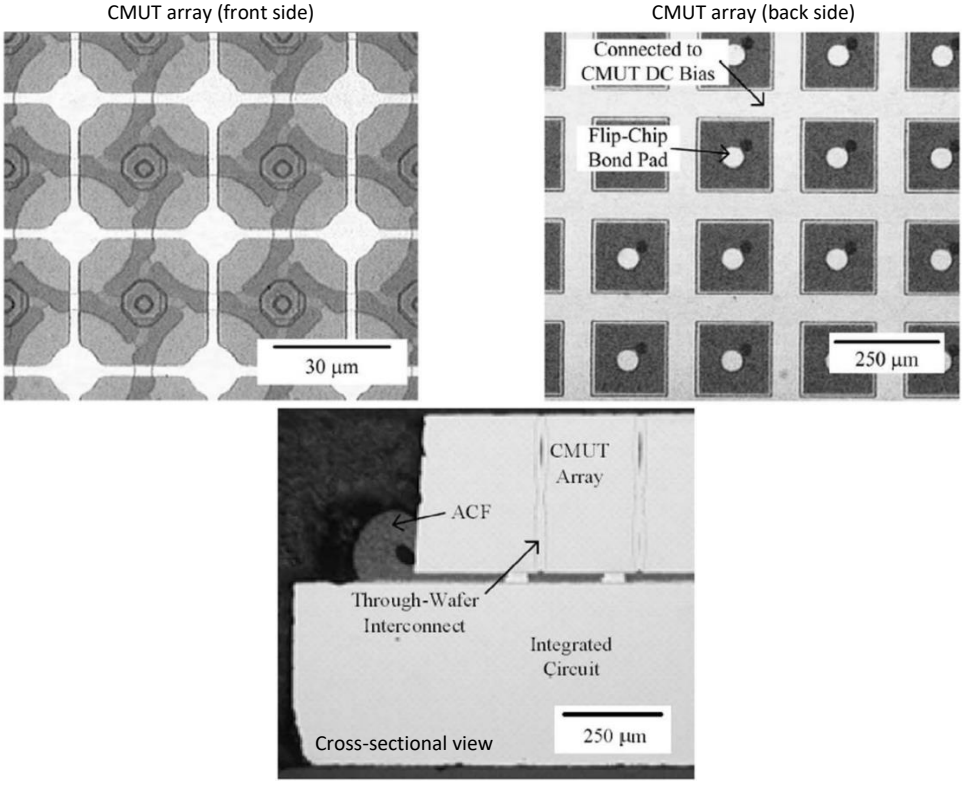

(b)

Fig. 2.19: (a) Integration of a 2D CMUT array on ASICs with flip-chip bonding using an interposer PCB board, reprinted from [182], ©2013, with permission from IEEE. (b) Direct integration of a 2D CMUT array on an ASIC using through-silicon vias, reprinted from [193], ©2008, with permission from IEEE.

ficial layer is introduced to increase the separation between the piezoelectric transducer and the CMOS chip [195]. As illustrated in Fig. 2.20(b), an alternative solution involves a double-sided dicing technique, where the piezoelectric sheet is pre-diced from the bottom

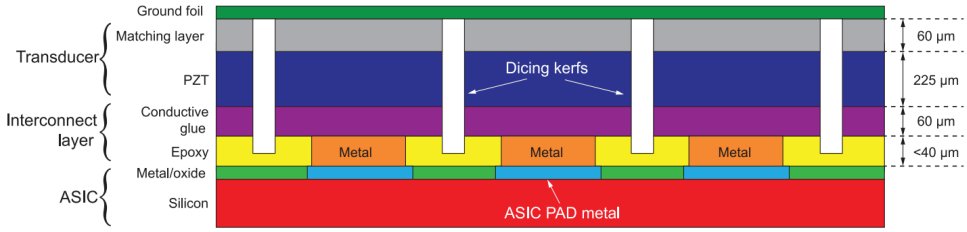

(a)

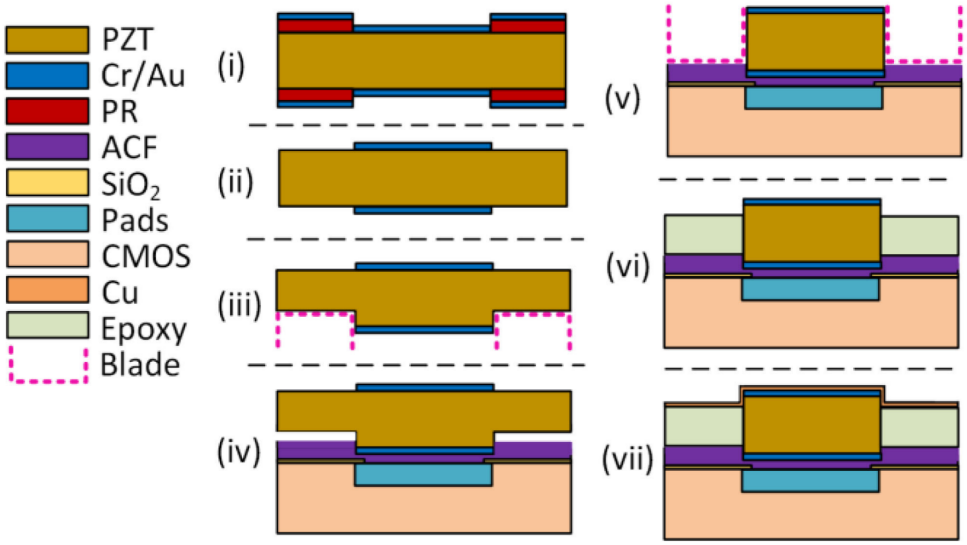

(i) PZT contact deposition, (ii) patterning, (iii) back side dicing, (iv) adhesion to the ASIC using ACF, (v) PZT top side dicing, (vi) kerf filling, and (vii) top metalization

(b)

Fig. 2.20: (a) Monolithic integration of a 2D PZT array on the ASIC, reprinted from [195], ©2015, with permission from IEEE. (b) PZT on ASIC integration flow, reprinted from [40], ©2021, with permission from IEEE.

side by about 20% of its thickness before being placed on the ASIC. Subsequently, the top side is diced by 80% of the thickness after placing the piezoelectric sheet on the ASIC [40], [196]. Once dicing is complete, the top sides of the piezoelectric transducers are usually connected together using an aluminum foil [195]. However, the thickness of the foil can adversely affect the acoustic performance of the ultrasound transducer. An alternative is to use a thin conductive cap to connect the top sides of the piezoelectric transducers to the common potential, which mitigates the acoustic attenuation in the top connection [197]. The monolithic integration of piezoelectric transducers on ASIC leads to higher transmission efficiency and compact size. However, it comes with the risk of fabrication failures on expensive ASIC wafers. Additionally, the size of the dicing saw blade determines the kerf size of the 2D array, limiting the minimum achievable pitch size. Consequently, this constraint restricts the development of very high-frequency piezoelectric 2D phased arrays [46]; a detailed study on high-frequency phased arrays is offered in Chapter 3.

2.6. US Transducers for Preclinical Studies

This chapter has provided a review of the latest materials and methods used in the development of US transducers that have a wide range of applications. Of particular interest is the emerging field of ultrasound neuromodulation, a technique that enables the development of minimally invasive and precise treatments for neurological disorders. As this application continues to evolve, the necessity for preclinical experiments before progressing to human trials becomes apparent. Preclinical experiments on small animals like rodents allow for the evaluation of both the safety and efficacy of the US treatment. Initial studies in US neuromodulation have employed commercially available single-element ultrasound transducers. However, the bulky size of these ultrasound transducers often makes them inaccurate for use on small animals. Furthermore, they require a mechanical setup to adjust the location of the focal spot, which increases the overall size of the US system and limits the experiments to anesthetized animals. These limitations highlight the need for US transducers tailored to US neuromodulation experiments on small animal models.

In recent years, significant progress has been made in developing customized US transducers specifically for preclinical studies involving rodents. A primary issue with traditional single-element US transducers is their relatively large size, making them unsuitable for experiments on rodents. To address this, as depicted in Fig. 2.21, researchers have designed wearable form factor single-element US transducers [49]–[52]. These devices, while compact enough to be used on awake animals, unfortunately, produce a fixed and broad focal spot, which affects the precision and reliability of neuromodulation experiments. To enhance the resolution of the focal spot, an acoustic lens is added to the single-element US transducer [198]. Yet, such transducers lack the capability for beam steering, which is crucial for accurately targeting specific brain regions. Phased array transducers, which allow for electronic beam steering, present a solution to this problem [48]. However, their use in preclinical studies is limited by the complexity of their design, which includes numerous connections between the transducer array and the electronic pulser unit. This complexity results in an increased overall size of the US transducer setup, making it less suitable for use with awake animals. One solution to simplify the connectivity involves reducing the number of transducer elements within the array by randomly removing some elements [42] (Fig. 2.21). However, this reduction can linearly decrease the generated acoustic intensity [199], potentially leading to insufficient intensity for effective neuromodulation. To overcome these challenges, there has been a move towards integrating CMOS electronics directly with 2D piezoelectric transducers to create a more compact phased array US transducer [40]. However, the typically low operating voltage of standard CMOS chips limits the acoustic intensity that can be achieved [40]. In response, high-voltage CMOS chips have been developed in conjunction with CMUT technology to achieve the higher intensities needed for effective neuromodulation [53]. Nevertheless, this approach is not without drawbacks, as the higher voltages required for CMUTs lead to increased power consumption and excessive heat generation, which poses a risk of tissue damage during experiments. In addition, the low operation frequency of this US phased array results in poor spatial resolution, while precise focal spots are needed for preclinical experiments on rodents.

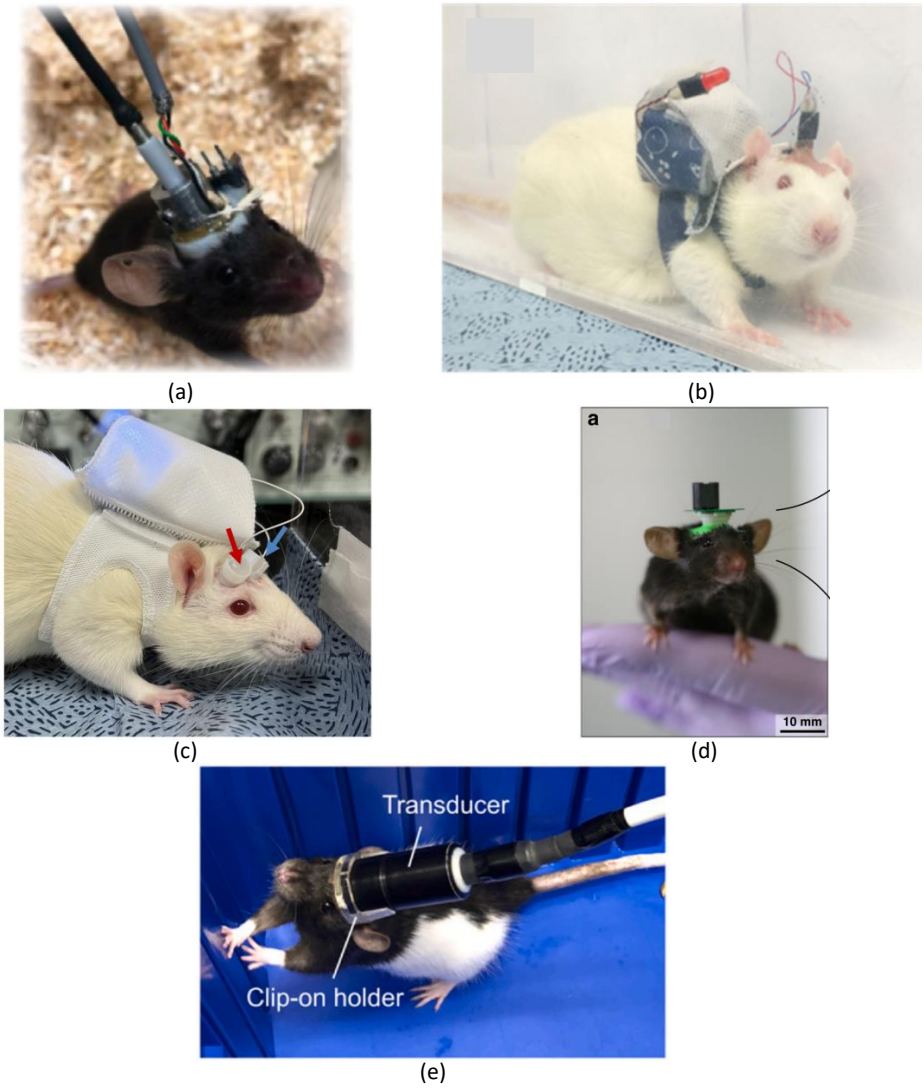

Fig. 2.21: US transmitters for preclinical US neuromodulation studies on rodents, (a) single-element US transducer, reprinted from [50] under CC BY-NC-ND 4.0, (b) wearable single-element US transducer, reprinted from [51], ©2020, with permission from IEEE, (c) wearable single-element US transducer, reprinted from [52] under CC BY 4.0, (d) focused single-element US transducer, reprinted from [198] under CC BY 4.0, and (e) sparse phased array US transducer, reprinted from [42] under CC BY-NC-ND 4.0.

2.7. Discussion and Research Questions

Ultrasound neuromodulation is a rapidly evolving field within neuroscience and clinical neurology, offering a precise and noninvasive modality to treat neurological conditions. Despite its potential, a significant technological gap currently limits preclinical US neuromodulation studies on small animals, which are essential for developing treatments for

humans. Most existing US transducers designed for preclinical research are bulky and produce a wide and fixed focal spot, which is far from the ideal technology. To meet the demands of accurate preclinical US neuromodulation experiments, there is a pressing need for a miniaturized and power-efficient US transducer. Such a device must be small enough to be mounted on the heads of small animals without causing discomfort or obstruction, which is needed for studies on awake animals. Additionally, it is important that this transducer supports electronic beam steering to adjust the focal spot's location electronically. This feature is crucial for correcting any misalignments that occur during the transducer's implantation, ensuring that the interested brain regions are precisely targeted without the need to move the device physically. Furthermore, the different biological targets in the brain that relate to specific disease pathways, where the 10 μm - 100 μm wide neurons are the fundamental building blocks, demand US transducers capable of generating a focal spot with high spatial resolution. Moreover, the device must also ensure that the focal intensity is sufficient to modulate neuronal activity effectively, as discussed in Section 2.2.2. Finally, the US transducer must be highly power-efficient to enable battery-powered operation in freely moving animals and to mitigate heat generation, which is particularly important to prevent any thermal damage to delicate neural tissues.

To meet all the abovementioned criteria and enable the design of a new class of US transducers tailored for US neuromodulation in preclinical settings, the following research questions were derived:

1. How do the electrical and physical parameters of a 2D phased array US transducer influence the acoustic properties of the generated US beam?

2. What are the optimal phased array US transducer properties that maximize the spatial resolution of the US focal spot while minimizing power consumption?

3. What is the maximum frequency of a US phased array transducer that can form a focal spot without generating grating lobes?

4. How can electronic circuits improve the energy efficiency of the US phased array transducers?

5. What is the optimal 2D phased-array US transmitter ASIC for US neuromodulation pre-clinical studies in rodents?

The first question is a basic as well as important question for these US systems, where the electrical, mechanical, and acoustic domains influence each other. Electrical signals drive the piezoelectric transducers with a specific frequency and amplitude, which results in the mechanical vibration of transducer elements. Then, the 2D array of piezoelectric transducers with a given length, resonance frequency, and pitch size generate a US beam with a focal spot. The US parameters of the US focal spot, such as US intensity and spatial resolution, heavily depend on the physical parameters of the piezoelectric transducer array and the electrical characteristics of the driving pulses. Therefore, a comprehensive study on US phased array US transducers is needed to find out the answer to the first question. This study allows for the implementation of a highly power-efficient 2D phased array US transducer, which is needed for preclinical US neuromodulation research. The

second question investigates the ways to improve the spatial resolution of a 2D phased array transducer. This study involves the physical and electrical parameters of the 2D phased array transducer, including the resonance frequency and the length of the array. The third question studies the practical challenges of improving the spatial resolution by increasing the frequency. As discussed in this chapter, higher frequencies lead to higher spatial resolution, which is desired for US neuromodulation applications. However, the pitch size between the elements in phased array transducers inversely depends on the resonance frequency. In other words, higher frequencies lead to higher precision at the cost of smaller pitch sizes. This is particularly important to prevent the generation of grating lobes in the US beam profile. Shrinking the pitch size poses severe constraints on the fabrication of piezoelectric transducers on the CMOS substrate. Furthermore, in a pixel-level pitch-matched 2D array, the area of every beamforming channel is the same size as the US transducer element. In this regard, increasing the frequency limits the available area for implementing a beamforming circuit. Therefore, this research question studies the maximum frequency that is practically achievable, taking into account system-level optimizations, circuit design, and microfabrication of the ultrasound transducers. The fourth research question corresponds to the overall power efficiency of the 2D US transducer. In an ideal lossless US transducer, all the electrical power is converted to acoustic energy. However, in a real US transducer, there are losses in the electrical, mechanical, and acoustic domains. Even though utilizing proper fabrication and integration techniques allows for the minimization of the mechanical and acoustic losses in the US transducer, minimizing the electrical losses demands innovative circuits. In a driving ASIC, there are two main sources of losses: the first source of the electrical losses is the parasitic capacitance of the US transducer and the interconnection between the driver and the transducer element. Although this power is delivered to the US transducer element, it does not contribute to the electromechanical conversion process. Therefore, a study is needed to develop innovative circuits to minimize the power loss due to these parasitic capacitances. Another source of the power loss is the power consumed by the CMOS chip, which is not delivered to the US transducer, such as the power consumed by the low-voltage beamforming circuits and the high-voltage driving circuit. Therefore, a comprehensive system-level study of 2D phased-array circuit architectures is needed to minimize the power consumption of the beamforming circuits. Finally, the fifth question highlights the required design considerations to develop a 2D phased array US transducer for US neuromodulation studies on mice and rats. These design considerations include the overall size of the ASIC, the maximum depth of penetration, the required spatial resolution, compatibility with the direct integration with piezoelectric elements, and the heat generated by dissipated energy. The answer to this research question should satisfy the design considerations. For instance, the size of the animal's brain, the maximum depth of the brain, and the required spatial resolution and US intensity at the focal spot define the size of the ASIC, the operation frequency, and the amplitude of the driving signals. Moreover, this research question underscores the design considerations for implementing a power-efficient scheme for the beamforming circuits, investigating the effect of different beamforming schemes on the power consumption of the channels. The next concern is related to heat dissipation; thus, temperature monitoring circuits are required to avoid overheating of the tissue. Furthermore, since the ASIC must be compatible with the direct integration with piezoelectric

elements, comprehensive design thinking is needed to implement a compatible layout for aligning the piezoelectric transducer on top of the ASIC and performing the final dicing.

3

System-Level Study of Phased Array Transmitters

3.1. Introduction

In recent years, new ultrasound biomedical applications, such as ultrasound neuromodulation [41], [45], [200], high-intensity ultrasound ablation [76], [121], ultrasonic power transfer and communication for medical implants [201]–[207] have been emerging, as visualized in Fig. 3.1. These growing applications require different sonication parameters compared to traditional US imaging systems [208], [209], such as long bursts of US waves with peak acoustic intensities above 1 W/cm^2 and pulse duration in the millisecond range [26]. Moreover, while in ultrasound imaging applications, the focused ultrasound beam is typically optimized in terms of lateral spatial resolution for high-precision scan lines, in the abovementioned applications, the target is to ideally match the volumetric spatial resolution of the focal spot with the small size of ultrasonically powered implants, which can be as small as 0.065 mm^3 [205], [206], and cover the micrometer-sized neurons with remarkable precision. This is of particular importance in pre-clinical research to match the scales of the focal spot dimensions to the rodent nervous system [41], [200], [210], and in emerging human applications such as sub-cranial visual cortex stimulation for the blind [211], [212] and peripheral nerve stimulation [70].

Furthermore, these modern applications demand electronic beam steering to adjust the location of the focal spot to the desired target. The steerability plays a crucial role in US power delivery applications to align the US beam to the US receiver and, hence, maximize the power transfer efficiency [213]. In US neuromodulation and ablation, unlike the mechanical movement of the transducer, electronic beam steering allows precise and fast adjustment of the focal spot location, enabling the targeting of multiple regions with a single US transducer [40]. This is particularly important in ultrasound ablation applications, such as ablation of uterine fibroids, where one US transducer can detect and guide the US

Parts of this chapter have been published in "A 2D Ultrasound Phased-Array Transmitter ASIC for High-Frequency US Stimulation and Powering," in *IEEE Trans. Biomed. Circuits Syst.,* June 2023 [46].

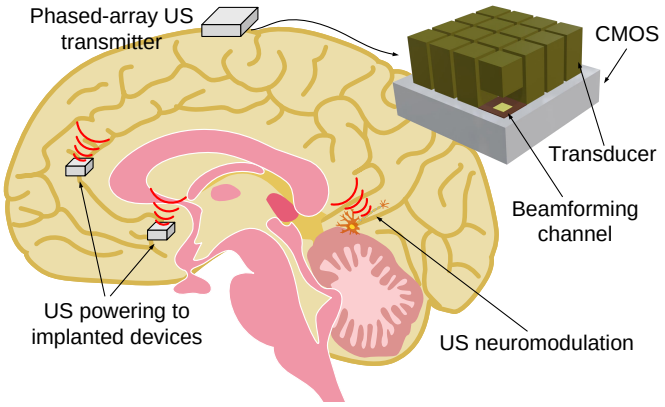

Fig. 3.1: A conceptual 2D ultrasound phased-array transmitter, performing both US neuromodulation and power delivery to implanted devices with a single transmitter.

beam to ablate the fibroids [214], [215]. In addition to the beam steering, a small form factor is a vital characteristic of future US transmitters for these applications, enabling the implementation of wearable and implantable US transducers.

Conventional US transmitters used in US neuromodulation and US powering utilize bulky, fixed-focus, single-element transducers that need complex mechanical translation to change the location of the focal spot [27], [216]. As discussed in Chapter 2, the single-element transducers not only suffer from poor spatial resolution but also are not applicable to wearable applications due to their large form factor and the need for bench-top electronic signal generators and power amplifiers. Mechanical focusing techniques have been utilized to generate high spatial resolution focal spots; however, they lack the capability to steer the US beam [135], [136]. Phased array transducers allow for electronic beam steering by employing an array of transducer elements, each controlled independently by a specific driver. This configuration enables the arbitrary adjustment of the focal spot at the cost of complex interconnections between the US transducer array and the electronic drivers, resulting in a large form factor. In order to overcome these limitations, researchers have been pursuing miniaturized US phased array transducers and interfacing electronics. In particular, the maximum level of integration and performance can be achieved by direct integration of 2D arrays of ultrasound transducers on top of pitch-matched ASICs [40], [53]. Therefore, phased array US transducers are capable of satisfying all characteristics needed for modern US biomedical applications.

Implementing a 2D US phased array transducer demands analyzing a broad range of acoustic, mechanical, and electrical parameters. Despite recent efforts, the literature still lacks a comprehensive system-level study on 2D US phased array US transmitters. [144] has presented a design methodology for finding the optimal transducer array geometry; however, it was limited to 1D US phased arrays. In [40], a system-level analysis for 2D arrays was given, where the influence of array size and beamforming timing resolution on the properties of focused ultrasound waves is shown. However, this analysis was limited to 10-MHz ultrasound waves, and no insights about power consumption were given. This chapter presents a detailed system-level study to investigate the influence of 2D US

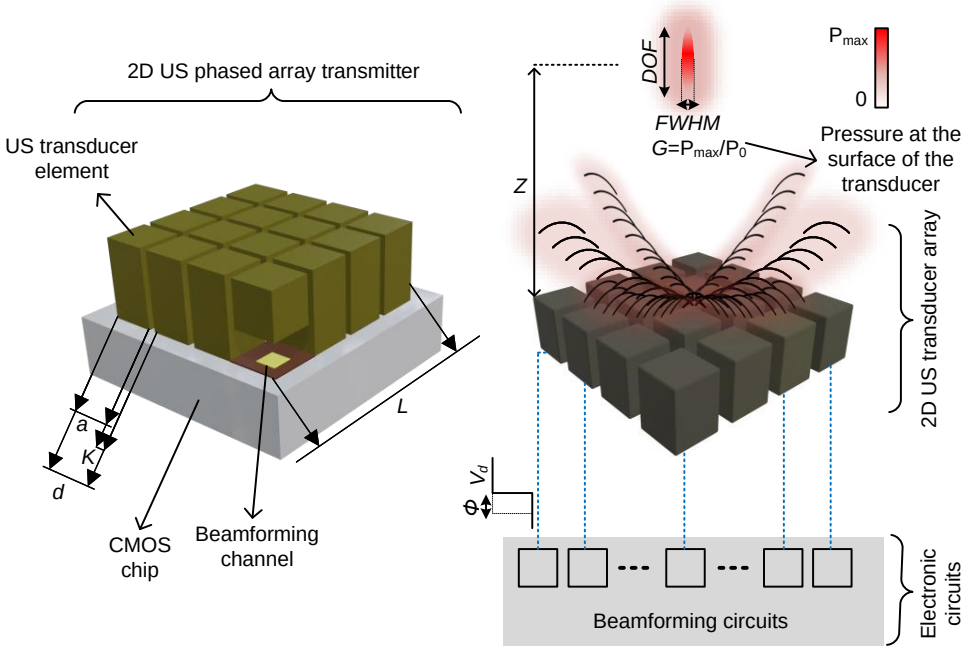

Fig. 3.2: Principal properties of a 2D phased-array ultrasound transmitter.

phased-array transmitter parameters on the volumetric resolution and US intensity of the focus spot, to guide the design of 2D phased-arrays with minimum pixel area and power consumption towards the high-frequency operation. Furthermore, this system-level study analyzes the influence of phased array parameters on the overall power consumption of the driving circuit. Moreover, it evaluates the effect of phase quantization resolution on the steerability of the phased array, allowing the optimization of the electronic circuits in terms of power consumption and complexity.

3.2. 2D Phased Array Beamforming

In a 2D phased-array US transmitter, as shown in Fig. 3.2, an $N \times N$ 2D array of electronic beamforming circuits drives the pitch-matched US transducers with a driving signal with a given center frequency (f_{US}), phase (Φ) and driving voltage (V_d). The beamforming channels are directly connected to a 2D array of $N \times N$ US transducer elements with element size and the inter-element pitch size of a and d, respectively. Assuming that the transducers are fabricated using a dicing saw process [40], the kerf size created by the dicing saw blade is defined as K. Therefore, the length and the effective length of the transducer array, denoted as L and L_{eff}, are calculated from:

$$L = (N \times d) - K \tag{3.1}$$

$$L_{\text{eff}} = N \times a \tag{3.2}$$

Every beamforming channel drives its corresponding US transducer element with a signal with a given phase that is related to the distance of the element from the focal spot. As depicted in Fig. 3.3(a), when the transducer elements are driven with signals with certain delays, the generated ultrasound waves will arrive at the same time at the focal spot, which, due to constructive interference, leads to the generation of a focal spot. Moreover, manipulation of the delays allows for the steering of the focal spot in all three directions. The value of these delays depends on the accurate calculation of the distance from every element to the focal spot. As shown in Fig. 3.3(b), these distances are calculated using a spherical polar coordinate system with the direction cosines of u and r, which are defined as follows:

$$u = \frac{X}{R} = \sin(\theta) \cdot \cos(\alpha) \tag{3.3}$$

$$r = \frac{Y}{R} = \sin(\theta) \cdot \sin(\alpha) \tag{3.4}$$

where θ and α are typically referred to as the azimuth and elevation angles. The azimuth angle is usually measured in the vertical plane and dictates how the beam is steered or focused vertically up and down relative to the array. The elevation angle is measured in the horizontal plane and shows how the beam is steered or focused horizontally left and right. Therefore, the distance from the center element to the focal point is calculated from

$$R = \frac{Z}{\cos(\theta)} \tag{3.5}$$

where Z is the focal spot depth, as shown in Fig. 3.3(b). The delay of every transducer element in the row and column of i and j is calculated from

$$\text{Delay}\,(i,j) \;=\; \frac{R}{v} \;\times\; \left(1 - \sqrt{\left(u - \frac{ds_i}{R}\right)^2 + \left(r - \frac{ds_j}{R}\right)^2 + \cos^2(\theta)} \right) \tag{3.6}$$

where v is the sound speed in the medium and ds_i and ds_j are the distance of the corresponding element from the center of the array along the x and y directions [217].

By programming the beamforming circuits with specific phases according to the speed of sound in the medium and the relative position of each transducer within the array [217], a focused ultrasound wave is created at a given focal spot depth (Z), with a focus gain (G) and a volumetric spatial resolution (Vol_{res}), as shown in Fig. 3.2. Considering a cylindrical focal spot, the Vol_{res} and G are given by

$$Vol_{\text{res}} = 1/6 \cdot \pi \cdot DOF \cdot FWHM^2 \tag{3.7}$$

$$G \propto \frac{L_{\text{eff}}}{Z \cdot \lambda} \tag{3.8}$$

where DOF (3.9) is the depth of field, representing the spatial resolution in the axial direction, and the $FWHM$ (3.10) is the full width at half maximum, representing the spatial resolution in the lateral direction.

$$DOF \propto \lambda \cdot \left(\frac{Z}{L}\right)^2 \tag{3.9}$$

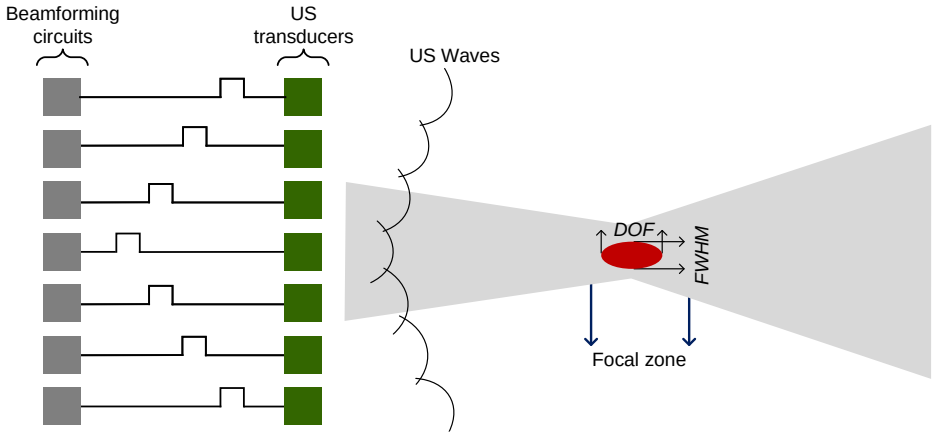

(a)

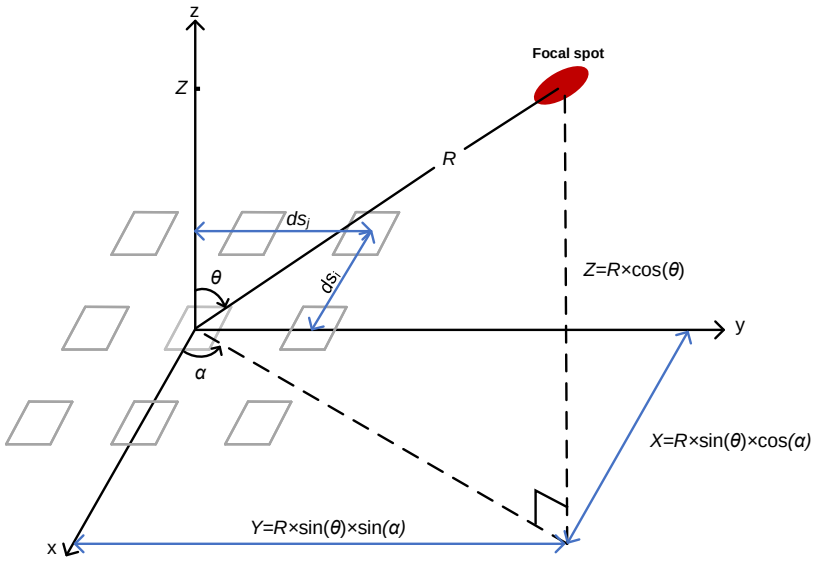

(b)

Fig. 3.3: (a) phasing of the driving pulses to focus and steer the US beam. (b) the position of the 2D array and the focal spot in the coordinate system.

$$FWHM \propto \lambda \cdot \frac{Z}{L} \tag{3.10}$$

On the other hand, the maximum focal depth $Z_{\max}$ is close to the natural focal spot of the array without the beamforming and is obtained from

$$Z_{\max} \approx \frac{L^2}{\pi\lambda} \tag{3.11}$$

Furthermore, to avoid the appearance of grating lobes in the beam profile, d must respect

this condition

$$d = \frac{\lambda}{1 + \sin(\theta_{max})} \tag{3.12}$$

where θ_{max} is the maximum steering angle along the azimuth direction. Therefore, to reach the maximum steering of 90°, the pitch size must be equal to $\lambda/2$ or, in other words, half sound wavelength.

The performance of 2D phased-array US transmitters for US non-imaging applications is maximized when a focal spot with the lowest Vol_{res} and the highest G is achieved. Considering Equation 3.7 and Equation 3.8, increasing the operation frequency and the array geometry improves the desired acoustic properties. However, the pitch size limitation to half US wavelength poses several challenges to the fabrication of the US array and implementation of pitch-matched circuits. The following section will investigate the influence of electrical, physical, and acoustic parameters of a 2D phased array US transducer on each other.

3.3. System-Level Analysis

This section offers a system-level analysis of 2D US phased array transducers utilizing the k-Wave Toolbox in Matlab [218]. It examines the influence of operation frequency, length of the array, the kerf size, and the phase quantization resolution on the spatial resolution and the intensity of the focal spot, and the overall power consumption of the electronic circuit. The study aims to optimize phased array transducers while minimizing the complexity and power consumption of the electronic circuits. Since this research thesis is focused on developing 2D US phased arrays for US neuromodulation studies on rodents, particularly rats, the geometry and depth of the focal spot are limited to 10 mm [219]. Nonetheless, the findings are applicable to other array geometries and broader applications.

3.3.1. K-Wave Toolbox

The k-Wave Toolbox is a robust MATLAB toolbox designed for time-domain simulation of acoustic wave fields [218], making it a functional tool for applications that involve US wave propagation in a medium. The toolbox leverages a k-space pseudo-spectral method to solve the acoustic wave equations, enabling efficient and accurate simulations. This capability is particularly valuable in designing phased array ultrasound transducers, as it allows for precise modeling of ultrasound wave propagation within the medium, facilitating the development and optimization of these complex devices.

In Fig. 3.4, a brief flow of acoustic simulations using the k-Wave Toolbox is presented. The simulation of a 2D phased array ultrasound transducer in k-Wave begins with defining the number of grid points and their spacing based on the frequency, the size of the array, and the medium properties. Next, the medium's properties, including the speed of sound (v), the density (ρ), and the medium attenuation coefficient, are specified. Then, the transducer properties a, d, and N are defined. Considering the steering angles (θ and α), f_{US}, and Z, the phase delays for the driving signals of each element are calculated using Equation 3.6. Subsequently, a 2D array of source pressures corresponding to the transducer elements is created to mimic the actual ultrasound transducers. A sensor mask is defined to record data in the medium. Finally, the kspaceFirstOrder2D function is used to

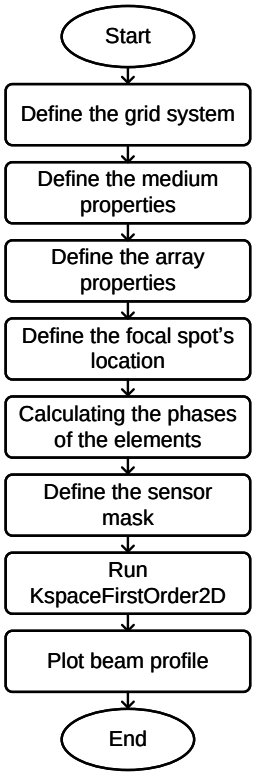

Fig. 3.4: Utilized flowchart for running the k-Wave simulations.

run the k-Wave simulation, utilizing the defined grid, medium properties, initial pressure source, and sensor mask. The simulation output, which includes pressure values recorded at each sensor point over time, is analyzed to form the final beam profile and calculate critical acoustic parameters, such as Vol_{res} and G.

3.3.2. Center Frequency

Firstly, the influence of f_{US} on the focal spot properties is investigated. As outlined in Equation 3.7 and Equation 3.8, increasing the frequency results in a smaller sound wavelength, which enhances spatial resolution and phased array gain. However, this improvement comes at the cost of higher acoustic absorption in the tissue, which increases exponentially with the frequency (Table 2.1). In the context of pre-clinical experiments with rodents or in the case of cortical and peripheral nerve interfaces in large animals and humans, the penetration depth of ultrasound is in the order of 5-10 mm. Hence, the acoustic absorption in soft tissue, which increases with frequency at a rate of 0.75 dB/cm/MHz, is not highly penalizing the frequency up-scaling. Nonetheless, the fabrication of piezoelectric ultrasound transducers typically involves a dicing saw process with a blade thickness that determines the kerf size, K, typically in the range of tens of µm. Since K cannot be made arbitrarily small, higher frequencies lead to a reduction in L_{eff}, which subsequently

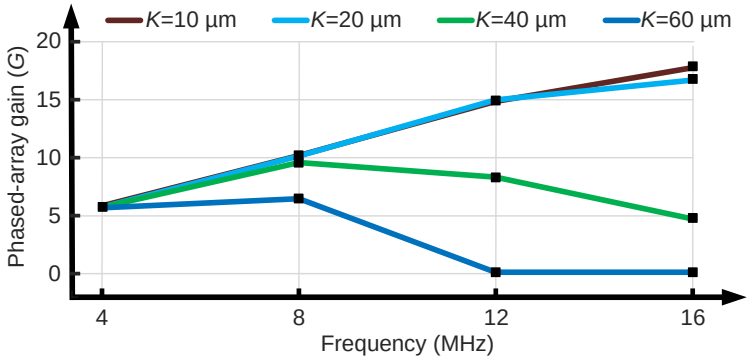

(a)

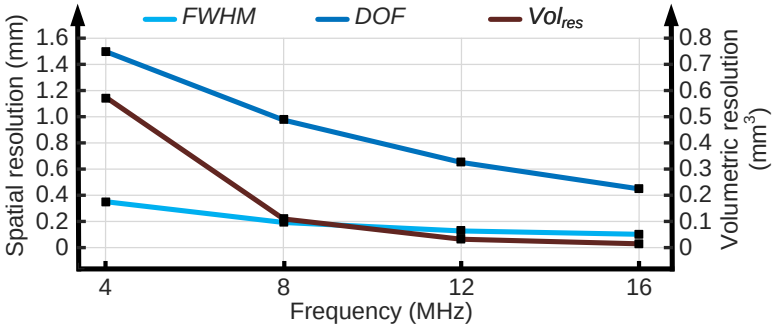

(b)

Fig. 3.5: The influence of center frequency on phased array gain and spatial resolution. During the k-Wave simulation, the total length of the array and the pitch size were fixed to 2 mm, and the sound half-wavelength. In (b), K is set to 20 µm.

lowers G.

To investigate all the abovementioned tradeoffs, simulations were performed using the k-Wave Toolbox. To reduce the simulation time, the total size of the 2D array was set to $2{\times}2$ mm^2. In the case of pre-clinical experiments with rodents, L is limited to < 10 mm due to the maximum size of the craniotomy for direct interface between the chip and the brain; thus, the chosen value is also in line with experimental requirements. Furthermore, the absorption coefficient of the brain has been included in the medium properties such that absorption is modeled correctly. The US transducers were configured to form a focal spot at a depth of 2 mm, and the kerf size K was swept during the simulation to study its effect on the beam profile properties. As illustrated in Fig. 3.5(a), increasing the frequency leads to a higher phased-array gain for frequencies up to 16 MHz for kerf sizes of 20 µm or lower. For kerf sizes of 40 µm or larger, G starts to drop for frequencies above 8 MHz. Thus, for high frequencies, it is recommended to minimize K as much as the microfabrication processes allow [220], ideally to values much lower than d.

Regarding the spatial resolution of the focused ultrasound beam, as expected from Equation 3.7 and as depicted in Fig. 3.5(b), it increases with frequency, thus leading to bet-

ter $FHWM$, DOF, and, consequently, Vol_{res}. For these simulations, the kerf size and the length of the array are fixed to 20 µm and 2 mm. Varying the kerf size from 10 µm to 60 µm does not affect the spatial resolution significantly. This is in agreement with Equation 3.9 and Equation 3.10, showing that the spatial resolution depends on the array length rather than the effective aperture length. Furthermore, the improvement of the spatial resolution with the frequency is less significant for frequencies above 12 MHz. Higher frequencies also lead to improved Vol_{res} and G, as shown in Fig. 3.5. However, considering the available fabrication methods to develop 2D array piezoelectric transducers, increasing the frequency above 12 MHz imposes practical challenges on the fabrication of 2D piezoelectric transducers without significantly improving the performance of the phased array transducer. Moreover, in a pitch-matched 2D array, the size of the transducer elements is aligned with the area of the beamforming circuits. Therefore, increasing the frequency reduces the pitch size, and, hence, limits the available area to implement a high-voltage beamforming channel. Chapter 4 investigates the smallest circuit area required for implementing a high-voltage beamforming channel.

3.3.3. Size of the Array

As outlined in Equation 3.7 and Equation 3.8, besides the f_{US}, the array length L has a direct influence on Vol_{res}, while the array effective length L_{eff} determines the phased array gain G. Increasing the array length enhances G, DOF, and $FWHM$. However, DOF improves much faster than $FWHM$ with increasing the frequency. The k-Wave simulations were performed to investigate the effect of the array length on the US focusing performance. In these simulations, the kerf size is fixed to 20 µm, and the pitch size matches the sound half-wavelength. Fig. 3.6(a) depicts the effect of expanding the number of elements, N, or the array length L, on the G. It is evident that increasing the array length for a given center frequency leads to a higher G, as described by Equation 3.8. Moreover, the phased-array gain increases at a higher rate for higher frequencies. Additionally, Fig. 3.6(a) demonstrates that G does not significantly improve with increasing the array effective length after a given threshold, which at 12 MHz corresponds to an array length of 5 mm. The value of this threshold depends on the frequency and the depth of the focal spot. While higher frequencies have smaller thresholds than lower frequencies, deeper focal spots have larger thresholds than superficial focal spots. Therefore, the optimization of the phased arrays should always be conducted considering the deepest focal spots; in the case of preclinical studies on rodents, the highest required Z is around 10 mm. On the other hand, since increasing L_{eff} does not improve G at superficial focal spots after reaching the threshold length, some of the transducer elements can be disabled to minimize power consumption.

Fig. 3.6(b) depicts the influence of the array length on $FWHM$, showing that increasing L leads to smaller $FWHM$. The same behavior is also expected with Vol_{res} and DOF, in line with Equation 3.7 and Equation 3.8. Similar to the focal spot gain, the spatial resolution does not improve further after reaching a specific threshold, which depends on the frequency and the focal spot depth.

In 2D US phased arrays, the maximum achievable penetration depth (Z_{max}) is close to the natural focal spot of the array when a planar wave is applied to the transducer elements. Like single-element piezoelectric transducers, Z_{max} of 2D phased arrays depends

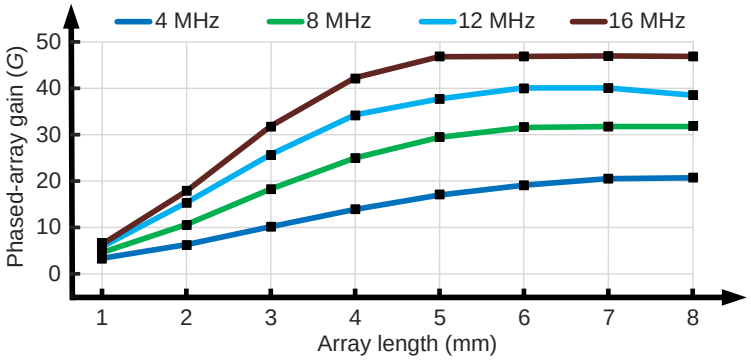

(a)

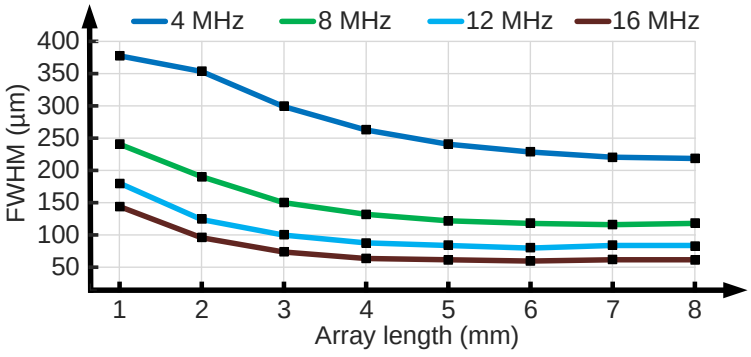

(b)

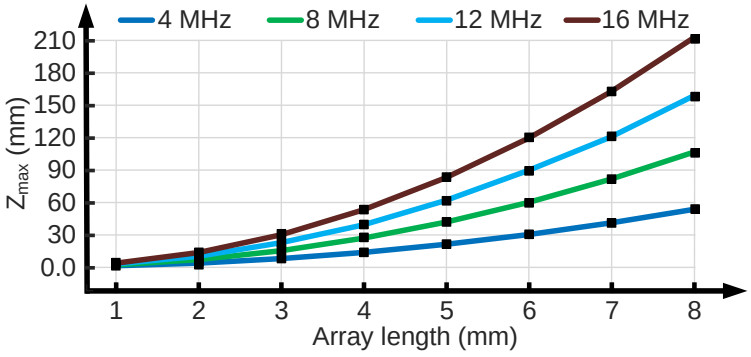

(c)

Fig. 3.6: The effect of array length on (a) phased-array gain, (b) lateral resolution, and (c) maximum depth of focal spot for a 2D US phased-array transmitter. The pitch size matches the sound half-wavelength, and the focal depth in (a) and (b) is equal to 2 mm. A kerf size of 20 µm was considered for all the abovementioned simulations.

on the frequency and the length of the array. As shown in Fig. 3.6(c), $Z_{\max}$ increases with both the array length and the frequency despite the higher acoustic attenuation at higher frequencies.

As depicted in Fig. 3.6, increasing the array length improves the spatial resolution as well as the phased array gain. However, the larger L results in a larger array, limiting the transducer's suitability for implantable and wearable applications. In other words, in the context of preclinical experiments, the maximum length of a 2D array is limited to the maximum length and width of rodent brains. Therefore, in such applications, it is recommended to first optimize the array length and then find the optimum frequency based on the required $Z_{\max}$, Vol_{res}, and G.

3.3.4. Phase Quantization Resolution

As discussed earlier, phasing the driving signal of the US transducers allows electronic beam steering and focusing of the US waves. An example of a driving signal corresponding to an ultrasound transducer within a 30×30 array, with a focal depth of 2mm, and the azimuth and elevation angles of zero is illustrated in Fig. 3.7(a). Since non-imaging applications, such as US ablation, neuromodulation, and power delivery, require bursts of continuous ultrasound waves, the periodicity of continuous waves can be explored, and absolute phase differences can be replaced by phase differences wrapped to 2π, which allows for simpler circuitry and avoids the need for high-resolution and high-frequency counters [53]. Although continuous analog phases can be implemented with a simple current-starved inverter, developing linear analog phases requires precise control over the charging and discharging current of the inverter, increasing the complexity and power consumption of the beamforming channels [221]. Additionally, each beamforming channel needs an analog phase generator with an analog input; thus, an $N \times N$ array requires N^2 analog inputs to program the phase of every beamforming channel, making implementation of dense 2D arrays impractical. To overcome these limitations, quantized digital phases can be used instead. The quantized phases can be implemented with simple, low-power digital circuits, allowing for easier control of the phase of each beamforming channel and, hence, making it feasible to implement dense 2D arrays. In the literature, different phase quantization resolutions have been utilized [40], [53], However, they either have not studied the effect of the phase quantization resolution on the US performances or have used over-designed resolutions, which resulted in higher power consumption and larger beamforming channel area. In this regard, this study aims to use k-Wave simulations to find the optimum phase quantization resolution to perform beam steering at the cost of the lowest power consumption.

To perform these simulations, a 40×40 array of US transducers with the center frequency of 12 MHz and kerf size of 20 μm is utilized while the pitch size is set to sound half-wavelength. Fig. 3.7(b) shows the normalized pressure versus the phase quantization resolution. From these results, it is evident that the normalized focal pressure does not significantly improve for phase quantization resolutions above three bits. Calculating the spatial resolution confirms that three-bit resolution is the optimum phase quantization resolution. To evaluate the sensitivity of the phase quantization resolution to the focal depth and frequency, k-Wave simulations have been performed in different depths and frequencies utilizing three-bit and ten-bit phase quantization. The simulation results showed that in all cases, there was not a significant change between the spatial resolution and the focal pressure of the three-bit and ten-bit phase quantization. Furthermore, it is also important to study the effect of the phase quantization resolution on the beamform-

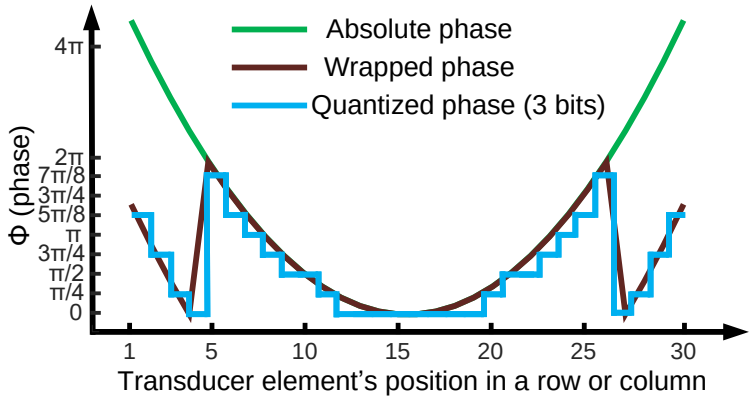

(a)

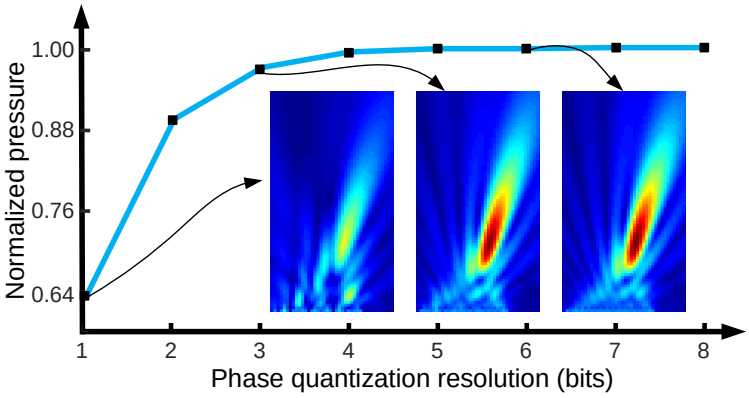

(b)

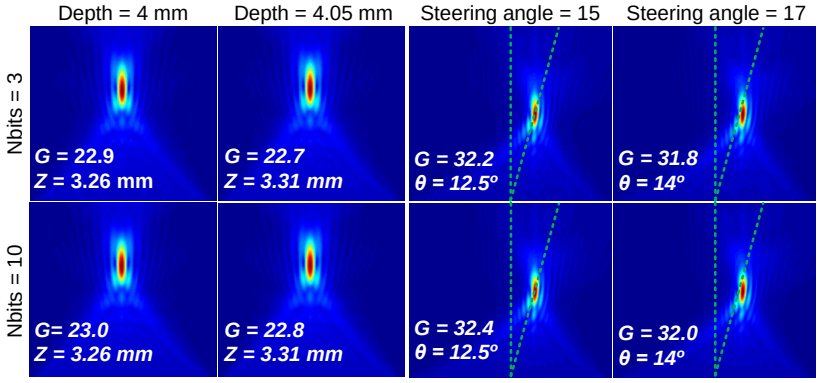

(c)

Fig. 3.7: (a) Phase of US transducers for a given row or column in a 2D US phased array, highlighting the difference between the absolute phase and 3-bit phase quantization. (b) and (c) show the effect of phase quantization on the focal spot properties and steering capability of a 2D phased-array; a 40×40 phased-array with a center frequency of 12 MHz and a kerf size of 20 µm was considered for the k-Wave simulations. It is evident that 3 bits is the optimum resolution to quantize the phase of the driving signals.

ing capability of the US transducer. Therefore, two sets of k-Wave simulations utilizing three-bit and ten-bit phase quantization have been conducted. In these simulations, the depth of the focal spot has moved by 50 µm, and the steering angle has changed by 2°. As demonstrated in Fig. 3.7(c), reducing the phase quantization resolution from ten to three bits does not affect the steering capabilities in both axial and lateral directions. In this regard, it can be inferred that three-bit phase quantization is sufficient for implementing a phased-array US transducer independent from the center frequency. As a result, three-bit phase quantization resolution reduces the circuit complexity in comparison with other works [40], [53], enabling the implementation of low-area beamforming channels needed for high-frequency phased arrays.

3.3.5. Steering of the Focal Spot

The phased array gain and the volumetric resolution also depend on the location of the focal spot, and they vary for different steering angles or Z. As outlined in Equation 3.7 and Equation 3.8, increasing the focal depth degrades the spatial resolution and the phased array gain. In order to verify these equations, k-Wave simulations have been conducted using a 66×66 array of US transducers with center frequency and kerf size of 12 MHz and 20 µm, respectively. The properties of the array were chosen in line with the preclinical US neuromodulation application in rodents. In this regard, the size of the array, the frequency, and the kerf size were chosen in a way to maximize G and Vol_{res} at the focal spot. Fig. 3.8(a) shows the influence of the focal depth on the phased-array gain and the volumetric resolution. In these simulations, the steering angles are zero, and the focal depth has swept from 2 mm to the maximum depth of 10 mm. It is evident that the ultrasound beam characteristics degrade with increasing the focal depth. Fig. 3.8(b) depicts the beam profiles generated by the same array when the beam is focused at a depth of 10 mm and the azimuth angles of 0° and 10°. Changing the steering angle from 0° to 10° degrades the phased array gain and the *FWHM*. However, the *DOF* interestingly improves in the steering angle of 10°. This could be because at 0°, all elements propagate ultrasound waves parallel to the focal spot. In contrast, at 10°, some elements on the right side propagate ultrasound waves perpendicular to the focal spot, resulting in a shorter *DOF*. Although the beam profile in Fig. 3.8(b) is intended to be focused at a depth of 10 mm, the actual focal depth occurred at 7.8 mm, indicating a focal depth offset in the beam profile, which happens in arrays with small Fresnel numbers [222]. It is crucial to account for this offset during the design of the 2D ultrasound phased array transmitter. Additionally, an accurate phased array design must consider worst-case scenarios for spatial resolution and phased array gain, which occur when the beam is focused at the maximum distance from the transducer surface.

3.3.6. Power Consumption Analysis

Power consumption plays a critical role in designing ultrasound phased-array transducers. Although increasing the frequency and the array length improves the US beam parameters, it increases the power consumption. Higher frequencies raise the dynamic power consumption of the beamforming channels, and extending the array length increases the number of beamforming channels, thereby raising the overall power consumption. Figure 3.9 illustrates the overall power consumption of the electronic circuits as a function

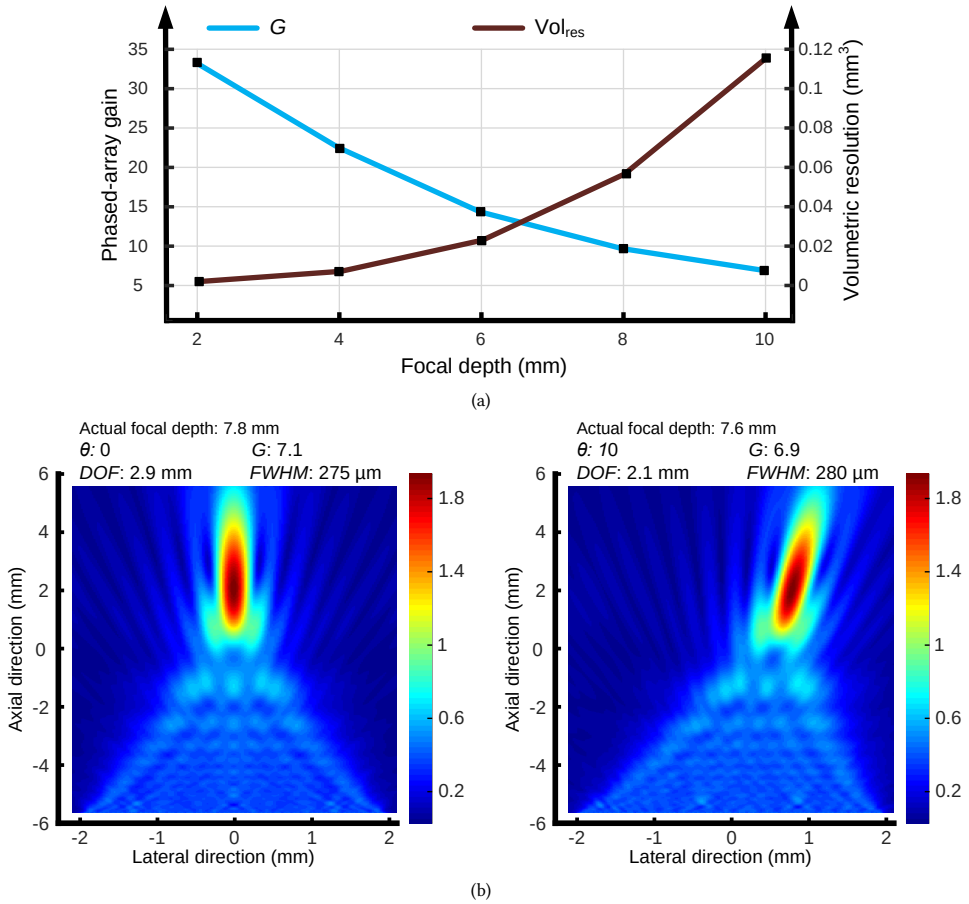

Fig. 3.8: (a) The influence of the focal depth and (b) steering angle on volumetric resolution and phased-array gain of a 2D phased array, a 66×66 US phased-array with center-frequency of 12 MHz and kerf size of 20 µm was considered for the k-Wave simulations.

of frequency and array length, based on electrical simulation results of a 20-V beamforming circuit [223]. The piezoelectric transducer is modeled using a Butterworth-van-Dyke model derived from an electrical impedance estimation near the resonance frequency. The BVD model is approximated by a capacitor in parallel with a resistor at the resonance frequency. The values of the capacitor and resistor depend on the size of the piezoelectric transducer element and the operating frequency. A detailed method for calculating the electrical model of the piezoelectric transducer is provided in Chapter 4. According to Equation 3.8, G increases directly with L_{eff} and f_{us}. However, as depicted in Fig. 3.9, power consumption also rises with the number of elements and the resonant frequency. The dynamic power consumption can be expressed as:

$$P_{\text{dynamic}} = C \cdot V_{\text{d}}^2 \cdot f_{\text{US}} \tag{3.13}$$

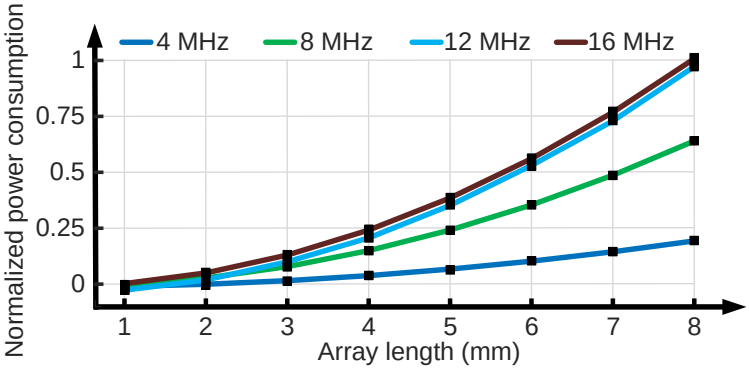

Fig. 3.9: Simulated power consumption of a 2D US phased-array transmitter for different frequencies and array lengths.

where C and V_d are the piezoelectric transducer's clamp capacitance and driving voltage, respectively. Therefore, increasing the frequency has a linear relationship with G, but it also reduces the electrical impedance of the piezoelectric elements. On the other hand, while doubling the array length doubles G, it also quadruples the number of elements and, thus, the power consumption. As shown in Fig. 3.9, although increasing the frequency leads to slightly lower power consumption than increasing the array length, G improves slightly more with increasing the array length according to Fig. 3.6(a). On the other hand, as depicted in Fig. 3.6(b), increasing the frequency improves the spatial resolution further than increasing the array length. In this regard, the choice of increasing either the frequency or the array size depends on the application of the phased array transmitter. In applications that require higher spatial resolution, increasing the frequency results in the most power-efficient choice. On the contrary, increasing the array length leads to higher G at the cost of lower power consumption for applications where higher G is needed. In a similar way, doubling V_d doubles G but also quadruples the power consumption, as described by 3.13. It is worth mentioning that, as shown in Fig. 3.9, the total power consumption of 12-MHz and 16-MHz 2D phased arrays is approximately the same. This can be attributed to the fact that the size of the ultrasound transducers becomes comparable to the kerf size at frequencies above 12 MHz. Consequently, although the frequency increases from 12 MHz to 16 MHz, the effective piezoelectric load decreases, resulting in approximately the same power consumption as the 12-MHz array.

3.4. Discussion

As discussed in this chapter, the driving voltage, phase quantization resolution, frequency, and array length significantly influence the acoustic and electrical parameters of the phased array, such as G, *DOF*, *FWHM*, and power consumption. Therefore, the electrical and physical parameters of the array should be optimized to maximize focal gain and spatial resolution while minimizing power consumption. Regarding phase quantization resolution, it has been demonstrated that a three-bit resolution is optimal for quantizing the phase of the beamforming channels. Since increasing the frequency is the most power-efficient method to achieve high spatial resolution, it is the primary parameter to be selected. This chapter

highlighted that achieving high frequencies is primarily limited by the kerf size resulting from the dicing process. Considering the thickness of the current dicing saws, the effective area of the piezoelectric transducer element decreases significantly at frequencies above 16 MHz. For instance, in a 20-MHz phased array, achieving a beam profile without grating lobes requires a pitch size of 37 µm. With a 20 µm dicing saw, the width of the remaining piezoelectric element is approximately 17 µm, resulting in a loss of around 80% of the piezoelectric material. Consequently, the resonance frequency is chosen between 12-16 MHz to optimize the performance of the ultrasound array while minimizing piezoelectric material loss and power consumption. Even though increasing the number of elements, or the length of the array, improves the volumetric resolution and the phased-array gain, it comes at the cost of extra complexity and a larger form factor. As this research has focused on developing ultrasound transducers for US neuromodulation experiments on rodents, the small size of rodent brains, particularly those of rats and mice [219], imposes a limit on the maximum array length. In this regard, two 2D phased array transmitter ASICs have been investigated, designed, and characterized, as will be described in Chapter 5, which presents a comprehensive discussion of the factors involved in selecting the appropriate array size. Lastly, increasing the driving voltage enhances the pressure at the focal spot but results in higher power consumption. Furthermore, adjusting the driving voltage allows the control of the US pressure at the focal spot. Therefore, an adjustable high-voltage pulser is desired to deliver pulses with controllable amplitudes to the piezoelectric transducers. Chapter 4 focuses on developing high-frequency beamforming channels capable of delivering high-voltage pulses to the ultrasound transducer elements. This development is essential for creating high-performance 2D phased array transducers.

4

Beamforming Channels

4.1. Introduction

THE electrical properties of the driving signals and the physical parameters of the 2D transducer array significantly impact the acoustic parameters of the focal spot as well as the overall power consumption of the driving ASIC. As explored in Chapter 3, optimizing both the electrical and physical parameters of the phased array is essential to maximize overall transmit efficiency. Increasing the f_{US} is the most power-efficient way to enhance G and Vol_{res}. However, increasing f_{US} necessitates a smaller pitch size in the phased array, as preventing the appearance of the grating lobes in the beam profile demands a pitch size of sound half-wavelength (Equation 3.12). Consequently, the reduction in pitch size limits the available area for implementing a beamforming channel, posing challenges to delivering high-voltage (HV) pulses to the piezoelectric transducers. In response to these challenges, this chapter first examines the minimum area required to implement an HV beamforming channel, which is needed for achieving higher f_{US}. According to this study, two 36-V and 20-V beamforming channels are implemented, corresponding to a phased array with f_{US} of 12 MHz and 15 MHz, respectively. Following this, this chapter focuses on the design of a power-efficient pulser to minimize electrical losses in the beamforming channels and enhance overall transmit efficiency. In this regard, a pulser utilizing a charge recycling technique has been developed to minimize the electrical power losses in the beamforming channels and, hence, improve the overall power efficiency.

4.2. High-Frequency Beamforming Channels

4.2.1. Introduction

As discussed in Chapter 2, reliable preclinical US neuromodulation studies on rodents demand 2D phased array US transducers capable of generating focal spots with high p and

Parts of this chapter have been published in "A High-Frequency Beamforming Channel for Ultrasound Stimulation and Ultrasonic Powering," in *Proc. IEEE Biomed. Circuits Syst. Conf. (BioCAS)*, Oct. 2022 [223], and "An Energy-Efficient High-Voltage Pulser for High-Frequency Ultrasound Medical Applications," in *Proc. IEEE Biomed. Circuits Syst. Conf. (BioCAS)*, Oct. 2023 [224]

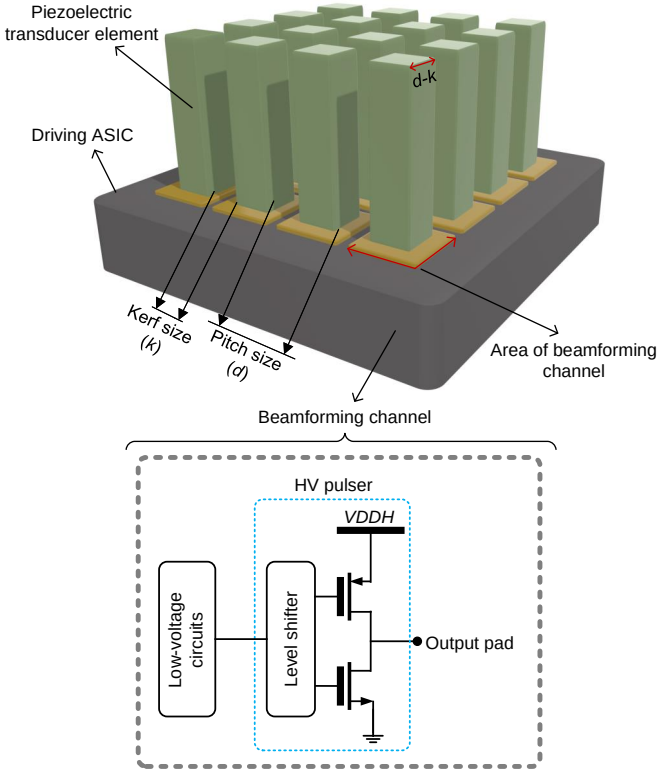

Fig. 4.1: A conceptual 2D ultrasound phased array transmitter, showing how the minimum achievable kerf size and the area of beamforming channel limits the minimum pitch size, and hence the maximum f_{US}.

fine Vol_{res}. Chapter 3 revealed that increasing f_{US} leads to higher G and improved Vol_{res}. In order to avoid the generation of grating lobes in the US beam profile, the pitch size must be equal to the sound half-wavelength (Equation 3.12). [40] has proposed an 8-MHz 2D phased array US transducer for US neuromodulation applications while the pitch size is limited to 0.91 λ, which leads to the appearance of grating lobes in the beam profile. Therefore, the pitch size must proportionally decrease as f_{US} increases to avoid grating lobes. This requirement limits the available area for implementing a beamforming channel in a pixel-level pitch-matched structure, which is required for the direct integration of the piezoelectric transducers on top of the driving ASIC. As illustrated in Fig. 4.1, the minimum achievable kerf size and the minimum area required to implement a beamforming channel determine the minimum achievable pitch size, and thus the maximum achievable f_{US}. As explored in Section 3.3, the kerf size in the 2D piezoelectric arrays is constrained by the minimum blade thickness of the dicing saw. Considering the available blades capable of cutting through high-frequency piezoelectric transducers, the minimum kerf size ranges from 10 µm to 20 µm [225], [226]. As shown in Fig. 3.5, by utilizing these kerf sizes, increasing the frequency leads to improved G and f_{US} for frequencies up to 16 MHz, which corresponds to a pitch size of 46 µm. However, the minimum pitch size is also limited by

the minimum area required to implement an HV beamforming channel, which is discussed in this section. In this regard, two small area 36-V and 20-V beamforming channels are implemented, which occupy an area of 62.5×62.5 μm^2 and 50×50 μm^2, corresponding to f_{US} of 12 MHz and 15 MHz, respectively. These beamforming channels enable the implementation of high-frequency 2D phased array US transducers without generating any grating lobes in the beam profile.

4.2.2. Beamforming Channel Area Minimization

Beamforming channels play a critical role in 2D phased array ultrasound transducers, as they enable controlling the phase of the driving pulses and, hence, allowing US beam focusing and steering. Additionally, the beamforming channels deliver HV pulses, typically in the range of tens of volts, to the ultrasound transducer elements, which are necessary for generating focal spots with high US pressure. As illustrated in Fig. 4.1, beamforming channels are composed of two main parts: low-voltage (LV) circuits and an HV pulser. The low-voltage circuits allow controlling f_{US}, burst duration, and phase of the driving signal, which is necessary for US beam focusing and steering. The HV pulser, on the other hand, amplifies the signals generated by the low-voltage circuits and delivers them to the ultrasound transducer elements. While the low-voltage circuits are implemented using standard CMOS transistors, the HV pulser typically requires HV DMOS transistors, which can withstand higher drain-source voltages compared to standard CMOS transistors at the cost of occupying a larger area. Typically, HV DMOS transistors occupy a significantly larger area compared to the standard low-voltage CMOS transistors since an HV insulation ring is needed for HV transistors. Furthermore, it is obvious that transistors with larger drain-source voltage occupy a larger area, revealing a tradeoff between the occupied area and the driving voltage of the beamforming channels. Implementing 70-V beamforming channels requires an area of at least 120×120 μm^2, corresponding to the area needed for two HV transistors, low-voltage circuits, and the insulation distance between the LV and HV devices. Therefore, the area of a 70-V beamforming channel limits the f_{US} of the 2D phased array to 6 MHz. Therefore, it can be concluded that the maximum achievable f_{US} is limited by the driving voltage. In this work, the driving voltage is reduced to 36 V and 20 V in order to increase f_{US}. According to the data reported in the literature, driving amplitude of 36 V and 20 V can lead to sufficient levels of US pressure for performing successful US neuromodulation experiments [26], [227], [228]. Implementing 36-V and 20-V beamforming channels needs an active circuit area of 62.5×62.5 μm^2 and 50×50 μm^2, allowing to increase f_{US} up to 12 MHz, and 15 MHz, respectively. As discussed in Chapter 3, the kerf size is set to 20 μm corresponding to the minimum thickness of available dicing saws that can cut piezoelectric transducers [220]. Therefore, the 36-V beamforming channel, which limits the pitch size to 62.5 μm, leads to a piezoelectric element with an active area of 42×42 μm^2, as shown in Fig. 4.1. Similarly, the 20-V beamforming channel, which restricts the pitch size to 50 μm, results in a piezoelectric element with an active area of 30×30 μm^2.

4.2.3. Electrical Model of the Piezoelectric Transducers

The design and verification of beamforming channels' performance requires an electrical model for the piezoelectric transducers, ensuring the capability of the beamforming chan-

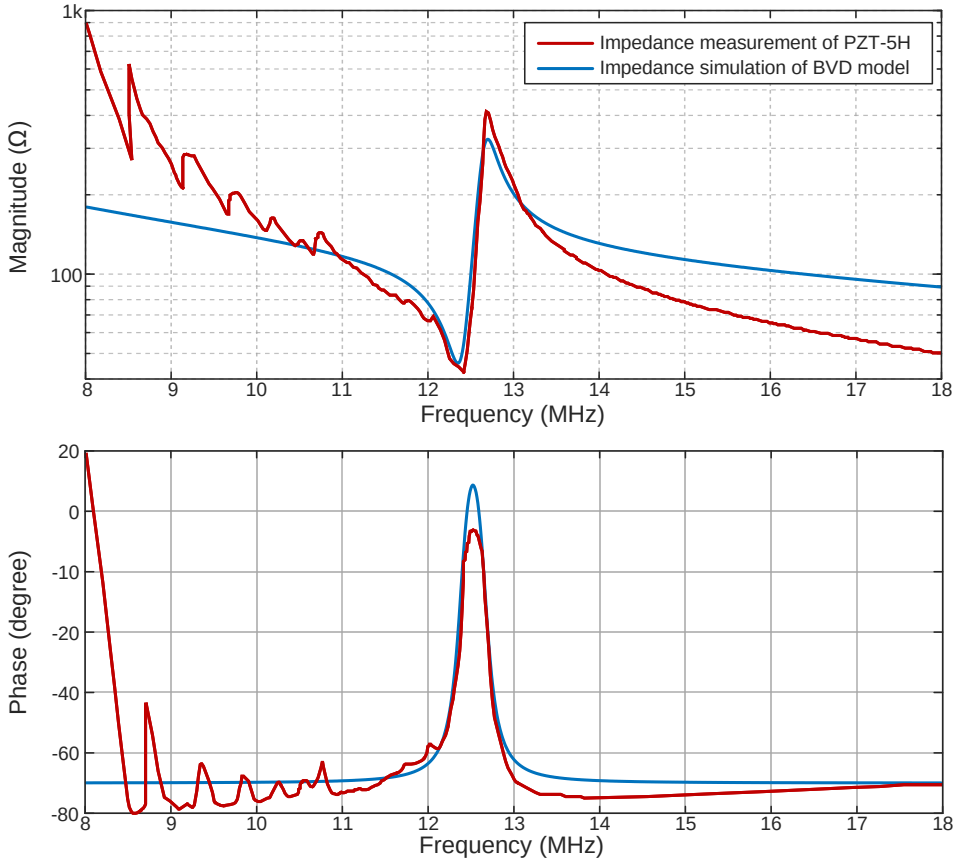

Fig. 4.2: Fitting the electrical impedance measurements of a 0.8×0.8 mm^2 12-MHz PZT-5H piezoelectric transducer, which is measured with an impedance analyzer, with the electrical stimulations of the complete BVD model.

nel to drive the piezoelectric load at the resonance frequency. As discussed in Section 2.3, the BVD model offers a simplified model to mimic the impedance and the resonance frequency of the ultrasound transducer. In order to calculate the value of the components in the BVD model, first, the impedance characteristic of a piezoelectric transducer, in this case, a 12-MHz PZT-5H transducer, is measured using an impedance analyzer (4294A, Keysight Technologies Inc.). However, since measuring the impedance of a 42×42 μm^2 piezoelectric transducer is practically challenging, a larger piezoelectric transducer is utilized. Then, the value of the components in the BVD model should be scaled proportional to the area to mimic the impedance characteristic of the 42×42 μm^2 piezoelectric transducer. In this regard, the impedance of a 0.8×0.8 mm^2 12-MHz PZT-5H transducer is measured using the impedance analyzer, as depicted in Fig. 4.2. To mimic the real environment when measuring the impedance, the PZT-5H transducer is immersed in water since water has similar ultrasound characteristics to the biological tissues [58]. Then, the parameters of the BVD model around the resonance frequency are calculated by means of

the least-square curve-fitting on the measured impedance through electrical simulations of the BVD model, as shown in Fig. 4.2 and Fig. 4.3. Since the impedance of a piezoelectric transducer scales approximately inversely with the area [205], the components of the BVD model for a 42×42 μm^2 PZT-5H, which are illustrated in Fig. 4.3, are calculated from:

$$C_{p2} = \left(\frac{A_1}{A_2}\right) \times C_{p1} = \left(\frac{42 \times 42\,\mu m^2}{800 \times 800 \mu m^2}\right) \times 141\,pF = 400\,fF \tag{4.1}$$

$$R_{s2} = \left(\frac{A_2}{A_1}\right) \times R_{s1} = \left(\frac{800 \times 800\,\mu m^2}{42 \times 42\,\mu m^2}\right) \times 55\,\Omega = 20\,k\Omega \tag{4.2}$$

$$L_{s2} = \left(\frac{A_2}{A_1}\right) \times L_{s1} = \left(\frac{800 \times 800\,\mu m^2}{42 \times 42\,\mu m^2}\right) \times 36.7\,\mu H = 13\,mH \tag{4.3}$$

$$C_{s2} = \left(\frac{A_1}{A_2}\right) \times C_{s1} = \left(\frac{42 \times 42\,\mu m^2}{800 \times 800 \mu m^2}\right) \times 4.5\,pF = 13\,fF \tag{4.4}$$

where A_1 and A_2 are the surface area of 0.8×0.8 mm^2 and 42×42 μm^2 12-MHz PZT-5H transducers, respectively. Similarly, the components of the BVD model for a 30×30 μm^2 15-MHz PZT-5H can be calculated from the components of the 0.8×0.8 mm^2 12-MHz PZT-5H transducer. In this case, in addition to the area of the piezoelectric transducer, the thickness of the piezo affects the impedance of the piezoelectric transducer. As shown in Equation 2.14, the resonance frequency of a piezoelectric US transducer is inversely proportional to the thickness of the transducer. In other words, lower thickness leads to higher resonance frequency and, hence, lower electrical impedance. The value of the BVD model for the 30×30 μm^2 15-MHz PZT-5H, which are shown in Fig. 4.3, are obtained from:

$$C_{p3} = \left(\frac{A_1 \times f_{US1}}{A_3 \times f_{US3}}\right) \times C_{p1} = \left(\frac{30\,\mu m \times 30\,\mu m \times 15\,MHz}{800\,\mu m \times 800\,\mu m \times 12\,MHz}\right) \times 141\,pF = 181\,fF \tag{4.5}$$

$$R_{s3} = \left(\frac{A_3 \times f_{US3}}{A_1 \times f_{US1}}\right) \times R_{s1} = \left(\frac{800\,\mu m \times 800\,\mu m \times 12\,MHz}{30\,\mu m \times 30\,\mu m \times 15\,MHz}\right) \times 55\,\Omega = 31\,k\Omega \tag{4.6}$$

$$L_{s3} = \left(\frac{A_3 \times f_{US3}}{A_1 \times f_{US1}}\right) \times L_{s1} = \left(\frac{800\,\mu m \times 800\,\mu m \times 12\,MHz}{30\,\mu m \times 30\,\mu m \times 15\,MHz}\right) \times 36.7\,\mu H = 21\,mH \tag{4.7}$$

$$C_{s3} = \left(\frac{A_1 \times f_{US1}}{A_3 \times f_{US3}}\right) \times C_{s1} = \left(\frac{30\,\mu m \times 30\,\mu m \times 15\,MHz}{800\,\mu m \times 800\,\mu m \times 12\,MHz}\right) \times 4.5\,pF = 8\,fF \tag{4.8}$$

where A_1 and f_{US1} are the area and the resonance frequency of the 0.8×0.8 mm^2 12-MHz PZT-5H and A_3 and f_{US3} are the area and resonance frequency of the 30×30 μm^2 15-MHz PZT-5H. The simplified BVD models, which consist of C_p and R_s, are utilized to design and simulate the beamforming channels, ensuring their capability to drive the piezoelectric transducer elements.

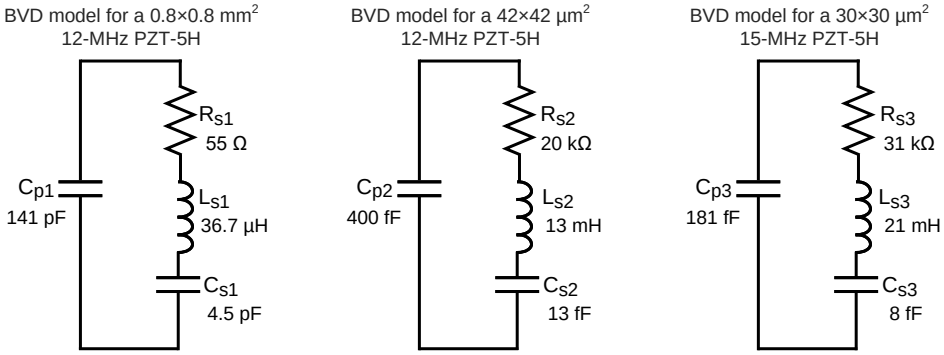

Fig. 4.3: BVD model for 12-MHz and 15-MHz PZT-5H transducer, which are obtained using the least-square curve fitting on the measured impedance of a 0.8×0.8 mm^2 12-MHz PZT-5H.

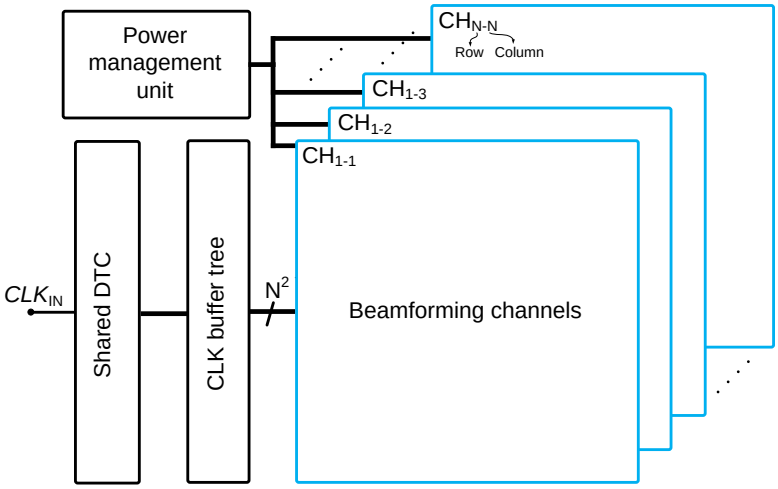

Fig. 4.4: System architecture of the driving ASIC for a 2D phased array US transmitter. The building blocks include the shared DTC, CLK buffer tree, and beamforming channels.

4.2.4. 12-MHz 36-V Beamforming Channel

As illustrated in Fig. 4.4, a conceptual driving ASIC architecture for phased array US transmitters consists of a power management unit (PMU), a digital-to-time converter (DTC), a clock buffer tree, and a 2D array of beamforming channels corresponding to a 2D array of ultrasound transducer elements. The PMU generates and regulates the LV and HV supplies needed by the other blocks within the ASIC. The shared DTC, in conjunction with the beamforming channels, generates the required phase for every US transducer element. While the overall system architecture will be discussed in more detail in Chapter 5, this chapter focuses on the beamforming channels.

As depicted in Fig. 4.5, the proposed 36-V beamforming channel includes a multiplexer, 3-bit shift register, 1-bit DTC, 1.8-5 V level shifter, high-voltage level shifter, and HV driver. As discussed in Chapter 3, 3-bit phase quantization resolution is enough to

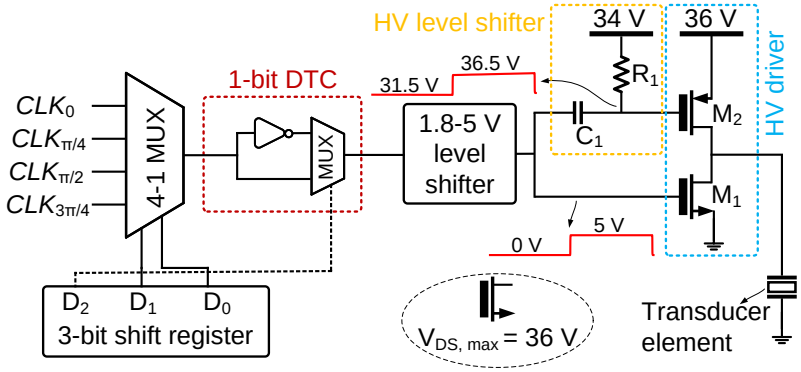

Fig. 4.5: The proposed 36-V beamforming channel, which delivers 12-MHz pulses to the US transducer elements and occupies a circuit area of 62.5×62.5 µm^2.

perform precise US beam steering. Therefore, a 3-bit shift register is utilized to store the data corresponding to the phase of the beamforming channel. The beamforming channel performs 1-bit in-channel phasing, while an external shared DTC is used to generate four clocks with a phase difference of $\pi/4$, allowing the reduction of the beamforming channel area, which is needed for HV and high-frequency operation. Based on the data stored in the shift register, the multiplexer passes one of the shared DTC's clocks to a 1-bit DTC, which is implemented utilizing a simple inverter and a two-to-one multiplexer that selects either the input clock or the inverted input clock. As illustrated in Fig. 4.6, the low-voltage level shifter boosts the clock level from 1.8 V to 5 V, which drives the HV NMOS transistor. However, turning on and off the HV PMOS transistor requires an HV level shifter to change the voltage level to 36 V. In the end, an HV class D amplifier drives the US transducer with 36-V phased clocks. The sizing of the HV transistors has a crucial impact on their ability to drive the piezoelectric load. On the other hand, over-designing the HV transistor affects both power efficiency and the available area for LV circuit implementation. Therefore, the best compromise was found with the sizes of HV NMOS and HV PMOS of 30 µm/2.2 µm and 40 µm/450 nm.

Regarding the HV level shifter, its area should be minimized in order not to penalize the achievable ultrasound frequency. Several architectures have been reported in the literature to implement an HV level shifter. Some works have utilized either bulky HV transistors [53], [229] or low voltage (LV) transistors in the deep-NW layer [230] at the cost of the significant separation distance between the transistors. Alternatively, for continuous pulses, a high-pass RC filter parallel with a diode shapes a high-voltage level shifter [53]. This work has adopted this architecture without the diode towards area minimization. As depicted in Fig. 4.5, since the protection diode is removed in this work, connecting the resistor to the 36-V supply results in a 33.5-38.5-V signal at the gate of the HV PMOS that may damage the transistor. In this regard, the top connection of R_1 is connected to 34 V, generating a 31.5-36.5-V pulse at the gate of the HV PMOS transistor. The 36-V and 34-V supply levels require a constant rise time and fall time in such a way that the gate-source voltage of the HV PMOS transistor never exceeds 5 V. For further scaling of the circuit, C_1 and R_1 are implemented utilizing a metal-oxide-metal (MOM) capacitor on top of the

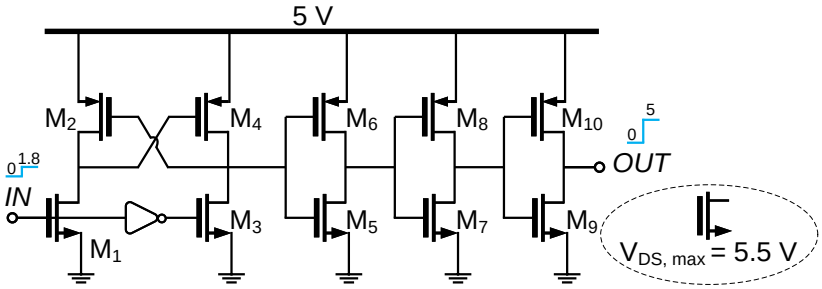

Fig. 4.6: The circuit diagram of the 1.8-5 V level shifter.

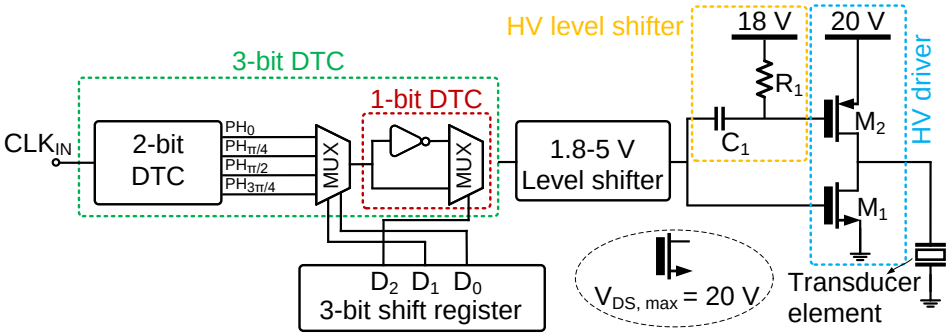

Fig. 4.7: The proposed 20-V beamforming channel, which delivers 12-MHz pulses to the US transducer elements and occupies a circuit area of 50×50 μm^2.

active circuit and the poly resistor, respectively. To push the corner frequency of the high-pass filter close to DC frequency, C_1 and R_1 are chosen large enough (i.e., 400 fF and 800 KΩ).

4.2.5. 15-MHz 20-V Beamforming Channel

As discussed in Chapter 3, increasing the f_{US} is the most power-efficient way to improve the focal G and Vol_{res} of the focal spot. On the other hand, the higher driving voltages also lead to higher US pressure at the focal spot. However, increasing the driving voltage requires employing larger HV transistors that increase the area of the beamforming channel and, hence, the pitch size. As a result, along with increasing the driving voltage, f_{US} is decreased to avoid the appearance of grating lobes in the beam profile. Therefore, to increase the f_{US} further, in the previous beamforming channel, the 36-V transistors are replaced with 20-V transistors, which occupy a smaller area compared with 36-V transistors. Consequently, the 20-V beamforming channel, which is illustrated in Fig. 4.7, allows the reduction of the beamforming channel area to 50×50 μm^2 and hence, increasing the f_{US} to 15 MHz. Furthermore, replacing the 36-V transistors with 20-V transistors adds enough area to perform in-channel 3-bit phasing using a 3-bit DTC.

Similar to the 36-V beamforming channel, the 20-V beamforming channel consists of a 3-bit shift register, 3-bit DTC, 1.8-5 V level shifter, HV level shifter, and HV driver, which are needed to deliver phased HV pulses to the US transducer elements. Firstly, the 2-bit

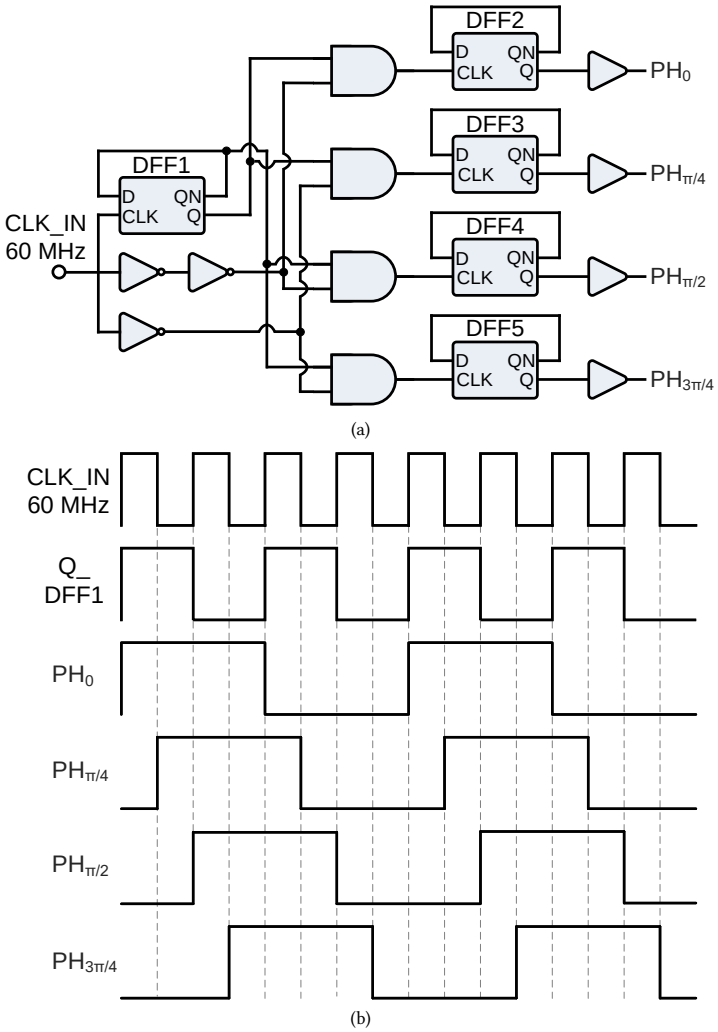

Fig. 4.8: (a) The schematic and (b) the timing diagram of the 2-bit DTC.

DTC, illustrated in Fig. 4.8(a), converts a 60-MHz clock to four 15-MHz clocks with a phasing resolution of $\pi/4$. As depicted in Fig. 4.8(b), the first flip-flop divides the input clock's frequency by a factor of two. Then, the phased clocks are generated by logically comparing the input clock and the inverted input clock with the outputs of the flip-flop. Then, a 4-1 multiplexer passes one of the phased clocks to the 1-bit DTC, corresponding to data stored in the beamforming channel. Next, the 1-bit DTC performs the most significant delay. Since the 3-bit DTC is implemented using digital circuits, the delayed clocks are less sensitive to process, voltage, and temperature (PVT) variations. Then, the phased clock is amplified by the level shifters to turn on and off the HV driver, which in the end, delivers 20-V 15-MHz phased pulses to the transducer element. Since the corner frequency of the HV level shifter was set to 500 kHz, the resistor and the capacitor in the HV level shifter

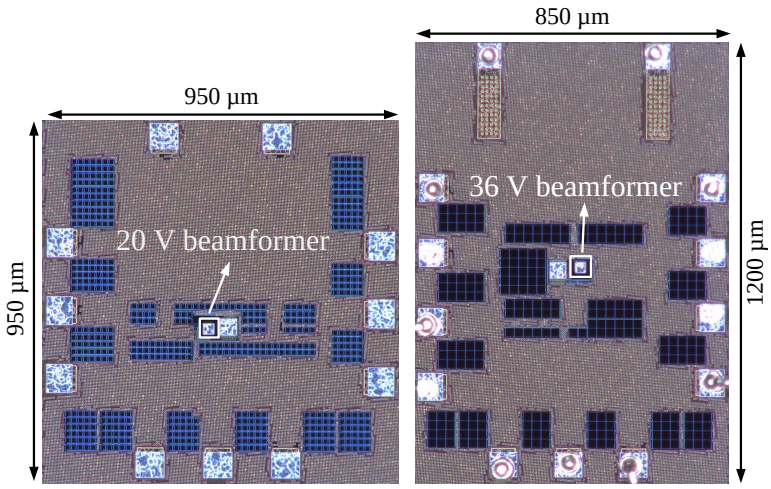

Fig. 4.9: The chip micrograph of the 36-V and 20-V beamforming channels.

are the same size as the ones in the 36-V beamforming channel. The HV NMOS and HV PMOS have a size of 20 µm/1.6 µm and 38 µm/400 nm, ensuring the capability of the HV driver to deliver 20-V pulses to the piezoelectric transducer elements at the cost of adding minimum parasitic capacitance to the output node.

4.2.6. Electrical Measurement Results

The proposed beamforming channels have been designed and fabricated in TSMC 0.18-µm BCD technology. The chip micrographs are shown in Fig. 4.9. Although the 36-V beamforming channel is implemented in an area of 62.5×62.5 µm^2, the total area of the chip, including pad and pad drivers, occupies 850×1200 µm^2. While the HV transistors are responsible for 70% of the occupied area, the LV circuits and HV level shifter occupy 23% and 7% of the beamforming channel area, respectively. The 20-V beamforming channel occupies 950×950 µm^2, although the beamformer is implemented in an area of 50×50 µm^2.

In order to characterize the electrical functionality of the CMOS chip, the ASIC was wire bonded on a printed circuit board (PCB). Then, the wire-bonded PCB was connected to a controller board, which includes the power management unit and a Spartan-7 FPGA development board (CMOD S7, Digilent). The outputs of the beamformer channels were measured by a picoprobe (12C, GGB Industries), which has an input impedance of 0.1 pF || 1 MΩ. To analyze the performance of the 36-V beamformer, four external 12-MHz delayed clocks were applied to the 36-V beamforming channel. The beamforming channel selects one of the delayed clocks according to the two least significant bits (LSBs) stored in the shift registers. Then, the most significant bit (MSB) determines whether the clock or inverted clock can pass to the level shifter. Different delay settings were applied to evaluate the circuit's functionality. The measurement results showed that the maximum differential non-linearity (DNL) is 3 ns which is less than half of the timing resolution (i.e., 5 ns). Fig. 4.10 depicts the output of the 36-V beamforming channel when two different configurations of "000" and "100" were applied to the shift registers. However, the voltage limit

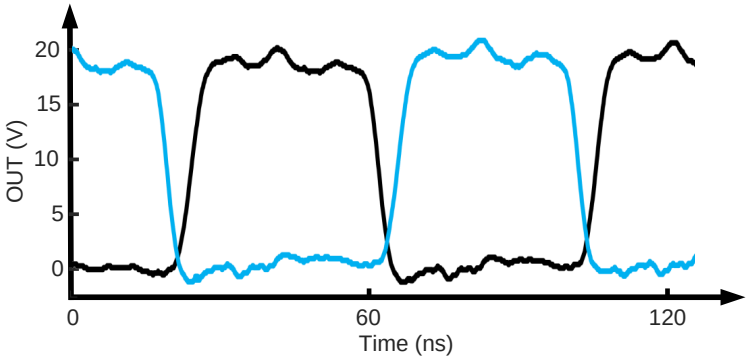

Fig. 4.10: Measured output waveform of the 36-V beamforming channel for two delay settings of "000" and "100".

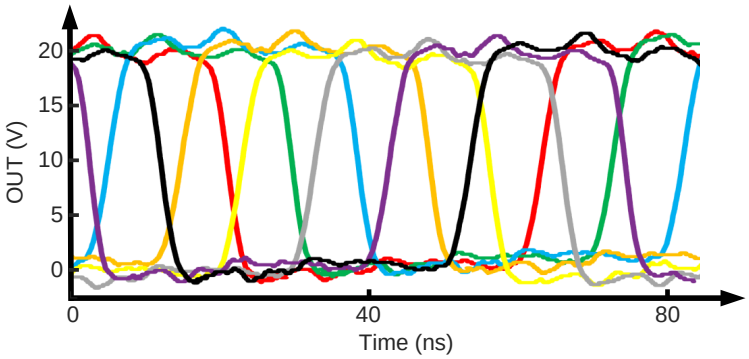

Fig. 4.11: Measured output waveform of the 20-V beamforming channel for eight different phase configurations.

of available high-voltage probes limited the applied voltage to 20 V during the measurements. The beamforming channel consumes 1.23 mA from the 36-V power supply, while the power consumption from low-voltage supplies is negligible compared to the current dissipated from the 36-V supply. During the measurements of the ASIC, no piezoelectric load is applied to the beamforming channel. In order to assess the driving capability of the 36-V beamforming channel, the simplified BVD model is utilized during the electrical stimulation of the beamforming channel. The utilized simplified BVD model consists of a 31 kΩ resistor in parallel with a 181 fF capacitor.

In the next step, the functionality of the 20-V beamforming channel was evaluated by applying a 60-MHz external clock to the ASIC. The in-channel 3-bit DTC converts the input clock to a 15-MHz clock with a given phase corresponding to the data stored in the shift register. To evaluate the capability of the beamforming channel in adjusting the phase of the delivered pulse, different delay settings were applied to the ASIC. Fig. 4.11 shows the transient output waveform of the 20-V beamforming channel for eight different phase configurations, verifying the capability of the beamforming channel to deliver 20-V pulses to the US transducer element with a 3-bit programmable phase. Since linearity is the most important characteristic of time-based circuits, the delay transfer function of the

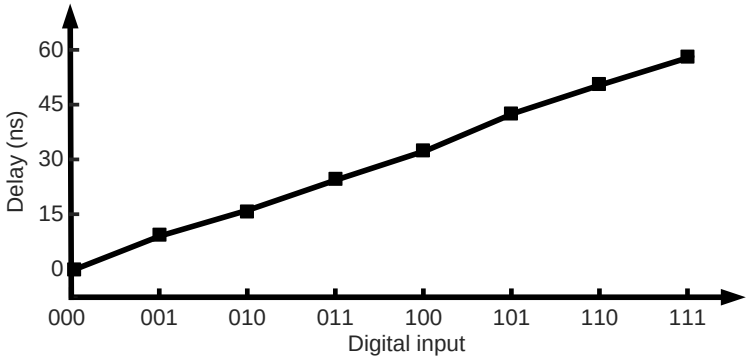

Fig. 4.12: Delay versus digital code transfer function of the 20-V beamforming channel.

20-V beamforming channel was measured, which is shown in Fig. 4.12. The measurement result showed that the maximum DNL of the delay-code transfer function is 2 ns, which is less than half of the timing resolution (i.e., 4.2 ns). The proposed beamforming channel consumes 960 µA from the 20-V power supply when no load is applied. Similar to the 36-V beamforming channel, electrical simulation utilizing the simplified BVD model for a 12-MHz PZT-5H transducer was performed to ensure the driving capability of the 20-V beamforming channel. The simplified BVD model consists of a 20 kΩ resistor in parallel with a 400 fF capacitor.

Table 4.1 shows this work against state-of-the-art beamforming circuits for non-imaging US applications. Unlike [40], the proposed beamforming channels can deliver up to 20 V and 36 V to the US transducer, showing the capability of the beamforming channel in delivering HV pulses to the US transducer elements, which is needed for maximizing the focal pressure. Furthermore, the beamforming channels occupy an area of 50×50 µm^2 and 62.5×62.5 µm^2, showing that the proposed beamforming channels can be utilized in high-frequency 2D phased array transducers. Unlike [53], the high operation frequency can lead to higher spatial resolution. In terms of phase quantization, this work has used 3-bit phase quantization, either at the pixel or at the periphery level, which can maximize focal pressure and spatial resolution, thus avoiding more area and power-consuming circuits as in [53] and [40].

4.2.7. Discussion

According to the findings in Chapter 3, increasing the f_{US} in 2D phased array US transducers leads to higher G and Vol_{res}. In addition, high-voltage pulses are desired as they directly increase the US pressure at the focal spot. However, HV transistors occupy a larger area, which, in turn, reduces the pitch size and, hence, the f_{US}. In this section, two small-area 36-V and 20-V beamforming channels are presented that pave the way for implementing high-frequency 2D phased array US transducers. The 36-V beamforming channel occupies an area of 62.5×62.5 µm^2, which corresponds to an operation frequency of 12 MHz. To increase the frequency further, the driving voltage is decreased to 20 V, leading to a smaller channel area and, hence, pitch size. The 20-V beamforming channel occupies a channel area of 50×50 µm^2, corresponding to f_{US} of 15 MHz. Although the driving voltage can

Table 4.1: Comparison of this work with state-of-the-art beamforming channels

	[209]	[53]	[40]	This work
Application	Imaging	Neuromod.	Neuromod.	Neuromod.
Technology	0.25-µm HV	0.18-µm HV	0.18-µm LV	0.18-µm HV
Frequency (MHz)	5	3.4	8.4	12 @ 36 V 15 @ 20 V
Pitch (µm)	250 (1.67 λ)	250 (0.57 λ)	135 (0.91 λ)	60 @ 36 V 50 @ 20 V (0.5 λ)
Out Vpp (V)	50	60	5	20 and 36
Phase quantization	10 bits	4 bits	6 bits	3 bits

be reduced further to increase the f_{US}, the acoustic simulations in Chapter 3 showed that increasing the frequency above 16 MHz does not improve the US performances in the focal spot. In terms of the driving voltage, 36 V is the maximum driving voltage that can be delivered to a 12-MHz pitch-matched 2D phased array, and any further increase in the driving voltage demands decreasing the f_{US}. Regarding the phase quantization resolution, this work has implemented a quantization resolution of three bits, which, as discussed in Chapter 3, allows maximum steerability at the cost of minimum circuit complexity and power consumption. Hence, the 36-V beamforming channel achieves 3-bit phase quantization through 1-bit in-channel phasing and 2-bit external phasing through a shared DTC, which is shared among all the beamforming channels. On the other hand, the 20-V beamforming channel performs 3-bit in-channel phase quantization using a 3-bit DTC. The measurement results proved the performance of the proposed beamforming channels in terms of driving capability up to 20 V while performing 3-bit phasing with a maximum DNL of half of the timing resolution.

4.3. Power-Efficient HV Pulser Using Charge Recycling

4.3.1. Introduction

As discussed in Chapter 2, 2D phased array US transmitters are a groundbreaking technology in ultrasound biomedical applications. In order to improve the G and Vol_{res} of the focal spot, the previous section focused on developing high-frequency beamforming channels. On the other hand, current phased array US transmitters suffer from poor power efficiency, causing excessive heat generation and limiting their performance. Thus, a power-efficient 2D phased array US transmitter is needed for further advances in these emerging applications, which can be achieved by improving the electromechanical conversion coefficient of the US transducers and developing power-efficient ASICs. The overall power efficiency of the transmitter ASIC is defined as:

$$\eta = \frac{\text{Electrical energy converted to mechanical energy}}{\text{Input electrical energy of the ASIC}} \tag{4.9}$$

In this context, while PMU, shared DTC, HV, LV, and level-shifter circuits in the beamforming channels are essential for phasing and delivering HV pulses to the US transducers (Fig. 4.13), the power consumed by these circuits does not contribute to electromechanical

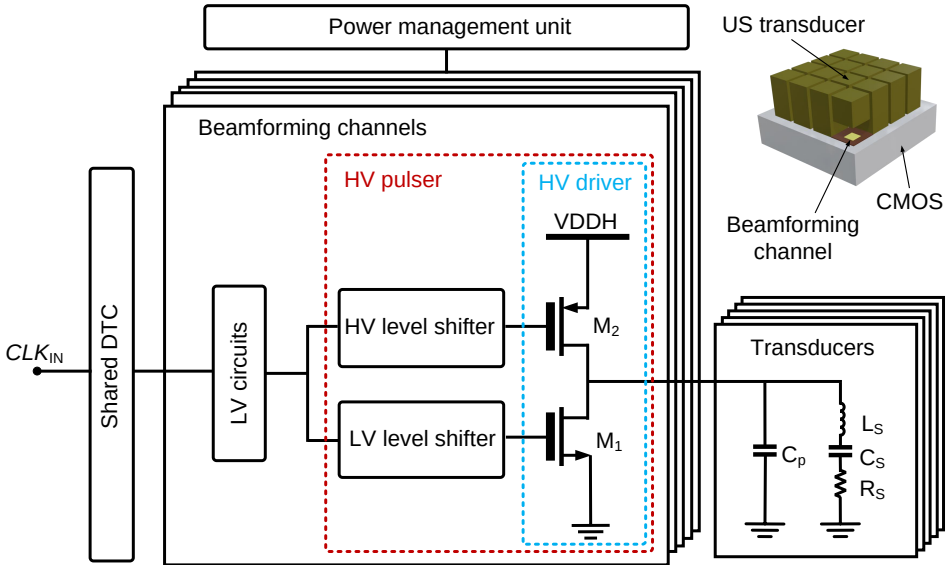

Fig. 4.13: System architecture of a typical 2D phased array US transmitter ASIC.

conversion. Therefore, enhancing the power efficiency of the transmitter ASIC requires reducing the power consumption of these components. Among the building blocks of a 2D US phased-array circuit, as shown in Fig. 4.13, the HV pulsers play a dominant role in the power consumption of the whole ASIC since they dissipate current from an HV power supply [46]. The power efficiency of the HV pulser is degraded by switching losses and the CV^2f losses caused by the clamp capacitance of the US transducer element as well as the parasitic capacitance of the HV driver (Fig. 4.13). Furthermore, the output waveform of the HV pulser influences the power efficiency. Since piezoelectric transducers are required for efficient ultrasound conversion, functioning as narrow bandpass filters, they only pass the fundamental frequency of the waveform and filter out the harmonics. Thus, the harmonics' power is considered as electrical loss; hence, the higher the power of the harmonics, the lower the power efficiency. A class D amplifier employing two HV transistors is the most common way to implement an HV pulser. However, this structure not only occupies a large area but also results in higher parasitic capacitance and, hence, excessive dynamic power consumption [231]. Previous studies [232]–[242] have tried to improve the power efficiency of the HV pulser by adopting various techniques. [232] has utilized a stack of low-voltage transistors instead of HV transistors, leading to a reduction of the parasitic capacitance and hence, better power efficiency. [233] has used an energy replenishing technique using an inductor to save electrical energy and reuse it in the next phase; however, the inductor occupies a large area, making it impractical to utilize this method in 2D dense arrays. [234]–[237] have introduced multi-level pulse-shaping methods; however, adapting these techniques to a 2D phased-array results in a large occupied area per channel since they often require complicated controlling circuits to perform multi-level pulsing. [238] and [239] have used a charge redistribution method by connecting both terminals of the US transducer together. This technique is only suitable for US transduc-

ers in which both terminals of the transducer are accessible, which is not the case in bulk piezoelectric transducers. [240], [241] have utilized a large external capacitor to store the charge of the US transducers and reuse it in the next phases. This section aims to improve the power efficiency of the HV pulser by reducing the CV^2f losses caused by C_p of the piezoelectric transducer and the parasitic capacitance of HV switches in the driver. This is achieved by utilizing a charge recycling method suitable for high-frequency phased arrays of piezoelectric transducers. Considering the tradeoff between frequency and budget area per channel, the frequency was set to 15 MHz corresponding to a budget area per channel of 50×50 μm^2 [223]. Two small capacitors per beamforming channel are utilized to save the charge of the US transducer in the discharging phase and reuse it in the next charging phase. As a result, the proposed circuit reduces the power consumption by 40.9% compared to the conventional HV pulser.

4.3.2. System Architecture

Since bulk piezoelectric transducers have higher electromechanical conversion coefficients than CMUTs and PMUTs [40], 2D phased array US transmitters based on piezoelectric transducers offer higher power efficiency. On the other hand, while CMUTs and PMUTs are CMOS-compatible [53], piezoelectric transducers follow a different fabrication and integration process on top of the ASIC [40]. As a result, only one terminal of the piezoelectric transducers is accessible by the corresponding beamforming channels, while the other terminal of the piezoelectric transducers is connected to a shared ground potential. Therefore, the current charge redistribution techniques for CMUTs and PMUTs cannot be applied to piezoelectric transducers. To overcome this challenge, this section aims to design a power-efficient high-voltage pulser that is compatible with the integration on a 2D array of piezoelectric transducers, allowing to improve the overall power efficiency.

As shown in Fig. 4.13, the conventional pulser charges the transducer to $VDDH$ in the first phase and discharges it to ground in the next phase, suffering from CV^2f power loss caused by the parasitic capacitance, C_p, of the transducer. To achieve a power-efficient pulser for piezoelectric transducers, similar to the SSHC technique in power harvesting applications, a capacitor in parallel with the US transducer can be utilized to store the transducer charge before discharging the transducer to ground and reuse it in the next phase, as shown in Fig. 4.14. The operation principle is as follows. At first, only S_1 is closed, charging the US transducer to $VDDH$. The total charge stored in the transducer is:

$$Q_{tr} = C_p \cdot VDDH \tag{4.10}$$

In the next phase, S_1, S_3 and S_4 are open and S_2 is closed. Then, C_p and C_1 share their charge. Assuming that C_1 has an initial charge of $Q_{1\text{-initial}}$, then, the total charge stored in the capacitors is:

$$Q_{tr} + Q_{1\text{-initial}} = (C_1 + C_p) \cdot V_1 \tag{4.11}$$

where V_1 is the voltage over the capacitors after they share their charge together. Therefore, the charge stored in C_1 after the charge sharing is:

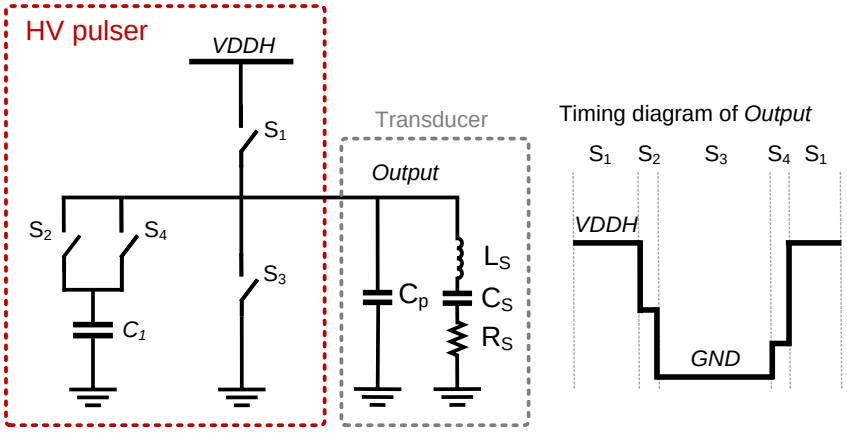

Fig. 4.14: System-level architecture of the proposed charge recycling technique using one storage capacitor.

$$Q_1 = C_1 \cdot V_1 = C_1 \cdot \frac{C_p \cdot VDDH + Q_{1\text{-initial}}}{C_1 + C_p} \tag{4.12}$$

And the energy stored in C_1 is:

$$E_1 = \frac{1}{2 \cdot C1} \cdot Q_1^2 = \frac{1}{2} \cdot \frac{(C_p \cdot VDDH + Q_{1\text{-initial}})^2}{C_1 + 2C_p + \frac{C_p^2}{C_1}} \tag{4.13}$$

In the third phase, S_3 discharges the residual charge of the US transducer to ground. Next, similar to the second phase, while other switches are open, S_4 connects the transducer and C_1 together, allowing C_1 to share its charge with C_p. Consequently, part of the charge over the transducer in the first phase is stored in C_1 before discharging it to ground; then, this charge is reused in the next phase of operation, allowing to reduce CV^2f power loss and, hence, improve the overall power efficiency.

To save power further, more storage capacitors can be added to the system. As shown in Fig. 4.15, two storage capacitors are utilized in parallel to the US transducer. In this structure, at first, S_1 charges the transducer to $VDDH$. In the next phase, S_{2-1} stores the charge of the transducer in C_1 while other switches are open. Then, the remaining charge of the transducer is shared with C_2 via S_{2-2}. Next, S_3 discharges the remaining charge of the transducer to ground. afterwards, S_{4-2} connects C_2 to the transducer, allowing C_2 to share its charge with the transducer. In the final step, S_{4-1} transfer the charge of C_1 to the US transducer. More charge can be recycled by adding more storage capacitors; however, it results in a more occupied area and switching loss. Therefore, the topology of two storage capacitors is chosen to gain the highest power efficiency at the cost of the lowest occupied area.

4.3.3. Transistor-Level Implementation

Conventional class D pulsers utilize HV transistors to deliver HV pulses to the US transducers. However, these HV transistors occupy a relatively large area, posing severe challenges in designing a power-efficient HV pulser for a high-frequency 2D phased array

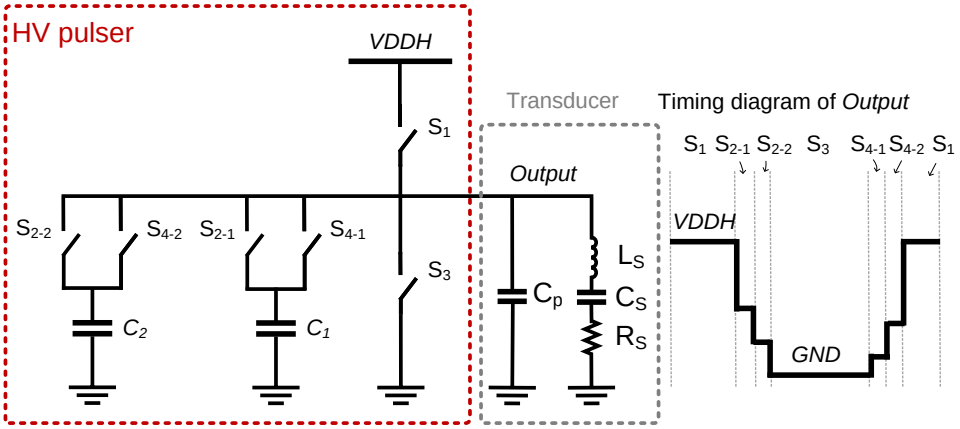

Fig. 4.15: System-level architecture of the proposed power-efficient HV pulser utilizing two parallel storage capacitors.

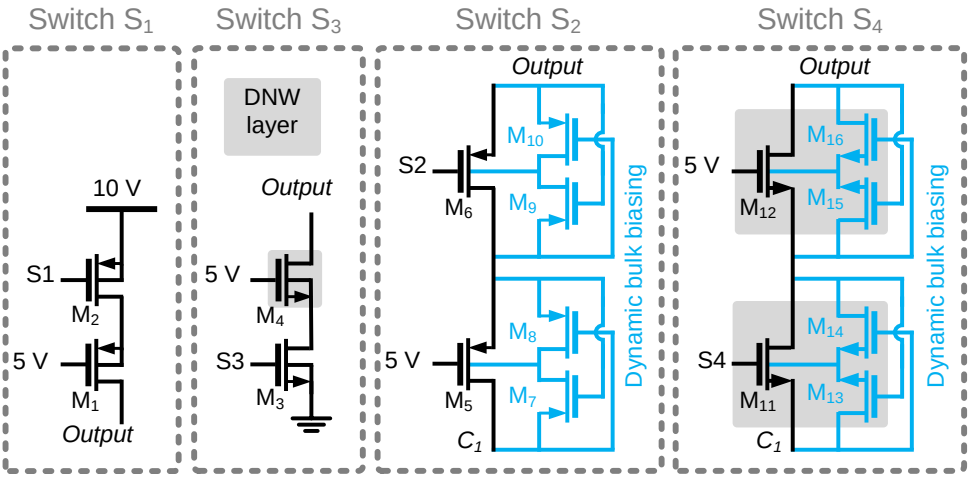

Fig. 4.16: Circuit diagram of HV switches for proposed the power-efficient pulser.

ASIC. Furthermore, they add large parasitic capacitance to the output node, which degrades the power efficiency. To overcome these problems, this work has utilized a stack of standard 5-V CMOS transistors to implement the HV switches required for the proposed power-efficient pulser. Considering the limited area per channel for a 2D US phased-array ASIC, the driving voltage of the proposed pulser was set to 10 V. In the proposed structure, Fig. 4.14, charging (i.e., S_1) and discharging (i.e., S_3) switches are connected to the output node and fixed power rails. Therefore, the polarity of the voltage over these switches does not change during the operation of the pulser. Thus, as depicted in Fig. 4.16, a stack of two PMOS transistors and two NMOS transistors are used to implement S_1 and S_3, respectively, ensuring that the V_{GS} and V_{DS} of these transistors never exceed 5 V. Since one terminal of these switches is applied to a fixed potential, the bulks of these transistors are connected to their source, requiring an NMOS transistor in Deep-NW. The charge recycling switches,

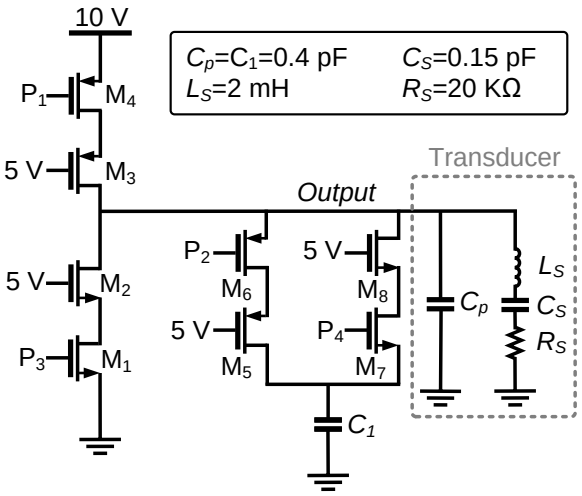

(a)

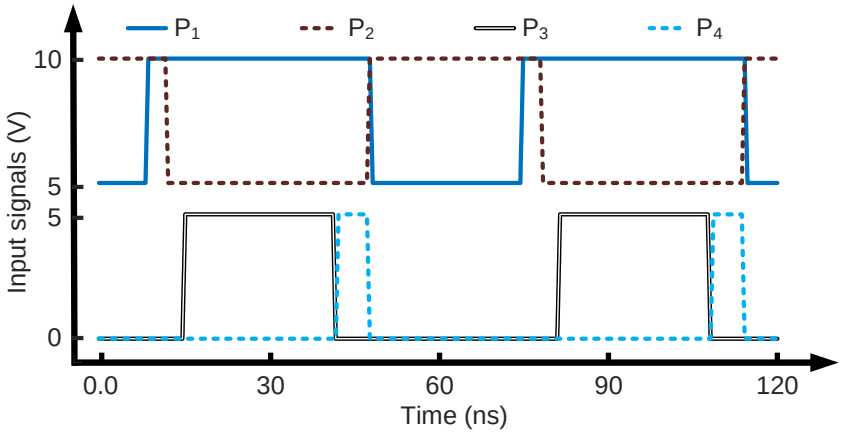

(b)

Fig. 4.17: (a) The schematic and (b) the timing diagram of the proposed HV pulser utilizing one-step charge recycling.

S_2 and S_4 in Fig. 4.14, are connected between two variable nodes. Therefore, the polarity of the voltage over these two switches changes during the operation of the pulser. The output node and the voltage over C_1 change from 0 to 10 V. Thus, to implement S_2, a stack of two PMOS transistors is utilized, as illustrated in Fig. 4.16. While M_5 is biased to a fixed potential of 5 V, M_6 turns on and off the switch controlled by a 5-10 V pulse. Similarly, as shown in Fig. 4.16, S_4 is implemented using a stack of two NMOS transistors, which is controlled by M_7 with a 0-5 V pulse. Although the bulk of NMOS and PMOS transistors must be connected to the lowest and highest potential over the drain-source of the transistor, respectively, the polarity fluctuation over the drain-source of the transistors in S_2 and S_4 may connect the bulk to an unsafe potential and leads to a large leakage current.

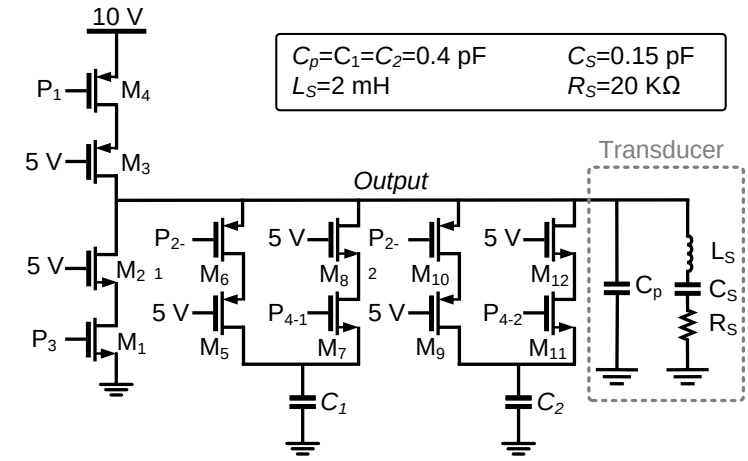

(a)

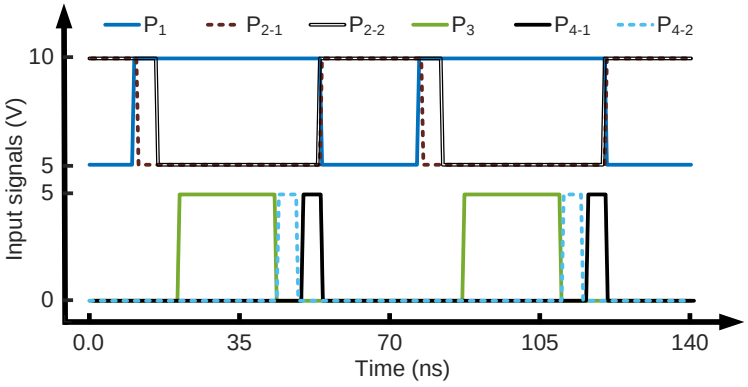

(b)

Fig. 4.18: (a) The schematic and (b) the timing diagram of the proposed two-step charge recycling HV pulser.

In this regard, as depicted in Fig. 4.16, dynamic bulk biasing is utilized to confirm that the bulk of the transistors is connected to a safe potential during low-to-high and high-to-low transitions.

The power-efficient one-step HV pulser, as illustrated in Fig. 4.14, is implemented utilizing the stacked switches, as depicted in Fig. 4.17(a). The bulk connection and deep-NW layer have not been shown to avoid complexity. The timing diagram of the proposed circuit is illustrated in Fig. 4.17(b), describing the principle of the operation. In the first phase, P_1 goes from 10 V to 5 V. As a result, M_4 charges the *Output* to 10 V. In the next phase, P_1 and P_2 change to 10 V and 5 V. Therefore, M_4 is off, and M_6 is on, discharging C_p to C_1. They share their charges until acquiring the same potential. Then, P_3 changes from 0 to 5 V; thus, the residual charge of the transducer is discharged to ground. While P_2 is still 5 V to ensure that V_{GS} of M_6 does not exceed 5 V, M_7 prevents discharging of C_1. Finally, P_4 goes to 5 V, allowing C_1 to share its charge with C_p. Consequently, the charge

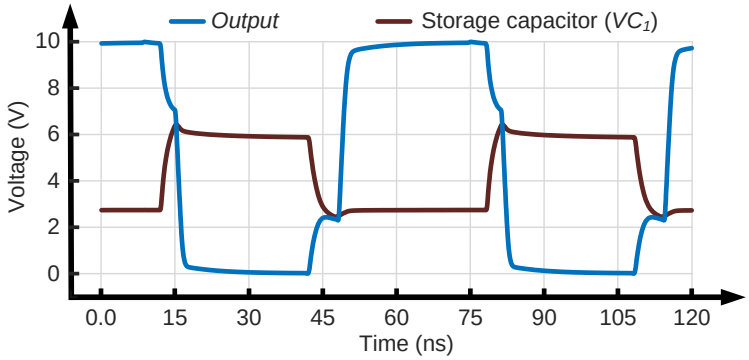

Fig. 4.19: Transient waveforms of the proposed one-step charge recycling pulser.

of the transducer is recycled for the next phase, resulting in a power-efficient pulser.

In order to improve the power efficiency further, the HV pulser in Fig. 4.15 is proposed, which allows recycling more charge using two parallel capacitors. Fig. 4.18(a) and Fig. 4.18(b) depict the circuit diagram of this HV pulser. Similar to the pulser in Fig. 4.17(a), M_4 charges $Output$ to 10 V in the first phase. Then, M_4 is turned off, and P_{2-1} turns on M_6, which transfers a portion of the transducer's charge to C_1. In the next phase, P_{2-2} turns on M_{10}, and the transducer shares its charge with C_2. By the end of these two phases, the remaining charge of the transducer is discharged to ground through M_1. Then, the charge over the transducers is transferred back to the transducer using M_{11} and M_7 in two consecutive phases of P_{4-2} and P_{4-1}. In the end, M_4 charges the transducer to 10 V in the next cycle.

Although conventional HV pulser requires one level shifter to turn on and off the HV PMOS, the proposed HV pulsers in Fig. 4.17(a) and Fig. 4.18(a) require two and three level shifters which may affect the power efficiency. To avoid excessive power consumption by the level shifters, this work has used low-power latch-based level shifters. Furthermore, beamforming channels with the same phase in a 2D phased-array ASIC can be applied to a shared level shifter, reducing the effect of the level shifter on the overall power efficiency.

4.3.4. Electrical Simulation Results

The proposed HV pulsers have been designed and simulated in TSMC 0.18-µm CMOS technology. To evaluate the functionality of the proposed circuit, four 15-MHz external clocks, as depicted in Fig. 4.17(b), were applied to the one-step charge recycling HV pulser. Fig. 4.19 shows the transient output waveforms and the voltage of the storage capacitor, revealing the recycling functionality of the proposed pulser. While the conventional HV pulser consumes 1.17 mW, the proposed one-step charge recycling HV pulser consumes 901 µW with the same driving voltage and load. As a result, the proposed HV pulser shows 29.8% power saving compared with the conventional HV pulser utilizing HV transistors. It is worth mentioning that the power saving of the proposed circuit compared with the conventional HV pulser using stacked architecture is 23.1%.

To validate the functionality of the proposed two-step charge recycling HV pulser, six 15-MHz external clocks were applied to the circuit, as depicted in Fig. 4.18(b). Fig. 4.20

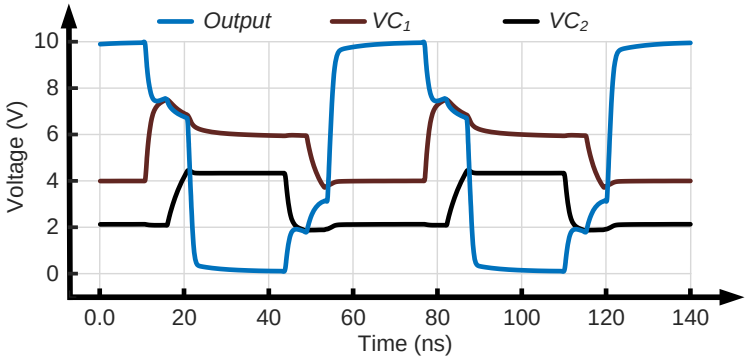

Fig. 4.20: Transient waveforms of the proposed two-step charge recycling pulser.

illustrates the voltage of the storage capacitors and the HV pulser's output waveform, verifying the proposed circuit's power-saving functionality. The voltage of the first storage capacitor, VC_1, changes between 4 V to 6 V, and the voltage of the second capacitor, VC_2, varies between 2 V to 4 V. In the first phase, the transducer is charged to 10 V. Then, the charge of the transducer is shared with C_1, resulting in a drop in the output voltage from 10 V to 7.5 V. In the next phase, the transducer's charge is shared with C_2, causing a voltage drop from 7.5 V to 6.5 V. After discharging the transducer to ground, the charge of C_2 and C_1 is shared with the transducer, which increases the transducer's voltage from 0 to 3.1 V in two consecutive phases. The proposed two-step charge recycling HV pulser consumes 830 µW of power, including the power consumed by the required level shifters. Therefore, the proposed HV pulser shows 40.9% and 33.6% power savings compared to the conventional HV pulsers using HV transistors and the stacked architecture.

Table 4.2 compares the proposed two-step charge recycling HV pulser with the state-of-the-art power-efficient HV pulsers. The proposed HV pulser operates at 15 MHz, the highest among other works, and delivers 10 V pulses to the piezoelectric transducers. The proposed two-step charge recycling HV pulser achieves 40.9% power reduction related to the conventional HV pulser, which is higher than the power reduction in [234] and [239]. The techniques presented in [233] and [235] provide better power reduction; however, they are not applicable to a 2D array of high-frequency piezoelectric transducers. In summary, to the best of the author's knowledge, the proposed US HV pulser constitutes the first power-efficient HV pulser that operates at 15 MHz and can be integrated with a 2D array of piezoelectric transducers, which highly empowers US neuromodulation and ultrasonic powering preclinical research.

4.3.5. Discussion

This work presents a high-frequency power-efficient HV pulser for US biomedical applications. The proposed pulser utilizes a per-channel two-step charge recycling method to reduce power consumption by 40.9% with respect to the conventional US HV pulser. The presented US HV pulser delivers 15-MHz pulses with an amplitude of 10 V to the US transducers. Unlike other works, this method can be applied to a high-frequency 2D array of piezoelectric transducers, resulting in better electroacoustic conversion efficiency

Table 4.2: Comparison of this work with state-of-the-art beamforming channels

	[233]	[234]	[235]	[239]	This work
CMOS process	0.18-μm HV	0.18-μm HV	0.18-μm HV	0.18-μm LV	0.18-μm LV
Frequency (MHz)	1	2.5	1	5	15
Driving Vpp (V)	30	30	27	13.2	10
Load	PZT	CMUT	PMUT	PMUT	PZT
Pulser type	charge recycling	multi-level	supply multiplier	charge recycling	charge recycling
Power reduction*	73.1%	38%	62.9%	32.8%	40.9%
Verification	measurement	measurement	measurement	measurement	simulation

*The power reduction is related to the power consumed by the conventional HV pulser.

and spatial resolution demanded by US neuromodulation and ultrasonic power transfer applications.

4.4. Conclusion

As beamforming channels have a crucial role in transmitter ASICs, this chapter focused on developing beamforming circuits. As discussed in Chapter 3, although increasing the frequency leads to higher G, and Vol_{res}, the pitch size should be reduced to avoid the appearance of grating lobes in the beam profile. Consequently, increasing the frequency reduces the available area to implement beamforming circuits, forming a tradeoff between the frequency and the available area for the beamforming channels. Since higher frequencies are desired, particularly for applications where higher spatial resolution is needed, this chapter developed low-area beamforming channels that can deliver 12-MHz 36-V pulses to the US transducers. Chapter 5 utilizes these beamforming channels to implement a high-frequency phased array transmitter ASIC.

Besides the frequency, the power consumption of the beamforming channels has a crucial impact on the overall power efficiency of the ASIC. In this regard, a power-efficient HV pulser is developed in Chapter 4, which leads to 40.9% power saving with respect to the conventional US HV pulser. This HV pulser allows for the implementation of power-efficient US transmitters, which are needed for wearable and implantable US neuromodulation applications.

5

Prototype Development for a 2D Phased Array Transmitter ASIC

5.1. Introduction

In recent years, new ultrasound biomedical applications have emerged, including ultrasound neuromodulation [41]–[45], [200], and ultrasonic power delivery medical implants [201]–[207], as visualized in Figure 5.1. As discussed in Chapter 2, these applications demand novel ultrasound transmitters capable of steering focused ultrasound waves in 3D with high spatial resolution and US pressure while having a miniaturized form factor. However, conventional US transmitters used in ultrasound neuromodulation and ultrasound powering utilize bulky, fixed-focus, single-element transducers that need complex mechanical translation to change the location of the focal spot [27], [216]. Furthermore, they are not applicable to wearable applications due to their large form factor and the need for bench-top electronic signal generators and power amplifiers. In order to overcome these limitations, researchers have been pursuing miniaturized and high-performing ultrasound transducers and interfacing electronics. In particular, the maximum level of integration and performance can be achieved by direct integration of 2D arrays of ultrasound transducers on top of pitch-matched high-voltage beamforming ASICs. In [53], a 2D beamformer chip integrated with a 2D array of CMUTs for wearable US neuromodulation was proposed. The choice of CMUT transducers demanded the design of a 60-V power amplifier per channel in order to achieve the necessary acoustic intensity for neuromodulation. The use of 60-V DMOS transistors drastically increases the area per channel, which limited the ultrasound frequency to 3.4 MHz. In addition, the large minimum sizes of 60-V DMOS transistors and their resultant parasitic capacitance, when compared

Parts of this chapter have been published in "A 2D Ultrasound Phased-Array Transmitter ASIC for High-Frequency US Stimulation and Powering," in *IEEE Trans. Biomed. Circuits Syst.,* June 2023 [46].

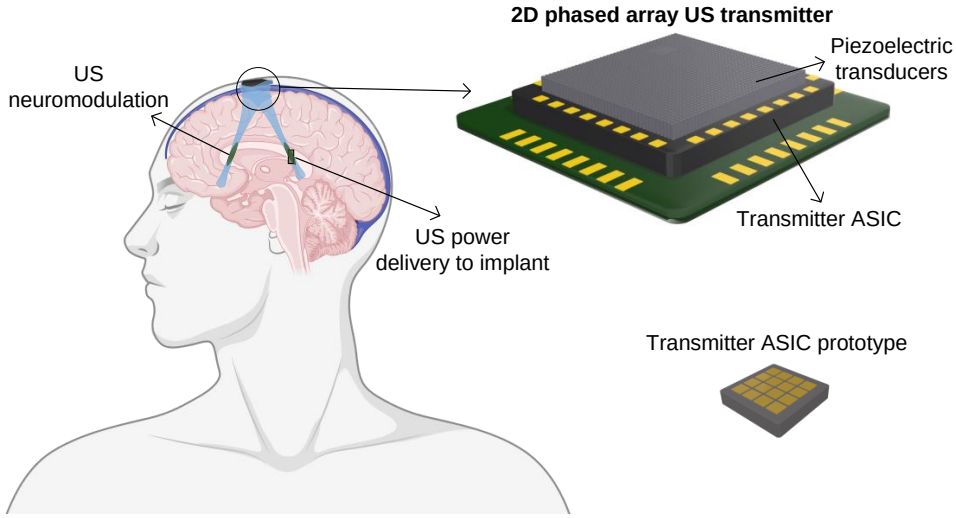

Fig. 5.1: A application of a 2D ultrasound phased array transmitter in performing US stimulation and ultrasonic power delivery to implanted devices.

with the CMUT impedance, resulted in an over-dimensioned power amplifier, hence increased power consumption. Finally, each channel included a digital beamforming circuit based on a custom finite-state machine (FSM) and counter approach. In order to achieve the necessary timing resolution for precise acoustic focusing, the proposed digital beamformer required a clocking frequency 16 times larger than the ultrasound frequency. This reduces the scalability of the ultrasound frequency towards high spatial resolution and further contributes to the increased power dissipation, which dominated over the 60-V driver for low duty cycle conditions. Overall, the high power consumption and the corresponding thermal dissipation drastically limit the pulse duration specifications for US stimulation. Another 2D phased-array ASIC integrated with piezoelectric transducers has been presented in [40]. This work proposed a split beamformer system, with a shared coarse beamformer implemented with a delay locked loop (DLL) and a fine beamformer per channel implemented with a phase interpolator, which allows for a higher frequency of operation without the large penalty of dynamic power consumption as previous work. However, as demonstrated in Chapter 3, the 6-bit beamformer is over-designed, which leads to an unnecessarily larger circuit area and power dissipation. Finally, the driver circuit utilizes 5-V transistors, which, despite the higher electroacoustic transmit efficiency of PZT in comparison with CMUTs [40], only lead to a focal pressure of 100 kPa, which is normally insufficient for ultrasound neuromodulation [26].

Despite recent efforts, the literature still lacks an ASIC matched with the abovementioned requirements of non-imaging US applications, where high spatial resolution, power efficiency, and high driving voltage are simultaneously achieved. The main challenge towards achieving high-frequency 2D US phased-array operation with high-voltage capabilities relates to the tradeoff between the reduced area of the pitch-matched ASIC beamforming channels and the large area required by high-voltage transistors. Chapter 3 presented a comprehensive system-level study on US phased-array transmitters to optimize

the phased-array US transmitters in terms of spatial resolution along with power efficiency and US intensity. Following the results of this study, we utilized the high-frequency beamforming channel in Chapter 4 to implement a 2D phased array transmitter ASIC to verify the findings of Chapter 3. As a result, a 12-MHz pitch matched 12×12 phased array ASIC working at 20-V amplitude, and 3-bit phasing was designed and experimentally validated to demonstrate high-frequency phased-array operation.

5.2. System-Level Design

As shown in Chapter 3, increasing the frequency is the most power-efficient way to improve G and Vol_{res} of the focal spot. Considering the available blades that can cut through the piezoelectric transducers, which corresponds to a minimum kerf size of 20 µm, it was demonstrated that increasing the frequency beyond 16 MHz does not enhance G and Vol_{res} significantly. On the other hand, in a 16-MHz pitch-matched 2D array, a blade size of 20 µm results in losing more than 75% of the active piezoelectric area, resulting in the decrease of US pressure at the focal spot. In this regard, the frequency of the 2D phased array transmitter ASIC is set to 12 MHz to achieve the highest Vol_{res} at the cost of 54% and 29% reduction in the active area of the piezoelectric transducers for a kerf size of 20 µm and 10 µm, respectively. Regarding the driving voltage, it has been demonstrated in Chapter 4 that in a pitch-matched 2D phased array, increasing the frequency reduces the available area to implement a beamforming channel. On the other hand, HV transistors with higher V_{ds} occupy a larger area, leading to a tradeoff between the frequency and the driving voltage. According to Chapter 4, 36-V HV transistors are the largest HV devices that can fit in a circuit area of 62.5×62.5 µm^2, corresponding to a frequency of 12 MHz. However, to meet the electrostatic discharge (ESD) requirements in the 2D array, the 36-V transistors are replaced with 20-V transistors to respect the needed distance between the HV beamforming channels. Consequently, the maximum driving voltage is set to 20 V. As discussed in Chapter 3, a phase quantization resolution of three bits is sufficient to perform precise US beam focusing and steering; thus, the ASIC should perform a 3-bit phase quantization. Regarding the size of the array, since the goal of this ASIC is to verify the findings of Chapter 3, the size of the 2D array is set to 750×750 µm^2, which corresponds to a 12×12 array of 12-MHz 20-V beamforming channels with an active area of 62.5×62.5 µm^2.

The 2D phased-array transmitter ASIC, as depicted in Fig. 5.2, involves a shared DTC, a clock buffer tree, and a 12×12 array of beamforming channels. The shared DTC transforms an external clock into delayed clocks with specific timing resolution. Then, a clock buffer tree distributes these clocks among beamforming channels that deliver 20 V to US transducers. Considering the small available circuit area in high-frequency phased arrays, the beamforming channels utilize the shared DTC to generate specific phases for every transducer element. In the layout of every beamforming channel, while most of the metal layers are utilized for internal routing, power distribution among the channels, and implementing the output pad, only a portion of metal 3 is available for distributing the output clocks of the shared DTC among the beamforming channels. Therefore, utilizing a 3-bit shared DTC leads to complicated routing challenges in the layout, in particular when scaling up the array size. In this regard, as shown in Fig. 5.3, the shared DTC is configured to generate four phased clocks corresponding to two LSBs while the MSB is implemented

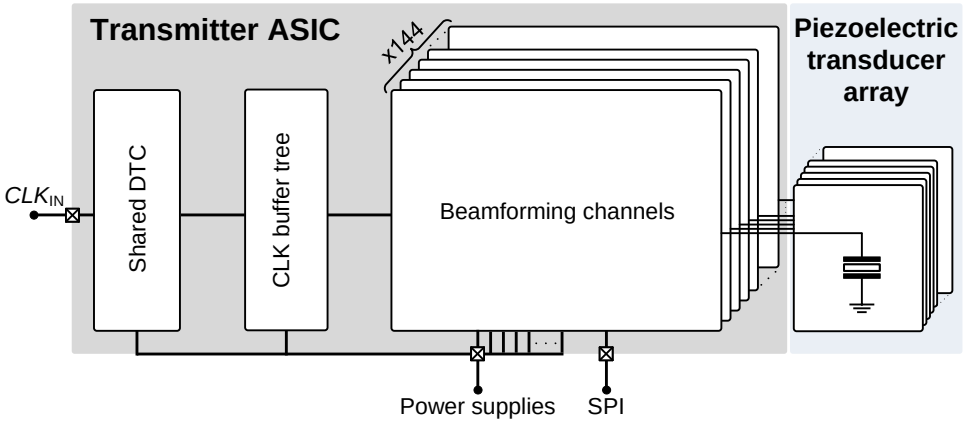

Fig. 5.2: System architecture of the transmitter ASIC showing the building block and the required external signals and power supplies.

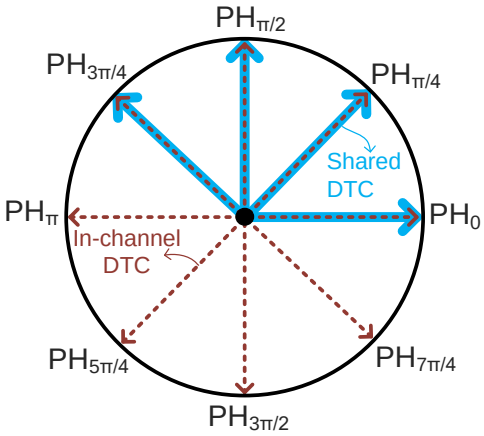

Fig. 5.3: Phasing diagram of the beamforming circuits. While the DTCs in the beamforming channels define the MSB, the shared DTC controls the phase corresponding to the two LSBs.

in the beamforming channels. Therefore, the 3-bit phase quantization is performed by utilizing a 2-bit shared DTC and a 1-bit in-channel DTC. The required clocks and power supplies for the ASIC are provided externally. The transmitter ASIC is compatible with the integration of a 12×12 array of piezoelectric transducers. To model the electrical behavior of the piezoelectric transducers during the design and simulation of the ASIC, the simplified BVD model for the 12-MHz 40×40 μm^2 PZT-5H transducer introduced in Chapter 4 is utilized. The simplified BVD model mimics the behavior of the PZT-5H transducer element at the resonance frequency, which includes a 20-kΩ resistor in parallel with a 400-fF capacitor.

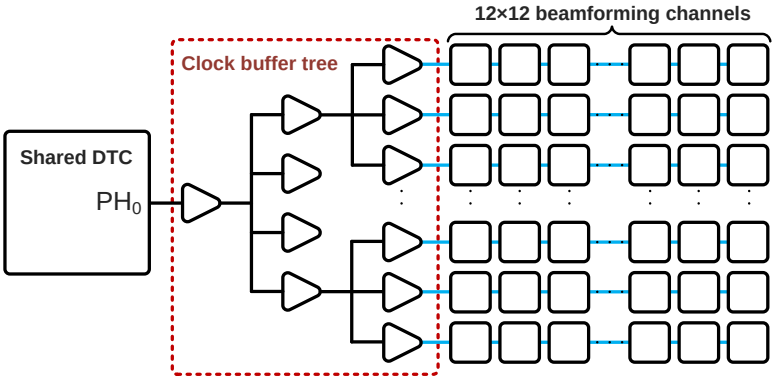

Fig. 5.4: The distribution of the phased clocks of the shared DTC among the beamforming channels utilizing the clock buffer tree.

5.3. Transistor-Level Implementation

In order to realize a 2D phased array transmitter ASIC, the system architecture in Fig. 5.2 is introduced, which can deliver HV phased pulses to the piezoelectric transducers. The shared DTC is the same shared DTC presented in Chapter 4 (Fig. 4.8). The shared DTC converts a 48-MHz clock to four 12-MHz clocks with a phasing resolution of $\pi/4$. Then, the clock buffer tree distributes these phased clocks among the beamforming channels. Since the shared DTC is connected to 144 beamforming channels, the clock buffer tree breaks down the fanouts of the shared DTC. The clock buffer tree allows the shared DTC to not only drive the large load caused by gates of the beamforming channels but also deliver the phased clocks to the beamforming channels with a low clock skew. As shown in Fig. 5.4, each row of beamforming channels is connected to a digital buffer, and then these buffers are connected to the shared DTC, ensuring that every row receives the phased clocks without any delay. It is worth mentioning that the last beamforming channel receives the buffered clocks with a given delay. However, taking into account the distance between the first and the last beamforming channel, this delay is ignorable compared with the timing resolution needed to perform 3-bit phasing.

The beamforming channels in the 2D array are based on the 36-V beamforming channel presented in Chapter 4. However, the 36-V transistors are replaced with 20-V transistors to respect the needed distance between the HV beamforming channels. Moreover, a non-overlapping clock generator is used to reduce the dynamic losses of the HV driver. The modified schematic is illustrated in Fig. 5.5. According to the data stored in the 3-bit shift register, which is related to the phase of the beamforming channel, the 4-1 multiplexer chooses one of the shared DTC clocks. Next, the 1-bit DTC performs the most significant phasing by adding a phase of 0 or π to the signal. Then, the dead time generator adds a time interval between the rising and falling edges of the signals driving the HV transistors. Since driving the HV transistors requires a pulse with an amplitude of 5 V, the 1.8-5 V level shifters, shown in Fig. 4.6, are utilized to translate the voltage levels of 1.8 V to 5 V. In the end, the HV driver delivers 12-MHz 20-V phased pulses to the piezoelectric transducers.

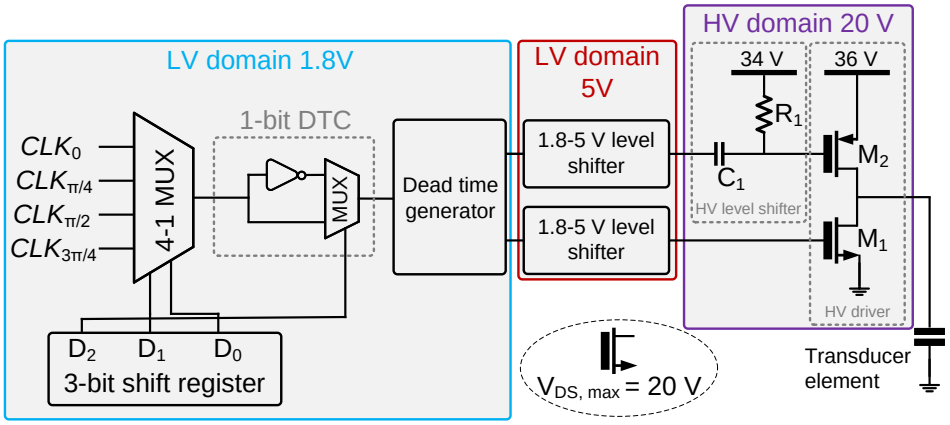

Fig. 5.5: The circuit diagram of the 12-MHz 20-V beamforming channel, which occupies an active area of 62.5×62.5 μm^2.

5

5.4. Measurement Results

The transmitter ASIC has been designed and fabricated in TSMC 0.18-µm BCD technology. The chip micrograph of the 2D phased array transmitter ASIC is shown in Fig. 5.6(a), occupying an active area of 900×1300 μm^2, including I/O pads. Fig. 5.6(b) shows the layout of the pitch-matched beamforming channel that occupies a silicon area of 62.5×62.5 μm^2. The area breakdown reveals that the HV transistors occupy 57% of the channel area, while the LV circuits and HV level shifter are accountable for 36% and 7% of the pixel area, respectively.

Delivering the required supply levels to the phased array transmitter involves several key steps. First of all, system-level power budgeting has been done to determine the overall current dissipation from every power supply level. Moreover, a large pad, VSS_TOP in Fig. 5.6(a), is considered to connect the top plates of the piezoelectric transducers to a common ground. Secondly, properly sized power lines are utilized to distribute the required voltage levels inside the chip according to the current budget for every row. Since the 20-V power supply drives the relatively large load of piezo transducers, the whole metal-five layer is used to distribute the 20-V level from two power pads across the channels. Off-chip components on the test board provide power conversion and regulate the required voltage levels. Since the gate and the source of the HV PMOS are connected to the 18-V and 20-V power supplies, improper power sequencing may damage the HV transistors. In this regard, the same type of low dropout regulators (LDOs) are used to regulate the required HV voltage levels from the same source. Moreover, the load difference between the 18-V and 20-V power supply is compensated in the test board to ensure the correct power sequencing during the start-up and shut-down cycle. In order to characterize the electrical functionality of the CMOS chip, the ASIC was wire bonded on a PCB. Then, the wire-bonded PCB was connected to a controller board, which includes the power management unit and a Spartan-7 FPGA development board (CMOD S7, Digilent). The measurement results presented here were obtained by supplying the chip with a 48-MHz input clock and by directly probing the output pads using a 12C picoprobe.

First, to validate the phasing configurability of the CMOS chip, a 48-MHz clock was ap-

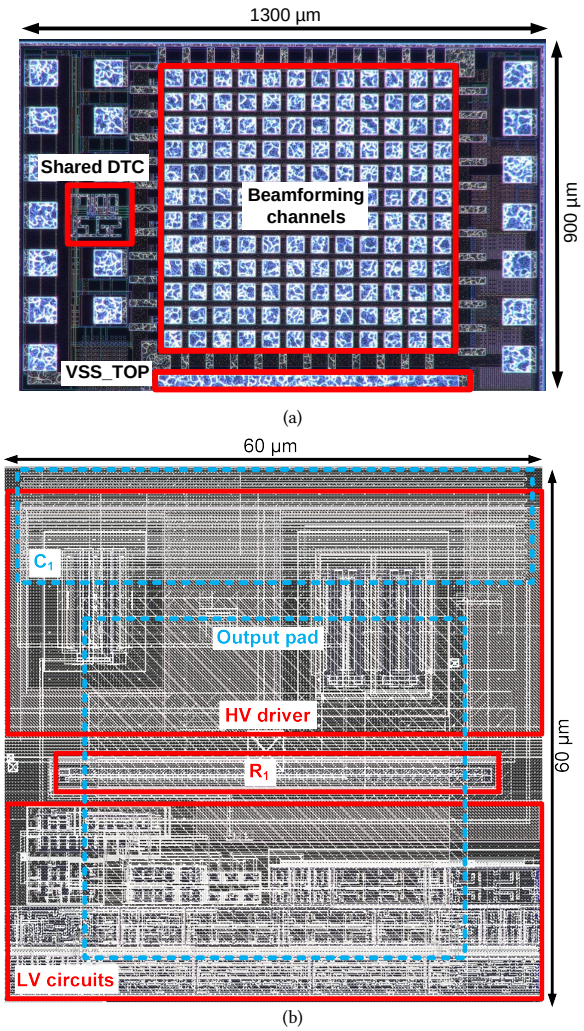

Fig. 5.6: (a) The micrograph of the CMOS chip with 12×12 beamforming channels. (b) The layout of a single beamforming channel.

plied to the ASIC. Then, the shift registers of the beamforming channels were programmed with random phases using the FPGA of the test board. Fig. 5.7 illustrates the output signals of the shared DTC, revealing the expected phases with negligible errors. The maximum measured jitter is around 500 ps, which is dominated by the accuracy of the measurement setup and the jitter of the input signal from the FPGA. However, this value is smaller than the required timing resolution of 10 ns. In the next step, the outputs of eight random beamforming channels with different programmed delays were measured. Fig. 5.8 depicts the transient measured outputs of the beamforming channels, showing that the phases of the outputs are aligned with their programmed phases. The delay transfer function of the measured beamforming channels is shown in Fig. 5.9, where each data point

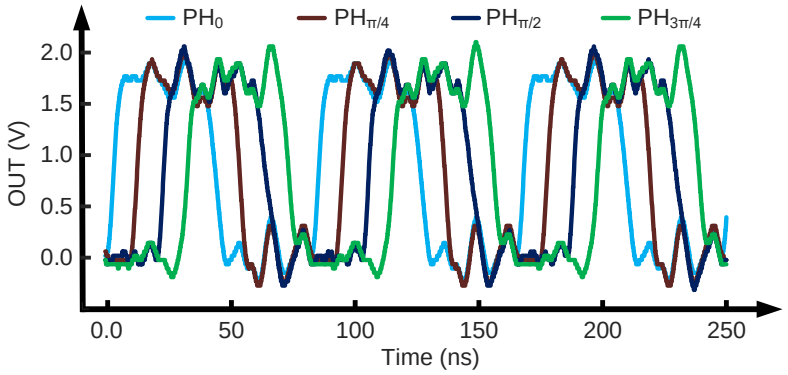

Fig. 5.7: The measured output waveforms of the shared DTC.

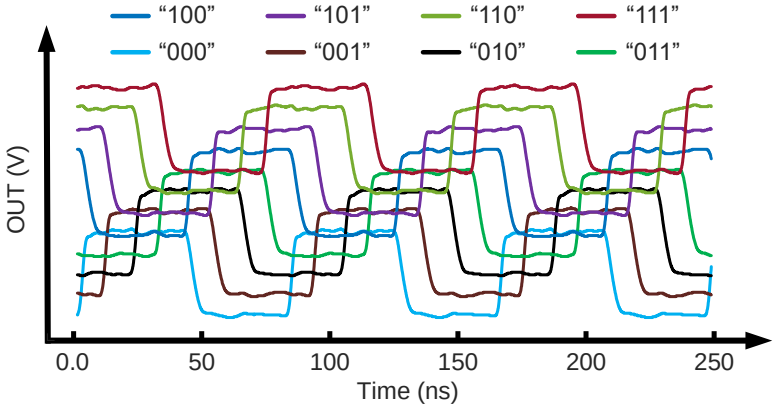

Fig. 5.8: The measured output waveforms of the beamforming channel for eight different delay configurations. It is worth mentioning that the amplitude of each pulse is 20 V.

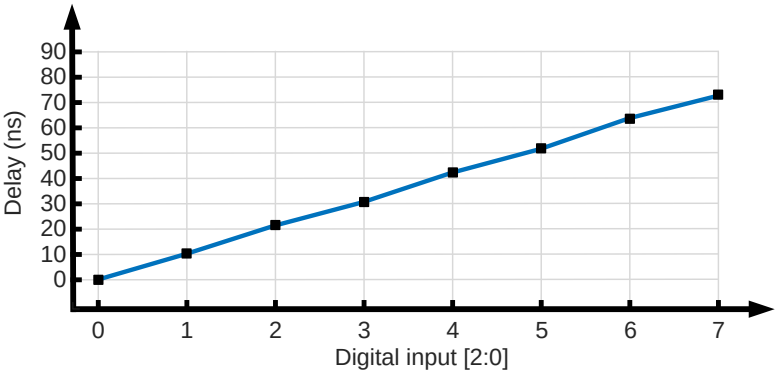

Fig. 5.9: The delay transfer function of eight randomly selected beamforming channels across the array, showing the linearity of the beamformer circuits.

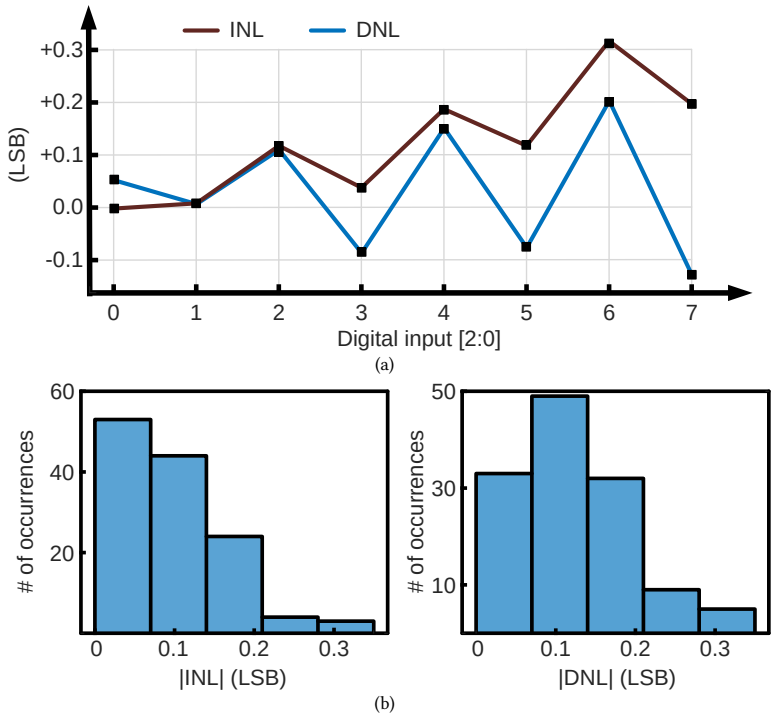

Fig. 5.10: (a) The measured INL and DNL for a beamformer channel in the center of the array. (b) The histograms of measured |INL| and |DNL| for 16 randomly selected beamforming channels from two different chips.

was obtained from a different channel, and the corresponding INL and DNL are shown in Fig. 5.10(a). Furthermore, the delay transfer functions of 16 random beamforming channels from two chips were measured to characterize the uniformity of phases across the beamforming channels. As depicted in Fig. 5.10(b), the maximum |INL| and |DNL| of the measured transfer functions of the beamforming channels are less than 0.35 LSB, which guarantees the monotonicity, with low variability between the two measured chips.

The beamforming channels were designed to drive US transducers with resonance frequencies up to 16 MHz. In this work, the pitch size is set to 62.5 µm, corresponding to a 12 MHz phased array without any grating lobes in the beam profile, where every beamforming channel drives its pitch-matched US transducer. An array of 2×2 beamforming channels driven with the same phase increases the real pitch size to 120 µm, meaning that the CMOS chip can drive an array of 6-MHz US transducers without any concerns about the grating lobes. The beamforming channels can be grouped more to increase the real pitch size further. Fig. 5.11 shows the measured outputs of a transmit channel with different center frequencies, confirming the proper phasing of the ASIC in different center frequencies.

Since changing the acoustic intensity at the focal spot demands varying levels of the HV power supply, the CMOS chip was powered with different supply levels. To perform this controllability, a bench-top programmable power management unit controlled the

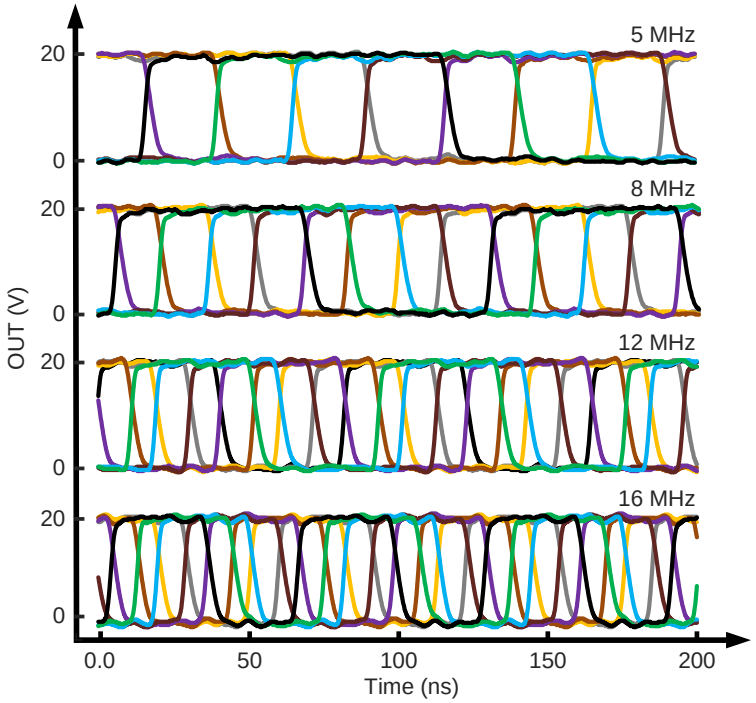

Fig. 5.11: Measured output waveforms of the beamforming channels for various working frequencies while performing 3-bit phasing.

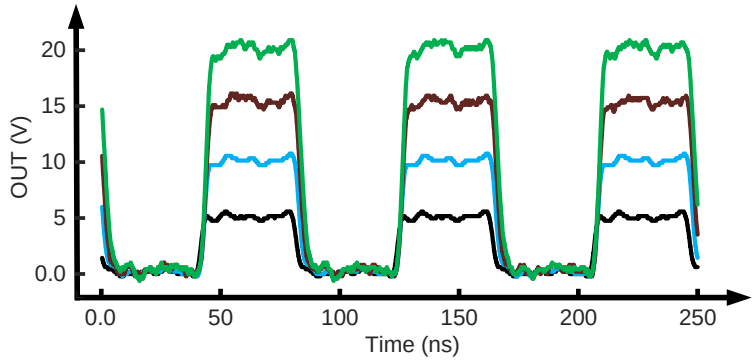

Fig. 5.12: Measured output waveforms of the beamformer channels for various power supply levels.

delivered voltage level to the beamforming channel. In this regard, the source of the HV PMOS and the top connection of the resistor in the HV level shifter are connected to the same potential. This may affect the driveability of the beamforming channels; however, the HV PMOS is over-designed to compensate for this situation. This can also be achieved by connecting both sources of the HV PMOS and the HV level shifter to different potentials at the cost of a more complicated power management unit. Fig. 5.12 reveals that the

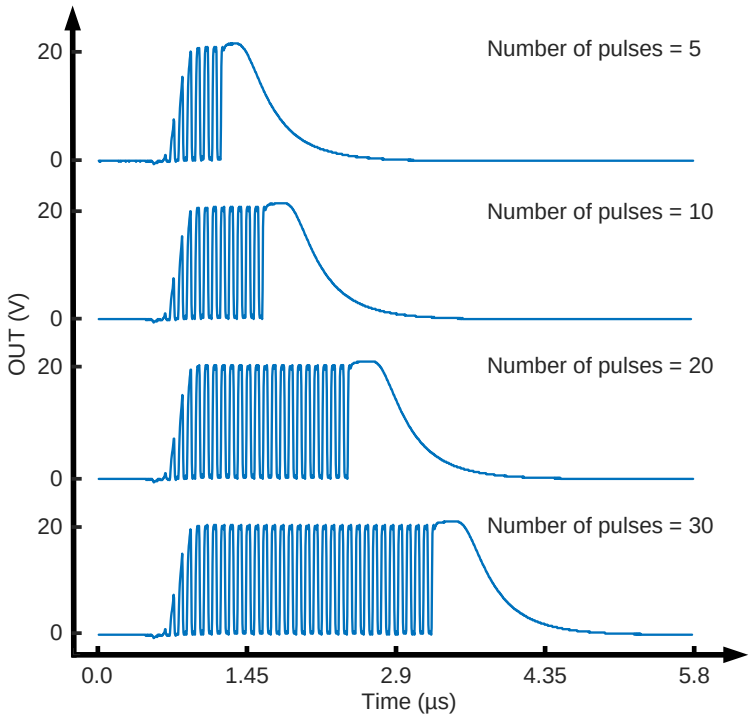

Fig. 5.13: Measured output waveforms of the beamformer channels while the pulse duration was controlled.

beamforming channels can generate pulses with variable driving levels from 5 V to 20 V. Furthermore, the ASIC needs to allow for precise duty cycling to control the pulse duration in ultrasound neuromodulation. Fig. 5.13 reveals the chip's ability to adjust the pulse duration of the driving signals by controlling the transmitted pulses to the course DTC through the test board. Even though only four different examples from 5 to 30 pulses are shown, the ASIC can operate with an arbitrary number of pulses.

To validate its beam-steering capability, the ASIC was programmed to generate driving signals corresponding to a focal spot at a depth of 2 mm and a steering angle of 0 in both azimuth and elevation planes. The output signals of the beamforming channels were measured for a time duration of 10 µs. Then, a k-Wave simulation was performed for a 12×12 array of 12 MHz acoustic source with a pitch size of 62.5 µm. Fig. 5.14 compares the beam profile when the measured signals are applied as the acoustic source with the beam profile simulated with ideal signals. There is a negligible difference between simulation and measured signals in terms of phased-array gain, *DOF*, and *FWHM*. It is worth mentioning that while sinusoidal waveforms have been utilized during the simulation, the measured pulses are squared pulses which have led to higher *G*.

Fig. 5.15 depicts the power consumption breakdown of the CMOS chip. First, the ASIC was driven by continuous pulses to measure the maximum power consumption of the blocks. In this case, the HV drivers, including only HV PMOS and HV NMOS, contribute to 44 percent of the total power consumption where no load was applied. This is

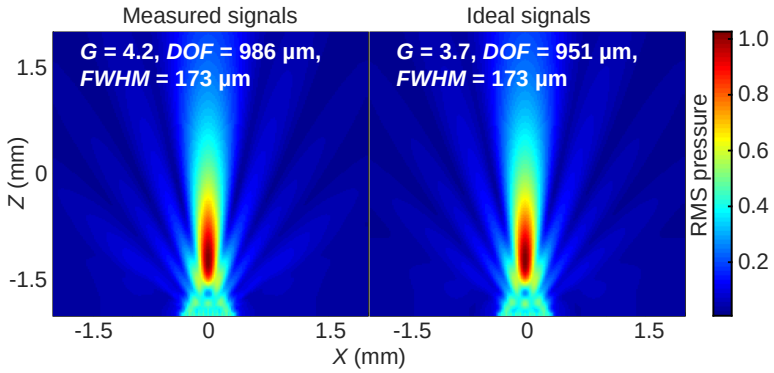

Fig. 5.14: K-Wave simulation results using the measured electrical signals as acoustic sources for a depth of 2 mm.

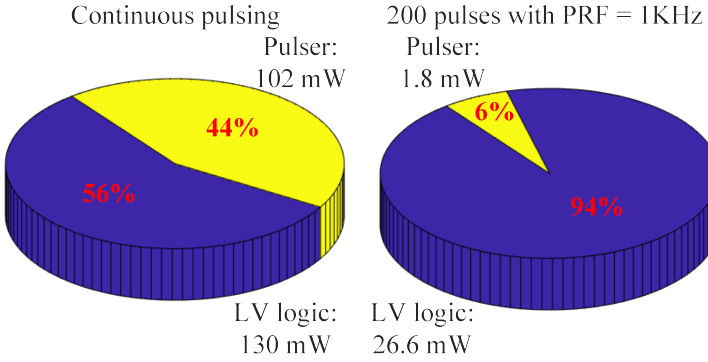

Fig. 5.15: Measured power consumption breakdown of the CMOS chip for continuous pulsing and 200-pulse bursts with PRF of 1 kHz.

mainly due to the large parasitic capacitance of HV transistors and the array pads. However, in US neuromodulation, a burst of continuous pulses with a given *PRF* is utilized. In this regard, 200 pulses with PRF of 1 kHz were applied to the ASIC. In this case, the LV circuits dominate the power as expected, and the total power consumption decreases to less than 30 mW. It is worth pointing that the 5-V, 18-V, and 20-V power supplies are only applied to the HV beamforming channels in the phased array transmitter, and the 1.8-V power supply is shared between the beamforming channels and the shared DTC. Comparing the size of the shared DTC with the beamforming circuitry clarifies that most of the power consumption from the 1.8-V power supply is rooted in the LV logic circuits of the beamforming channels.

5.5. Discussion

Table 5.1 shows the comparison between the proposed work and the state-of-the-art 2D phased-array US transmitters. In terms of the center frequency, this work operates at 12 MHz, the highest among all other works. Furthermore, the pitch size in the center frequency of 12 MHz respects the sound half-wavelength, unlike the others, which can lead to a high-resolution focal spot without any grating lobes in the beam profile, regardless

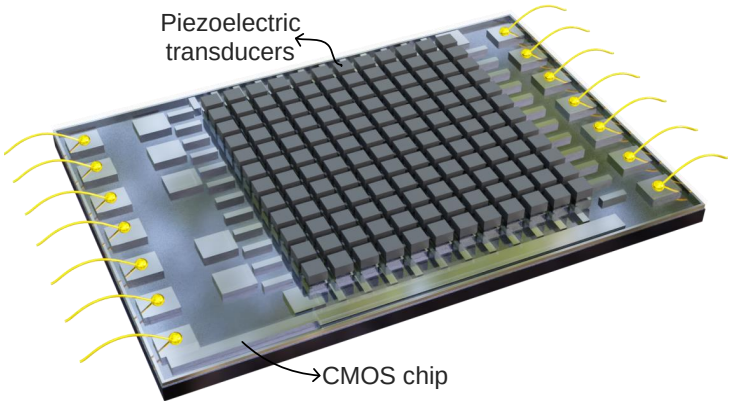

Fig. 5.16: Envisioned CMOS chip integrated with a 2D array of piezoelectric transducers.

of the steering angle in both the azimuth and elevation planes. Furthermore, the driving signals of the on-chip HV pulsers are four times larger when compared to [40], which only operates at 5 V with limited output intensity, and are lower than [53], which alleviates dynamic power consumption by the ASIC. Since no load is applied to the proposed ASIC, a circuit-level simulation has been done to investigate the effect of piezo load on power consumption.

As shown in Table 5.1, integrating the piezoelectric transducers with the CMOS chip will increase the dynamic power consumption; however, the power consumption is still lower than [53] because piezoelectric transducers require lower driving voltages than CMUT transducers. In addition, this work has shown that 3-bit phase quantization leads to sufficient focal pressure and spatial resolution while avoiding unnecessarily higher power-consuming and complex circuits [40], [53], and quantization lobes in the field of view.

In summary, to the best of the author's knowledge, this work constitutes the first 2D pitch-matched ultrasound phased-array transmitter operating at frequencies exceeding 10 MHz and driving voltages exceeding 5 V. By providing an unprecedented combination of spatial resolution, spatial configurability, and small size, this approach can highly empower ultrasound neuromodulation and ultrasound powering pre-clinical research with rodents, as well as potentiate high-precision sub-cranial cortical stimulation and peripheral nerve stimulation in large animal models and humans. Since this work is used for demonstrating high-frequency operation, the total size of the array is small, which limits the maximum penetration depth to less than 3 mm. This work will continue with the integration of the US transducers with the CMOS chip as illustrated in Fig. 5.16, for a larger array size towards deeper penetration depth and *in vivo* validation.

5.6. Conclusion

This chapter presents a 20-V 12×12 phased array transmitter ASIC, which can allow the implementation of a high spatial resolution and acoustic intensity US transmitter for non-imaging applications. The presented design methodology in Chapter 3 allowed us to define the beamforming ASIC's optimum frequency and phasing resolution. Considering the constraint on the fabrication procedure of piezoelectric transducers, the center frequency

was set to 12 MHz to achieve a fine spatial resolution and high-intensity focal spot. In addition, k-Wave simulation results showed that 3-bit phase quantization allows proper steering of the US beam without affecting the spatial resolution and US intensity at the focal spot.

The abovementioned system-level study guided the design of a 2D pitch-matched beamforming ASIC that generates 12-MHz pulses with 20-V amplitude. The ASIC consists of a shared DTC and pitch-matched 12×12 beamforming channels, where every channel occupies an area of 62.5×62.5 μm^2, corresponding to half of the ultrasound wavelength. The measurement results proved the functionality of the phased-array transmitter ASIC in terms of phase quantization, showing a maximum DNL of 0.35 LSB. In order to validate the beam-focusing capabilities of the ASIC, the output waveforms of the beamforming channels were applied to k-Wave, showing a precise focal spot on the determined depth. The CMOS chip allows changing the US intensity of the focal spot by driving the transducers with controllable voltage levels up to 20 V. Although the beamforming ASIC is designed for a center frequency of 12 MHz, it performs 3-bit phasing with various working frequencies. Hence, the integration of this beamforming ASIC with US transducers with different resonance frequencies is possible. This work can pave the way to wearable ultrasound transmitters for emerging non-imaging applications and is tailored for pre-clinical experiments and neuromodulation of superficial neuronal circuits in large animals and humans.

Table 5.1: Comparison of this work with state-of-the-art beamforming circuits.

	[243]	[244]	[144]	[53]	[40]	This work
Application	HIFU	Neuromodulation	Neuromodulation	Neuromodulation	Neuromodulation and US powering	Neuromodulation and US powering
CMOS process	HV Maxim technology	Discrete	Discrete	0.18-µm HV	0.18-µm LV	0.18-µm HV
Chip area (mm^2)	8×8	N/A	N/A	8×8	5×4	0.9×1.3
# of TX	1024-2D	256-2D	16-1D	1024-2D	676-2D	144-2D
Beam steering	Center focus	2D	1D	2D	2D	2D
Phasing resolution	N/A	N/A	N/A	4-bits	6-bits	3-bits
Driving Vpp (V)	60	27-external	100-external	60	5	20
Pitch (µm)	250 (0.84λ)	1100 (0.74λ)	1060 (0.58λ)	250 (0.57λ)	135 (0.91λ)	62.5 (0.5λ)
Frequency (MHz)	5	1	0.833	3.4	8.4	12
Power consumption per channel (mW)	N/A	N/A	N/A	254[a] (measured)	N/A	1.6[b] (measured) 10.9[c] (simulated)

[a]Calculated average power consumption in the continuous pulsing mode. The CMUT transducers are integrated with the CMOS chip.
[b]Average power consumption in the continuous pulsing mode while no load is applied to the CMOS chip.
[c]Calculated average power consumption in the continuous pulsing mode. During the circuit-level simulation, the piezoelectric transducers were modeled as a load of 0.4 pF // 20 KΩ, and applied to the beamforming channels.

6

US-Guided US Transmitter ASIC for Preclinical Studies

6.1. Introduction

In recent years, ultrasound neuromodulation has gained attention as a noninvasive and precise technique to modulate neural activity, which can potentially offer new treatments for a broad range of neurological disorders [26], [124]. However, despite the potential of US neuromodulation, technological challenges continue to hinder its application in both preclinical and clinical research, as well as in therapeutic solutions for patients [245]. Since the conventional transducers utilized in clinical research are bulky, only acute treatments during hospital visits are currently possible [47], [49]. Additionally, the bulky form factor of these transducers limits the clinical experiments to transcranial focused ultrasound stimulation, which suffers from low spatial resolution as it utilizes lower sonication frequencies to reduce the US attenuation in the skull. Therefore, as discussed in Chapter 2, novel US transducers compatible with US neuromodulation applications are needed to improve the effectiveness and reliability in clinical settings.

Regarding the preclinical studies on US neuromodulation, there is a technological gap that hinders the adoption of ultrasound therapy in clinical applications. Preclinical studies are crucial before initiating clinical trials to verify the safety and effectiveness of a new treatment or medication. These studies primarily involve conducting experiments on rodents, which are the most commonly used animal models for these purposes [246]. Preclinical experiments on rodents demand a miniaturized device that fits their small head size without disturbing the animal, thus enabling the conduction of behavioral experiments on freely moving animals (Fig. 6.1), which are vital for understanding the effects of US neuromodulation in several neurological disorders such as depression [247], chronic pain [248], and Parkinson's disease [249]. Moreover, considering the small size of the rodents' brains (2 cm^3 in rats and 0.5 cm^3 in mice [250]) in comparison with the human brain (1200

Parts of this chapter are based on a draft paper, "An US-guided 2D phased array US transducer for preclinical US neuromodulation studies," in preparation.

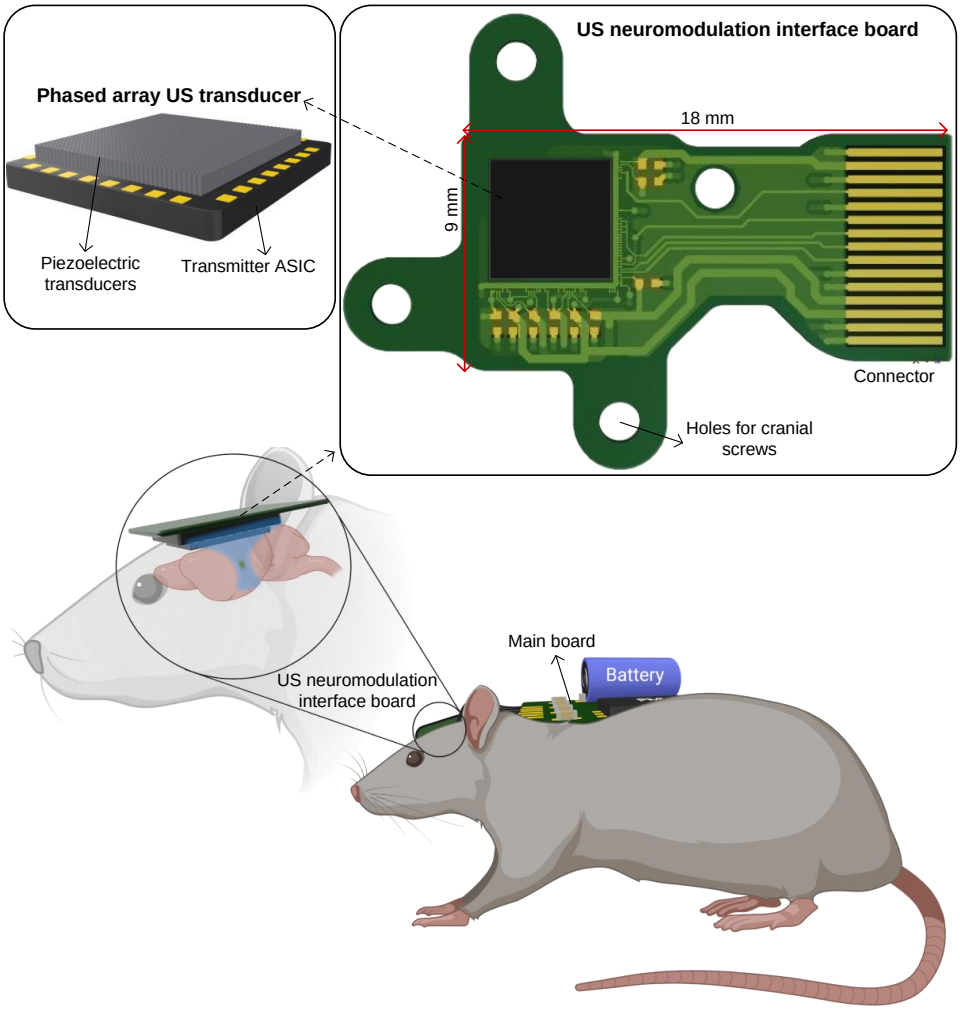

Fig. 6.1: Conceptual wearable US neuromodulation system for preclinical experiments on rodents, in this case rats. This chapter focuses on the development of the transmitter ASIC, which plays a crucial role in the phased array US transducer.

cm^3), the ultrasound beam should be focused on a much smaller volume in rodents than in humans, such that precise preclinical experiments can be conducted. Hence, preclinical experiments in rodents demand high-frequency US transducers capable of generating focal spots with high spatial resolution. even though literature suggests higher intensity thresholds for higher frequencies, scaling up the frequency to achieve higher spatial resolution in the context of experiments with rodents also offers other advantages towards increasing the focal intensity to meet potentially higher thresholds. Firstly, as seen in Chapter 3, the focal gain increases with frequency, leading to higher focal intensity, and secondly, the depth of the rodent's brain is much shallower than in humans, so acoustic ab-

sorption will have a much lesser effect in impeding higher focal intensity at the necessary focal depths in the range of 1-10 millimeters. Given the above, successful neuromodulation is also expected to happen at higher frequencies [26], with our solution offering a combination of high spatial resolution and high focal gain. Moreover, these transducers should enable US neuromodulation with configurable sonication parameters, such as duty cycle and pulse repetition frequency, as described in Chapter 2. This flexibility will allow neuroscientists to study how different sonication parameters affect the efficacy of US treatment [26]. Last but not least, accurate targeting of the correct brain region in the animal while avoiding disruption to its normal behavior necessitates electronic 3D beam steering to accurately adjust the focal spot's location. To the best of the author's knowledge, preclinical studies on ultrasound neuromodulation lack a proper ultrasound transducer that meets all the abovementioned requirements. The majority of ultrasound transducers described in the literature for preclinical studies are bulky, restricting experiments to head-fixed anesthetized animals [47], [48]. Therefore, these transducers not only compromise the precision of the experiment but also prevent conducting behavioral studies on freely moving animals. To address this limitation, researchers have developed wearable single-element ultrasound transducers specifically designed for preclinical research on rodents [49]–[52]. While these devices are compact enough for use on awake animals, they generate a fixed and broad focal spot that compromises the precision and reliability of neuromodulation experiments. An implantable US transmitter similar to the DBS electrodes with manufactured US transducers on the tip is introduced in [251]. Although this implantable US transmitter leads to a higher spatial resolution, it compromises the noninvasive nature of US neuromodulation, which is the main advantage of ultrasound over DBS. To enhance the resolution of the focal spot in a different way, an acoustic lens is added to the single-element ultrasound transducer [198]. However, these transducers lack the ability to steer the beam, which is essential for accurately targeting specific brain regions. Phased array transducers, which enable electronic beam steering, offer a solution to this issue. However, their application in preclinical studies is constrained by the complexity of their design, which involves numerous connections between the transducer array and the electronic pulser unit. This complexity increases the overall size of the ultrasound transducer setup, making it less suitable for use with small animals. One approach to simplifying connectivity is to reduce the number of transducer elements within the array by randomly removing some elements [42]. Nevertheless, this reduction will linearly decrease the generated acoustic intensity [199], hence potentially resulting in insufficient intensity for effective neuromodulation. To address these challenges, efforts have shifted towards integrating CMOS electronics directly with 2D piezoelectric transducers, aiming to create a more compact phased array ultrasound transducer [40]. However, the typically low operating voltage of standard CMOS chips restricts the achievable acoustic intensity. Alternatively, high-voltage CMOS chips have been developed alongside CMUT technology to reach the higher intensities required for effective neuromodulation [53]. However, the higher voltages necessary for CMUTs increase power consumption and generate excessive heat, posing a risk of tissue damage during preclinical experiments. Additionally, the low operational frequency of the US phased array proposed in [53] results in poor spatial resolution, while precise focal spots are essential for preclinical experiments on rodents. Another important aspect of US neuromodulation devices is the ability to

monitor the actual location and intensity of the focal spot for therapy guidance. This is particularly important in higher frequencies, where the size of the focal spot is reduced. Therefore, the location of the focal spot is prone to errors caused by the refraction due to the large blood vessels or the movement of the brain. In this context, although the above-mentioned US transmitters enable US neuromodulation experiments to be performed, they all lack monitoring capabilities. Therefore, accurate and reliable targeting in US neuromodulation demands real-time feedback on the location and the intensity at the focal spot. Current methods in monitoring the US focal spot primarily rely on magnetic resonance imaging (MRI) [252]–[254]. Although MRI-guided US neuromodulation is reliable, it requires costly MRI machines, demanding complicated US transducers that are compatible with magnetic fields, and, more importantly, impedes behavioral experiments from being conducted. Another approach to implementing real-time monitoring is using US imaging [54], [255]. Conventional B-mode US imaging only provides anatomical information but does not offer any insight into the location of the focal spot. However, several US imaging techniques, such as acoustic radiation force imaging (ARFI) [256], shear wave imaging [257], and harmonic motion imaging (HMI) [258], use radiation forces to generate local displacements within the tissue, which can be tracked using cross-correlation algorithms [259], allowing the monitoring of the focal spot's location. [54] and [260] have utilized commercially available US transducers to implement US-guided systems. However, these US transducers are bulky and do not fit the heads of rodents. In this context, as illustrated in Fig. 6.1, the objective of this work is to develop a US-guided US transmitter ASIC that can be integrated with piezoelectric transducers possessing a high electromechanical coupling coefficient. This chapter, therefore, describes a transmit ASIC with 66×66 array of transmit channels capable of delivering up to 12-MHz 20-V phased pulses to a 2D array of piezoelectric transducers while allowing for high frame rate US imaging to monitor the location of the focal spot. Although this US transmitter is designed particularly for preclinical US neuromodulation applications, it can be utilized on other applications such as US powering to implanted devices, where the beam steering and US imaging capability of the ASIC allow for correcting the misalignment between the transmitter and receiver [206].

6.2. System-Level Design

6.2.1. Neuromodulation Mode

According to the findings in Chapter 3, volumetric spatial resolution and phased array gain benefit from high ultrasound frequencies and large aperture sizes. As discussed in Section 5.2, the f_{US} has an optimal value of 12 MHz, enabling to obtain the highest G and Vol_{res} that is practically achievable using piezoelectric transducers. On the other hand, considering the tradeoff between the f_{US} and beamforming channel area, the driving voltage is set to 20 V to meet the ESD requirements in the 2D array (Section 5.2). While the optimum values are chosen for the f_{US} and driving voltage, increasing the aperture size allows for further improvement of volumetric spatial resolution and phased array gain. However, in the case of preclinical US neuromodulation on rats, the aperture size is limited by the maximum size of the craniotomy, which still allows for conducting behavioral experiments without disturbing the animal. Hence, a methodology to define the maximum aperture

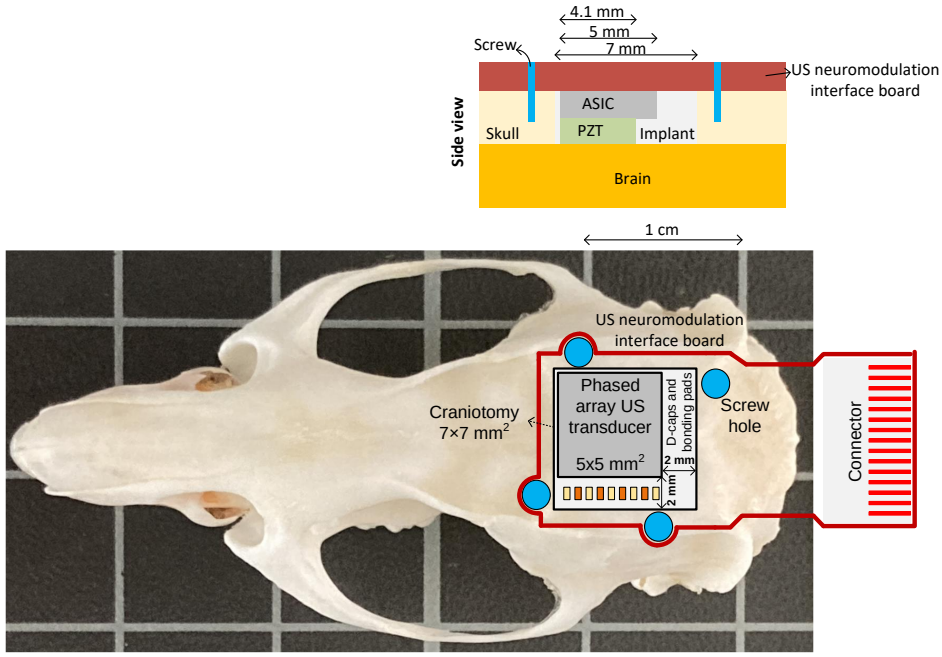

Fig. 6.2: The conceptual US neuromodulation interface board which fits on the head of an adult rat.

size, given these constraints, is needed for the field of preclinical US neuromodulation. To define the maximum aperture, the implantation procedure needs first to be analyzed in relation to the wearable US neuromodulation setup, which includes a main board and a US neuromodulation interface board, which are connected together through a flexible cable, as illustrated in Fig. 6.1. As depicted in Fig. 6.2, the US neuromodulation interface board consists of a connector and an implant, which includes the phased array US transducer, the decoupling capacitors, and bonding pads. In order to avoid the displacement of the US neuromodulation interface board on top of the rat's head, the board is fixed to the skull using screws and dental cement, which is a traditional procedure in fixing implantable devices to the brain of rodents in DBS studies [247]. Considering that the brain of an adult rat has a length, width, and thickness of approximately 21 mm, 16.1 mm, and 9.8 mm, respectively [219], and taking into account the area needed for fixing the screws, a craniotomy of 7×7 mm^2 is considered to place the implant on top of the brain. As shown in Fig. 6.2, a space of 2×7 mm^2 from the left and the bottom side of the implant is reserved for the decoupling capacitors and bonding pads. Therefore, an area of 5×5 mm^2 is available for implementation of the phased array US transducer, which consists of the transmitter ASIC and the 2D array of piezoelectric transducers directly integrated on top of the ASIC. Therefore, the available area for implementing the transmitter ASIC is set to 25 mm^2. According to the prototype ASIC developed in Chapter 5, 0.9 mm from the left and the bottom side of the ASIC is reserved for the power distribution among the transmit channels and implementation of the shared blocks. In this regard, a circuit area of 4.1×4.1 mm^2

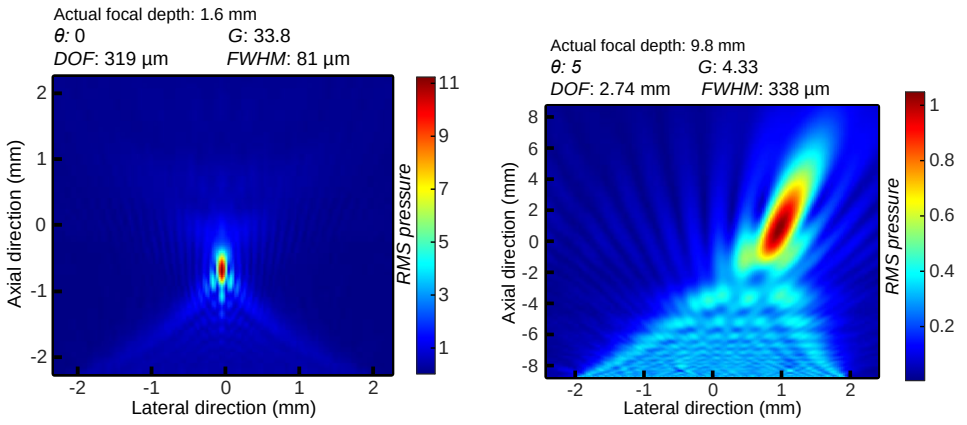

(a) (b)

Fig. 6.3: The beam profile for a 66×66 array of 12-MHz US transducers generated by the k-Wave toolbox. The US focal spot is focused on depths of (a) 1.6 mm and (b) 9.8 mm, representing the maximum depth of the rat's brain.

is available for implementing the 2D array of transmit channels. Hence, considering an active area of 62.5×62.5 µm^2 needed for implementing a 12-MHz 20-V transmit channel (Chapter 5), a 66×66 array of transmit channels fits in the available area. As depicted in Fig. 6.3(a), the k-Wave simulations for this 2D array show that the array generates a focal spot with a high focal spot gain of 33.8 and fine volumetric resolution of 0.001 mm^3 for a focal depth of 1.6 mm. Furthermore, as depicted in Fig. 6.3(b), the simulation results prove that the array is sufficiently large to achieve a phased array gain of 4.33 at the maximum depth of the rat's brain, i.e., 9.8 mm, while performing beam steering with an angle of 5°, verifying the compatibility of the 2D array with deep brain US neuromodulation within the rat brain.

Another important consideration in the system-level design is the power dissipated by the transmitter ASIC, which plays a critical role in defining the properties of the phased array as it may lead to excessive heat and cause damage to the brain of the animal. Furthermore, in order to avoid complexity in the design of the PMU and relax the peak current specifications for battery-powered operation, a current profile in which the average current is close to the peak transient current is more desirable. Although Chapter 3 showed that 3-bit phase quantization resolution is enough for precise beam steering, as piezoelectric transducers dissipate a high current during the pulse transitions, lower phasing resolutions result in driving a larger group of piezoelectric transducers with the same phase, as shown in Fig. 6.4. Consequently, lower phase quantization resolutions lead to a higher difference between the peak current and the average current and, hence, a more complicated PMU and more stringent specifications for the battery. In order to study the influence of the phase quantization resolution on the current profile, electrical simulations for two 66×66 arrays of HV drivers have been conducted. While both arrays are similar, they are configured for two different phase quantization resolutions of 3 and 4 bits. As shown in Fig. 6.4, the number of elements with the same phase in the array is approximately the same for all phase configurations. In this regard, to simplify the simulation of the large array, all the elements across the 66×66 arrays were equally divided into 8 and 16 groups,

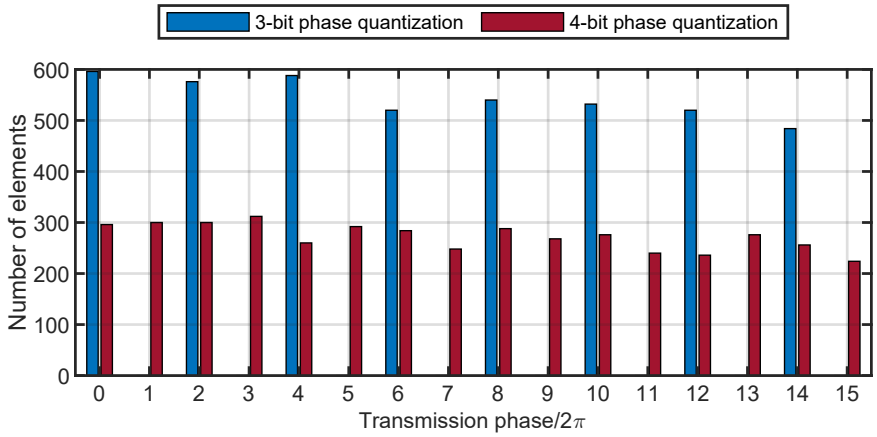

Fig. 6.4: The influence of phase quantization resolution on the number of elements in the 2D array driven with the same phase. The data of this graph is achieved from a 12-MHz 66×66 array of US transducers focused at a depth of 5 mm from the surface of the transducer, while the phase quantization resolution is swept from 3 to 4 bits.

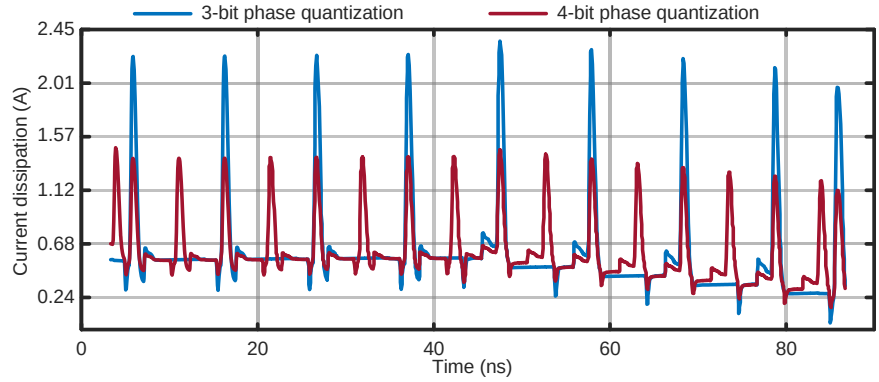

Fig. 6.5: The current dissipated by a 20-V supply powered to a 66×66 array of transmit channels while performing 3-bit and 4-bit phase quantitation. This graph is achieved by electrical simulation of the HV drivers when they are equally divided among all possible phases. During the simulations, the BVD model for a 12-MHz PZT-5H, which was introduced in Section 4.2, is utilized.

corresponding to the phase quantization resolution of 3 and 4 bits, respectively. All the elements in each group are driven with the same phase. The dissipated current from the 20-V supply is shown in Fig. 6.5, showing that increasing the phase quantization resolution from 3 bits to 4 bits reduces the peak current from the 20-V power supply by a factor of approximately two. Although increasing the phase quantization resolution reduces the peak transient current further, it comes at the cost of more complicated transmit channels and, hence, higher power consumption by the LV circuits. In this regard, the phase quantization resolution is set to four bits to reduce the gap between the peak and the average currents of the ASIC. Although the fourth bit does not affect the beam steering capability, it leads to a more relaxed current specification for the battery.

6.2.2. Imaging Mode

As discussed in Section 6.1, advanced ultrasound imaging techniques such as acoustic radiation force imaging and shear wave imaging allow for monitoring the displacement caused by an ultrasound push, enabling the ultrasound neuromodulation device to monitor the location of the focal spot. Acoustic Radiation Force Imaging and shear wave imaging are advanced ultrasound imaging techniques that leverage the concept of acoustic radiation force to evaluate the mechanical properties of tissues, particularly their stiffness or elasticity [261]. In this Imaging technique, first, a focused ultrasound beam produces a localized "push" or acoustic radiation force, leading to the transient displacement of the tissue. Then, the ultrasound system uses high-frame-rate imaging to detect the displacement or the shear waves [262], [263]. In order to meet the requirement of high-frame-rate imaging, planar wave transmission can be utilized for tracking the displacement caused by the push signal [54]. There are several works in the literature that have utilized US imaging to detect the tissue displacement caused by an ultrasound push [54], [257]. To monitor the tissue displacement caused by the US neuromodulation push, [54] have utilized two US probes with different US frequencies for US imaging and US neuromodulation. Although this method allows for real-time monitoring of the focal spot during ultrasound neuromodulation, utilizing two large probes with different frequencies restricts the adoption of this technique for wearable applications. The work presented in [257] has utilized a single US transducer for both transmission and tracking of the displacement in the tissue. While [257] has used this method for tissue elasticity mapping, this method also allows for tracking of tissue displacement during ultrasound neuromodulation. Moreover, this method is more suitable for wearable applications as it utilizes a single transducer for ultrasound transmission and reception. In this work, we are going to perform the US imaging after sending the US neuromodulation pulse. As a result, this work utilizes the same frequency for US imaging and neuromodulation, avoiding the complicated integration of piezoelectric transducers with different resonance frequencies on the ASIC substrate. Still, designing an ASIC to operate at 12 MHz featuring both imaging and neuromodulation modes presents several challenges. On one hand, US neuromodulation ideally requires full aperture and pitch-matched transmission capabilities to maximize the focal gain; on the other hand, US imaging ideally requires full aperture pitch-matched receiving capabilities to maximize the SNR. However, combining both ideal scenarios in the same chip poses several challenges. [185] has designed a full-aperture pitch-matched 2D beamforming circuit, where each pixel includes both receiving and transmit functionality, as shown in Fig. 6.6(a). This work, however, can only operate up to a frequency of 6 MHz while keeping the required pitch between channels half of the ultrasound wavelength. At 12 MHz compared to 6 MHz, only one-quarter of the area is available for the pixel circuitry which poses severe limitations to this approach at increasing frequencies. Therefore, for a frequency of 12 MHz, the required circuits for both transmission and imaging cannot fit within the limited area restricted by the pitch-matched approach. In order to overcome this problem, we can allocate some elements in the 2D array for only transmission or reception, as depicted in Fig. 6.6. The RX elements can be distributed with a given pattern among the transmit channels (Fig. 6.6(b)). However, this approach leads to large side lobes in the beam profile [264]. Alternatively, the receiver channels can also be placed around the transmit channels, as illustrated in Fig. 6.6(c). However, considering the small pixel

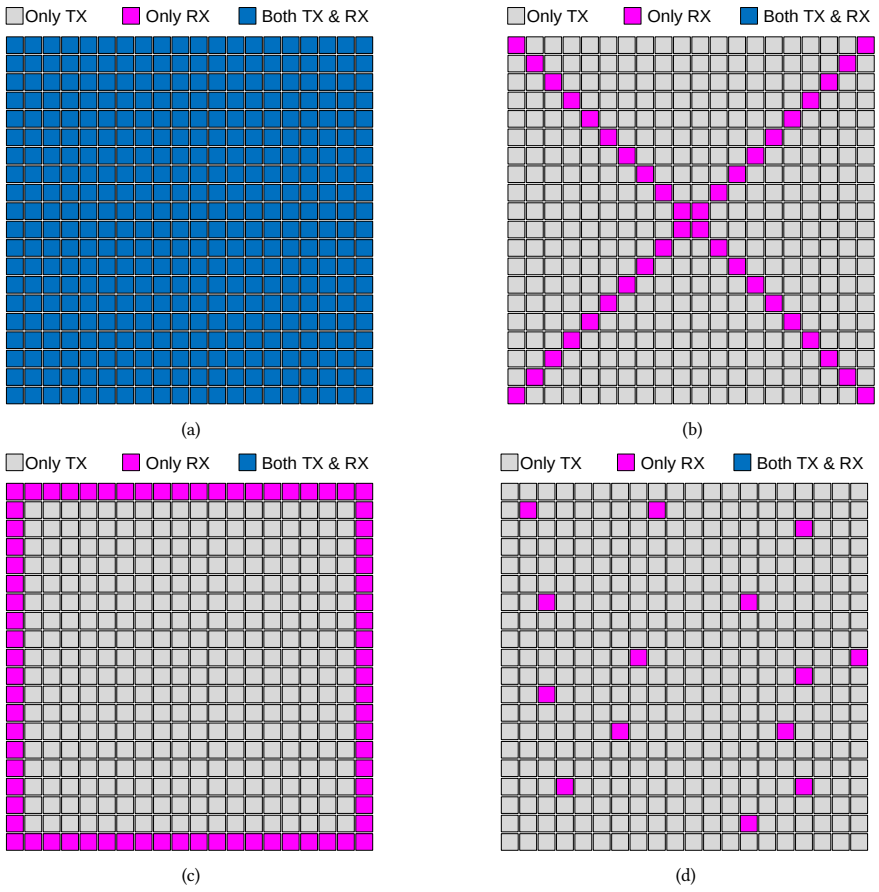

Fig. 6.6: The possible patterns for implementing a 2D transmit and receiver array; (a) full aperture Tx-RX array, (b) RX elements are placed diagonally, (c) RX elements are placed at the edge of the 2D array, and (d) RX elements are distributed randomly across the 2D array.

area at 12 MHz and the large area needed for implementing the RX circuits, this approach leads to removing a high number of transmitters, which may affect the focal gain. Given the above-mentioned challenges in implementing a single chip featuring both US imaging and US neuromodulation capabilities at a frequency as high as 12 MHz, this work proposes a method by which sparse RX elements are embedded within a full aperture TX array, as depicted in Fig. 6.6(d). This way, full TX aperture is slightly sacrificed to make space for RX channels. Furthermore, by making the imaging array sparse, RX elements are randomly distributed, and with a considerably smaller number of RX elements in comparison with the TX array, the TX beamforming capabilities for US neuromodulation are expected to be maintained while still allowing a US imaging array to be designed in the same chip. However, since frequencies of 12 MHz impose a maximum area per channel of $62.5 \times 62.5\ \mu^2$, designing a full imaging front-end with digital output has yet to be achieved [185]. Hence, while still preserving the properties above, we performed a study to investigate the transmit beam profile by removing groups of N transmit channels instead

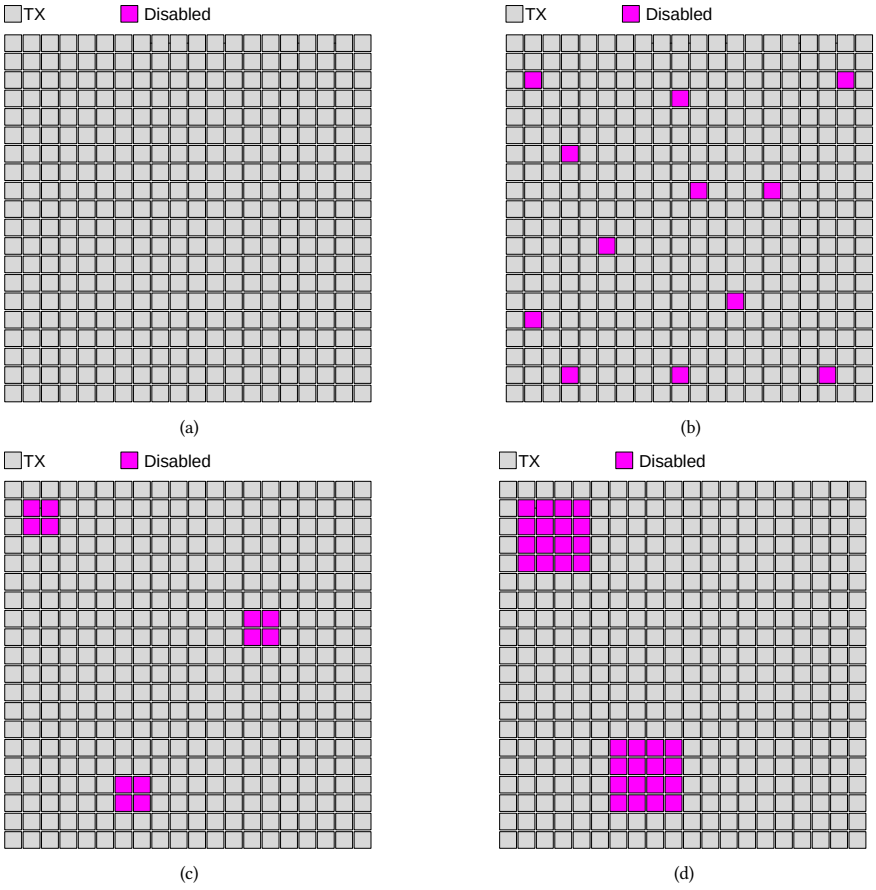

Fig. 6.7: The examples of the utilized patterns during the k-wave simulation. Although the simulations have been run for a 66×66 array, here, a 20×20 array is shown for simplicity. (a) No TX element is disabled. (b) 3% of TX elements with a group of 1×1 are disabled. (c) 3% of TX elements in a group of 2×2 are disabled. (d) 9% of TX elements in a group of 4×4 are disabled.

of a single channel, thus largely relaxing the area requirements for a full RX front-end. Initially studied in [199], this work uses k-wave to expand on the prior simulations by investigating the effect of removing a group of N transmit channels on the phased array gain. In this regard, a 66×66 array of 12-MHz transmit elements is created in the k-Wave toolbox. Then, the influence of allocating a TX element for RX is investigated by disabling that element during the transmit simulations. In each simulation, a sub-set of the transmit channels from 0% to 9% of the total elements in the 2D array with a step size of 3% are removed. In other words, in order to investigate the effect of the number of removed elements on the focal gain, four different percentages of elements are removed, i.e., 0%, 3%, 6%, and 9%. Then, as depicted in Fig. 6.7, in each step, the removed transmit channels are grouped into sub-arrays with different sizes of 1×1, 2×2, 4×4, 6×6, and 8×8, leading to 16 different configurations during the simulations. Fig. 6.8 shows the normalized pressure at the focal spot with respect to the pressure at the surface of the transducer. In agreement

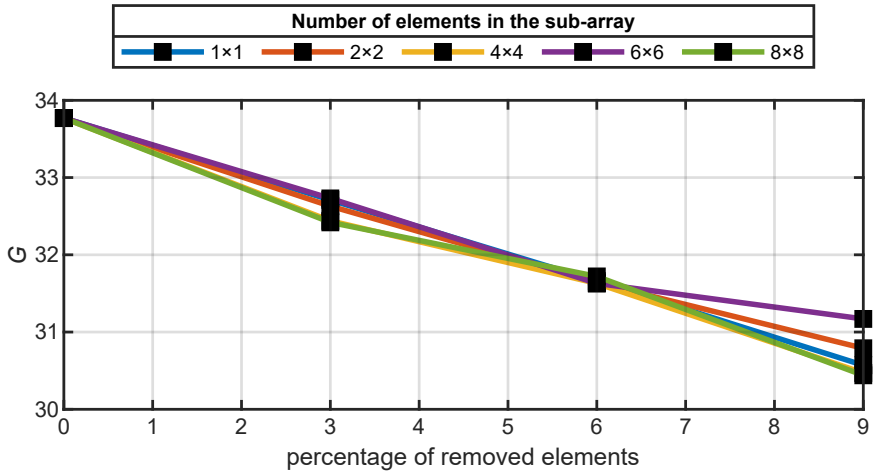

Fig. 6.8: The effect of removing a group of transmitters in the 2D array on the focal spot gain. 66×66 array of 12-MHz elements are utilized to perform these k-Wave simulations, while the focal spot is set to 2 mm away from the surface of the transducer.

with previous findings, the phased array gain drops linearly with the number of removed elements; however, given the low number of TX removed, the effect on the focal gain is acceptable. As a consequence, it can be concluded that a group of transmit elements can be removed to make enough space for implementing the receiving channels with relaxed area requirements. In order to ensure that the transducer is capable of generating a sufficient level of US pressure required for US neuromodulation, while most of the channels in the 2D array are transmitters, 3% of the elements in the 2D array were allocated to receiver channels, which counts for 128 receiver channels. Considering the area needed to implement fronted circuits for the receiver, every 16 disabled TX elements are grouped in a configuration of 4×4 sub-array to form enough area for implementing a receiver group. Each receiver group will be connected to 12 piezoelectric elements on top of the ASIC. In addition, 4 pads are left unconnected in each group, generating enough area in each receiver group, which will be justified in Section 6.4. As shown in Fig. 6.9, eight receiver groups are randomly distributed in the 2D array, which are connected to 96 piezoelectric transducers to receive the echoes.

After the integration with piezoelectric transducers, the ASIC will be connected to 4228 TX piezoelectric transducer elements and 96 RX piezoelectric transducer elements. The operation of the ASIC includes two phases: the neuromodulation phase and the imaging phase, as depicted in Fig. 6.10. In the neuromodulation phase, the TX elements transmit phased ultrasound pulses to form focused and steerable focal spots to perform precise ultrasound neuromodulation. During the imaging mode, the ASIC allows for synthetic aperture imaging, in which ultrasound pulses are transmitted using one or multiple transmit elements, and the echoes are received by one or multiple RX elements at a time, separately from each RX in each group, allowing for synthetic aperture imaging. Although the ASIC allows for compound planar wave and phased transmission from one or multiple elements with an arbitrary pattern, in this work, we aim for compound planar wave transmission from all TX elements to maximize the frame rate. After the transmission of

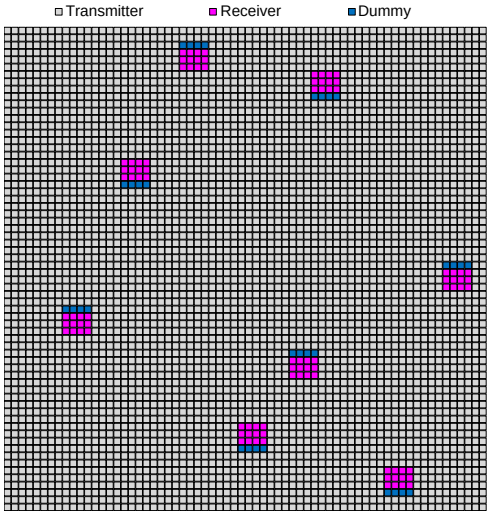

Fig. 6.9: Configuration of transmit and receive channels in the 2D array with 66×66 elements.

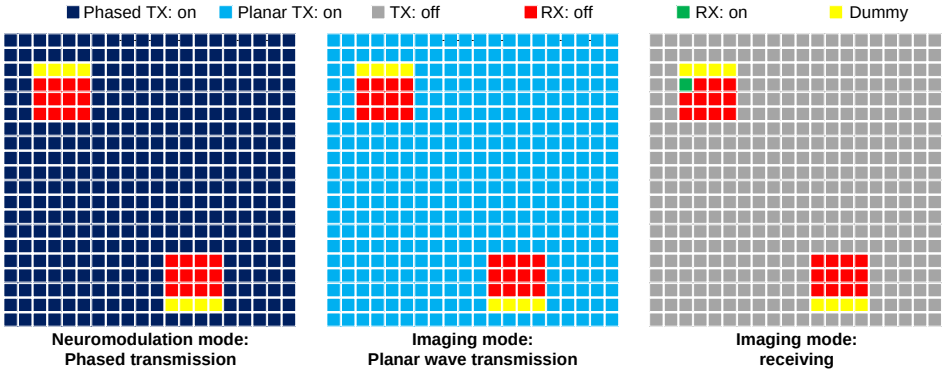

Fig. 6.10: The working principle of the ASIC, which includes phased wave transmission for US neuromodulation, planar wave transmission for imaging, and receivers to record the resulted echoes. Although the ASIC includes a 66×66 array with 8 groups of receivers, a 20×20 array with two groups of receivers is shown in this figure for simplicity.

the planar waves, the ASIC allows for either recording the echo from one RX element or from 16 elements at the same time. In this regard, considering full TX transmission with 5 compound planar waves through all TX elements and receiving the echoes from 96 RX elements in 6 successive steps, the ASIC can achieve a maximum imaging frame rate of 2500 fps; however, utilizing the conventional planar wave transmission may increases the frame rate further.

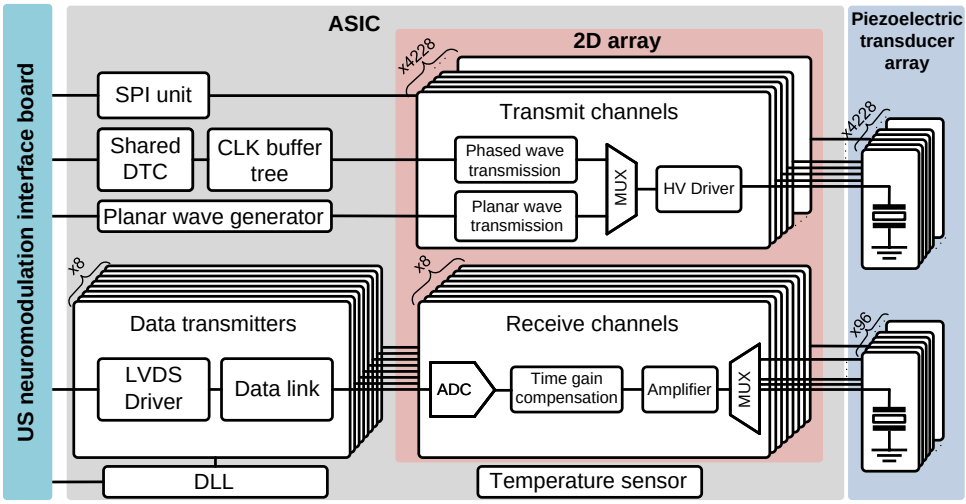

Fig. 6.11: The system-level diagram of the phased array transmitter ASIC.

6.3. Transistor-Level Implementation

6.3.1. ASIC Architecture

The architecture of the ASIC is shown in Fig. 6.11. The ASIC includes 4228 transmit channels and 8 groups of receive channels. While every transmit channel is directly connected to a given piezoelectric transducer element, each receiver channel will be connected to a group of 12 piezoelectric transducer elements through an analog multiplexer. The transmit channels are capable of delivering phased and planar wave pulses, which are generated by a shared DTC or a planar wave generator. The SPI unit is responsible for loading the data corresponding to the phase of each transmit channel to the internal shift registers of the transmit channels. Each receive channel includes an amplifier to amplify the weak signals generated by the piezoelectric transducer elements. Then, a time gain compensation stage is utilized to reduce the requirement for the input dynamic range. Next, an ADC is utilized to digitize the analog input data, which is encoded and transferred to the external board through a data link and an LVDS driver. Considering the limited budget area for implementing the receive channels, the data transmitters are placed on the edge of the ASIC while the receive channels are inside the 2D array. The DLL generates the required high-frequency clocks for the data transmitters. Furthermore, the required input clocks and power supplies for the ASIC are provided using an external interface board. The data generated by the receive channels is also transmitted to this interface board for further processing and image construction. Finally, in this work, a temperature sensor is utilized to measure the temperature of the ASIC during the neuromodulation. The following subsections describe the internal blocks of the ASIC in more detail. For the ASIC design, the piezoelectric transducers were modeled with the simplified BVD model of the 12-MHz 40×40 μm^2 PZT-5H transducer introduced in Chapter 4. The utilized simplified BVD model consists of a 20-kΩ resistor in parallel with a 400-fF capacitor.

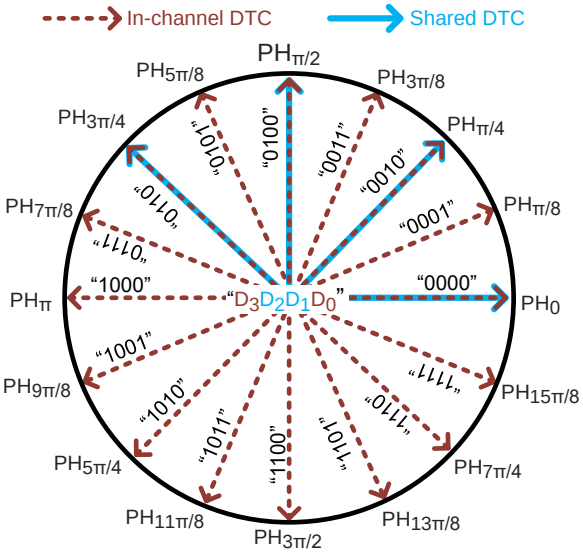

Fig. 6.12: The phasing diagram of the beamforming circuits. while the shared DTC performs the phasing corresponding to D_2 and D_1, the 2-bit in-channel DTC in the transmit channel adds phases related to the MSB (i.e., D_3) and LSB (i.e., D_0).

6

6.3.2. Transmit Channels

As discussed in the previous section, the ASIC is capable of driving the US transducers with phased pulses for US neuromodulation and planar pulses for US imaging. To implement the transmit circuits for phased transmission, the same approach discussed in Chapter 5 is utilized. As depicted in Fig. 6.11, the SPI unit loads the data corresponding to the phase of the transmit channels to the internal shift registers. As discussed in Section 6.2.1, the phase quantization resolution was set to 4 bits corresponding to the tradeoff between the peak transient current and the power consumption of the ASIC. Considering the limited area of 62.5×62.5 μm^2 for implementing the transmit channels, a 4-bit DTC in each transmit channel results in a large occupied area. On the other hand, utilizing a 4-bit DTC, which is shared among all transmit channels, leads to routing difficulties at the layout level. In this regard, as discussed in Chapter 5, controlling the phase of the signals is achieved by a shared 2-bit DTC, which is shared among all transmit channels, coupled with a 2-bit in-channel DTC in every transmit channel, corresponding to the tradeoff mentioned above. Taking into account the limited area of the transmit channels, the in-channel DTC must occupy a small area. As shown in Fig. 6.12, the MSB, i.e., D_3, and LSB, i.e., D_0, can be easily implemented using an inverter and a simple delay element, respectively, leading to a small occupied area. Therefore, D_3 and D_0 are implemented using the in-channel DTC, and D_2 and D_1 are implemented using the shared DTC. The shared DTC generates four signals with a phasing resolution of $\pi/4$, which are then distributed among transmit channels using a CLK buffer tree (Chapter 5, Fig. 5.4). In order to implement the shared DTC, the same DTC as the DTC introduced in Chapter 4 (Fig. 4.8) is utilized. The shared DTC is implemented based on a simple counter-based DTC, converting a 48-MHz input clock into four 12-MHz phased clocks with a phasing resolution of $\pi/4$. Although this DTC benefits

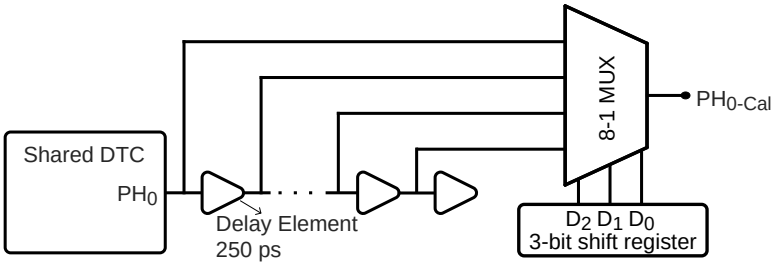

Fig. 6.13: The schematic of the calibration circuit for the shared DTC introduced in Chapter 4 (Fig. 4.8). Although only the calibration circuit for PH_0 is depicted, other phased clocks also have the same calibration circuit.

from circuit simplicity, errors in the duty cycle of the input clock may have a negative effect on the linearity of the DTC. Therefore, as shown in Fig. 6.13, a calibration circuit is utilized to compensate for the errors in the duty cycle of the input clock. The calibration circuit adds a given phase with a step delay of 250 ps to the output clocks of the shared DTC according to the calibration code stored in the 3-bit shift registers. Considering the phase quantization resolution of 4 bits at 12 MHz, the timing LSB is 5.2 ns. Keeping into account a maximum delay error of half of LSB, the sum of the delay errors in the shared DTC and the in-channel DTCs should not exceed 2.6 ns, which half of this budget (i.e., 1.3 ns) is considered as an allowed delay error in the shared DTC while the other half is reserved for possible errors in the beamforming channels. The total delay error in the shared DTC is the sum of the error by the shared DTC and the calibration circuit. However, as shared DTC and the calibration circuit are purely digital circuits with relatively large sizes, they are less sensitive to PVT and mismatch variations, which was also in agreement by the monte-carlo simulations. In fact, most of the delay errors at the output clocks of the shared DTC are caused by the errors in the input clock. As discussed in Chapter 5, the shared DTC is sensitive to the errors in the duty cycle of the input clock. Therefore, while a duty cycle of 50% is desired, any error in the duty cycle of the input clock is translated as a delay error at the output of the shared DTC. The input clock of the shared DTC is supplied from an external FPGA through external level shifters and buffers. In this regard, the input clock of the shared DTC always has a duty cycle offset from the desired value of 50%. However, the value of this offset is independent of the ASIC and can be calculated during the measurements. Then, the calibration circuit corrects the delay error by adding a certain delay, with a maximum value of 1.75 ns, to the output clock of the shared DTC.

The transmit channel is responsible for delivering a high-voltage pulse to the ultrasound transducer elements. The schematic of the transmit channel is depicted in Fig. 6.14. The principle of the operation for phased continuous wave transmission is as follows: first of all, according to D_2 and D_1 stored in the shift register, the 4-1 multiplexer selects one of the shared DTC's phased clocks. Then, the 2-bit DTC performs the in-channel phasing corresponding to the MSB (i.e., D_3) and LSB (i.e., D_0). In the next step, the burst duration and the duty cycle of the driving pulses are set by the period and the duty cycle of the *Burst* signal, which is supplied from the external board. In addition, the *En* bit stored in the shift register allows to enable or disable a given transmit channel in the 2D array. Therefore, when the *Burst* signal or the *En* bit are "*low*", the 4-1 multiplexer connects the HV driver to VDD, leading to no signal transmission. When *Burst* and *En* are "*high*", *Mode* signal

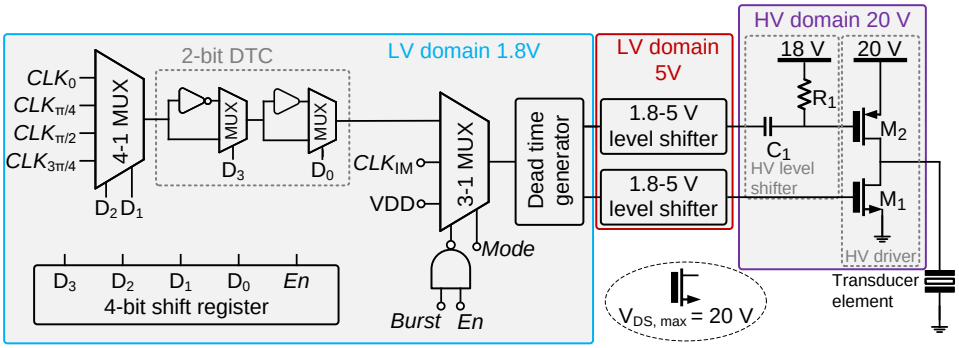

Fig. 6.14: The schematic of the 12-MHz 20-V transmit channel, which occupies an area of 62.5×62.5 μm^2.

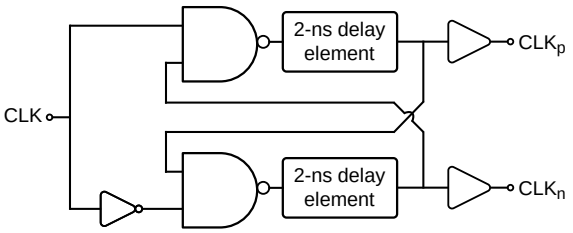

Fig. 6.15: The circuit diagram of the dead time generator.

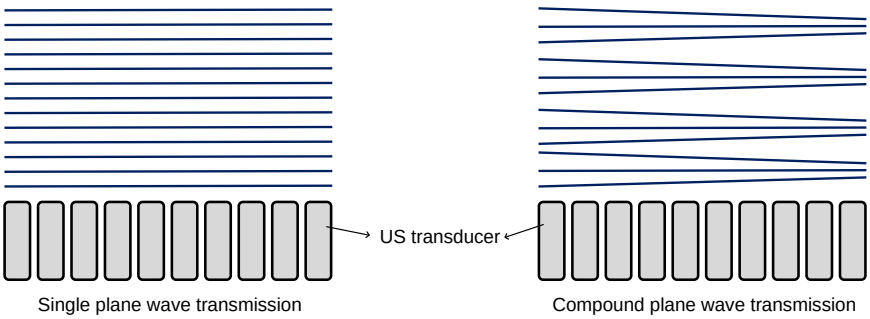

Fig. 6.16: The schematic representing the single plan wave transmission and the compound plan wave transmission.

defines the mode of the transmission. In this case, when *Mode* is "*low*", the phased transmission is activated; hence, the 4-1 multiplexer passes the output clock of the in-channel DTC to the dead time generator. On the contrary, when the *Mode* signal is "*high*", the planar wave transmission is activated; therefore, the CLK_{IM} signal is passed to the dead time generator, which generates two non-overlapping clocks for the HV NMOS and HV PMOS transistors, leading to reduction of the dynamic losses in the HV driver (Fig. 6.15). Since driving the HV NMOS and PMOS requires a pulse with an amplitude of 0-5 V and 15-20 V, respectively, the LV and HV level shifters are utilized to amplify the amplitude of the LV signals, as described in Chapter 4. Finally, the same HV driver as the driver presented in Chapter 4 is utilized to deliver 20-V pulses to the piezoelectric transducers.

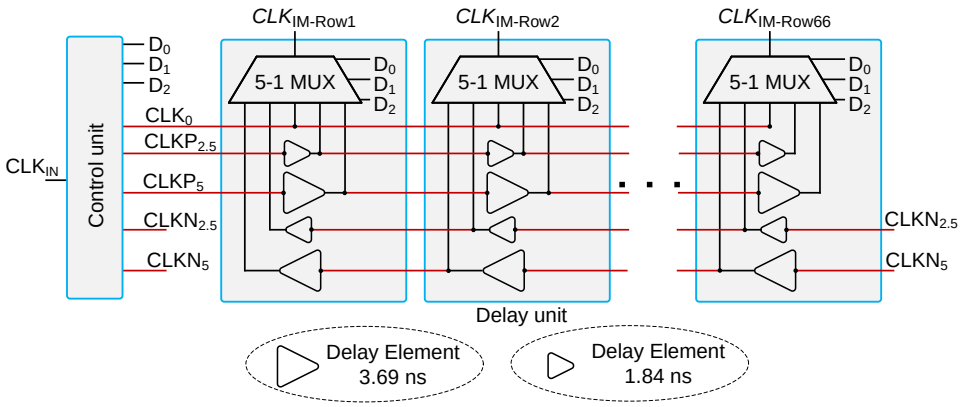

Fig. 6.17: The schematic of the planar wave generator.

In order to perform the planar wave transmission, the piezoelectric transducer elements must be driven with the same phase (Fig. 6.16). This technique of US imaging allows for achieving higher frame rates at the cost of lower image quality [265]. In order to improve the image quality, as shown in Fig. 6.16, compound plane wave transmission can be utilized, in which plane waves with multiple angles are transmitted [261]. In order to achieve a balance between the frame rate and image quality [54], the ASIC is designed in a way to transmit compound plane waves with angles of ±5°, ±2.5°, and 0. In order to perform this configuration, the CLK_{IM} of the transmit channels in each row are connected together. As shown in Fig. 6.11, a planar wave generator is utilized to generate the delayed clocks, i.e., CLK_{IM}, for each row. In order to implement a wave transmission with a certain angle, there should be a given delay between CLK_{IM} signals applied to the rows in the 2D structure. The delay value depends on the pitch size between the transmit channels and the desired angle. In other words, after the first element sends an ultrasound pulse, the second element should send an ultrasound pulse with a certain delay to generate an angled planar wave. The amount of this delay depends follows the simple triangle rule. In this regard, delays of 3.69 ns and 1.84 ns between two consecutive rows are needed to transmit planar waves with angles of 5° and 2.5°, respectively. The schematic of the planar wave generator is shown in Fig. 6.17. The control unit passes the input clock to the delay units according to the desired transmission angle. The delay units are responsible for generating a delay of 0, 1.84 ns, and 3.69 ns between the CLK_{IM} signals applied to two consecutive rows. While the delay of zero leads to a transmission angle of zero, delays of 1.84 ns and 3.69 ns result in transmission angles of +2.5° and +5°, respectively. Changing the direction of the applied clock to the delay units chain allows for changing the polarity of the transmission. In other words, changing the direction of the input clock allows for the generation transmission angles of -2.5° and -5°.

6.3.3. Receiver Channels

The detailed system-level architecture of the receiver channels is shown in Fig. 6.18. As discussed in Section 6.2.1, a group of 4×4 transmit elements have been removed to make an area of 250×250 μm^2 for implementing the receiver chain. The receiver chain is divided

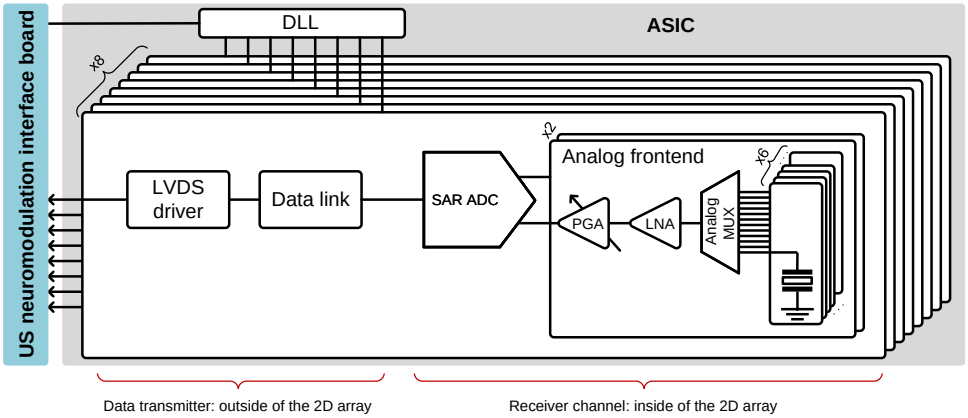

Fig. 6.18: The system-level architecture of the receiver channels.

into two parts: receiver channels and data transmitters. Considering the relatively large occupied area of the receiver chain, the receiver channels are implemented in the area of 250×250 μm^2 inside the 2D array while the data transmitters are implemented on the edge of the ASIC. While 12 piezoelectric transducer elements are connected to each receiver channel, 4 piezoelectric elements are left non-connected to make enough space for separating the LV and HV circuitry. Taking into account the small size requirements of the US neuromodulation interface board (Section 6.2.1), the number of connections between the ASIC and the board must be minimized. In this regard, every six transducer elements are connected to one analog front-end using an analog multiplexer. Then, to reduce the number of connections further, every two front-ends are connected to one ADC. Finally, the digital data is serialized and transferred to the interface board utilizing a data link and LVDS driver.

The signal attenuation of ultrasound waves in the tissue in dB can be expressed as follows:

$$A_{\text{att}} = \alpha \times 2 \times Z \times f_{\text{US}}^{y} \tag{6.1}$$

where α is the acoustic attenuation coefficient, y is the power law exponent for the acoustic attenuation coefficient, and Z is the imaging depth. Considering the frequency of 12 MHz and α and y of 0.58 and 1.3 for the brain, the signal attenuation is 29 dB for the maximum depth of 1 cm, corresponding to the maximum thickness of an adult rat's brain. Moreover, detecting the displacement in the tissue requires a minimum SNR of 30 dB [54]. Therefore, considering a 3 dB noise threshold [239], a total dynamic range (DR) of 62 dB is needed to receive the US echoes. Since the attenuation of US waves in the tissue is time-dependent, a time gain compensation unit can be utilized to reduce the required DR. This work has utilized a programmable gain amplifier (PGA) that provides 0-26 dB gain at a step size of 13 dB. In each transmit-receive cycle, the gain increases from the lowest to the highest setting, allowing for achieving sufficient linearity for the initially received strong echoes and detecting the weak echoes that arrive later [186]. As the PGA offers a programmable gain of 26 dB, the required DR of 62 dB is decreased to 36 dB. Moreover, the received signals are combined externally to construct the image; hence, the DR will in-

crease by $\sqrt{12 \times 8} \simeq 10$ dB [266], which is proportional to the number of receive elements; in this case 8 receive groups with 12 receive elements per group. In this regard, the ADC is required to cover a DR of at least 26 dB.

The circuit diagram of the analog front-end is shown in Fig. 6.19(a). It consists of an analog multiplexer, a TIA, a PGA, and an ADC driver. The analog multiplexer connects one of the piezoelectric transducer elements to the amplifier block. Previously, voltage amplifiers [267], TIAs [266], and charge amplifiers [268] have been utilized to amplify the received signals of the piezoelectric transducers. Considering the high input resistance of piezoelectric elements (i.e. 20 kΩ for 40×40 μm^2 12-MHz PZT-5H, refer to Chapter 4), a TIA is a power efficient topology to amplify the current signal generated by the piezoelectric transducer elements, rather than conventional voltage amplifiers which relay on the impedance of the piezoelectric transducer elements to convert the generated current to the voltage. Since the impedance of the piezoelectric transducer depends on the size of the piezoelectric element, any changes in the size of the element during the fabrication cause a voltage error. In this regard, as piezoelectric transducers convert mechanical displacements to electrical charges, a TIA is a suitable circuit to sense the current signal and convert it to an output voltage independent of the impedance of the piezoelectric transducer. It is also possible to utilize a charge amplifier to convert the input charge to voltage. However, charge amplifiers with capacitive feedback demand large decoupling capacitors to separate the DC voltage of the amplifier input from the DC voltage of the piezoelectric transducer, while in a TIA, the common mode voltage of the OTA is set by the resistive feedback. The gain of the TIA is set by the feedback resistor of 100 kΩ, ensuring that the input-referred noise of the analog front-end is less than the noise of the piezoelectric transducer elements [266]. A capacitor is added in parallel with the resistor to improve the stability of the TIA and limit the -3-dB bandwidth to 25 MHz. The TIA has utilized a folded-cascode OTA to ensure sufficient loop gain in the TIA (Fig. 6.19(b)). The PGA is implemented with an inverting amplifier using a switchable capacitive network. The PGA offers a gain of 0, 13 dB, and 26 dB. The PGA has an input capacitance of 640 fF and feedback capacitors of 32 fF, 144 fF, and 640 fF. In the lowest gain setting, S1 and S2 are closed, offering a gain of 0 dB for strong echoes. Then, S2 opens, setting the gain of the PGA to 13 dB. For the weak echoes, S1 and S2 are open, allowing the PGA to amplify the echoes with a gain of 26 dB. The architecture of the OTA used in the PGA is similar to that used in the TIA. Finally, a two-stage analog buffer is utilized to drive the large input capacitance of the ADC. The first stage amplifies the signal with a gain of 6 dB and converts the single-ended input signal to differential outputs. To implement this amplifier, a fully differential current reuse OTA is utilized, as shown in Fig. 6.19(c). The last stage is not only responsible for driving the capacitive DAC of the SAR ADC but also isolates the analog front-end chain from the switching noises of the SAR ADC. In order to implement this buffer, a single-ended OTA is utilized, as shown in Fig. 6.19(d).

Converting analog signals to digital data not only allows for further cable count reduction but also paves the way for on-chip signal processing toward fully integrated wearable or implantable applications. In this regard, this work has utilized an ADC to digitize the analog signal amplified by the analog front-end circuitry. As discussed in this section, the ADC is required to cover a DR of at least 26 dB. However, detecting the displacement in the tissue demands an SNR of 30 dB [54]. Different configurations of ADCs, such as SAR

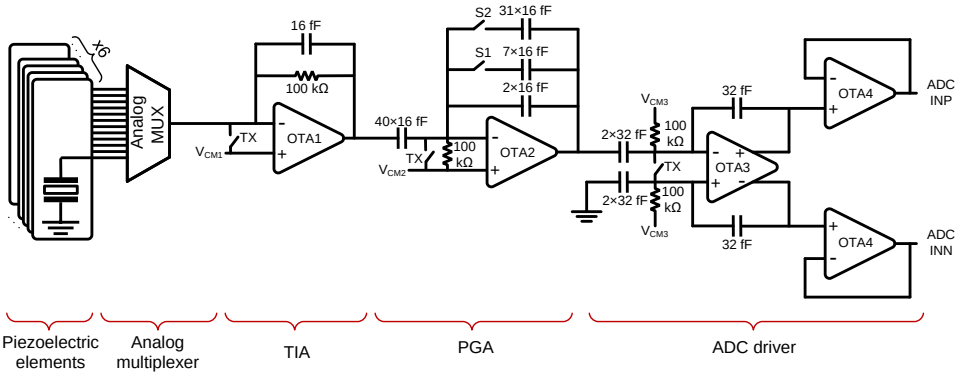

(a)

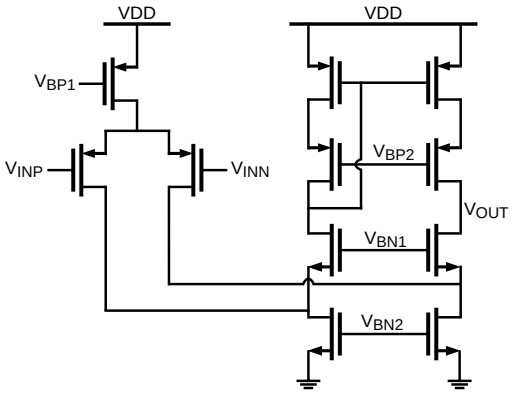

(b)

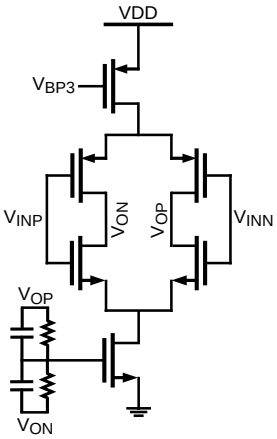

(c)

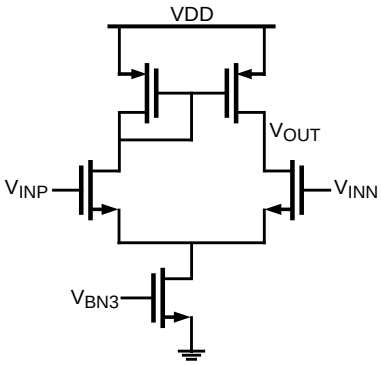

(d)

Fig. 6.19: The schematic of (a) analog front-end, (b) OTA1 and OTA2, (c) OTA3 and (d) OTA4.

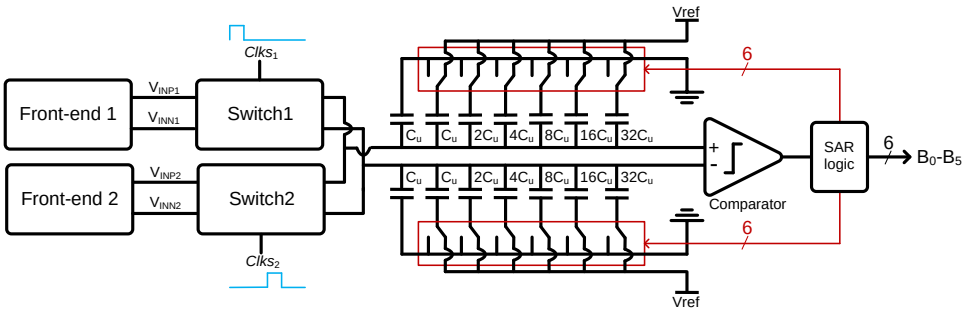

Fig. 6.20: Circuit diagram of the designed 6-bit 96 MS/s SAR ADC.

ADC [189], [239], pipeline ADC [269], and delta-sigma ADC [156], have been utilized in ultrasound imaging applications. Among others, SAR ADC is a good choice for the above-mentioned SNR as it offers a good compromise between power and area consumption. In this regard, considering a 30-dB SNR and a margin for possible SNR drop, a 6-bit 96 MS/s SAR ADC is designed [270] (Fig. 6.20). The high sampling rate of the SAR ADC allows for the digitization of 4 samples per input pair per each cycle of 12 MHz. In other words, the ADC takes 8 samples from the output signals of the front-end chains, ensuring that no antialiasing is happening during the entire bandwidth of the piezoelectric transducers. Furthermore, it allows for asynchronous operation, eliminating the need for an external clock. In the utilized configuration, two analog front-ends are connected to the SAR ADC through two switches. As shown in Fig. 6.20, first, $Clks_1$ goes "High", allowing Switch1 to sample the output signal of Front-end1 into the capacitive DAC of the SAR ADC. When $Clks_1$ goes "Low," the comparator coupled with the SAR logic starts operation to quantize the sampled voltage. After each conversion, the generated bit is transmitted to the data link for encoding and transmission to the interface board. In the next phase, $Clks_2$ goes "High", enabling Switch2 to sample the output signal of Front-end2 into the DAC of the SAR ADC. Then, the comparison starts, and the SAR logic generates the data. All clocks needed for the operation of the SAR ADC are asynchronous, and the sampling clocks, i.e., $Clks_1$ and $Clks_2$, are generated in the DLL unit inside the ASIC.

The overview of the data transmitters is shown in Fig. 6.21. Each receiver channel in the ASIC is connected to a data transmitter at the periphery of the chip, outside of the 2D array area. At the end of each conversion cycle, the generated 6-bit data is transmitted to the data link. As shown in Fig. 6.21, data links include a multiplexer that allows for the transmission of either the ADC's data or the alignment byte, which enables the receiver of the external FPGA to find the actual data in the stream of the serial data. The utilized alignment word is compatible with conventional transmit/receive protocols, such as GTP transceivers. In this approach, first, the alignment byte is transmitted. Then, when the receiver detects the alignment byte in the data stream, the Data link starts the transmission of the ADC's data. In order to convert the 6-bit data generated by the ADC to an 8-bit standard data frame, two alignment bits are added at the end of each data. In each data transmission cycle, the 8-bit data is serialized and transmitted to the LVDS driver if the transmission is enabled (i.e., *TX-En* is "High"). As shown in Fig. 6.22, in the end, the LVDS driver transmits the data stream with a high data rate of 768 Mb/s to the receivers of the

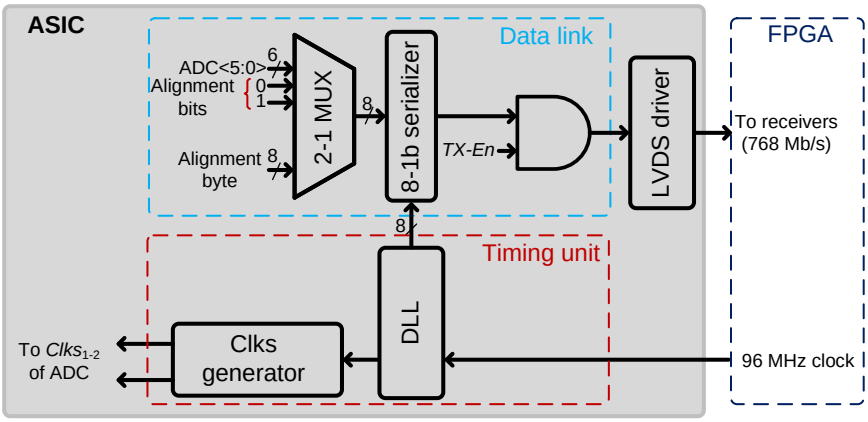

Fig. 6.21: Block diagram of the data offloading from the ASIC to the external board.

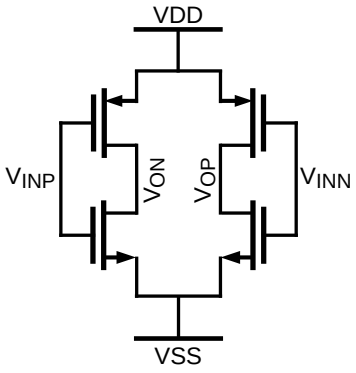

Fig. 6.22: The schematic of the LVDS driver.

FPGA. It is worth mentioning that the alignment bits and enabling bits, such as *TX-En*, are adjustable by changing the values stored in the internal registers in the ASIC, which has not been drawn for the sake of simplicity. A DLL has been utilized to generate the required clocks for the serializer from an external 96 MHz clock (Fig. 6.23). The Clks generator is responsible for generating the required clocks for the sample and hold circuits of the ADC from the external 96 MHz clock. Next, the DLL generates 8 equally delayed pulses from the 96-MHz clock, which is utilized to serialize the data and transmit it through the LVDS driver.

6.3.4. Temperature Sensor

The transmit channels in the transmitter ASIC dissipate a large current from the 20-V supply, leading to a temperature rise in the ASIC, which may raise the temperature at the surface of the transducer and cause damage to the animal's brain. Moreover, as discussed in Chapter 2, if the temperature rise in the ASIC reaches the Curie temperature of the piezoelectric transducers, it may lead to depolarization and degrade the performance of the piezoelectric material. Therefore, avoiding any damage to the piezoelectric transducer

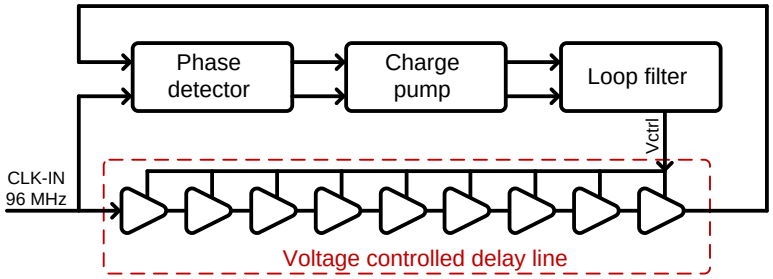

Fig. 6.23: The block diagram of the DLL.

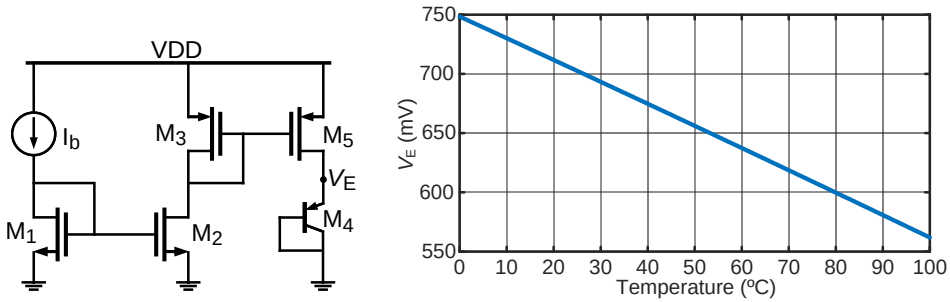

(a) (b)

Fig. 6.24: (a) The schematic of the BJT temperature sensor (b) the variation of V_{BE} of the BJT transistor with temperature.

and the animal's brain demands monitoring the temperature rise in the ASIC. Since the temperature rises from the steady-state temperature when the ASIC is off, represents the heat generation in the ASIC, a diode-connected BJT transistor, as shown in Fig. 6.24(a), is utilized as a temperature sensor [271]. In this configuration, while the emitter is biased with a constant current, the collector is shorted to the base and is connected to the ground, making the transistor behave like a diode with a more predictable temperature behavior. The key principle in BJT transistors is that the base-emitter voltage ($|V_{BE}|$) decreases monotonically with a negative first-order temperature coefficient of about -1.9 mV/C at room temperature, as illustrated in Fig. 6.24(b). This temperature coefficient is achieved through simulation at TSMC 180 nm BCD technology. To measure the temperature, the voltage across the base-emitter junction, i.e., V_E) is monitored by an external ADC. In this ASIC, we aim to measure the temperature rise inside the chip as a function of the applied duty cycle and *PRF*. In this regard, the simple temperature sensor, which is shown in Fig. 6.24(a), meets the required accuracy for this application. However, monitoring the actual temperature rise in the tissue that is in contact with the US transducer demands more accurate temperature sensing on the surface of the piezoelectric transducers.

6.4. Physical Implementation

The transmitter ASIC has been realized in TSMC 0.18-µm BCD technology. The chip micrograph of the transmitter ASIC is depicted in Fig. 6.25(a), which occupies a total area of 5×5 mm^2, including the I/O pads. While the 2D transmit and receive array occupies an

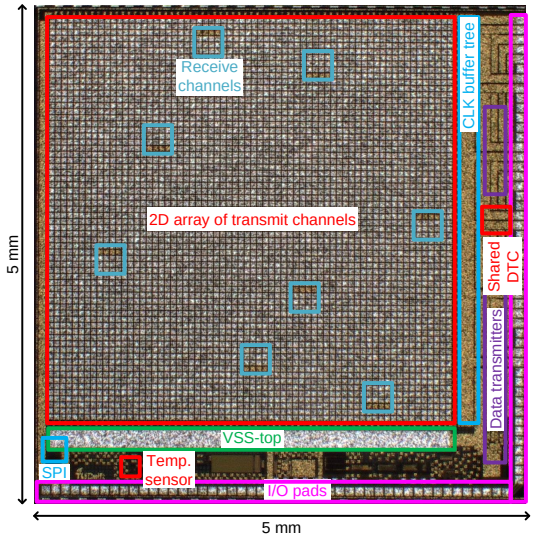

(a)

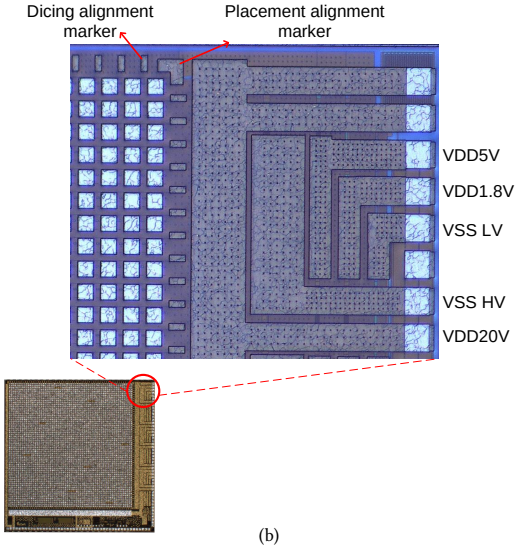

(b)

Fig. 6.25: (a) The micrograph of the CMOS chip with 66×66 transmit channels, occupying a total area of 5×5 mm^2. (b) The zoom-in micrograph of the ASIC shows the distribution of the power tracks among the 2D array and the alignment markers.

active area of 4.1×4.1 mm^2, the rest of the chip is utilized to implement the shared blocks and distribute power and driving signals among the transmit channels. As discussed in Section 6.2.1, the receiver channels are distributed randomly across the 2D array of transmit channels, as depicted in Fig. 6.25(a). However, the data transmitters corresponding to each receiver channel are implemented outside the 2D array in order to avoid very large gaps between the transmit channels. A large ground pad (i.e., VSS-top in Fig. 6.25(a)) is

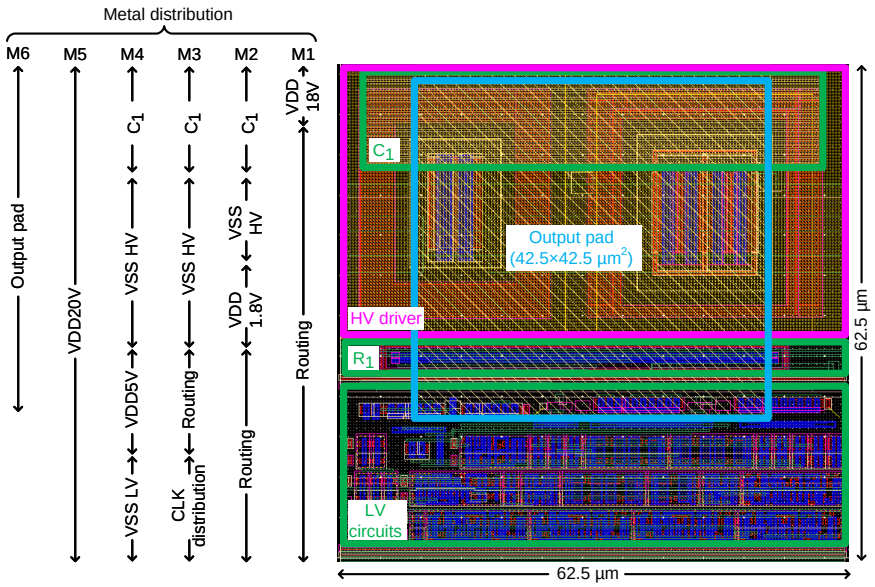

Fig. 6.26: The layout of a single transmit channel which occupies an active area of 62.5×62.5 µm^2.

considered to connect the top connection of the piezoelectric transducers to the ground. As shown in Fig. 6.25(a), the I/O pads are placed on the right and bottom sides of the chip, allowing the possible combination of four ASICs together and form a larger phased array US transmitter for preclinical studies on larger animals such as sheep. The required power supplies on the right side of the ASIC are responsible for the equal distribution of the required power supplies to the 2D transmitter array. As depicted in Fig. 6.25(b), in order to minimize the electrical resistance of the power lines, these have been implemented using wide and thick tracks of Metal 6. Since the transmit channels dissipate the highest current from the 20-V power supply, the tracks associated with the 20-V supply are directly connected to every row of the 2D array. Other supplies are distributed using Metal 6 and then are connected to every row of the 2D array using other metal layers. In order to make the ASIC compatible with the direct integration of piezoelectric transducers reported in [40], as shown in Fig. 6.25(b), two large squares of alignment markers are added to the top left and bottom right of the 2D array to facilitate the precise placement of a 4.1×4.1 mm^2 piezoelectric transducer on the ASIC using a flip chip bonder tool [40]. Additionally, dicing alignment markers corresponding to a blade thickness of 20 µm are added to every row and column of the 2D array to guide the dicing of the piezoelectric transducer into small elements of 42.5×42.5 µm^2.

Fig. 6.26 shows the layout of the pitch-matched transmit channel that occupies a circuit area of 62.5×62.5 µm^2. While HV transistors are accountable for 58% of the transmit channel area, the LV circuits and the HV level shifter occupy 34% and 8% of the area, respectively. As shown in Fig. 6.26, to minimize the occupied area of the transmit channel, the capacitor and the resistor of the HV level shifter are implemented using the MOM structure using Metal 2-4 on top of the HV transistors and a poly resistor, respectively. Parts of Metal 1-3 are utilized to perform the in-channel routing between the LV and HV

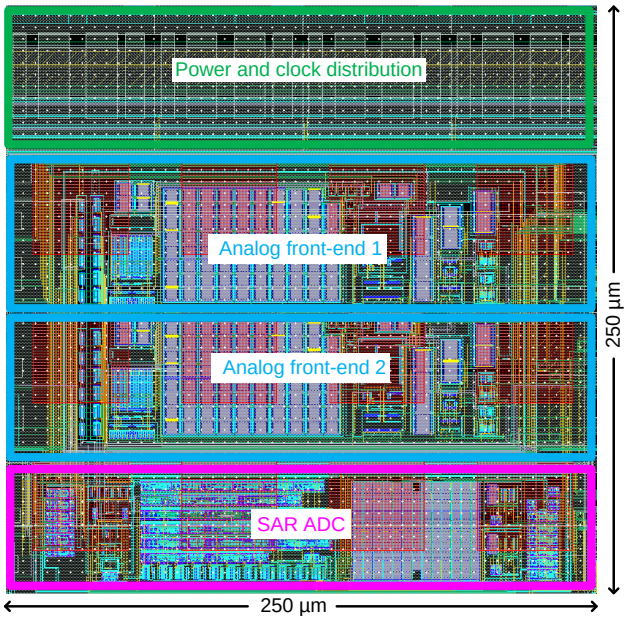

Fig. 6.27: The layout of a receive channel which occupies an active area of 250×250 µm^2.

components. While the clock buffer tree distributes the phased clocks of the shared DTC among rows of the transmit channels in the 2D array, part of Metal 3 is used to distribute these clocks among the transmit channels in a single row. Depending on the current dissipation of every supply level, parts of Metal 1-5 are allocated to distribute the power supplies among the transmit channels. Metal 5 not only supplies 20-V power to the transmit channels but also shields C_1 from the HV fluctuations in the output pad, which is implemented with Metal 6. The layout of the receiver channel is shown in Fig. 6.27. Although each transmit channel occupies an active area of 62.5×62.5 µm^2, the receive channel occupies an area of 250×250 µm^2. In other words, each transmit channel is connected to one pad, while a receiver channel is connected to 16 pads, of which 12 pads are connected to 12 piezoelectric elements, and 4 pads are left unconnected. The dummy elements are utilized to make enough room for adding the HV guard ring around the receiver groups. Since the receiver channels disturb the power and clock delivery to the transmit channels in the same rows, the area below the dummy pads is utilized for power and clock distribution among the transmit channels. Furthermore, the integration of the ASIC with 6 MHz piezoelectric transducers necessitates having an odd number of receiver pads. In this case, the real pitch size increases to 125 µm, meaning that each 6 MHz piezoelectric transducer will be connected to four transmit channels which are driven with the same phase. In this regard, the transmit pads may short to the even rows of the receiver pads and cause damage to the receiver circuits. Therefore, the non-connected pads serve as a dummy to avoid any short circuit between high-voltage transmitters and low-voltage receivers.

6.5. Electrical Verification

6.5.1. Measurement Results of the Transmitters

As discussed in the previous section, the ASIC has been realized in TSMC 0.18-µm technology. In order to evaluate the functionality of the transmitters, the measurement setup illustrated in Fig. 6.28 is utilized. The ASIC is wire bonded to a child PCB, which includes the ASIC, the decoupling capacitors, and the connector. A parent board transfers the needed power supplies and the commands to the child board using a micro coaxial cable. The required voltage levels, which include 1.8 V, 5 V, 18 V, and 20 V, are supplied from an external DC power supply to the parent board. After the voltage regulation using the LDOs on the parent board, the clean voltage levels are supplied to the transmitter ASIC. In order to prevent any damage to the ASIC, a proper power-up and power-down sequence is needed. In the power-up sequence, the LV supplies are the first to go up, in which the first 1.8 V supply and then the 5-V supply turns on. Since the gate and the source of the HV PMOS transistors are connected to the 18-V and 20-V levels, these supplies should go on and off simultaneously. In this regard, the same type of LDOs are utilized to generate 18-V and 20-V supplies, in which large decoupling capacitors in the output of the HV regulators are utilized to compensate for the load capacitance difference between the source and the gate of the HV PMOS transistors. During the power-down sequence, HV supplies first go off simultaneously; following that, the 5-V and then 1.8-V supply turns off. Although the current PMU is implemented with external LDOs and DC power supplies, the future setup for preclinical experiments utilizes a custom PMU designed by SiliconGate Lda. The required command signals to program and configure the ASIC are sent from a graphical user interface (GUI), which is designed in Matlab. The user enters the focal spot's location and the sonication parameters in the GUI. Then, the GUI calculates the data corresponding to the required phase for every transmit channel to form a focal spot at the given location. Then, the phase data of the transmit channels and the command signals are sent to a Spartan-7 FPGA development board (CMOS S7, Digilent). Then, the FPGA loads data to the SPI of the ASIC and generates the required pulses corresponding to the defined burst duration and duty cycle defined by the user. As shown in Fig. 6.28, a picoprobe (12C, GGB Industries), which has an input impedance of 0.1 pF $\|$ 1 MΩ, and a probe station are utilized to measure the HV pulses generated by the transmit channel. The measurement results presented here were obtained by directly probing the output pads without a load applied to the transmit channels.

First of all, in order to verify the phasing functionality of the shared DTC, a 48-MHz clock was applied to the ASIC. Then, the shift registers of the transmit channels were configured with codes corresponding to the output phases of the shared DTC. As illustrated in Fig. 6.29, the transient output waveforms verify that the shared DTC generates the expected phases with a maximum INL of 0.9 ns. Although this timing error is smaller than the needed timing resolution of 5.21 ns for 4-bit phase quantization, the calibration circuit, as depicted in Fig. 6.30, is capable of modifying the timing errors, verifying that the calibration circuit allows adjusting the phase of the shared DTC with a timing resolution of 250 ps.

In the next step, the functionality of the transmit channels was characterized. To validate the driveability of the transmit channels, the ASIC has been programmed with a phase of "0000". Then, the output pad of the transmit channel was measured by the 12C

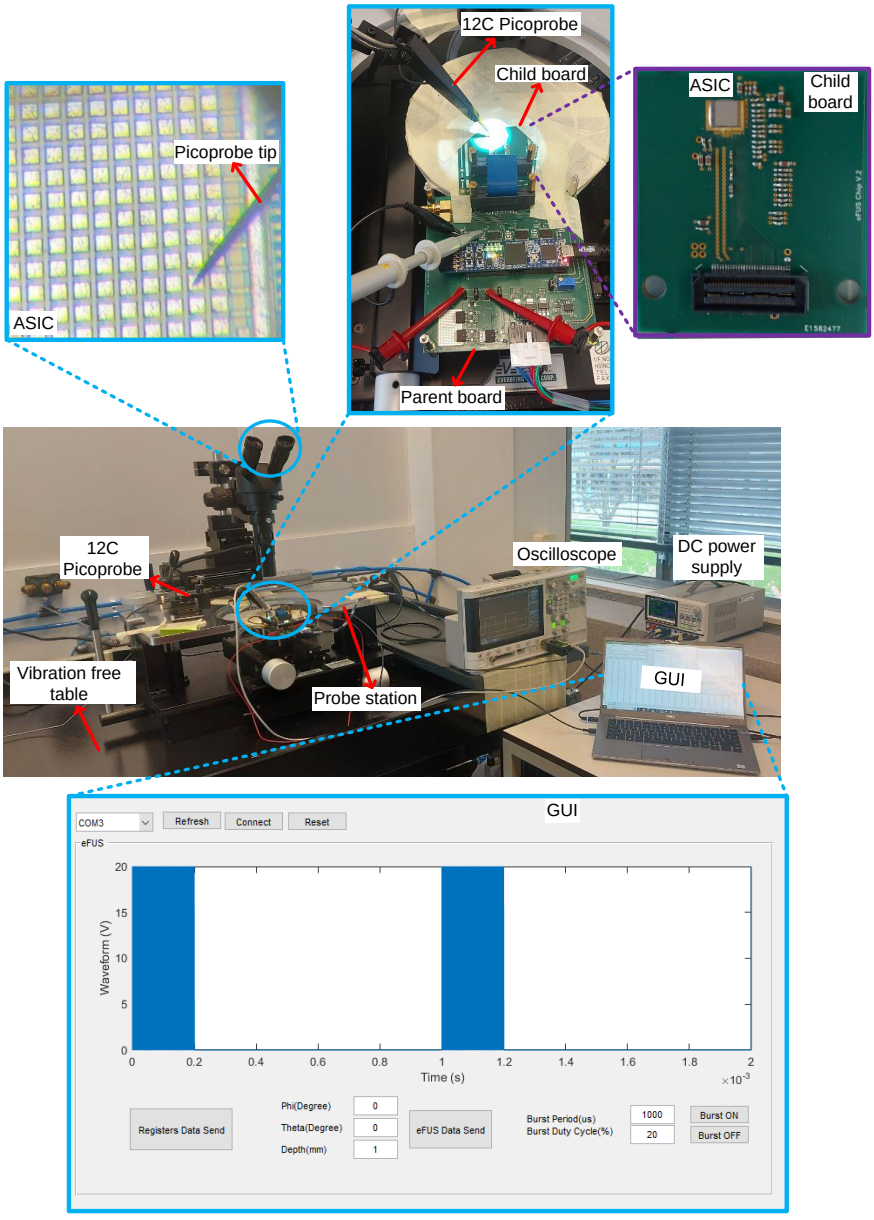

Fig. 6.28: The measurement setup for electrical characterization of the ASIC, including the probe station, the test boards, and the GUI.

picoprobe. The transient waveforms of the output pad are depicted in Fig. 6.31. As wire-bonding the small pads of the transmit channels was challenging, simulation results were utilized to justify the drivability of the transmit channels. In this regard, the ability of the transmit channel to drive the BVD model (Section 4.2) was verified during the transient

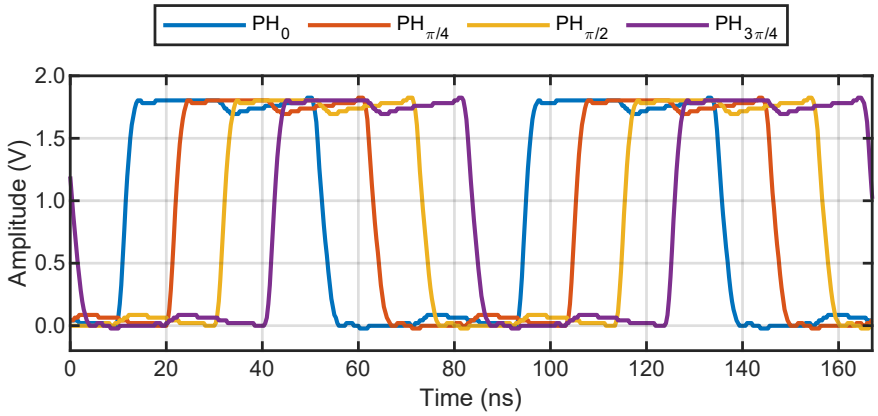

Fig. 6.29: The measured transient waveforms of the shared DTC for different phase configurations.

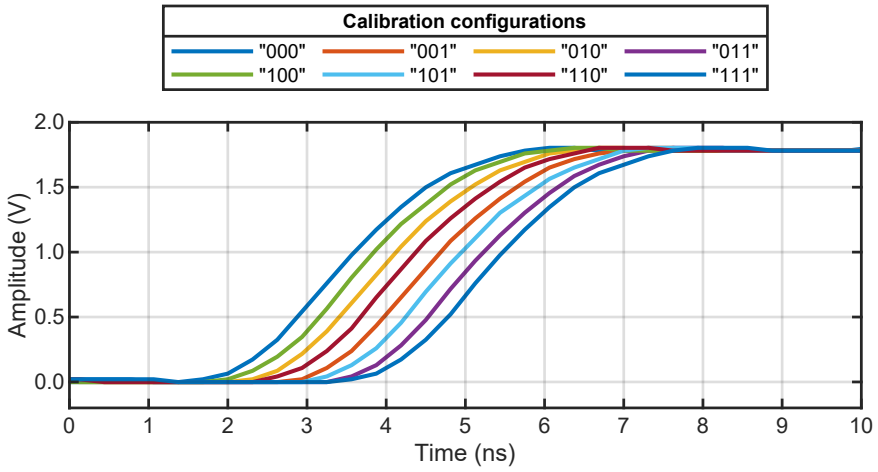

Fig. 6.30: The measured transient waveforms of the shared DTC for different calibration configurations.

simulation (Fig. 6.31). Since the ASIC may be integrated with other piezoelectric transducers than 12-MHz PZT-5H, resistive loads of 10 kΩ and 5 kΩ are applied to the transmit channel, corresponding to piezoelectric transducers with lower resistive loads. The simulation results, as illustrated in Fig. 6.31, show that the transmit channel can deliver 19.2 V and 18 V to 10-kΩ and 5-kΩ resistive loads. Although it may seem that the transmit channels are overdesigned for driving 12-MHz 40×40 μm^2 PZT-5H transducers, the size of the HV transistors was intentionally chosen larger to make the ASIC flexible in driving different loads of piezoelectric transducers. In order to verify the phasing capability of the transmit channel, the transmit channels in the ASIC were programmed with 16 different configurations corresponding to 4-bit phase quantization. Fig. 6.32 illustrates the transient waveforms of the transmit channel's output while performing 4-bit phase quantitation. The transmit channels generate 20-V pulses with the desired phases with respect to the programmed configuration. In order to measure the linearity of the transmit channels, the delay-programmed code transfer function of the measured transmit channel is

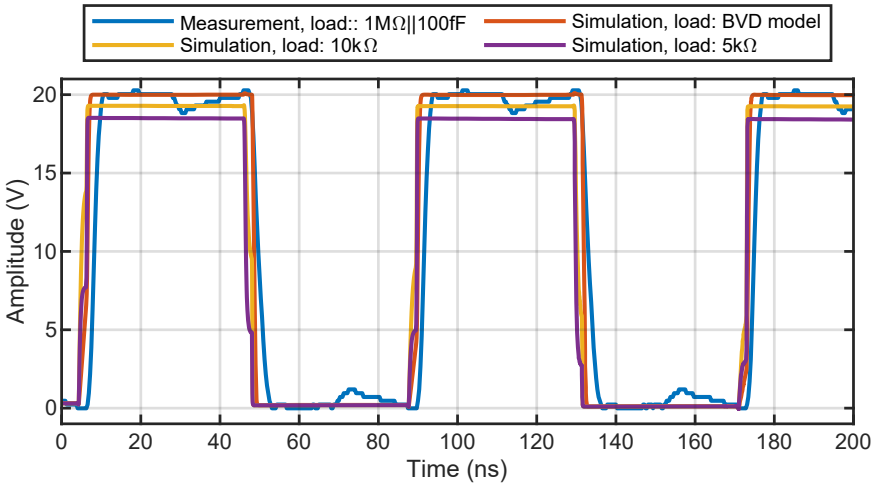

Fig. 6.31: The driving capability of the transmit channels in delivering HV pulses to the piezoelectric load. The only load during the measurement is the load of the HV probe (i.e., 1 MΩ||100 fF). For the simulations, three different loads are used, including the complete BVD model for 12-MHz 40×40 μm^2 PZT-5H (Section 4.2) and resistive loads of 5 kΩ and 10 kΩ.

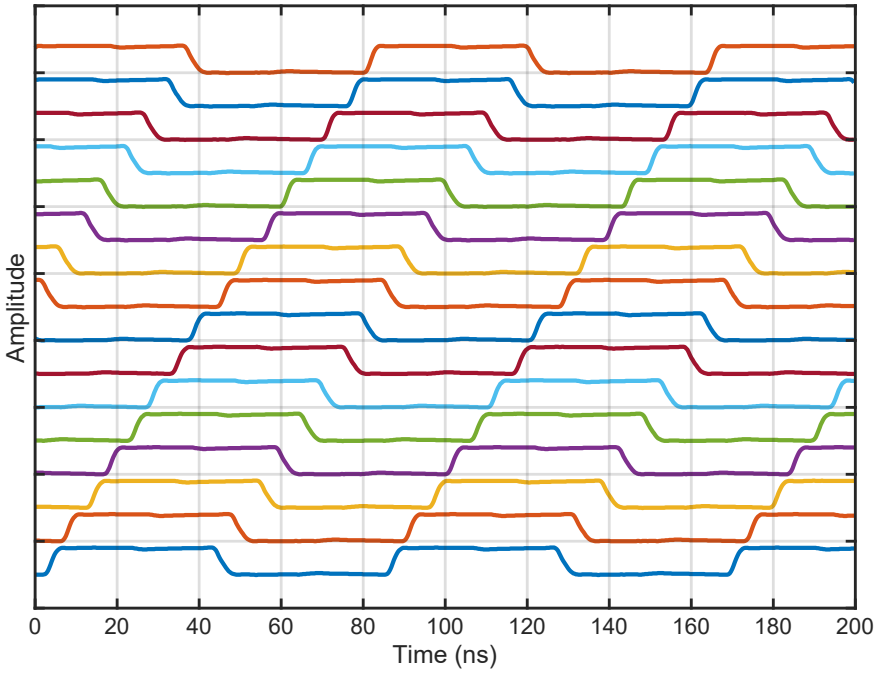

Fig. 6.32: The measured transient waveforms of a transmit channel in the center of the array for 16 different phase configurations.

calculated, as shown in Fig. 6.33. The transmit channel can linearly generate phases with respect to the programmed phases. In order to measure the alignment of the generated and

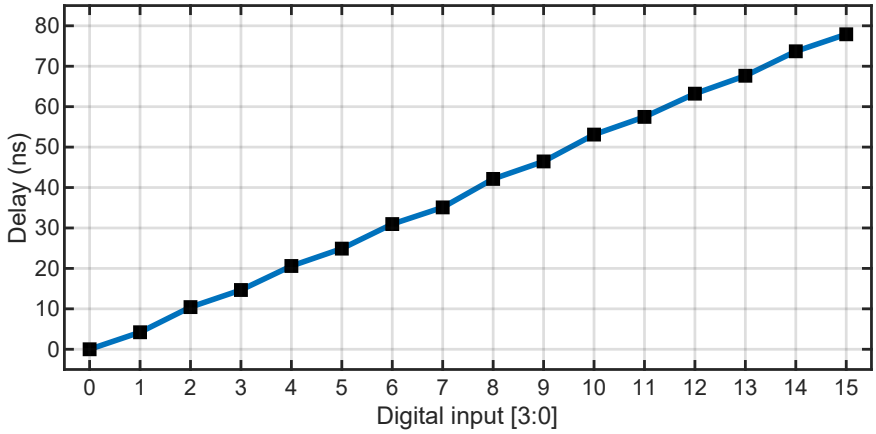

Fig. 6.33: The measured delay-code transfer function of a single transmit channel in the center of the array, verifying the linearity of the beamforming circuit.

the expected phases, the DNL and INL of the delay-programmed code were measured for each phase configuration. As depicted in Fig. 6.34, |INL| that represents the alignment of the generated phases with the expected phases, has a maximum of 0.26 delay LSB, which corresponds to a negligible delay error of 1.35 ns for a delay LSB of 5.21 ns. Considering the INL for odd digital inputs shows that the input code LSB is responsible for generating a non-linearity of 0.2 delay LSB, which is caused by the timing errors in the in-channel DTC in the transmit channel. The |DNL|, which is a measure of the timing steps between the programmed codes, has a maximum of 0.35 delay LSB, corresponding to a delay error of 1.82 ns for a delay LSB of 5.21 ns. In order to evaluate the phasing linearity of the transmit channels across the 2D array, the delay-programmed code transfer functions with respect to a transmit channel in the center of the 2D array were measured for diagonal transmit channels across the array. The histograms of the |INL| and |DNL| for the measured transmit channels are shown in Fig. 6.35. While |INL| and |DNL| have a maximum of 0.5 delay LSB and 0.4 delay LSB, respectively, in most phasing configurations, the |INL| and |DNL| are smaller than 0.2 delay LSB. Although 3-bit phase quantization is enough for precise beam steering (Chapter 3), the measurement results verified that the transmit channels across the 2D array are capable of performing 4-bit phasing, meeting the required phase resolution for beam steering and reducing the transient peak currents.

The transmitter ASIC is optimized for driving a 2D array of 12-MHz piezoelectric transducers with a pitch size of 62.5 μm in order to avoid the appearance of grating lobes in the beam profile (Chapter 3). In this configuration, every transmit channel drives its corresponding piezoelectric transducer, leading to a pitch-matched structure. However, a group of 2×2 transmit channels driven with the same phase increases the real pitch size to 125 μm. Therefore, the integration of 6-MHz piezoelectric transducer elements with a pitch size of 125 μm with the transmitter ASIC allows the implementation of a 6-MHz phased array US transducer without generating any grating lobes in the beam profile. In addition, while a pitch size equal to the sound half-wavelength leads to a maximum steering capability of π along the azimuth direction, a limited steering angle can satisfy the needs for specific applications, such as powering to implanted devices that have a fixed location in

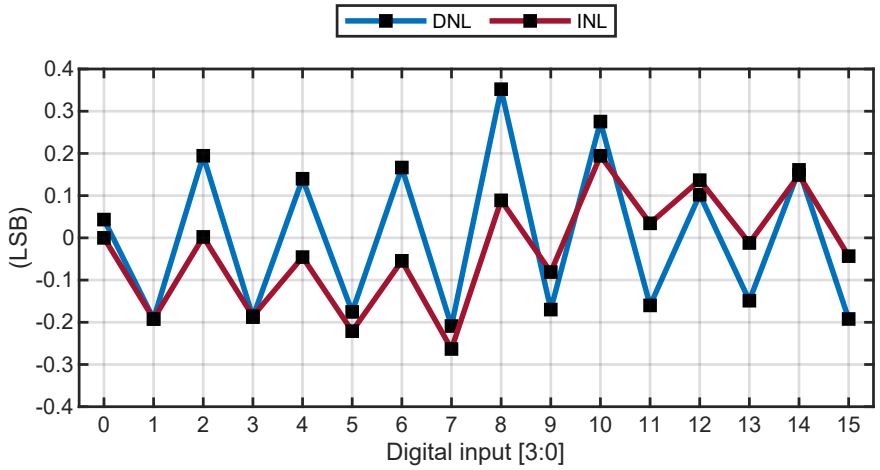

Fig. 6.34: The measured INL and DNL for a beamformer channel in the center of the array.

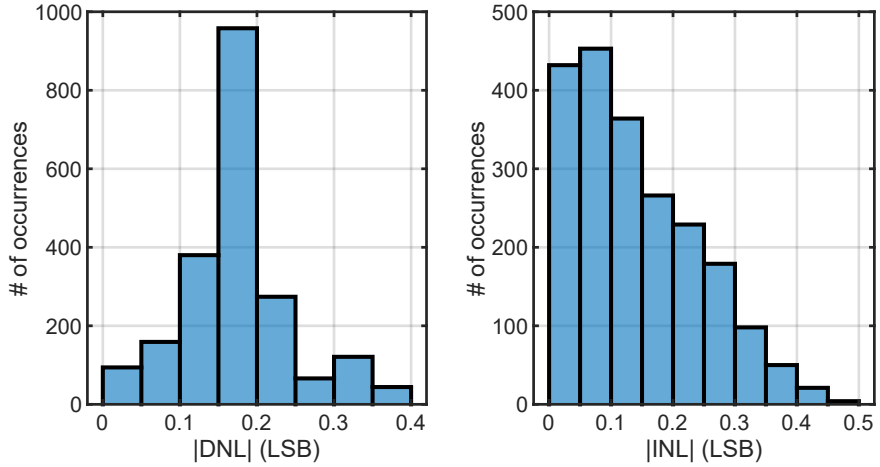

Fig. 6.35: The histograms of measured |INL| and |DNL| for 131 transmit channels that are selected diagonally across the 2D array.

the tissue. In these cases, the pitch size can be more than the sound half-wavelength; in other words, piezoelectric transducers with higher resonance frequencies than 12 MHz can be integrated with the transmitter ASIC. Although integration of the piezoelectric transducers with different resonance frequencies and pitch sizes on one or a group of transmit channels is physically possible, the transmitter ASIC is required to perform proper 3-bit phasing independent from the operation frequency. In order to verify the phasing functionality of the transmitter ASIC for different operating frequencies, 16-MHz, 32-MHz, 48-MHz, and 64-MHz pulses were applied to the shared DTC of the ASIC, generating 20-V pulses with operating frequencies of 4-MHz, 8-MHz, 12-MHz, and 16-MHz, respectively. Then, the transmit channels within the ASIC were programmed with eight different phase configurations corresponding to 3-bit phasing quantization. The measurement results, as

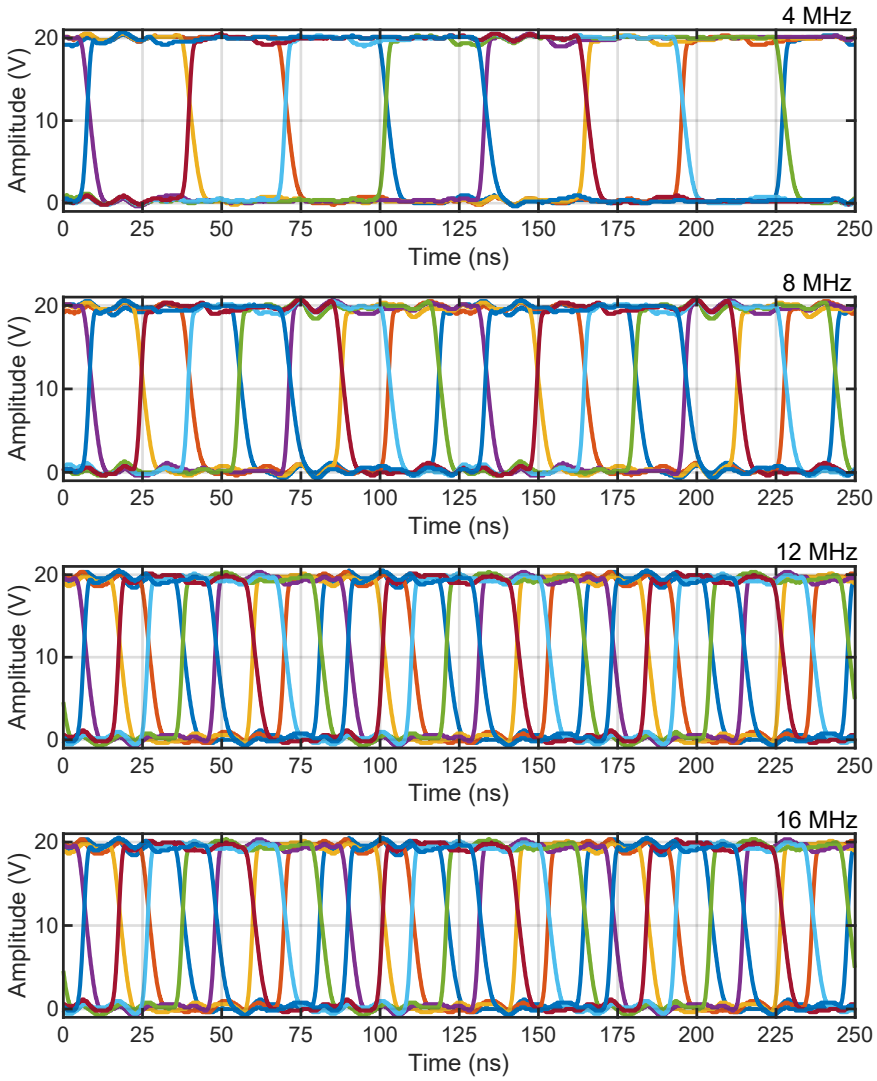

Fig. 6.36: The measured output waveforms of a transmit channel for various working frequencies while performing 3-bit phasing.

depicted in Fig. 6.36, confirm that the transmitter ASIC performs proper phasing with enough accuracy in different operating frequencies, showing the ability of the transmitter ASIC in beam steering independent from the operation frequency.

In order to find the optimum parameters for modulating the neurons with ultrasound, comprehensive preclinical experiments on US neuromodulation demand adjusting the intensity at the focal spot, which can be achieved by controlling the driving voltage of the transmitter ASIC. In order to validate the controllability of the transmitter ASIC in terms of the driving voltage, a bench-top programmable power management unit is connected

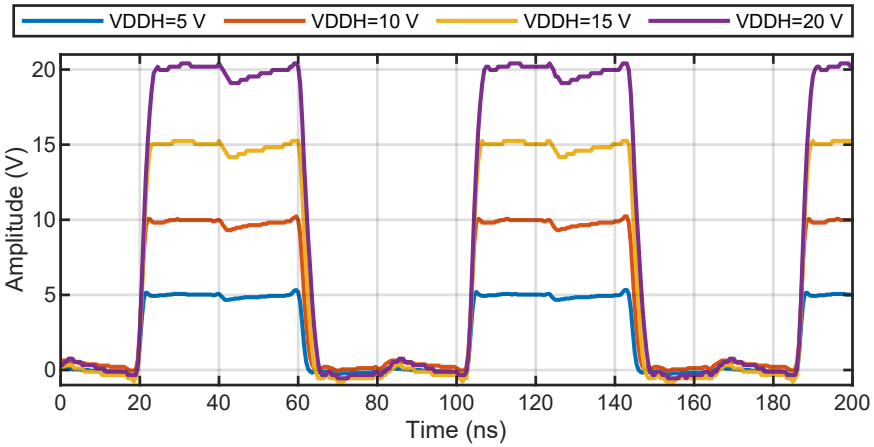

Fig. 6.37: The measured output waveforms of the beamformer channels for various power supply levels.

to the transmitter ASIC to provide the HV power supply. In this configuration, the source of the HV PMOS transistors in the HV driver and the top connection of the resistor in the HV level shifter (Fig. 6.14) are connected to the same potential. As the size of HV PMOS was chosen to be a bit larger than the needed size, connecting the source of HV PMOS and the top connection of the resistor together does not significantly influence the drivability of the transmit channels. At the cost of a more complicated programmable PMU, it is also possible to connect the source of the HV PMOS and the top connection of the resistor to a different potential. As shown in Fig. 6.37, different supply levels are applied to the HV supply of the transmitter ASIC, validating the functionality of the ASIC in delivering pulses with an adjustable amplitude of up to 20 V to the piezoelectric transducer elements, while no load is applied to the beamforming channels.

As a burst of pulses is utilized in US neuromodulation, comprehensive preclinical experiments demand a US transducer capable of generating US pulses with an adjustable *PRF* and *DC*. In the transmitter ASIC, an external clock as a *Burst* signal is utilized to adjust the *PRF* and *DC* of the generated HV pulses. In order to characterize the performance of the ASIC in controlling the pulse duration, *Burst* signals with different pulse durations have been applied to the transmitter ASIC, as illustrated in Fig. 6.38. The transmitter ASIC can generate HV pulses with adjustable *PRF* and *DC*. As discussed in Chapter 2, although previous US experiments have reported achieving US neuromodulation with a broad range of *DC*s, most studies have utilized a *PRF* of 1 kHz. As shown in Fig. 6.39, in order to show the ability of the ASIC to generate a typical waveform used in US neuromodulation, the transmitter ASIC has been configured to generate 20-V pulses with a *PRF* and *DC* of 1 KHz and 50%, respectively.

The measured power consumption of the ASIC as a function of the *DC* is shown in Fig. 6.40. It is worth mentioning that the "Power 20 V" represents the power consumption from the 20-V power supply, which is used to generate 20-V and 18-V supply levels needed for the transmit channels; however, as the 18-V supply level is connected to the gate of the HV PMOS transistors, the current dissipation from this supply level is negligible compared with the power consumed from the 20-V supply level. Moreover, no external loads have

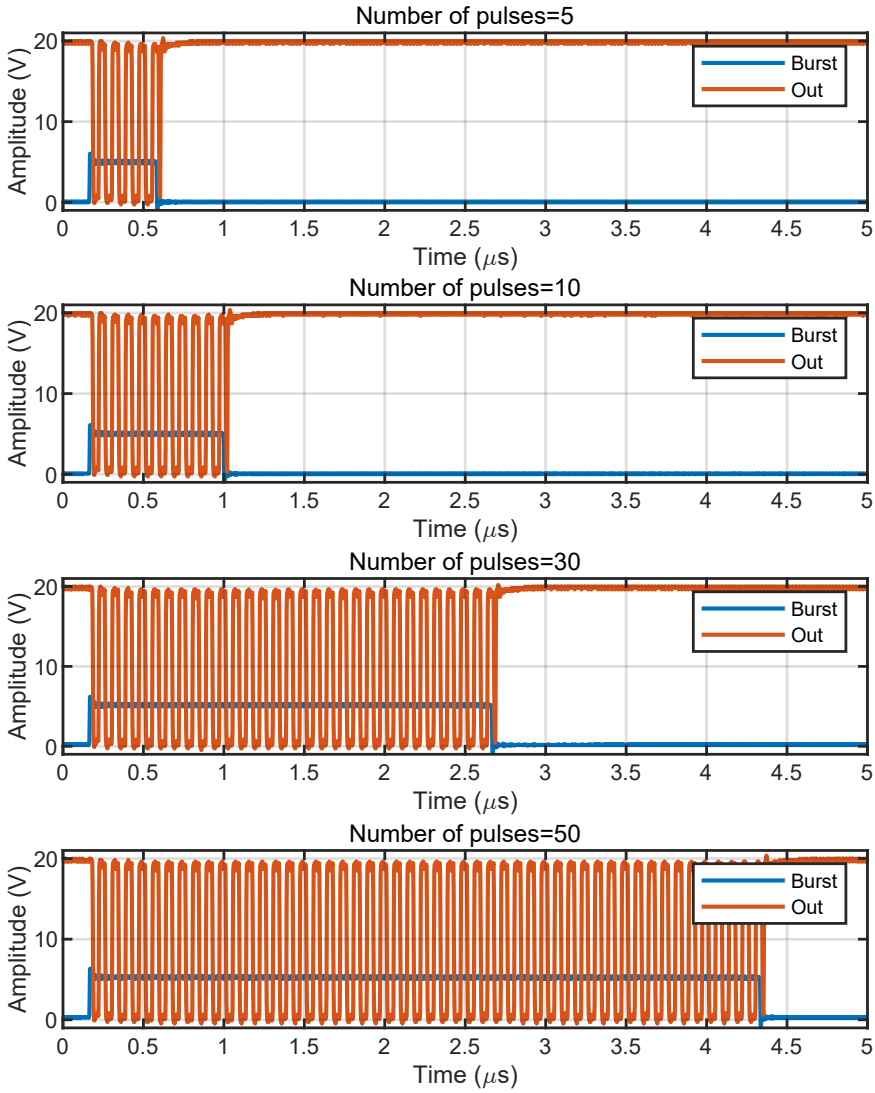

Fig. 6.38: The measured output waveforms of the beamformer channels while the pulse duration was controlled.

been applied to the transmit channels; thus, the measured power consumption from the 20-V power supply represents only the power consumed by the HV drivers, not the total power delivered to the piezoelectric transducers. From Fig. 6.40, the power consumption from every power supply increases linearly with the *DC*. Furthermore, for every *DC*, the power consumed from the 20-V, 5-V, and 1.8-V power supply is approximately responsible for 72%, 24%, and 4% of the total power consumption, respectively. The power consumed by the transmitter ASIC leads to a temperature rise in the ASIC, which can be measured by monitoring the V_{BE} of the diode-connected BJT that acts as a temperature sensor. In this regard, the temperature sensor is biased with a current of 10 µm, and then the analog

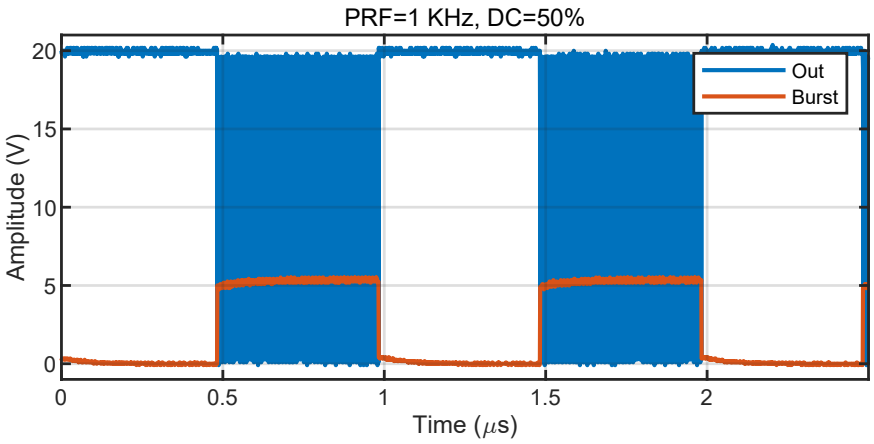

Fig. 6.39: The measured output waveforms of the beamformer channels for typical sonication parameters of *PRF*=1 KHz and *DC*=50%.

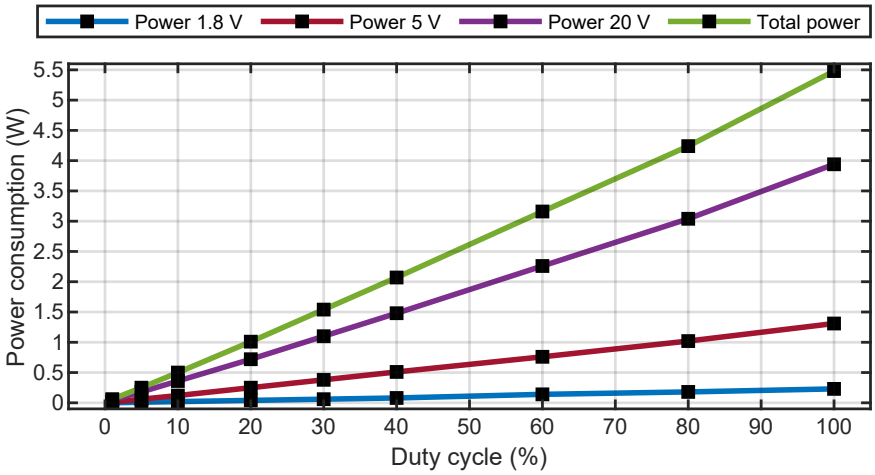

Fig. 6.40: The measured power consumption breakdown of the CMOS chip.

voltage of V_{BE} (i.e., V_E in Fig. 6.24(a)) is connected to a 12-bit 1 MS/s SAR-ADC of the FPGA. After performing an averaging of 256 times, the digitized data is sent to the GUI. Then, the GUI performs another 512 times averaging and divides the measured voltage by the temperature sensitivity of the BJT transistor, which, according to the simulation, was around 1.9 mV/°C (Fig. 6.24(b)). Next, the temperature difference from the steady-state temperature when the ASIC is off demonstrates the temperature rise as a result of the current dissipation in the ASIC. In order to mimic a real scenario, the ASIC was programmed with given phases corresponding with forming a focal spot at a depth of 5 mm from the surface of the transducer with a steering angle of zero. As shown in Fig. 6.41, before turning on the *Burst* signal, the temperature of the ASIC was measured for 30 seconds. Then, all 4228 transmit channels turn on for 60 seconds, generating 20-V 12-MHz pulses with a *PRF* of 1 KHz. Finally, the ASIC turned off, and the temperature was recorded for another

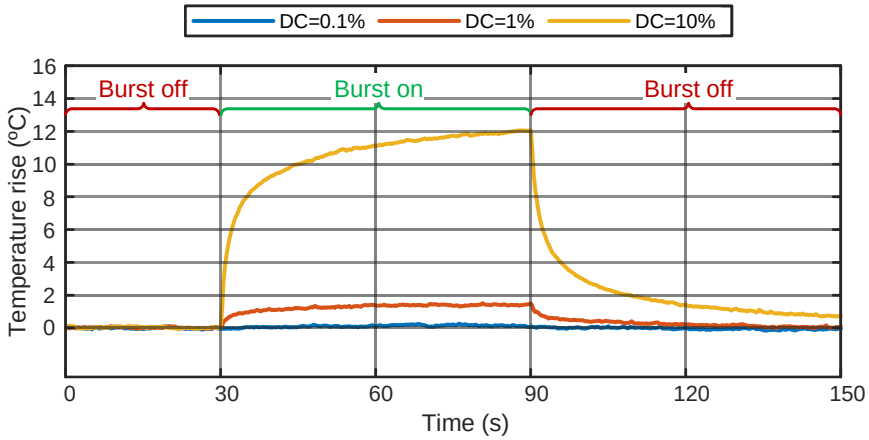

Fig. 6.41: The temperature rise in the ASIC before, during, and after turning on the whole ASIC to generate 20-V 12-MHz pulses with a *PRF* of 1 KHz. During this experiment, the transmit channels were configured to form a focal spot at a depth of 5 mm and a steering angle of zero.

60 seconds. This experiment has been repeated for three different *DC*s of 0.1%, 1%, and 10%. As shown in Fig. 6.41, the temperature rise increases with *DC*; although the temperature rise is negligible for a *DC* of 0.1%, it reaches a temperature rise of 12°C for a *DC* of 10%. It is worth mentioning that this measurement does not include the loads of piezoelectric transducers. In this regard, higher temperature rises are expected when the ASIC is integrated with piezoelectric transducers. Although this measurement is achieved by utilizing a *PRF* of 1 kHz, most recent studies on US neuromodulation have utilized a *PRF* in the range of 0.1-1 kHz [112]. In terms of the utilized duty cycle, studying the reported experiments reveals that, although most of the experiments on stimulation and suppression of the neural activity have utilized a duty cycle of 50% and 5% [112], respectively, there are studies that have achieved ultrasound stimulation or suppression of neural activity with duty cycles as low as 1% [272].

6.5.2. Simulation Results of the Imaging Circuits

In this work, the imaging circuits were designed to demonstrate that full aperture TX systems operating at a high frequency of 12 MHz could also include a sub-aperture imaging system. Given the focus on the TX part of the system, the imaging circuits were validated via simulation, only. In this regard, this section presents the simulation results of the planar wave transmitters, the receiver channels, and the data transmitters. As discussed in the previous section, the transmit channels in the ASIC can also generate compound planar waves to perform high frame-rate ultrasound imaging. In order to simulate the ASIC in terms of planar wave propagation, an imaging pulse, which is a single pulse of 12 MHz, was used as an input while the transmit channels were configured in imaging mode. The transmitters were programmed to generate planar wave pulses with angles of 0, 2.5, and 5 degrees, with the output waveforms of five consecutive transmit channels shown in Fig. 6.42. The delays between consecutive transmit channels are 3.77 ns and 1.75 ns for transmit angles of 2.5 and 5 degrees, respectively, verifying the functionality of the ASIC

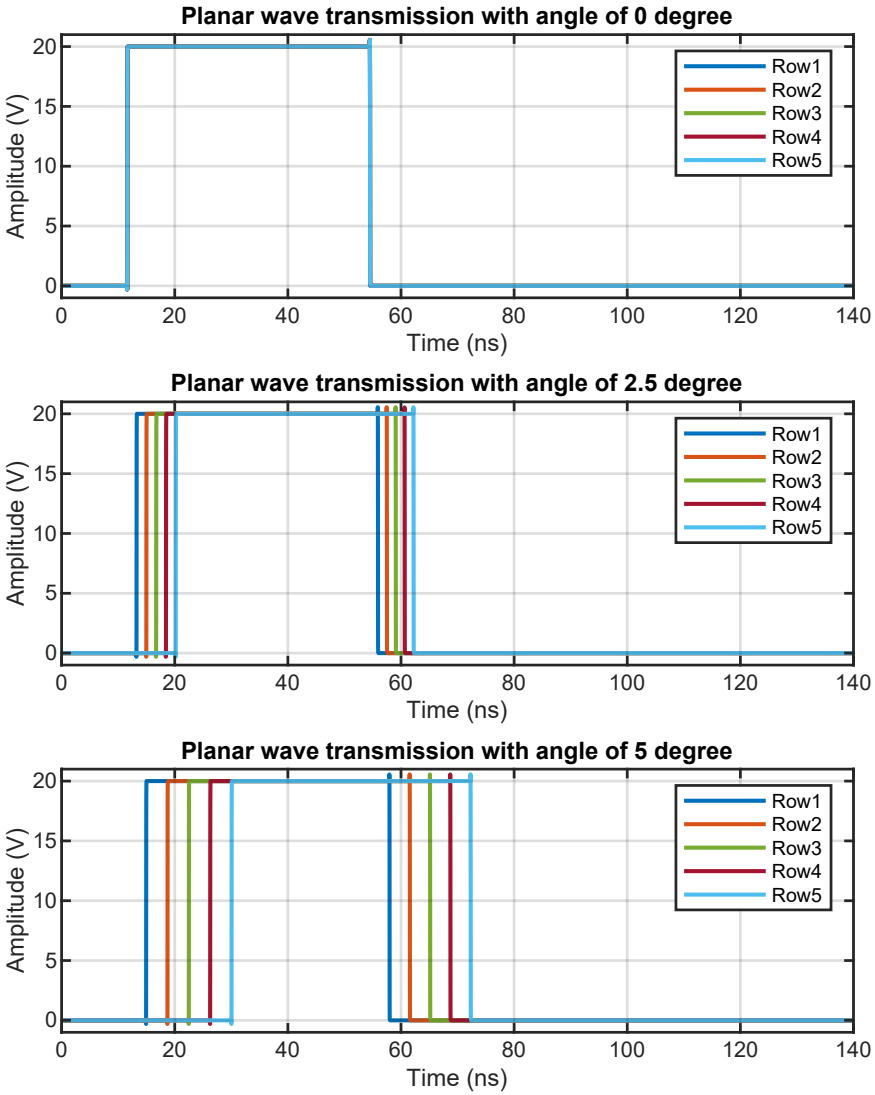

Fig. 6.42: The transient output waveform of the transmit channels while the ASIC was configured to generate planar waves with transmit angles of 0, 2.5, and 5 degrees.

in generating compound planar waves.

Fig. 6.43 depicts the receive transfer function of the analog front-end, which is obtained by applying sinusoidal inputs of varying frequency to the input of the AFE. When the PGA gain is set to 0 dB, the input current is converted to a voltage signal by the LNA with a gain of 100 dBΩ. The simulation results show the expected gain range of 102 dBΩ to 128 dBΩ with a gain step of 13 dBΩ. In the highest gain setting, the cut-off frequency is set to 23.2 MHz. The input-referred noise spectrum is shown in Fig. 6.44. This spectrum is achieved for different PGA gain settings. The input-referred noise is lower in the highest

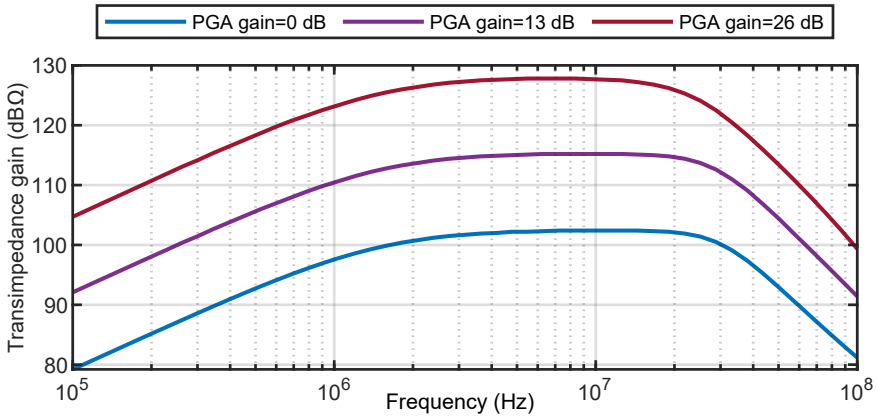

Fig. 6.43: The simulated transfer function of the analog front-end for different PGA gain settings.

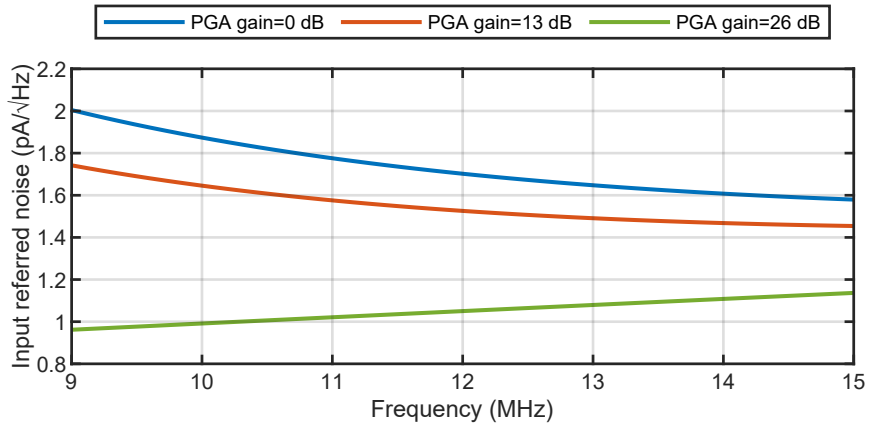

Fig. 6.44: The input referred noise of the analog front-end.

gain configuration; however, as the gain slightly decreases with frequency in the in-band frequencies (Fig. 6.43, the input-referred noise also increases slightly with frequency in the highest gain frequency. Considering a bandwidth of 50% for the piezoelectric transducer [266], the total input-referred in-band (9-15 MHz) noise is 4.25 nA and 2.57 nA for the lowest and highest gain setting. In order to evaluate the linearity and SNR of the receive signal chain, a sinusoidal input was applied to the analog front-end, while the digitized data at the output of the ADC was utilized to plot the frequency spectrum, which is shown in Fig. 6.45. The simulation results show a 35.1-dB in-band (9-15 MHz) SNR. The skirt around the fundamental frequency may be due to a limited number of points in the simulation. This can be improved by choosing large FFT points. However, it leads to longer simulation time.

The data generated by the ADCs is transmitted to the interface board using the data transmitters inside the ASIC. As discussed in the previous section, the data transmitters include a DLL, data links, and LVDS drivers. In order to verify the functionality of the DLL, a 96-MHz clock was applied to the DLL. The output signal of the DLL is shown in Fig.

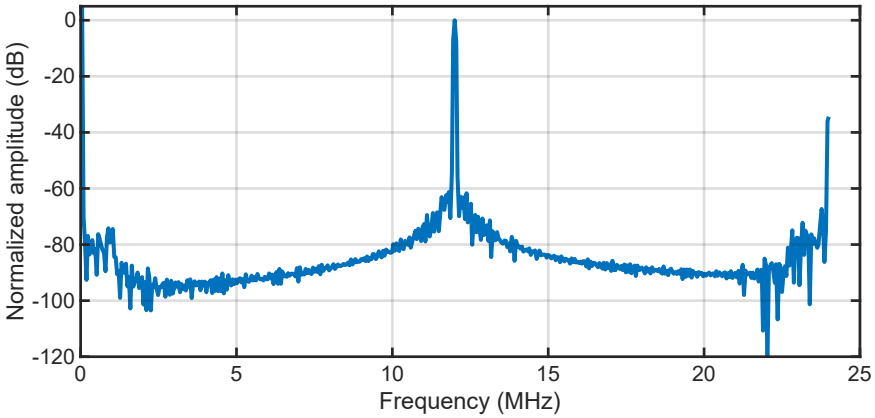

Fig. 6.45: The output spectrum of the receive signal chain for a 12-MHz sinusoidal input signal.

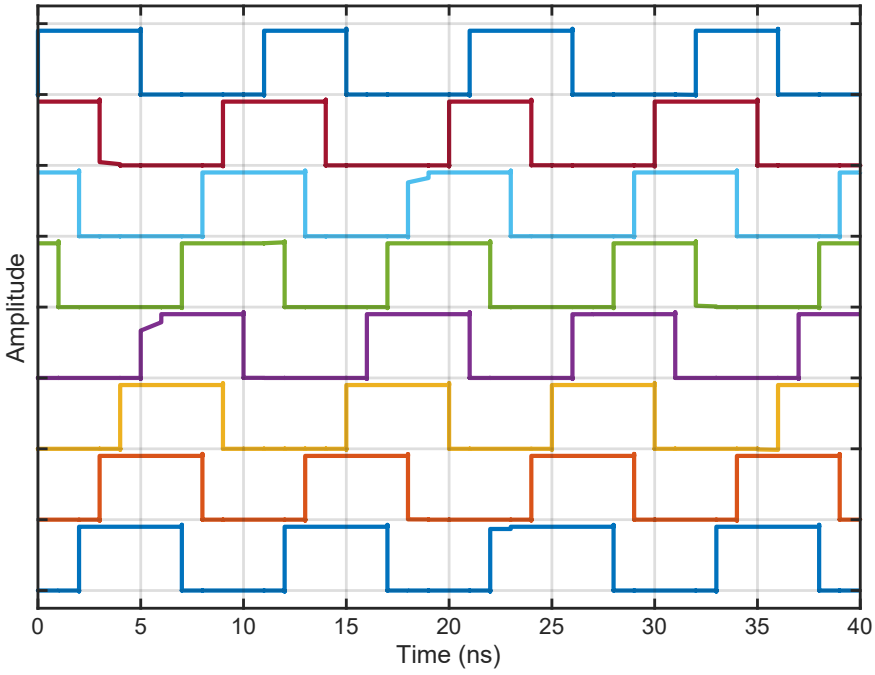

Fig. 6.46: The output signals of the DLL, which are applied to the data link.

6.46, verifying the functionality of the DLL in dividing a 96-MHz clock into eight equally delayed clocks required for the data links. Then, the whole data transmitter is simulated, including the DLL, data link, and LVDS driver. Fig. 6.47 illustrates the differential output of the LVDS driver while model of the bond pad and the wire bonds is applied to the LVDS driver.

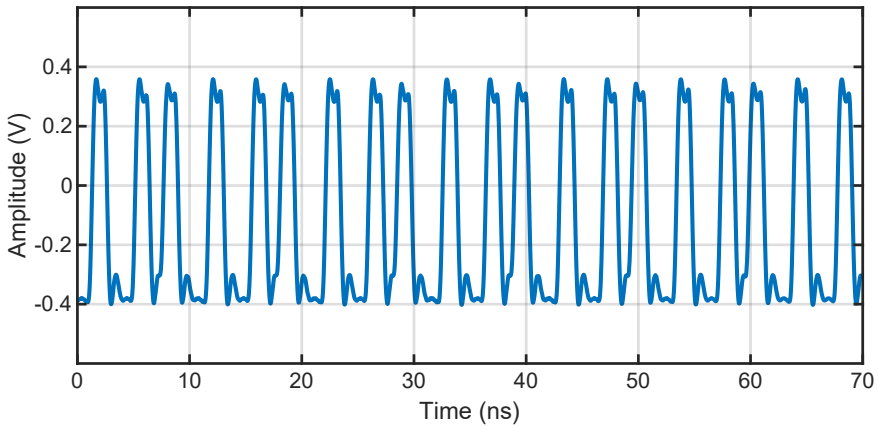

Fig. 6.47: The output signals of the LVDS driver.

6.6. Discussion

Table 6.1 compares this work against the state-of-the-art 2D phased array transmitter ASICs. According to the author's knowledge, this work offers the first ASIC for US neuromodulation featuring imaging capabilities with frequency above 10 MHz. The transmit ASIC includes 4228 transmit channels to perform preclinical US neuromodulation experiments with rats. The transmit channels can perform both phased wave transmission for neuromodulation and compound planar wave transmission for high-frame-rate US imaging. The ASIC includes 8 receiver channels, in which every receiver channel will be connected to 12 piezoelectric transducers. Since this ASIC consumes relatively large transient power, in order to reduce the gap between the peak transient current and the average current, the phase quantization resolution has increased from 3 bits to 4 bits, facilitating the design of the PMU chip and reducing the peak current specifications of the battery for future battery-powered operation. In terms of frequency, this work operates at 12 MHz, offering the highest frequency among the state-of-the-art phased-array transmitter ASICs. Hence, this transmitter ASIC, after the integration with the piezoelectric transducers, can form a focal spot with a volumetric resolution as small as 0.001 mm^3. In terms of the phasing capability, the transmitter ASIC performs 4-bit in-chip beamforming, allowing the ASIC to steer the focal spot without significant influence on US intensity and spatial resolution at the focal spot while avoiding unnecessarily complicated circuits and high power-consuming circuits [40]. Regarding the pitch size, the transmit channels of this work occupy an area of 62.5×62.5 μm^2 which is compatible with pitch-matched configuration, leading to a steerable focal spot in the 3D space without any grating lobes in the beam profile. Unlike [244], the driving signals of the piezoelectric transducers are generated in the ASIC, delivering HV pulses to the piezoelectric transducers with a maximum amplitude of 20 V, which is four times higher than the amplitude of the US transmitter presented in [40] that operates at 5 V and, hence, leads to a limited US intensity. On the other hand, the transmitter ASIC presented in [243] and [53] generate pulses with an amplitude of 60 V, which is needed to drive the CMUT transducers, resulting in increasing the dynamic power consumption of the chip. The transmitter ASIC consumes a power of 1.26

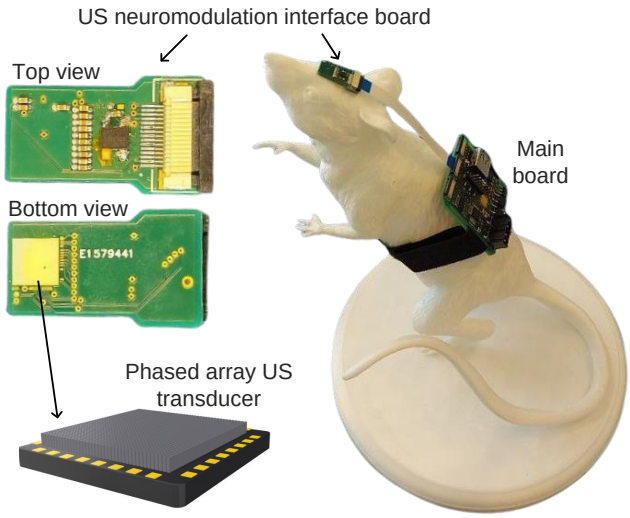

Fig. 6.48: The envisioned application of the US phased array transducer on preclinical US neuromodulation studies on rats.

mW per transmit channel; however, this represents the power consumption of the ASIC whiteout a load applied to the ASIC. In order to obtain an estimation of the power consumption of the transmitter ASIC after the integration with the piezoelectric transducers, the complete BVD model (Section 4.2) is utilized to perform circuit-level simulation, which showed that the power consumption per channel has increased to 5.2 mW, which is dominated by the current dissipation from the 20-V supply. In summary, this work presents a high-voltage, high-frequency 2D phased array transmitter ASIC, in which its integration with piezoelectric transducers leads to a small form factor phased array US transducer. Considering the potential of the ASIC in generating a steerable focal spot with high spatial resolution coupled with its small size, as shown in Fig. 6.48, this ASIC can highly empower preclinical US neuromodulation studies on rodents, such as rats. This work will be followed by the integration of the piezoelectric transducers on the transmitter ASIC for *in vivo* validation.

6.7. Conclusion

This chapter presents a 66×66 array US-guided US transmitter ASIC, which can deliver 12-MHz planar and phased pulses with an amplitude of 20 V, allowing for the implementation of a US transducer for preclinical US neuromodulation experiments on rodents, such as rats. Considering the discussions in Chapter 3, the frequency was set to 12 MHz to gain a high G and Vol_{res}, which is practically achievable with piezoelectric transducers. Taking into account the discussions in Chapters 4 and 5, the driving voltage was chosen at 20 V, allowing for the implementation of a pitch-matched high-voltage beamforming circuit to drive the piezoelectric transducers. Since this work aims to develop a transmitter ASIC for preclinical US neuromodulation studies on rats, the size of the transmitter ASIC was fixed to 5×5 mm^2 corresponding to the small size of the rat's brain. In this regard, con-

sidering the area needed for implementing the shared circuits, the number of channels in the 2D array was set to 4356, corresponding to a 66×66 array of same-sized piezoelectric elements. Although, in Chapter 3, it was shown that 3 bits phase quantization is enough for performing precise US beam steering, the phase quantization resolution in this work was increased to 4 bits to reduce the peak transient current dissipated from the 20-V supply and, hence, facilitate the design of the PMU. To implement 4-bit in-chip phasing, a 2-bit shared DTC along with a 2-bit in-channel DTC was utilized, corresponding to the tradeoff between the power consumption per channel and the complexity of distributing the shared DTC's phased clocks among the transmit channels in the layout level. Furthermore, a temperature sensor was added to the ASIC to monitor the temperature rise in the ASIC. The measurement results proved the functionality of the transmitter ASIC in generating 12-MHz 20-V pulses with a phase quantization resolution of 4 bits. The measurement results demonstrated that the |DNL| and |INL| across the 2D array were less than 0.4 delay LSB and 0.5 delay LSB, respectively, verifying the linearity of the phasing circuits.

The ASIC also includes eight groups of receiver channels, which are connected to 96 receive piezoelectric transducers. The ASIC allows for monitoring the location of the focal spot using synthetic aperture imaging, in which the echoes received by the 96 RX elements are digitized in 6 successive pulse-echo sequences. To add receiver channels to the 2D array, a sub-array of 4×4 transmit channels is replaced with a receive channel. In order to investigate the effect of the transmit channels removal on the US beam profile, k-Wave simulations have been conducted, showing the negligible influence of the removed transmit channels on the acoustic parameters of the focal spot. In order to minimize the number of connections between the ASIC and the interface board, each group of six piezoelectric transducers will be connected to a front-end circuit using an analog multiplexer. The front-end circuit amplifies the echoes and reduces the input dynamic range of the received echoes. Then, to reduce the number of connections further, each group of two front-end circuits is connected to one ADC, which digitizes the received input signals. Then, the digital data is sent to the main board through the data transmitters in the ASIC to enable the image construction, hence allowing for monitoring of the location of the focal spot. This work will follow with the integration of the piezoelectric transducers on the transmitted ASIC, leading to a miniaturized phased array US transmitter ASIC suitable for preclinical US neuromodulation experiments on rats.

Table 6.1: Comparison of this work with state-of-the-art transmitter ASICs.

	[243]	[244]	[53]	[40]	[46]	This work
Application	HIFU	US neuromo.	US neuromo.	US neuromo. US powering	US neuromo. US powering	US neuromo. US powering
CMOS process	Maxim HV	Discrete	0.18-µm HV	0.18-µm LV	0.18-µm HV	0.18-µm HV
Chip area (mm^2)	8×8	N/A	8×8	5×4	0.9×1.3	5×5
# of TX	1024-2D	256-2D	1024-2D	676-2D	144-2D	4228-2D
Imaging capability	No	No	No	No	No	Yes
Beam steering	Center focus	2D	2D	2D	2D	2D
Phasing resolution	N/A	N/A	4-bits	6-bits	3-bits	4-bits
Driving Vpp (V)	60	27-external	60	5	20	20
Pitch (µm)	250 (0.84λ)	1100 (0.74λ)	250 (0.57λ)	135 (0.91λ)	62.5 (0.5λ)	62.5 (0.5λ)
Frequency (MHz)	5	1	3.4	8.4	12	12
Power consumption per channel (mW)	N/A	N/A	254[a] (meas.)	N/A	1.6[b] (meas.) 10.9[c] (simu.)	1.26[b] (meas.) 5.2[d] (simu.)

[a]Calculated average power consumption from the measurement results in the continuous pulsing mode. The CMUT transducers are integrated with the CMOS chip.
[b]Average power consumption in the continuous pulsing mode while no load is applied to the CMOS chip.
[c]Calculated average power consumption in the continuous pulsing mode. During the circuit-level simulation, the piezoelectric transducers were modeled as a load of 0.4 pF||20 KΩ 4.2, and applied to the transmit channels.
[d]Calculated average power consumption in the continuous pulsing mode extracted from circuit-level simulation when the piezoelectric load is modeled with the complete BVD model introduced in Section 4.2.

7

Conclusions and Recommendations

7.1. Introduction

This chapter concludes the thesis by expressing the key messages of the research project, the main contributions, and the recommendations for future research. Section 7.2 highlights the motivations and challenges for developing a US transmitter for preclinical US neuromodulation experiments. Then, a brief review of every chapter is presented to describe how this research thesis has addressed these challenges. Next, Section 7.3 describes the main contributions of this work in addressing the main challenges in developing an ultrasound transmitter for preclinical US neuromodulation applications. Finally, Section 7.4 presents the recommendations for future research projects that can follow this research thesis.

7.2. Conclusions

Ultrasound neuromodulation represents a rapidly evolving field within neuroscience and clinical neurology, offering a precise and noninvasive modality to treat neurological conditions. However, the technological challenges hinder the potential of US neuromodulation. The large size of the conventional US transmitters restricts clinical research to acute and TFUS treatments during hospital visits. Taking into account US attenuation in the skull, the sonication frequency in TFUS is typically limited to below 1 MHz, resulting in a low spatial resolution. In this regard, precise home treatments utilizing US neuromodulation require implantable US transmitters placed on the brain surface with a partially removed skull, allowing for increasing the frequency and, hence, improving the spatial resolution. In addition to the clinical research, the technological gap in the preclinical studies restricts the efficacy and reliability of US neuromodulation experiments on rodents, which are the typical animal models for developing new treatments. Preclinical US neuromodulation studies lack a proper US transmitter to fit rodents' heads. Currently used US transmitters in preclinical research are bulky, which not only restricts the experiments to head-fixed

anesthetized animals but also does not allow conducting of behavioral studies on freely moving animals. In this regard, there is a need for developing a minimally invasive miniaturized US transmitter, enabling preclinical US neuromodulation studies on freely moving rodents with high spatial resolution and 3D control over the focal spot location anywhere in the brain.

Chapter 2 explores the recent findings in the field of US neuromodulation and provides a summary of the optimum sonication parameters for reliable US neuromodulation. Then, a comprehensive review is conducted to study the available US transducers, their driving electronics, and the integration techniques to form the final US transmitter, gaining an insight into the best methods for implementing a US transmitter that meets the required sonication and physical requirements for preclinical US neuromodulation on rodents. In addition to having a small form factor, the US transmitter should support electronic beam steering to correct for the misalignment that may occur during the US transmitter implantation, which can be achieved by utilizing a US phased array transmitter. Furthermore, considering the small size of the neurons, high-frequency US transmitters are needed to maximize the spatial resolution. Moreover, a proper US transmitter demands electronic circuits capable of generating not only phased pulses needed for phased array beam steering but also high-voltage pulses required for achieving a sufficient level of US intensity to perform reliable US neuromodulation. In this regard, this research thesis aims to develop a high-voltage and high-frequency transmitter ASIC suitable for the integration with a 2D array of piezoelectric transducers, forming a miniaturized US phased array transmitter for preclinical research on rodents.

Chapter 3 offers a system-level study on 2D phased array US transmitters, in which the driving voltage, the phase quantization resolution, the frequency, and the array length significantly influence the power consumption of the ASIC and the spatial resolution and the US intensity at the focal spot. The introduced system-level study allows optimizing the electrical and physical parameters of the phased array to maximize focal gain and spatial resolution while offering the lowest power consumption. In terms of frequency, the system-level study has shown that although increasing the frequency improves the focal gain and the spatial resolution, it is primarily limited by the kerf size resulting from the dicing process. In this regard, the effective area of the piezoelectric transducer elements decreases significantly at frequencies above 16 MHz; hence, the resonance frequency is chosen between 12-16 MHz, considering the tradeoff between the spatial resolution and the active area of the piezoelectric transducers. The length of the array also directly improves the spatial resolution and the focal gain; however, it is limited by the size of the rodents' heads. Regarding the phase quantization resolution, the system-level study demonstrated that 3-bit resolution is optimal for quantizing the phase of the beamforming channels.

Chapter 4 describes the development of high frequency and high voltage beamforming channels needed to improve the focal gain and spatial resolution in US phased array transmitters. Considering the tradeoff between the area of the beamforming channel and the frequency, this chapter first tried to find the minimum area needed to implement a high-frequency and HV beamforming channel. In this regard, in this chapter, we developed 36-V 12-MHz and 20-V 15-MHz beamforming channels in TSMC 0.18 µm BCD technology, highlighting that the maximum driving voltages for a pitch-matched 12-MHz and 15-MHz beamforming channel are 36 V and 20 V. The measurement results proved the function-

ality of the beamforming channels in generating high-voltage phased pulses. Since the beamforming channels dissipate current from a high-voltage supply, the high power consumption of the transmitter ASIC raises the temperature in the ASIC and may damage the piezoelectric transducers and the biological tissues. To reduce power consumption further, this chapter also introduced a power-efficient HV pulser that utilizes a per-channel two-step charge recycling method. The presented HV pulser is capable of delivering 15-MHz 10-V pulses to the piezoelectric transducers. The simulation results showed that the power consumption was reduced by 40.9% compared with that of the conventional HV pulser.

Chapter 5 presents a 20-V 12×12 phased array transmitter ASIC to validate the findings in Chapter 3. The transmitter ASIC consists of a shared DTC and a 12×12 array of 20-V beamforming channels with a channel area of 62.5×62.5 μm^2 corresponding to a frequency of 12 MHz. The measurement results validated the phasing functionality of the transmitter ASIC, showing a maximum DNL of 0.35 delay LSB. The k-Wave simulation results utilizing the measured pulses of the transmitter ASIC showed the capability of the ASIC to form a precise focal spot at the desired depth. The ASIC is also capable of controlling the US intensity by adjusting the driving voltage. Moreover, the ASIC performs 3-bit phasing for a broader range of frequencies, allowing it to be integrated with US transducers with different resonance frequencies.

Chapter 6 introduces a phased array transmitter ASIC, which can be integrated with a 2D array of piezoelectric transducers, forming a US transmitter for preclinical US neuromodulation studies on rats. The transmitter ASIC includes a 66×66 array of beamforming channels, which generate 12-MHz pulses with an amplitude of 20 V. Considering the findings in other chapters, the frequency and the driving voltage were set to 12 MHz and 20 V to maximize the spatial resolution and the US intensity at the focal spot. Since this transmitter ASIC aims for preclinical studies on rats, the size of the ASIC was defined by the size of the rat's heads, leading to a 66×66 array of beamforming channels with an active area of 62.5×62.5 μm^2. Although it has been demonstrated in Chapter 3 that 3-bit phase quantization resolution is enough for precise US beam steering, the phase quantization resolution has been increased to 4 bits to reduce the peak transient current dissipated from the 20-V supply, avoiding complicated circuitry in the PMU. In this regard, a 2-bit shared DTC along with a 2-bit in-channel DTC are utilized to perform 4-bit phase quantization, offering a good tradeoff between the power consumption of the transmitter ASIC and the complexity of routing of shared DTC's phased clocks among the beamforming channels in the layout level. Moreover, a temperature sensor was utilized to measure the temperature rise in the ASIC. The measurement results proved the functionality of the transmitter ASIC in delivering 12-MHz 20-V pulses with a phase quantization of 4 bits. Phased array US transmitters allow for electronically adjusting the location of the focal spot. However, reliable US neuromodulation also demands monitoring the location of the focal spot and the delivered intensity to the tissue. In this regard, in order to implement real-time feedback on the location of the focal spot, imaging pixels are added to the 2D transmitter array, allowing for performing US imaging after every cycle of US wave transmission. This work continues toward the integration with piezoelectric transducers, and then, *in vivo* verification.

7.3. Main Contributions

1. **System-level study of 2D phased array US transmitters: (Chapter 3)**

   Although phased array US transmitters are widely common in the medical field, there was a lack of a comprehensive study on the propagation of the US waves from a 2D phased array US transmitter in biological tissue. This gap in the system-level study of phased array US transmitters prevents the designers from optimizing the US transmitters for therapeutic applications. In this regard, this research thesis has conducted a system-level analysis to study the influence of the phased array's physical parameters on the power consumption of the ASIC, the focal gain, and the spatial resolution of the US focal spot. This simulation has been conducted using the k-Wave toolbox in Matlab, modeling the propagation of US waves in the brain that was the focus of our research. The simulation results proved that increasing the frequency improves the focal gain and spatial resolution of the focal spot; however, it shows that the kerf size influences the focal gain negatively at frequencies higher than 16 MHz. Since the phase quantization resolution affects the complexity and the power consumption of the driving electronics, simulation studies have been performed to examine the influence of the phase quantization resolution on the focal spot properties. The simulation results showed that 3-bit phase quantization resolution is sufficient for performing precise US beam steering. This system-level study paves the way for implementing an optimum phased array transmitter in terms of power consumption and focal spot properties. This contribution addresses research questions 1 and 2 in Chapter 2.

2. **High-frequency HV beamforming channel: (Chapter 4)**

   In order to maximize the spatial resolution for achieving precise neuromodulation, high-frequency phased array US transmitters are needed. However, increasing the frequency results in smaller pitch sizes and, consequently, smaller areas to implement an HV beamforming channel. The beamforming channels reported in the literature occupy a large area, which restricts the development of high-frequency phased array US transmitters. Thus, in this chapter, we have developed area-efficient high-voltage beamforming channels to develop a high-frequency transmitter ASIC. In this regard, a 36-V 12-MHz beamforming channel was developed; then, to increase the frequency further, a 20-V 15-MHz beamforming channel was implemented. The high-frequency beamforming channels were designed and realized in TSMC 0.18-µm BCD technology. The measurement results proved the functionality of the beamforming channels in generating phased HV and high-frequency pulses. These low-area HV beamforming channels allow for implementing a high-frequency phased array transmitter, leading to higher spatial resolution in the US focal spot. This contribution addresses research question 3 in Chapter 2.

3. **Power-efficient HV pulser using two-step charge recycling: (Chapter 4)**

   Beamforming channels play a dominant role in the overall power consumption of the transmitter ASIC. While conventional beamforming channels suffer from poor power efficiency, in this work, we introduced a power-efficient 10-V pulser. The proposed pulser utilizes two per-channel capacitors to store the charge at the end

of every phase and reuse it at the start of the next phase. Simulation results in TSMC 0.18-µm BCD technology demonstrated that the power-efficient HV pulser reduces the power consumption by 40.9% compared with the conventional HV pulser. The proposed HV pulser enables the implementation of power-efficient phased array US transmitters needed for wearable and implantable applications. This contribution addresses research question 4 in Chapter 2.

4. **12×12 array 12-MHz 20-V transmitter ASIC: (Chapter 5)**

   High-frequency phased array transmitter ASICs are needed to achieve higher spatial resolution at the US focal spot. While the literature lacks a high-frequency transmitter ASIC, we have developed a 12-MHz 12×12 transmitter ASIC. Each beamforming channel occupies an active area of 62.5×62.5 μm^2, corresponding to the US half-wavelength at 12 MHz to prevent the appearance of grating lobes in the beam profile. The transmitter ASIC has been realized in TSMC 0.18-µm BCD technology. The measurement results verify the capability of the ASIC in generating 20-V phased pulses with 3-bit resolution while the maximum DNL was 0.35 delay LSB. This contribution addresses research questions 3 and 5 in Chapter 2.

5. **US-guided 66×66 array 12-MHz 20-V transmitter ASIC for preclinical US neuromodulation on rats: (Chapter 6)**

   Currently, a technological gap impedes performing the preclinical US neuromodulation studies on rodents, which is a key step before developing any treatments. There is a lack of a miniaturized US transmitter that fits the rodents' heads and generates a steerable focal spot with high spatial resolution. In this regard, corresponding to the size of rats' brains, a 12-MHz 66×66 phased array transmitter ASIC was developed, which is capable of driving the piezoelectric transducers with a controllable pulse duration and an amplitude of 20 V. Furthermore, a temperature sensor has been utilized to measure the temperature increase in the ASIC, allowing to avoid tissue damage due to the excessive heat generation. The ASIC has been designed and implemented in TSMC 0.18-µm BCD technology. The measurement results confirm the ability of the ASIC to generate 20-V pulses with a phase quantization resolution of 4 bits. Furthermore, 8 groups of 12 receivers are added to the 2D array by randomly removing transmitter elements. These receiving channels allow for performing US imaging to monitor the location of the focal spot. The simulation results have verified the functionality of the imaging circuits. This work continues with the electrical validation of the receivers through measurements of the ASICs. Then, the ASIC will be integrated with a 2D array of piezoelectric transducers, leading to a high-frequency US-guided phased array US transmitter, which paves the way for extensive preclinical experiments in the field of US neuromodulation. This contribution addresses research question 5 in Chapter 2.

7.4. Recommendations for Future Research

This thesis has developed a phased array transmitter ASIC that can be integrated with piezoelectric transducers to form a US transmitter, empowering researchers to perform

preclinical US neuromodulation studies. This section provides recommendations to pave the way for the implementation of US neuromodulation therapies.

- The consumed power by US transmitter ASICs may lead to excessive heat generation and cause tissue damage in wearable and implantable US neuromodulators. In this regard, further efforts are needed to minimize the power consumption of the transmitter ASIC. In order to improve the power efficiency of the beamforming channels introduced in Section 4.2, the HV transistors can be replaced with a stack of three 5-V transistors, delivering 15-V pulses to the US transducers, similar to the 10-V pulser in Section 4.3. However, the storage capacitors can be shared among a group of beamforming channels to avoid large storage capacitors per channel. This method not only reduces the parasitic capacitance of the driver transistors but also allows for recycling the charge stored on the parasitic capacitance of the US transducer.

- Improving the overall power efficiency of the US transmitters also requires developing loss-less techniques to integrate the piezoelectric transducers on transmitter ASICs. The overall efficiency of the US transmitters can be achieved by developing proper backing and matching layers for dense 2D arrays of piezoelectric transducers with high electromechanical conversion coefficients, such as PMN-PT, allowing to enhance the overall transmit efficiency by increasing the US transducer quality factor and by reducing the acoustic impedance mismatch between the tissue and the piezoelectric transducer.

- Since power dissipation is one of the critical design aspects in US transmitter ASICs, it may cause excessive heat and damage the tissue. Hence, proper cooling systems are needed to avoid any damage to the tissue or the piezoelectric transducers. This can be achieved by developing a microfluidic cooling system integrated with the transmitter ASIC [273].

- This work has focused on developing US transmitters for preclinical US neuromodulation studies. In the next steps, translating the findings from preclinical studies to human applications requires developing flexible phased array US transducers suitable for wearable and implantable applications. Developing a flexible phased array US transducer not only requires specialized methods to make the US transducer flexible but also demands active phase correction techniques to form a US focal spot, depending on the shape of the transducer.

References

[1] *World health organization*, 2024. [Online]. Available: https://www.who.int/.

[2] V. L. Feigin, T. Vos, E. Nichols, *et al.*, "The global burden of neurological disorders: Translating evidence into policy", *The Lancet Neurol.*, vol. 19, no. 3, pp. 255–265, Mar. 2020.

[3] Z. L. Teo, Y.-C. Tham, M. Yu, *et al.*, "Global prevalence of diabetic retinopathy and projection of burden through 2045: Systematic review and meta-analysis", *Ophthalmology*, vol. 128, no. 11, pp. 1580–1591, 2021.

[4] V. L. Feigin, T. Vos, F. Alahdab, *et al.*, "Burden of neurological disorders across the us from 1990-2017: A global burden of disease study", *JAMA neurology*, vol. 78, no. 2, pp. 165–176, 2021.

[5] V. L. Feigin, M. Brainin, B. Norrving, *et al.*, "World stroke organization (WSO): Global stroke fact sheet 2022", *International Journal of Stroke*, vol. 17, no. 1, pp. 18–29, 2022.

[6] Z. Ou, J. Pan, S. Tang, *et al.*, "Global trends in the incidence, prevalence, and years lived with disability of parkinson's disease in 204 countries/territories from 1990 to 2019", *Frontiers in public health*, vol. 9, p. 776 847, 2021.

[7] E. Beghi, "The epidemiology of epilepsy", *Neuroepidemiology*, vol. 54, no. 2, pp. 185–191, 2020.

[8] A. Achar and C. Ghosh, "COVID-19-associated neurological disorders: The potential route of CNS invasion and blood-brain barrier relevance", *Cells*, vol. 9, no. 11, p. 2360, 2020.

[9] E. Xu, Y. Xie, and Z. Al-Aly, "Long-term neurologic outcomes of COVID-19", *Nature medicine*, vol. 28, no. 11, pp. 2406–2415, 2022.

[10] F. Ceban, S. Ling, L. M. Lui, *et al.*, "Fatigue and cognitive impairment in post-COVID-19 syndrome: A systematic review and meta-analysis", *Brain, behavior, and immunity*, vol. 101, pp. 93–135, 2022.

[11] S. Abu-Rumeileh, A. Abdelhak, M. Foschi, H. Tumani, and M. Otto, "Guillain–Barré syndrome spectrum associated with COVID-19: An up-to-date systematic review of 73 cases", *Journal of neurology*, vol. 268, no. 4, pp. 1133–1170, 2021.

[12] N. J. Abbott, A. A. Patabendige, D. E. Dolman, S. R. Yusof, and D. J. Begley, "Structure and function of the blood–brain barrier", *Neurobiology of disease*, vol. 37, no. 1, pp. 13–25, 2010.

[13] A. Akhtar, A. Andleeb, T. S. Waris, *et al.*, "Neurodegenerative diseases and effective drug delivery: A review of challenges and novel therapeutics", *Journal of controlled release*, vol. 330, pp. 1152–1167, 2021.

[14] C. Giaccotto, R. E. Santerre, and J. A. Vernon, "Drug prices and research and development investment behavior in the pharmaceutical industry", *The Journal of Law and Economics*, vol. 48, no. 1, pp. 195–214, 2005.

[15] A. B. Csoka and M. Szyf, "Epigenetic side-effects of common pharmaceuticals: A potential new field in medicine and pharmacology", *Medical hypotheses*, vol. 73, no. 5, pp. 770–780, 2009.

[16] C. Oriuwa, A. Mollica, A. Feinstein, *et al.*, "Neuromodulation for the treatment of functional neurological disorder and somatic symptom disorder: A systematic review", *Journal of Neurology, Neurosurgery & Psychiatry*, vol. 93, no. 3, pp. 280–290, 2022.

[17] *Parkinson's foundation*, 2024. [Online]. Available: https://www.parkinson.org/.

[18] *Epilepsy foundation*, 2024. [Online]. Available: https://www.epilepsy.com/.

[19] A. Chopra, B. T. Klassen, and M. Stead, "Current clinical application of deep-brain stimulation for essential tremor", *Neuropsychiatric disease and treatment*, pp. 1859–1865, 2013.

[20] H. Li, L. Cui, J. Li, Y. Liu, and Y. Chen, "Comparative efficacy and acceptability of neuromodulation procedures in the treatment of treatment-resistant depression: A network meta-analysis of randomized controlled trials", *Journal of affective disorders*, vol. 287, pp. 115–124, 2021.

[21] J. K. Jolly, S. K. Wagner, P. Martus, *et al.*, "Transcorneal electrical stimulation for the treatment of retinitis pigmentosa: A multicenter safety study of the OkuStim system (TESOLA-study)", *Ophthalmic research*, vol. 63, no. 3, pp. 234–243, 2020.

[22] Y. Shi, K. J. Burchiel, V. C. Anderson, and W. H. Martin, "Deep brain stimulation effects in patients with tinnitus", *Otolaryngology—Head and Neck Surgery*, vol. 141, no. 2, pp. 285–287, 2009.

[23] A. M. Lozano, N. Lipsman, H. Bergman, *et al.*, "Deep brain stimulation: Current challenges and future directions", *Nature Reviews Neurology*, vol. 15, no. 3, pp. 148–160, 2019.

[24] M. Hallett, "Transcranial magnetic stimulation: A primer", *Neuron*, vol. 55, no. 2, pp. 187–199, 2007.

[25] S. Barnett, B. Perry, J. Dalrymple-Alford, and L. Parr-Brownlie, "Optogenetic stimulation: Understanding memory and treating deficits", *Hippocampus*, vol. 28, no. 7, pp. 457–470, 2018.

[26] J. Blackmore, S. Shrivastava, J. Sallet, C. R. Butler, and R. O. Cleveland, "Ultrasound neuromodulation: A review of results, mechanisms and safety", *Ultrasound in medicine & biology*, vol. 45, no. 7, pp. 1509–1536, 2019.

[27] H. S. Gougheri, A. Dangi, S. R. Kothapalli, and M. Kiani, "A comprehensive study of ultrasound transducer characteristics in microscopic ultrasound neuromodulation", *IEEE Trans. Biomed. Circuits Syst.*, vol. 13, no. 5, pp. 835–847, Jun. 2019.

[28] J. Volkmann, "Deep brain stimulation for the treatment of parkinson's disease", *Journal of clinical neurophysiology*, vol. 21, no. 1, pp. 6–17, 2004.

[29] S. G. Boccard, E. A. Pereira, and T. Z. Aziz, "Deep brain stimulation for chronic pain", *Journal of Clinical Neuroscience*, vol. 22, no. 10, pp. 1537–1543, 2015.

[30] R. P. Munhoz, M. Picillo, S. H. Fox, *et al.*, "Eligibility criteria for deep brain stimulation in parkinson's disease, tremor, and dystonia", *Canadian Journal of Neurological Sciences*, vol. 43, no. 4, pp. 462–471, 2016.

[31] C. A. Artusi, L. Lopiano, and F. Morgante, "Deep brain stimulation selection criteria for parkinson's disease: Time to go beyond CAPSIT-PD", *Journal of clinical medicine*, vol. 9, no. 12, p. 3931, 2020.

[32] L. Morgante, F. Morgante, E. Moro, *et al.*, "How many parkinsonian patients are suitable candidates for deep brain stimulation of subthalamic nucleus? results of a questionnaire", *Parkinsonism & related disorders*, vol. 13, no. 8, pp. 528–531, 2007.

[33] S. Jiang, X. Wu, N. J. Rommelfanger, Z. Ou, and G. Hong, "Shedding light on neurons: Optical approaches for neuromodulation", *National Science Review*, vol. 9, no. 10, nwac007, 2022.

[34] M. White, M. Mackay, and R. G. Whittaker, "Taking optogenetics into the human brain: Opportunities and challenges in clinical trial design", *Open access journal of clinical trials*, pp. 33–41, 2020.

[35] M. Lindner, M. J. Gilhooley, S. Hughes, and M. W. Hankins, "Optogenetics for visual restoration: From proof of principle to translational challenges", *Progress in Retinal and Eye Research*, vol. 91, p. 101 089, 2022.

[36] H. R. Siebner, K. Funke, A. S. Aberra, *et al.*, "Transcranial magnetic stimulation of the brain: What is stimulated?–a consensus and critical position paper", *Clinical Neurophysiology*, vol. 140, pp. 59–97, 2022.

[37] S. Zibman, G. S. Pell, N. Barnea-Ygael, Y. Roth, and A. Zangen, "Application of transcranial magnetic stimulation for major depression: Coil design and neuroanatomical variability considerations", *European Neuropsychopharmacology*, vol. 45, pp. 73–88, 2021.

[38] H. W. Chase, M. A. Boudewyn, C. S. Carter, and M. L. Phillips, "Transcranial direct current stimulation: A roadmap for research, from mechanism of action to clinical implementation", *Molecular psychiatry*, vol. 25, no. 2, pp. 397–407, 2020.

[39] K. Funke, "Quite simple at first glance–complex at a second: Modulating neuronal activity by tDCS", *The Journal of Physiology*, vol. 591, no. Pt 16, p. 3809, 2013.

[40] T. Costa, C. Shi, K. Tien, J. Elloian, F. A. Cardoso, and K. L. Shepard, "An integrated 2D ultrasound phased array transmitter in CMOS with pixel pitch-matched beamforming", *IEEE Trans. Biomed. Circuits Syst.*, vol. 15, no. 4, pp. 731–742, Jul. 2021.

[41] W. J. Tyler, Y. Tufail, M. Finsterwald, M. L. Tauchmann, E. J. Olson, and C. Majestic, "Remote excitation of neuronal circuits using low-intensity, low-frequency ultrasound", *PloS one*, vol. 3, no. 10, e3511, Oct. 2008.

[42] T. Di Ianni, K. P. Morrison, B. Yu, K. R. Murphy, L. de Lecea, and R. D. Airan, "High-throughput ultrasound neuromodulation in awake and freely behaving rats", *Brain stimulation*, vol. 16, no. 6, pp. 1743–1752, 2023.

[43] H.-C. Kim, W. Lee, J. Kunes, *et al.*, "Transcranial focused ultrasound modulates cortical and thalamic motor activity in awake sheep", *Scientific reports*, vol. 11, no. 1, p. 19 274, 2021.

[44] P.-F. Yang, M. A. Phipps, A. T. Newton, *et al.*, "Neuromodulation of sensory networks in monkey brain by focused ultrasound with MRI guidance and detection", *Scientific reports*, vol. 8, no. 1, p. 7993, 2018.

[45] C. Sarica, J.-F. Nankoo, A. Fomenko, *et al.*, "Human studies of transcranial ultrasound neuromodulation: A systematic review of effectiveness and safety", *Brain Stimulation*, vol. 15, no. 3, pp. 737–746, 2022.

[46] H. Rivandi and T. L. Costa, "A 2D ultrasound phased-array transmitter ASIC for high-frequency US stimulation and powering", *IEEE Trans. Biomed. Circuits Syst.*, pp. 1–12, Jun. 2023.

[47] H. Kim, S. J. Taghados, K. Fischer, L.-S. Maeng, S. Park, and S.-S. Yoo, "Noninvasive transcranial stimulation of rat abducens nerve by focused ultrasound", *Ultrasound in medicine & biology*, vol. 38, no. 9, pp. 1568–1575, 2012.

[48] H. Estrada, J. Robin, A. Özbek, *et al.*, "High-resolution fluorescence-guided transcranial ultrasound mapping in the live mouse brain", *Science Advances*, vol. 7, no. 50, eabi5464, 2021.

[49] W. Lee, P. Croce, R. W. Margolin, A. Cammalleri, K. Yoon, and S.-S. Yoo, "Transcranial focused ultrasound stimulation of motor cortical areas in freely-moving awake rats", *BMC neuroscience*, vol. 19, pp. 1–14, 2018.

[50] K. R. Murphy, J. S. Farrell, J. L. Gomez, *et al.*, "A tool for monitoring cell type–specific focused ultrasound neuromodulation and control of chronic epilepsy", *Proceedings of the National Academy of Sciences*, vol. 119, no. 46, e2206828119, 2022.

[51] E. Kim, E. Anguluan, J. Kum, *et al.*, "Wearable transcranial ultrasound system for remote stimulation of freely moving animal", *IEEE Transactions on Biomedical Engineering*, vol. 68, no. 7, pp. 2195–2202, 2020.

[52] E. Kim, J. Kum, S. H. Lee, and H. Kim, "Development of a wireless ultrasonic brain stimulation system for concurrent bilateral neuromodulation in freely moving rodents", *Frontiers in Neuroscience*, vol. 16, p. 1 011 699, 2022.

[53] C. Seok, O. J. Adelegan, A. Ö. Biliroğlu, F. Y. Yamaner, and Ö. Oralkan, "A wearable ultrasonic neurostimulator—part ii: A 2D CMUT phased array system with a flip-chip bonded ASIC", *IEEE Trans. Biomed. Circuits Syst.*, vol. 15, no. 4, pp. 705–718, 2021.

[54] S. A. Lee, H. A. Kamimura, and E. E. Konofagou, "Displacement imaging during focused ultrasound median nerve modulation: A preliminary study in human pain sensation mitigation", *IEEE Trans. Ultrason. Ferroelectr. Freq. Control*, vol. 68, no. 3, pp. 526–537, 2020.

[55] W. C. Elmore, W. C. Elmore, and M. A. Heald, *Physics of waves*. Courier Corporation, 1985.

[56] N. M. Tole *et al.*, *Basic physics of ultrasonographic imaging*. World Health Organization, 2005.

[57] J. Arle and J. L. Shils, *Innovative neuromodulation*. Academic Press, 2017.

[58] T. L. Szabo, *Diagnostic ultrasound imaging: inside out*. Academic press, 2004.

[59] C. Pasquinelli, L. G. Hanson, H. R. Siebner, H. J. Lee, and A. Thielscher, "Safety of transcranial focused ultrasound stimulation: A systematic review of the state of knowledge from both human and animal studies", *Brain Stimulation*, vol. 12, no. 6, pp. 1367–1380, 2019.

[60] V. Goyal, S. Rajguru, A. I. Matic, S. R. Stock, and C.-P. Richter, "Acute damage threshold for infrared neural stimulation of the cochlea: Functional and histological evaluation", *The Anatomical Record: Advances in Integrative Anatomy and Evolutionary Biology*, vol. 295, no. 11, pp. 1987–1999, 2012.

[61] H. Kim, A. Chiu, S. D. Lee, K. Fischer, and S.-S. Yoo, "Focused ultrasound-mediated non-invasive brain stimulation: Examination of sonication parameters", *Brain stimulation*, vol. 7, no. 5, pp. 748–756, 2014.

[62] M. Plaksin, E. Kimmel, and S. Shoham, "Cell-type-selective effects of intramembrane cavitation as a unifying theoretical framework for ultrasonic neuromodulation", *eneuro*, vol. 3, no. 3, 2016.

[63] A. Fomenko, C. Neudorfer, R. F. Dallapiazza, S. K. Kalia, and A. M. Lozano, "Low-intensity ultrasound neuromodulation: An overview of mechanisms and emerging human applications", *Brain stimulation*, vol. 11, no. 6, pp. 1209–1217, 2018.

[64] J. K. Mueller, L. Ai, P. Bansal, and W. Legon, "Computational exploration of wave propagation and heating from transcranial focused ultrasound for neuromodulation", *Journal of neural engineering*, vol. 13, no. 5, p. 056 002, 2016.

[65] U. Food, D. Administration, *et al.*, "Marketing clearance of diagnostic ultrasound systems and transducers: Guidance for industry and food and drug administration staff", *Center for Devices and Radiological Health, US Food and Drug Administration, Rockville, MD, Tech. Rep*, 2019.

[66] P. P. Ye, J. R. Brown, and K. B. Pauly, "Frequency dependence of ultrasound neurostimulation in the mouse brain", *Ultrasound in medicine & biology*, vol. 42, no. 7, pp. 1512–1530, 2016.

[67] *U.s. food and drug administration*, 2023. [Online]. Available: https://www.fda.gov/.

[68] T. S. Riis, D. A. Feldman, L. C. Vonesh, *et al.*, "Durable effects of deep brain ultrasonic neuromodulation on major depression: A case report", *Journal of Medical Case Reports*, vol. 17, no. 1, p. 449, 2023.

[69] K. Yoon, W. Lee, J. E. Lee, *et al.*, "Effects of sonication parameters on transcranial focused ultrasound brain stimulation in an ovine model", *PloS one*, vol. 14, no. 10, e0224311, 2019.

[70] C. Puleo and V. Cotero, "Noninvasive neuromodulation of peripheral nerve pathways using ultrasound and its current therapeutic implications", *Cold Spring Harb. Perspect. Med.*, vol. 10, no. 2, a034215, Feb. 2020.

[71] W. Legon, L. Ai, P. Bansal, and J. K. Mueller, "Neuromodulation with single-element transcranial focused ultrasound in human thalamus", *Human brain mapping*, vol. 39, no. 5, pp. 1995–2006, 2018.

[72] E. N. Harvey, "The effect of high frequency sound waves on heart muscle and other irritable tissues", *American Journal of Physiology-Legacy Content*, vol. 91, no. 1, pp. 284–290, 1929.

[73] R. Meyers, W. J. Fry, F. J. Fry, L. L. Dreyer, D. F. Schultz, and R. F. Noyes, "Early experiences with ultrasonic irradiation of the pallidofugal and nigral complexes in hyperkinetic and hypertonic disorders", *Journal of neurosurgery*, vol. 16, no. 1, pp. 32–54, 1959.

[74] W. J. Fry, "Intense ultrasound—a new tool for neurological research", *Journal of Mental Science*, vol. 100, no. 418, pp. 85–96, 1954.

[75] Y. Tufail, A. Matyushov, N. Baldwin, *et al.*, "Transcranial pulsed ultrasound stimulates intact brain circuits", *Neuron*, vol. 66, no. 5, pp. 681–694, 2010.

[76] Y. Meng, K. Hynynen, and N. Lipsman, "Applications of focused ultrasound in the brain: From thermoablation to drug delivery", *Nature Reviews Neurology*, vol. 17, no. 1, pp. 7–22, 2021.

[77] Y. Yuan, J. Yan, Z. Ma, and X. Li, "Effect of noninvasive focused ultrasound stimulation on gamma oscillations in rat hippocampus", *Neuroreport*, vol. 27, no. 7, pp. 508–515, 2016.

[78] Y. Younan, T. Deffieux, B. Larrat, M. Fink, M. Tanter, and J.-F. Aubry, "Influence of the pressure field distribution in transcranial ultrasonic neurostimulation", *Medical physics*, vol. 40, no. 8, p. 082 902, 2013.

[79] X. Huang, Z. Lin, L. Meng, *et al.*, "Non-invasive low-intensity pulsed ultrasound modulates primary cilia of rat hippocampal neurons", *Ultrasound in Medicine & Biology*, vol. 45, no. 5, pp. 1274–1283, 2019.

[80] Y. Yuan, Y. Zhao, H. Jia, *et al.*, "Cortical hemodynamic responses under focused ultrasound stimulation using real-time laser speckle contrast imaging", *Frontiers in Neuroscience*, vol. 12, p. 269, 2018.

[81] H. A. Kamimura, S. Wang, H. Chen, *et al.*, "Focused ultrasound neuromodulation of cortical and subcortical brain structures using 1.9 MHz", *Medical physics*, vol. 43, no. 10, pp. 5730–5735, 2016.

[82] C. Aurup, H. A. Kamimura, and E. E. Konofagou, "High-resolution, focused ultrasound-mediated neuromodulation and detailed analysis of electromyography characteristics reveals a high degree of spatial specificity in elicited responses in mice in vivo", in *2018 IEEE International Ultrasonics Symposium (IUS)*, IEEE, 2018, pp. 1–4.

[83] G.-F. Li, H.-X. Zhao, H. Zhou, *et al.*, "Improved anatomical specificity of non-invasive neuro-stimulation by high frequency (5 MHz) ultrasound", *Scientific reports*, vol. 6, no. 1, p. 24 738, 2016.

[84] J. A. Fisher and I. Gumenchuk, "Low-intensity focused ultrasound alters the latency and spatial patterns of sensory-evoked cortical responses in vivo", *Journal of Neural Engineering*, vol. 15, no. 3, p. 035 004, 2018.

[85] H. Kim, S. Kim, N. S. Sim, *et al.*, "Miniature ultrasound ring array transducers for transcranial ultrasound neuromodulation of freely-moving small animals", *Brain stimulation*, vol. 12, no. 2, pp. 251–255, 2019.

[86] E. Kim, E. Anguluan, and J. G. Kim, "Monitoring cerebral hemodynamic change during transcranial ultrasound stimulation using optical intrinsic signal imaging", *Scientific reports*, vol. 7, no. 1, p. 13 148, 2017.

[87] H. Kim, M. Y. Park, S. D. Lee, W. Lee, A. Chiu, and S.-S. Yoo, "Suppression of EEG visual-evoked potentials in rats through neuromodulatory focused ultrasound", *Neuroreport*, vol. 26, no. 4, pp. 211–215, 2015.

[88] S.-S. Yoo, A. Bystritsky, J.-H. Lee, *et al.*, "Focused ultrasound modulates region-specific brain activity", *Neuroimage*, vol. 56, no. 3, pp. 1267–1275, 2011.

[89] J. W. Barnard, W. J. Fry, F. J. Fry, and R. F. Krumins, "Effects of high intensity ultrasound on the central nervous system of the cat", *Journal of Comparative Neurology*, vol. 103, no. 3, pp. 459–484, 1955.

[90] H. Hakimova, S. Kim, K. Chu, S. K. Lee, B. Jeong, and D. Jeon, "Ultrasound stimulation inhibits recurrent seizures and improves behavioral outcome in an experimental model of mesial temporal lobe epilepsy", *Epilepsy & Behavior*, vol. 49, pp. 26–32, 2015.

[91] B.-K. Min, A. Bystritsky, K.-I. Jung, *et al.*, "Focused ultrasound-mediated suppression of chemically-induced acute epileptic EEG activity", *BMC neuroscience*, vol. 12, pp. 1–12, 2011.

[92] W. Lee, S. D. Lee, M. Y. Park, *et al.*, "Image-guided focused ultrasound-mediated regional brain stimulation in sheep", *Ultrasound in medicine & biology*, vol. 42, no. 2, pp. 459–470, 2016.

[93] H. Guo, M. Hamilton, S. J. Offutt, *et al.*, "Ultrasound produces extensive brain activation via a cochlear pathway", *Neuron*, vol. 98, no. 5, pp. 1020–1030, 2018.

[94] R. F. Dallapiazza, K. F. Timbie, S. Holmberg, *et al.*, "Noninvasive neuromodulation and thalamic mapping with low-intensity focused ultrasound", *Journal of neurosurgery*, vol. 128, no. 3, pp. 875–884, 2017.

[95] D. Daniels, S. Sharabi, D. Last, *et al.*, "Focused ultrasound-induced suppression of auditory evoked potentials in vivo", *Ultrasound in medicine & biology*, vol. 44, no. 5, pp. 1022–1030, 2018.

[96] H.-C. Kim, W. Lee, D. S. Weisholtz, and S.-S. Yoo, "Transcranial focused ultrasound stimulation of cortical and thalamic somatosensory areas in human", *Plos one*, vol. 18, no. 7, e0288654, 2023.

[97] W. Lee, H. Kim, Y. Jung, I.-U. Song, Y. A. Chung, and S.-S. Yoo, "Image-guided transcranial focused ultrasound stimulates human primary somatosensory cortex", *Scientific reports*, vol. 5, no. 1, p. 8743, 2015.

[98] W. Lee, S. Kim, B. Kim, *et al.*, "Non-invasive transmission of sensorimotor information in humans using an EEG/focused ultrasound brain-to-brain interface", *PloS one*, vol. 12, no. 6, e0178476, 2017.

[99] W. Lee, Y. A. Chung, Y. Jung, I.-U. Song, and S.-S. Yoo, "Simultaneous acoustic stimulation of human primary and secondary somatosensory cortices using transcranial focused ultrasound", *BMC neuroscience*, vol. 17, pp. 1–11, 2016.

[100] W. Lee, H.-C. Kim, Y. Jung, *et al.*, "Transcranial focused ultrasound stimulation of human primary visual cortex", *Scientific reports*, vol. 6, no. 1, p. 34 026, 2016.

[101] P. S. Balasubramanian, A. Singh, C. Xu, and A. Lal, "Ghz ultrasonic chip-scale device induces ion channel stimulation in human neural cells", *Scientific Reports*, vol. 10, no. 1, p. 3075, 2020.

[102] S. Hameroff, M. Trakas, C. Duffield, *et al.*, "Transcranial ultrasound (TUS) effects on mental states: A pilot study", *Brain stimulation*, vol. 6, no. 3, pp. 409–415, 2013.

[103] S.-H. Liu, Y.-L. Lai, B.-L. Chen, and F.-Y. Yang, "Ultrasound enhances the expression of brain-derived neurotrophic factor in astrocyte through activation of TrkB-Akt and calcium-CaMK signaling pathways", *Cerebral cortex*, vol. 27, no. 6, pp. 3152–3160, 2017.

[104] I. Dilevicius, W. A. Serdijn, and T. L. Costa, "Stent with piezoelectric transducers for high spatial resolution ultrasound neuromodulation-a finite element analysis", in *2022 44th Annual International Conference of the IEEE Engineering in Medicine & Biology Society (EMBC)*, IEEE, 2022, pp. 4966–4969.

[105] R. L. King, J. R. Brown, W. T. Newsome, and K. B. Pauly, "Effective parameters for ultrasound-induced in vivo neurostimulation", *Ultrasound in medicine & biology*, vol. 39, no. 2, pp. 312–331, 2013.

[106] B. C. Gibson, J. L. Sanguinetti, B. W. Badran, *et al.*, "Increased excitability induced in the primary motor cortex by transcranial ultrasound stimulation", *Frontiers in neurology*, vol. 9, p. 1007, 2018.

[107] P. S. Yang, H. Kim, W. Lee, *et al.*, "Transcranial focused ultrasound to the thalamus is associated with reduced extracellular GABA levels in rats", *Neuropsychobiology*, vol. 65, no. 3, pp. 153–160, 2012.

[108] S. Sharabi, D. Daniels, D. Last, *et al.*, "Non-thermal focused ultrasound induced reversible reduction of essential tremor in a rat model", *Brain stimulation*, vol. 12, no. 1, pp. 1–8, 2019.

[109] J. Lee, J. C. Callaway, and R. C. Foehring, "Effects of temperature on calcium transients and Ca2+-dependent afterhyperpolarizations in neocortical pyramidal neurons", *Journal of neurophysiology*, vol. 93, no. 4, pp. 2012–2020, 2005.

[110] K. Ishibashi, K. Shimada, T. Kawato, *et al.*, "Inhibitory effects of low-energy pulsed ultrasonic stimulation on cell surface protein antigen C through heat shock proteins GroEL and DnaK in Streptococcus mutans", *Applied and Environmental Microbiology*, vol. 76, no. 3, pp. 751–756, 2010.

[111] Y. Yuan, J. Yan, Z. Ma, and X. Li, "Noninvasive focused ultrasound stimulation can modulate phase-amplitude coupling between neuronal oscillations in the rat hippocampus", *Frontiers in neuroscience*, vol. 10, p. 348, 2016.

[112] J. Dell'Italia, J. L. Sanguinetti, M. M. Monti, A. Bystritsky, and N. Reggente, "Current state of potential mechanisms supporting low intensity focused ultrasound for neuromodulation", *Frontiers in human neuroscience*, vol. 16, p. 872 639, 2022.

[113] B. Krasovitski, V. Frenkel, S. Shoham, and E. Kimmel, "Intramembrane cavitation as a unifying mechanism for ultrasound-induced bioeffects", *Proceedings of the National Academy of Sciences*, vol. 108, no. 8, pp. 3258–3263, 2011.

[114] R. T. Mihran, F. S. Barnes, and H. Wachtel, "Temporally-specific modification of myelinated axon excitability in vitro following a single ultrasound pulse", *Ultrasound in medicine & biology*, vol. 16, no. 3, pp. 297–309, 1990.

[115] J. Kubanek, J. Shi, J. Marsh, D. Chen, C. Deng, and J. Cui, "Ultrasound modulates ion channel currents", *Scientific reports*, vol. 6, no. 1, p. 24 170, 2016.

[116] R. Syeda, M. N. Florendo, C. D. Cox, *et al.*, "Piezo1 channels are inherently mechanosensitive", *Cell reports*, vol. 17, no. 7, pp. 1739–1746, 2016.

[117] K. Venkatachalam and C. Montell, "Trp channels", *Annu. Rev. Biochem.*, vol. 76, pp. 387–417, 2007.

[118] M. Lasser, J. Tiber, and L. A. Lowery, "The role of the microtubule cytoskeleton in neurodevelopmental disorders", *Frontiers in cellular neuroscience*, vol. 12, p. 165, 2018.

[119] G. T. Haar, "Ultrasound bioeffects and safety", *Proceedings of the Institution of Mechanical Engineers, Part H: Journal of Engineering in Medicine*, vol. 224, no. 2, pp. 363–373, 2010.

[120] E. E Konofagou, Y.-S. Tunga, J. Choia, T. Deffieuxa, B. Baseria, and F. Vlachosa, "Ultrasound-induced blood-brain barrier opening", *Current pharmaceutical biotechnology*, vol. 13, no. 7, pp. 1332–1345, 2012.

[121] F. Orsi, P. Arnone, W. Chen, and L. Zhang, "High intensity focused ultrasound ablation: A new therapeutic option for solid tumors", *Journal of cancer research and therapeutics*, vol. 6, no. 4, pp. 414–420, 2010.

[122] H. Baek, K. J. Pahk, M.-J. Kim, I. Youn, and H. Kim, "Modulation of cerebellar cortical plasticity using low-intensity focused ultrasound for poststroke sensorimotor function recovery", *Neurorehabilitation and neural repair*, vol. 32, no. 9, pp. 777–787, 2018.

[123] S.-S. Yoo, K. Yoon, P. Croce, A. Cammalleri, R. W. Margolin, and W. Lee, "Focused ultrasound brain stimulation to anesthetized rats induces long-term changes in somatosensory evoked potentials", *International journal of imaging systems and technology*, vol. 28, no. 2, pp. 106–112, 2018.

[124] H. A. Kamimura, A. Conti, N. Toschi, and E. E. Konofagou, "Ultrasound neuromodulation: Mechanisms and the potential of multimodal stimulation for neuronal function assessment", *Frontiers in physics*, vol. 8, p. 150, 2020.

[125] M. C. Sekhar, E. Veena, N. S. Kumar, K. C. B. Naidu, A. Mallikarjuna, and D. B. Basha, "A review on piezoelectric materials and their applications", *Crystal Research and Technology*, vol. 58, no. 2, p. 2 200 130, 2023.

[126] Q. Zhou, K. H. Lam, H. Zheng, W. Qiu, and K. K. Shung, "Piezoelectric single crystal ultrasonic transducers for biomedical applications", *Progress in materials science*, vol. 66, pp. 87–111, 2014.

[127] H. J. Chilabi, H. Salleh, E. E. Supeni, A. As' arry, K. A. M. Rezali, and A. B. Atrah, "Harvesting energy from planetary gear using piezoelectric material", *Energies*, vol. 13, no. 1, p. 223, 2020.

[128] Y. Chen, K.-H. Lam, D. Zhou, *et al.*, "High performance relaxor-based ferroelectric single crystals for ultrasonic transducer applications", *Sensors*, vol. 14, no. 8, pp. 13 730–13 758, 2014.

[129] M. Habib, I. Lantgios, and K. Hornbostel, "A review of ceramic, polymer and composite piezoelectric materials", *Journal of Physics D: Applied Physics*, vol. 55, no. 42, p. 423 002, 2022.

[130] A. Aabid, M. A. Raheman, Y. E. Ibrahim, *et al.*, "A systematic review of piezoelectric materials and energy harvesters for industrial applications", *Sensors*, vol. 21, no. 12, p. 4145, 2021.

[131] Y. Wu, Y. Ma, H. Zheng, and S. Ramakrishna, "Piezoelectric materials for flexible and wearable electronics: A review", *Materials & Design*, vol. 211, p. 110 164, 2021.

[132] Y. Yang, C. Wang, Y. Li, *et al.*, "Development of scalable 2D plane array for transcranial ultrasonic neuromodulation on non-human primates: An ex vivo study", *IEEE Transactions on Neural Systems and Rehabilitation Engineering*, vol. 28, no. 2, pp. 361–369, 2019.

[133] H. Zhao, C. He, L. Yan, and H. Zhang, "Development of a flexible broadband rayleigh waves comb transducer with nonequidistant comb interval for defect detection of thick-walled pipelines", *Sensors*, vol. 18, no. 3, p. 752, 2018.

[134] B. R. Tittmann, D. A. Parks, and S. O. Zhang, "High temperature piezoelectrics—a comparison", in *Proceedings of the 13th International Symposium on Nondestructive Characterization of Materials (NDCM-XIII), Le Mans, France*, 2013, pp. 20–24.

[135] K. Wong, S. Panda, and I. Ladabaum, "Curved micromachined ultrasonic transducers", in *IEEE Symposium on Ultrasonics, 2003*, IEEE, vol. 1, 2003, pp. 572–576.

[136] W. Lee and Y. Roh, "Ultrasonic transducers for medical diagnostic imaging", *Biomedical engineering letters*, vol. 7, no. 2, pp. 91–97, 2017.

[137] B. Hadimioglu, E. Rawson, R. Lujan, *et al.*, "High-efficiency fresnel acoustic lenses", in *1993 Proceedings IEEE Ultrasonics Symposium*, IEEE, 1993, pp. 579–582.

[138] D. Tarrazó-Serrano, S. Pérez-López, P. Candelas, A. Uris, and C. Rubio, "Acoustic focusing enhancement in fresnel zone plate lenses", *Scientific Reports*, vol. 9, no. 1, p. 7067, 2019.

[139] S. Rahimi, R. M. Jones, and K. Hynynen, "A high-frequency phased array system for transcranial ultrasound delivery in small animals", *IEEE Trans. Ultrason. Ferroelectr. Freq. Control*, vol. 68, no. 1, pp. 127–135, 2020.

[140] K. Saleh and N. Smith, "Two-dimensional ultrasound phased array design for tissue ablation for treatment of benign prostatic hyperplasia", *International Journal of Hyperthermia*, vol. 20, no. 1, pp. 7–31, 2004.

[141] D. H. Turnbull and F. S. Foster, "Beam steering with pulsed two-dimensional transducer arrays", *IEEE Trans. Ultrason. Ferroelectr. Freq. Control*, vol. 38, no. 4, pp. 320–333, 1991.

[142] L. G. Ullate, G. Godoy, O. Martinez, and T. Sánchez, "Beam steering with segmented annular arrays", *IEEE Trans. Ultrason. Ferroelectr. Freq. Control*, vol. 53, no. 10, pp. 1944–1954, 2006.

[143] C. Seok, F. Y. Yamaner, M. Sahin, and Ö. Oralkan, "A wearable ultrasonic neurostimulator-part I: A 1D CMUT phased array system for chronic implantation in small animals", *IEEE Trans. Biomed. Circuits Syst.*, vol. 15, no. 4, pp. 692–704, Jul. 2021.

[144] S. J. Ilham, Z. Kashani, and M. Kiani, "Design and optimization of ultrasound phased arrays for large-scale ultrasound neuromodulation", *IEEE Trans. Biomed. Circuits Syst.*, vol. 15, no. 6, pp. 1454–1466, 2021.

[145] P. Tipsawat, S. J. Ilham, J. I. Yang, Z. Kashani, M. Kiani, and S. Trolier-Mckinstry, "32 element piezoelectric micromachined ultrasound transducer (PMUT) phased array for neuromodulation", *IEEE open journal of ultrasonics, ferroelectrics, and frequency control*, vol. 2, pp. 184–193, 2022.

[146] M. R. Karafi and F. Khorasani, "Evaluation of mechanical and electric power losses in a typical piezoelectric ultrasonic transducer", *Sensors and Actuators A: Physical*, vol. 288, pp. 156–164, 2019.

[147] K. Uchino, Y. Zhuang, and S. O. Ural, "Loss determination methodology for a piezoelectric ceramic: New phenomenological theory and experimental proposals", *Journal of Advanced Dielectrics*, vol. 1, no. 01, pp. 17–31, 2011.

[148] W. P. Mason, "Equivalent electromechanical representation of trapped energy transducers", *Proceedings of the IEEE*, vol. 57, no. 10, pp. 1723–1734, 1969.

[149] F. Pop, B. Herrera, C. Cassella, and M. Rinaldi, "Modeling and optimization of directly modulated piezoelectric micromachined ultrasonic transducers", *Sensors*, vol. 21, no. 1, p. 157, 2020.

[150] S. Sherrit, S. P. Leary, B. P. Dolgin, and Y. Bar-Cohen, "Comparison of the Mason and KLM equivalent circuits for piezoelectric resonators in the thickness mode", in *1999 IEEE Ultrasonics Symposium. Proceedings. International Symposium*, IEEE, vol. 2, 1999, pp. 921–926.

[151] R. Krimholtz, D. A. Leedom, and G. L. Matthaei, "New equivalent circuits for elementary piezoelectric transducers", *Electronics Letters*, vol. 13, no. 6, pp. 398–399, 1970.

[152] K. S. Van Dyke, "The piezo-electric resonator and its equivalent network", *Proceedings of the Institute of Radio Engineers*, vol. 16, no. 6, pp. 742–764, 1928.

[153] R. Song, C. Christoffersen, S. Pichardo, and L. Curiel, "An integrated full-bridge class-de ultrasound transducer driver for hifu applications", in *2016 14th IEEE International New Circuits and Systems Conference (NEWCAS)*, IEEE, 2016, pp. 1–4.

[154] X. Jiang, W. T. Ng, and J. Chen, "A miniaturized low-intensity ultrasound device for wearable medical therapeutic applications", *IEEE Trans. Biomed. Circuits Syst.*, vol. 13, no. 6, pp. 1372–1382, 2019.

[155] Z. Yu, "Low-power receive-electronics for a miniature 3D ultrasound probe", 2012.

[156] M. D'Urbino, C. Chen, Z. Chen, *et al.*, "An element-matched electromechanical ΔΣ ADC for ultrasound imaging", *IEEE J. Solid-State Circuits*, vol. 53, no. 10, pp. 2795–2805, 2018.

[157] E. Moisello, L. Novaresi, E. Sarkar, P. Malcovati, T. L. Costa, and E. Bonizzoni, "PMUT and CMUT devices for biomedical applications: A review", *IEEE Access*, 2024.

[158] J. Li, W. Qu, J. Daniels, *et al.*, "Lead zirconate titanate ceramics with aligned crystallite grains", *Science*, vol. 380, no. 6640, pp. 87–93, 2023.

[159] J. M. Cannata, T. A. Ritter, W.-H. Chen, R. H. Silverman, and K. K. Shung, "Design of efficient, broadband single-element (20-80 MHz) ultrasonic transducers for medical imaging applications", *IEEE Trans. Ultrason. Ferroelectr. Freq. Control*, vol. 50, no. 11, pp. 1548–1557, 2003.

[160] V. T. Rathod, "A review of acoustic impedance matching techniques for piezoelectric sensors and transducers", *Sensors*, vol. 20, no. 14, p. 4051, 2020.

[161] S. Zhang, F. Li, X. Jiang, J. Kim, J. Luo, and X. Geng, "Advantages and challenges of relaxor-pbtio3 ferroelectric crystals for electroacoustic transducers–a review", *Progress in materials science*, vol. 68, pp. 1–66, 2015.

[162] F. Tian, Y. Liu, R. Ma, F. Li, Z. Xu, and Y. Yang, "Properties of PMN-PT single crystal piezoelectric material and its application in underwater acoustic transducer", *Applied Acoustics*, vol. 175, p. 107 827, 2021.

[163] K. Uchino, "Piezoelectric composite materials", in *Advanced Piezoelectric Materials*, Elsevier, 2017, pp. 353–382.

[164] F. Mokhtari, B. Azimi, M. Salehi, S. Hashemikia, and S. Danti, "Recent advances of polymer-based piezoelectric composites for biomedical applications", *Journal of the Mechanical Behavior of Biomedical Materials*, vol. 122, p. 104 669, 2021.

[165] S. Banerjee, S. Bairagi, and S. W. Ali, "A critical review on lead-free hybrid materials for next generation piezoelectric energy harvesting and conversion", *Ceramics International*, vol. 47, no. 12, pp. 16 402–16 421, 2021.

[166] K. Koga and H. Ohigashi, "Piezoelectricity and related properties of vinylidene fluoride and trifluoroethylene copolymers", *Journal of applied physics*, vol. 59, no. 6, pp. 2142–2150, 1986.

[167] P. L. van Neer, L. C. Peters, R. G. Verbeek, *et al.*, "Flexible large-area ultrasound arrays for medical applications made using embossed polymer structures", *Nature communications*, vol. 15, no. 1, p. 2802, 2024.

[168] M. S. Martins, C. L. Faria, T. Matos, *et al.*, "Wideband and wide beam polyvinylidene difluoride (PVDF) acoustic transducer for broadband underwater communications", *Sensors*, vol. 19, no. 18, p. 3991, 2019.

[169] D. Xue, Y. Zhou, H. Bao, C. Zhou, J. Gao, and X. Ren, "Elastic, piezoelectric, and dielectric properties of Ba (Zr0. 2Ti0. 8) O3-50 (Ba0. 7Ca0. 3) TiO3 Pb-free ceramic at the morphotropic phase boundary", *Journal of Applied Physics*, vol. 109, no. 5, 2011.

[170] J. Gao, D. Xue, W. Liu, C. Zhou, and X. Ren, "Recent progress on BaTiO3-based piezoelectric ceramics for actuator applications", in *Actuators*, MDPI, vol. 6, 2017, p. 24.

[171] J. Cai, Y. Wang, D. Jiang, *et al.*, "Beyond fundamental resonance mode: High-order multi-band ALN PMUT for in vivo photoacoustic imaging", *Microsystems & Nanoengineering*, vol. 8, no. 1, p. 116, 2022.

[172] X. Jiang, Y. Lu, H.-Y. Tang, *et al.*, "Monolithic ultrasound fingerprint sensor", *Microsystems & nanoengineering*, vol. 3, no. 1, pp. 1–8, 2017.

[173] K. Roy, J. E.-Y. Lee, and C. Lee, "Thin-film PMUTs: A review of over 40 years of research", *Microsystems & Nanoengineering*, vol. 9, no. 1, p. 95, 2023.

[174] A. S. Ergun, G. G. Yaralioglu, and B. T. Khuri-Yakub, "Capacitive micromachined ultrasonic transducers: Theory and technology", *Journal of aerospace engineering*, vol. 16, no. 2, pp. 76–84, 2003.

[175] I. Wygant, "A comparison of CMUTs and piezoelectric transducer elements for 2D medical imaging based on conventional simulation models", in *2011 IEEE International Ultrasonics Symposium*, IEEE, 2011, pp. 100–103.

[176] J. Joseph, B. Ma, and B. Khuri-Yakub, "Applications of capacitive micromachined ultrasonic transducers: A comprehensive review", *IEEE Trans. Ultrason. Ferroelectr. Freq. Control*, vol. 69, no. 2, pp. 456–467, 2021.

[177] A. Caronti, G. Caliano, R. Carotenuto, *et al.*, "Capacitive micromachined ultrasonic transducer (CMUT) arrays for medical imaging", *Microelectronics Journal*, vol. 37, no. 8, pp. 770–777, 2006.

[178] *Verasonics*, 2024. [Online]. Available: https://verasonics.com/.

[179] A. Javid, C. Zhao, and M. Kiani, "A 16-channel high-voltage ASIC with programmable delay lines for image-guided ultrasound neuromodulation", in *2022 IEEE Biomedical Circuits and Systems Conference (BioCAS)*, IEEE, 2022, pp. 419–423.

[180] H.-S. Yoon, C. Chang, J. H. Jang, *et al.*, "Ex Vivo HIFU experiments using a 32×32-element CMUT array", *IEEE Trans. Ultrason. Ferroelectr. Freq. Control*, vol. 63, no. 12, pp. 2150–2158, 2016.

[181] J. H. Jang, C. Chang, M. F. Rasmussen, *et al.*, "Integration of a dual-mode catheter for ultrasound image guidance and HIFU ablation using a 2-D CMUT array", in *2017 IEEE International Ultrasonics Symposium (IUS)*, IEEE, 2017, pp. 1–4.

[182] A. Bhuyan, J. W. Choe, B. C. Lee, *et al.*, "Integrated circuits for volumetric ultrasound imaging with 2-D CMUT arrays", *IEEE Trans. Biomed. Circuits Syst.*, vol. 7, no. 6, pp. 796–804, 2013.

[183] M. Gourdouparis, C. Shi, Y. He, *et al.*, "6.2 an ultrasound-powering TX with a global charge-redistribution adiabatic drive achieving 69% power reduction and 53° maximum beam steering angle for implantable applications", in *2024 IEEE International Solid-State Circuits Conference (ISSCC)*, IEEE, vol. 67, 2024, pp. 102–104.

[184] R. Salahi, M. Moezzi, and M. Kiani, "Self-image-guided ultrasonic transceiver design for reliably powering mm-sized implants", *AEU-International Journal of Electronics and Communications*, vol. 176, p. 155 125, 2024.

[185] Y. M. Hopf, D. S. dos Santos, B. W. Ossenkoppele, *et al.*, "A pitch-matched high-frame-rate ultrasound imaging ASIC for catheter-based 3-D probes", *IEEE J. Solid-State Circuits*, 2023.

[186] Y. M. Hopf, B. W. Ossenkoppele, M. Soozande, *et al.*, "A pitch-matched transceiver ASIC with shared hybrid beamforming ADC for high-frame-rate 3-D intracardiac echocardiography", *IEEE J. Solid-State Circuits*, vol. 57, no. 11, pp. 3228–3242, 2022.

[187] D. E. Dausch, K. H. Gilchrist, J. B. Carlson, S. D. Hall, J. B. Castellucci, and O. T. Von Ramm, "In vivo real-time 3-D intracardiac echo using PMUT arrays", *IEEE Trans. Ultrason. Ferroelectr. Freq. Control*, vol. 61, no. 10, pp. 1754–1764, 2014.

[188] D. Wildes, W. Lee, B. Haider, *et al.*, "4-D ICE: A 2-D array transducer with integrated ASIC in a 10-Fr catheter for real-time 3-D intracardiac echocardiography", *IEEE Trans. Ultrason. Ferroelectr. Freq. Control*, vol. 63, no. 12, pp. 2159–2173, 2016.

[189] C. Chen, Z. Chen, D. Bera, *et al.*, "A pitch-matched front-end ASIC with integrated subarray beamforming ADC for miniature 3-D ultrasound probes", *IEEE J. Solid-State Circuits*, vol. 53, no. 11, pp. 3050–3064, 2018.

[190] J.-Y. Um, Y.-J. Kim, S.-E. Cho, *et al.*, "An analog-digital hybrid RX beamformer chip with non-uniform sampling for ultrasound medical imaging with 2D CMUT array", *IEEE Trans. Biomed. Circuits Syst.*, vol. 8, no. 6, pp. 799–809, 2014.

[191] T. Kim, S. Shin, and S. Kim, "An 80.2 dB DR 23.25 mW/channel 8-channel ultrasound receiver with a beamforming embedded SAR ADC", *IEEE Trans. Circuits Syst. II: Exp. Briefs*, vol. 66, no. 9, pp. 1487–1491, 2018.

[192] Z. Kashani, S. J. Ilham, and M. Kiani, "Design and optimization of ultrasonic links with phased arrays for wireless power transmission to biomedical implants", *IEEE Trans. Biomed. Circuits Syst.*, vol. 16, no. 1, pp. 64–78, 2022.

[193] I. O. Wygant, X. Zhuang, D. T. Yeh, *et al.*, "Integration of 2D CMUT arrays with front-end electronics for volumetric ultrasound imaging", *IEEE Trans. Ultrason. Ferroelectr. Freq. Control*, vol. 55, no. 2, pp. 327–342, 2008.

[194] K. Chen, H.-S. Lee, and C. G. Sodini, "A column-row-parallel ASIC architecture for 3-D portable medical ultrasonic imaging", *IEEE J. Solid-State Circuits*, vol. 51, no. 3, pp. 738–751, 2015.

[195] C. Chen, S. B. Raghunathan, Z. Yu, *et al.*, "A prototype PZT matrix transducer with low-power integrated receive ASIC for 3-D transesophageal echocardiography", *IEEE Trans. Ultrason. Ferroelectr. Freq. Control*, vol. 63, no. 1, pp. 47–59, 2015.

[196] C. Shi, T. Costa, J. Elloian, and K. Shepard, "Monolithic integration of micron-scale piezoelectric materials with CMOS for biomedical applications", in *2018 IEEE International Electron Devices Meeting (IEDM)*, IEEE, 2018, pp. 4–5.

[197] G. K. Wardhana, T. L. Costa, and M. Mastrangeli, "An acoustically transparent electrical cap for piezoelectric ultrasound transducers on silicon", in *Proceedings*, MDPI, vol. 97, 2024, p. 50.

[198] G. Kook, Y. Jo, C. Oh, *et al.*, "Multifocal skull-compensated transcranial focused ultrasound system for neuromodulation applications based on acoustic holography", *Microsystems & Nanoengineering*, vol. 9, no. 1, p. 45, 2023.

[199] B. Koele, "Integrating ultrasound neuromodulation and imaging: A system concept for a non-invasive image-guided vagus nerve stimulator", M.Sc. Dissertation, Microelectronics Department, Delft University of Technology, The Netherlands, 2021.

[200] M. E. Downs, S. A. Lee, G. Yang, S. Kim, Q. Wang, and E. E. Konofagou, "Non-invasive peripheral nerve stimulation via focused ultrasound in vivo", *Phys. Med. Biol.*, vol. 63, no. 3, p. 035 011, Jan. 2018.

[201] J. Vo, T. C. Chang, K. I. Shea, M. Myers, A. Arbabian, and S. Vasudevan, "Assessment of miniaturized ultrasound-powered implants: An in vivo study", *J. Neural Eng.*, vol. 17, no. 1, p. 016 072, Feb. 2020.

[202] A. Rashidi *et al.*, "Ultrasonically powered and controlled microsystem for dual-wavelength optogenetics with a multi-load regulation scheme", *IEEE Solid-State Circuits Lett.*, vol. 6, pp. 33–36, Jan. 2023.

[203] L. Zhao, M. Annayev, Ö. Oralkan, and Y. Jia, "An ultrasonic energy harvesting IC providing adjustable bias voltage for pre-charged CMUT", *IEEE Trans. Biomed. Circuits Syst.*, vol. 16, no. 5, pp. 842–851, Oct. 2022.

[204] D. Seo *et al.*, "Wireless recording in the peripheral nervous system with ultrasonic neural dust", *Neuron*, vol. 91, no. 3, pp. 529–539, Jul. 2016.

[205] C. Shi, T. Costa, J. Elloian, Y. Zhang, and K. L. Shepard, "A 0.065-mm^3 monolithically-integrated ultrasonic wireless sensing mote for real-time physiological temperature monitoring", *IEEE Trans. Biomed. Circuits Syst.*, vol. 14, no. 3, pp. 412–424, Jun. 2020.

[206] C. Shi *et al.*, "Application of a sub–0.1-mm^3 implantable mote for in vivo real-time wireless temperature sensing", *Sci. Adv.*, vol. 7, no. 19, p. 6312, May 2021.

[207] S. H. Kondapalli, Y. Alazzawi, M. Malinowski, T. Timek, and S. Chakrabartty, "Multiaccess in vivo biotelemetry using sonomicrometry and m-scan ultrasound imaging", *IEEE Trans. Biomed. Eng.*, vol. 65, no. 1, pp. 149–158, Jan. 2018.

[208] C. Chen *et al.*, "A front-end ASIC with receive sub-array beamforming integrated with a 32×32 PZT matrix transducer for 3-D transesophageal echocardiography", *IEEE J. Solid-State Circuits*, vol. 52, no. 4, pp. 994–1006, Jan. 2017.

[209] A. Bhuyan *et al.*, "Integrated circuits for volumetric ultrasound imaging with 2-D CMUT arrays", *IEEE Trans. Biomed. Circuits Syst.*, vol. 7, no. 6, pp. 796–804, Dec. 2013.

[210] Y. Tsehay *et al.*, "Low-intensity pulsed ultrasound neuromodulation of a rodent's spinal cord suppresses motor evoked potentials", *IEEE Trans. Biomed. Eng.*, pp. 1–11, Jun. 2023.

[211] G. Lu *et al.*, "Transcranial focused ultrasound for noninvasive neuromodulation of the visual cortex", *IEEE Trans. Ultrason. Ferroelectr. Freq. Control*, vol. 68, no. 1, pp. 21–28, Jun. 2020.

[212] S. Cadoni *et al.*, "Sonogenetic stimulation of the brain at a spatiotemporal resolution suitable for vision restoration", *BioRxiv*, pp. 2021–11, Nov. 2021.

[213] R. V. Taalla, M. S. Arefin, A. Kaynak, and A. Z. Kouzani, "A review on miniaturized ultrasonic wireless power transfer to implantable medical devices", *IEEE access*, vol. 7, pp. 2092–2106, 2018.

[214] J. Chen, W. Chen, L. Zhang, *et al.*, "Safety of ultrasound-guided ultrasound ablation for uterine fibroids and adenomyosis: A review of 9988 cases", *Ultrasonics sonochemistry*, vol. 27, pp. 671–676, 2015.

[215] J. Qin, J.-Y. Chen, W.-P. Zhao, L. Hu, W.-Z. Chen, and Z.-B. Wang, "Outcome of unintended pregnancy after ultrasound-guided high-intensity focused ultrasound ablation of uterine fibroids", *International Journal of Gynecology & Obstetrics*, vol. 117, no. 3, pp. 273–277, 2012.

[216] A. N. Pouliopoulos, S. Y. Wu, M. T. Burgess, M. E. Karakatsani, H. A. Kamimura, and E. E. Konofagou, "A clinical system for non-invasive blood-brain barrier opening using a neuronavigation-guided single-element focused ultrasound transducer", *Ultrasound Med. Biol.*, vol. 46, no. 1, pp. 73–89, Jun. 2020.

[217] D. Turnbull and F. Foster, "Fabrication and characterization of transducer elements in two-dimensional arrays for medical ultrasound imaging", *IEEE Trans. Ultrason. Ferroelectr. Freq. Control*, vol. 39, no. 4, pp. 464–475, Jul. 1992.

[218] *K-Wave*, version 1.2, 2017. [Online]. Available: http://www.k-wave.org/.

[219] A. Gefen, N. Gefen, Q. Zhu, R. Raghupathi, and S. S. Margulies, "Age-dependent changes in material properties of the brain and braincase of the rat", *Journal of neurotrauma*, vol. 20, no. 11, pp. 1163–1177, 2003.

[220] X. Wang, Z. Yuan, P. Zhuang, T. Wu, and S. Feng, "Study on precision dicing process of SiC wafer with diamond dicing blades", *Nanotechnol. Precis. Eng.*, vol. 4, no. 3, p. 033 004, Jun. 2021.

[221] H. Rivandi, S. Ebrahimi, and M. Saberi, "A low-power rail-to-rail input-range linear delay element circuit", *AEU - International Journal of Electronics and Communications*, vol. 79, pp. 26–32, 2017.

[222] K. Lou, S. Granick, and F. Amblard, "How to better focus waves by considering symmetry and information loss", *Proceedings of the National Academy of Sciences*, vol. 115, no. 26, pp. 6554–6559, 2018.

[223] H. Rivandi, I. Ghosh, and T. L. Costa, "A high-frequency beamforming channel for ultrasound stimulation and ultrasonic powering", in *Proc. IEEE Biomed. Circuits Syst. Conf. (BioCAS)*, Nov. 2022, pp. 40–44.

[224] Y. Xiao, H. Rivandi, and T. L. Costa, "An energy-efficient high-voltage pulser for high-frequency ultrasound medical applications", in *Proc. IEEE Biomed. Circuits Syst. Conf. (BioCAS)*, IEEE, Oct. 2023, pp. 1–5.

[225] *Disco*, 2024. [Online]. Available: https://www.disco.co.jp/eg/products/blade/zhzz.html.

[226] *Disco*, 2024. [Online]. Available: https://www.disco.co.jp/eg/products/blade/z09.html.

[227] G. K. Wardhana, M. Mastrangeli, and T. L. Costa, "Maximization of transmitted acoustic intensity from silicon integrated piezoelectric ultrasound transducers", in *2022 IEEE International Ultrasonics Symposium (IUS)*, IEEE, 2022, pp. 1–4.

[228] C. Van Damme, G. K. Wardhana, A. I. Velea, V. Giagka, and T. L. Costa, "Feasibility study for a high-frequency flexible ultrasonic cuff for high-precision vagus nerve ultrasound neuromodulation", *IEEE Trans. Ultrason. Ferroelectr. Freq. Control*, 2024.

[229] M. Tan *et al.*, "A 64-channel transmit beamformer with±30-V bipolar high-voltage pulsers for catheter-based ultrasound probes", *IEEE J. Solid-State Circuits*, vol. 55, no. 7, pp. 1796–1806, Jul. 2020.

[230] A. Banuaji and H.-K. Cha, "A 15-V bidirectional ultrasound interface analog front-end IC for medical imaging using standard CMOS technology", *IEEE Trans. Circuits Syst. II: Exp. Briefs*, vol. 61, no. 8, pp. 604–608, Aug. 2014.

[231] D. Zhao *et al.*, "High-voltage pulser for ultrasound medical imaging applications", in *Proc. 13th Int. Symp. Integr. Circuits (ISIC)*, 2011, pp. 408–411.

[232] H.-K. Cha, D. Zhao, J. H. Cheong, B. Guo, H. Yu, and M. Je, "A CMOS high-voltage transmitter IC for ultrasound medical imaging applications", *IEEE Trans. Circuits Syst. II: Exp. Briefs*, vol. 60, no. 6, pp. 316–320, 2013.

[233] J. Choi *et al.*, "An energy-replenishing ultrasound pulser with 0.25 CV^2f dynamic power consumption", in *Proc. IEEE Int. Solid-State Circuits Conf. (ISSCC)*, vol. 64, 2021, pp. 486–488.

[234] K. Chen, H.-S. Lee, A. P. Chandrakasan, and C. G. Sodini, "Ultrasonic imaging transceiver design for CMUT: A three-level 30-Vpp pulse-shaping pulser with improved efficiency and a noise-optimized receiver", *IEEE J. Solid-State Circuits*, vol. 48, no. 11, pp. 2734–2745, 2013.

[235] K.-J. Choi, H. G. Yeo, H. Choi, and D.-W. Jee, "A 28.7 V modular supply multiplying pulser with 75.4% power reduction relative to CV^2f", *IEEE Trans. Circuits Syst. II: Exp. Briefs*, vol. 68, no. 3, pp. 858–862, 2020.

[236] G. Jung, C. Tekes, A. Pirouz, F. L. Degertekin, and M. Ghovanloo, "Supply-doubled pulse-shaping high voltage pulser for CMUT arrays", *IEEE Trans. Circuits Syst. II: Exp. Briefs*, vol. 65, no. 3, pp. 306–310, 2017.

[237] G. Jung *et al.*, "Supply-inverted bipolar pulser and Tx/Rx switch for CMUTs above the process limit for high pressure pulse generation", *IEEE Sens. J.*, vol. 19, no. 24, pp. 12 050–12 058, 2019.

[238] J. Tillak, S. Akhbari, N. Shah, L. Radakovic, L. Lin, and J. Yoo, "A 2.34 μJ/scan acoustic power scalable charge-redistribution pMUT interface system with on-chip aberration compensation for portable ultrasonic applications", in *Proc. IEEE Asian Solid-State Circuits Conf.*, 2016, pp. 189–192.

[239] J. Lee *et al.*, "A 36-channel auto-calibrated front-end ASIC for a pMUT-based miniaturized 3-D ultrasound system", *IEEE J. of Solid-State Circuits*, vol. 56, no. 6, pp. 1910–1923, 2021.

[240] H. Wu *et al.*, "An ultrasound ASIC with universal energy recycling for> 7-m all-weather metamorphic robotic vision", *IEEE J. Solid-State Circuits*, vol. 57, no. 10, pp. 3036–3047, 2022.

[241] S. Du and A. A. Seshia, "An inductorless bias-flip rectifier for piezoelectric energy harvesting", *IEEE J. of Solid-State Circuits*, vol. 52, no. 10, pp. 2746–2757, 2017.

[242] J. Choi, S. Youn, J. Y. Hwang, S. Ha, C. Kim, and M. Je, "Energy-efficient high-voltage pulsers for ultrasound transducers", *IEEE Trans. Circuits Syst. II: Exp. Briefs*, vol. 68, no. 1, pp. 19–23, Jan. 2020.

[243] H. S. Yoon *et al.*, "Ex vivo HIFU experiments using a 32×32 element CMUT array", *IEEE Trans. Ultrason. Ferroelectr. Freq. Control*, vol. 63, no. 12, pp. 2150–2158, Sep. 2016.

[244] Z. Zhang *et al.*, "New Sm-PMN-PT ceramic-based 2-D array for low-intensity ultrasound therapy application", *IEEE Trans. Ultrason. Ferroelectr. Freq. Control*, vol. 67, no. 10, pp. 2085–2094, Oct. 2020.

[245] A. Javid, S. Ilham, and M. Kiani, "A review of ultrasound neuromodulation technologies", *IEEE Trans. Biomed. Circuits Syst.*, 2023.

[246] B. Ellenbroek and J. Youn, "Rodent models in neuroscience research: Is it a rat race?", *Disease models & mechanisms*, vol. 9, no. 10, pp. 1079–1087, 2016.

[247] M. D. Döbrössy, C. Ramanathan, D. Ashouri Vajari, Y. Tong, T. Schlaepfer, and V. A. Coenen, "Neuromodulation in psychiatric disorders: Experimental and clinical evidence for reward and motivation network deep brain stimulation: Focus on the medial forebrain bundle", *European Journal of Neuroscience*, vol. 53, no. 1, pp. 89–113, 2021.

[248] L. di Biase, E. Falato, M. L. Caminiti, P. M. Pecoraro, F. Narducci, and V. Di Lazzaro, "Focused ultrasound (FUS) for chronic pain management: Approved and potential applications", *Neurology Research International*, vol. 2021, no. 1, p. 8 438 498, 2021.

[249] K. S. Lee, B. Clennell, T. G. Steward, A. Gialeli, O. Cordero-Llana, and D. J. Whitcomb, "Focused ultrasound stimulation as a neuromodulatory tool for parkinson's disease: A scoping review", *Brain Sciences*, vol. 12, no. 2, p. 289, 2022.

[250] K. Herfert, J. G. Mannheim, L. Kuebler, *et al.*, "Quantitative rodent brain receptor imaging", *Molecular Imaging and Biology*, vol. 22, pp. 223–244, 2020.

[251] J. F. Hou, M. O. G. Nayeem, K. A. Caplan, *et al.*, "An implantable piezoelectric ultrasound stimulator (ImPULS) for deep brain activation", *Nature Communications*, vol. 15, no. 1, p. 4601, 2024.

[252] L. H. Treat, N. McDannold, N. Vykhodtseva, Y. Zhang, K. Tam, and K. Hynynen, "Targeted delivery of doxorubicin to the rat brain at therapeutic levels using MRI-guided focused ultrasound", *International journal of cancer*, vol. 121, no. 4, pp. 901–907, 2007.

[253] K. Hynynen, "MRI-guided focused ultrasound treatments", *Ultrasonics*, vol. 50, no. 2, pp. 221–229, 2010.

[254] Y. Li, J. Lee, X. Long, *et al.*, "A magnetic resonance-guided focused ultrasound neuromodulation system with a whole brain coil array for nonhuman primates at 3 T", *IEEE Transactions on Medical Imaging*, vol. 39, no. 12, pp. 4401–4412, 2020.

[255] F. Wu, Z.-B. Wang, H. Zhu, *et al.*, "Feasibility of us-guided high-intensity focused ultrasound treatment in patients with advanced pancreatic cancer: Initial experience", *Radiology*, vol. 236, no. 3, pp. 1034–1040, 2005.

[256] S. Y. Lee, A. R. Cardones, J. Doherty, K. Nightingale, and M. Palmeri, "Preliminary results on the feasibility of using ARFI/SWEI to assess cutaneous sclerotic diseases", *Ultrasound in medicine & biology*, vol. 41, no. 11, pp. 2806–2819, 2015.

[257] J. Bercoff, M. Tanter, and M. Fink, "Supersonic shear imaging: A new technique for soft tissue elasticity mapping", *IEEE Trans. Ultrason. Ferroelectr. Freq. Control*, vol. 51, no. 4, pp. 396–409, 2004.

[258] C. Maleke and E. E. Konofagou, "In vivo feasibility of real-time monitoring of focused ultrasound surgery (FUS) using harmonic motion imaging (HMI)", *IEEE Transactions on biomedical Engineering*, vol. 57, no. 1, pp. 7–11, 2009.

[259] J. D'hooge, A. Heimdal, F. Jamal, *et al.*, "Regional strain and strain rate measurements by cardiac ultrasound: Principles, implementation and limitations", *European Journal of Echocardiography*, vol. 1, no. 3, pp. 154–170, 2000.

[260] L. Sandrin, M. Tanter, J.-L. Gennisson, S. Catheline, and M. Fink, "Shear elasticity probe for soft tissues with 1-d transient elastography", *IEEE Trans. Ultrason. Ferroelectr. Freq. Control*, vol. 49, no. 4, pp. 436–446, 2002.

[261] M. Tanter and M. Fink, "Ultrafast imaging in biomedical ultrasound", *IEEE Trans. Ultrason. Ferroelectr. Freq. Control*, vol. 61, no. 1, pp. 102–119, 2014.

[262] K. Nightingale, M. S. Soo, R. Nightingale, and G. Trahey, "Acoustic radiation force impulse imaging: In vivo demonstration of clinical feasibility", *Ultrasound in medicine & biology*, vol. 28, no. 2, pp. 227–235, 2002.

[263] A. P. Sarvazyan, O. V. Rudenko, S. D. Swanson, J. B. Fowlkes, and S. Y. Emelianov, "Shear wave elasticity imaging: A new ultrasonic technology of medical diagnostics", *Ultrasound in medicine & biology*, vol. 24, no. 9, pp. 1419–1435, 1998.

[264] J. Janjic, M. Tan, V. Daeichin, *et al.*, "A 2-D ultrasound transducer with front-end ASIC and low cable count for 3-D forward-looking intravascular imaging: Performance and characterization", *IEEE Trans. Ultrason. Ferroelectr. Freq. Control*, vol. 65, no. 10, pp. 1832–1844, 2018.

[265] W. Guo, Y. Wang, and J. Yu, "A sibelobe suppressing beamformer for coherent plane wave compounding", *Applied Sciences*, vol. 6, no. 11, p. 359, 2016.

[266] M. Tan, C. Chen, Z. Chen, *et al.*, "A front-end ASIC with high-voltage transmit switching and receive digitization for 3-D forward-looking intravascular ultrasound imaging", *IEEE J. Solid-State Circuits*, vol. 53, no. 8, pp. 2284–2297, 2018.

[267] C. Chen, Z. Chen, Z.-y. Chang, and M. A. Pertijs, "A compact 0.135-mW/channel LNA array for piezoelectric ultrasound transducers", in *ESSCIRC Conference 2015-41st European Solid-State Circuits Conference (ESSCIRC)*, IEEE, 2015, pp. 404–407.

[268] K. Shepard, T. Costa, K. Tien, and C. Shi, *Ultrasound phased array patch on flexible cmos and methods for fabricating thereof*, US Patent 11,937,981, Mar. 2024.

[269] K. Kaviani, O. Oralkan, P. Khuri-Yakub, and B. A. Wooley, "A multichannel pipeline analog-to-digital converter for an integrated 3-D ultrasound imaging system", *IEEE Journal of Solid-State Circuits*, vol. 38, no. 7, pp. 1266–1270, 2003.

[270] C.-C. Liu, S.-J. Chang, G.-Y. Huang, and Y.-Z. Lin, "A 10-bit 50-MS/s SAR ADC with a monotonic capacitor switching procedure", *IEEE Journal of Solid-State Circuits*, vol. 45, no. 4, pp. 731–740, 2010.

[271] P. Krummenacher and H. Oguey, "Smart temperature sensor in CMOS technology", *Sensors and Actuators A: Physical*, vol. 22, no. 1-3, pp. 636–638, 1990.

[272] P.-C. Chu, H.-L. Liu, H.-Y. Lai, C.-Y. Lin, H.-C. Tsai, and Y.-C. Pei, "Neuromodulation accompanying focused ultrasound-induced blood-brain barrier opening", *Scientific reports*, vol. 5, no. 1, p. 15 477, 2015.

[273] H. Zhu, F. Hu, H. Zhou, D. Z. Pan, D. Zhou, and X. Zeng, "Interlayer cooling network design for high-performance 3D ICs using channel patterning and pruning", *IEEE Transactions on Computer-Aided Design of Integrated Circuits and Systems*, vol. 37, no. 4, pp. 770–781, Jul. 2017.

List of Publications

1. **H. Rivandi**, G. Wardhana, E. Sarkar, M. Aqamolaei, and S. Desmarais, T. Costa, "Miniaturized and Conformable Focused Ultrasound Neurostimulators," in *Proc. Bioelectronic Interfaces: Mater. Devices and Applications (CyBioEl)*, Jun. 2024, pp. 1-5.

2. Y. Xiao, **H. Rivandi**, and T. L. Costa, "An Energy-Efficient High-Voltage Pulser for High-Frequency Ultrasound Medical Applications," in *Proc. IEEE Biomed. Circuits Syst. Conf. (BioCAS)*, Oct. 2023, pp. 1-5.

3. A. Rashidi, **H. Rivandi**, M. Grubor, A. Agostinho, V. Sádio, M. Santos, W. Serdijn, and V. Giagka, "Delta-Sigma Control Loop For Energy-Efficient Electrical Stimulation with Arbitrary-Shape Stimuli," in *Proc. IEEE Biomed. Circuits Syst. Conf. (BioCAS)*, Oct. 2023, pp. 1-5.

4. **H. Rivandi**, and T. L. Costa, "A 2D Ultrasound Phased-Array Transmitter ASIC for High-Frequency US Stimulation and Powering," in *IEEE Trans. Biomed. Circuits Syst.*, vol. 17, no. 4, pp. 701-712, June 2023.

5. **H. Rivandi**, I. Ghosh, and T. L. Costa, "A High-Frequency Beamforming Channel for Ultrasound Stimulation and Ultrasonic Powering," in *Proc. IEEE Biomed. Circuits Syst. Conf. (BioCAS)*, Oct. 2022, pp. 40-44.

6. **H. Rivandi**, E. Sarkar, G. Wardhana, and T. L. Costa, "An US-Guided 2D Phased Array US Transducer for Preclinical US Neuromodulation Studies," in preparation.